

**Structure-Reactivity Relationships in Heterogeneous  
Catalytic CO<sub>2</sub> Hydrogenation to CH<sub>4</sub> and CO on Low  
Loaded Precious Metal Catalysts**

**Dissertation**

Zur Erlangung des akademischen Grades

*doctor rerum naturalium (Dr. rer. nat.)*

der mathematisch-naturwissenschaftlichen Fakultät der

Universität Rostock

**vorgelegt von**

M.Sc. Sebastian Cisneros

Geboren am 11. Februar 1988 in Kolumbien

Rostock, 2024

**Gutachter:**

1. Gutachterin: Prof. Dr. Angelika Brückner

Leibniz Institut für Katalyse e.V. an der Universität Rostock

2. Gutachter: Prof. Dr. Jürgen Behm

Seniorprofessor

Institut für Theoretische Chemie, Universität Ulm

**Datum der Einreichung:** 30. August 2023

**Datum der Verteidigung:** 23. Januar 2024

*“Conservation and use of alternate energy sources are most desirable, but they cannot replace, by themselves, the “classic” energy sources in fulfilling mankind’s enormous energy demand.” George A. Olah in “Beyond Oil and Gas: The Methanol Economy”*

## Zusammenfassung

Niedrigbeladenen Edelmetall Katalysatoren wurden für die Herstellung von CH<sub>4</sub> und CO mittels der Hydrierung von CO<sub>2</sub> untersucht. Struktur-Reaktivität Beziehungen und Reaktionswege wurden anhand in-situ und ex-situ Charakterisierungen vorgeschlagen.

Die CO<sub>2</sub> Methanierung wurde an Ru/TiO<sub>2</sub> und Ru/ZrO<sub>2</sub> Katalysatoren recherchiert. Der Umsatzgrad des CO<sub>2</sub> auf einen sol-gel synthetisierten 0.9 wt.% Ru/TiO<sub>2</sub> Katalysator (100 % CH<sub>4</sub> Selektivität) übertraf die Leistung eines Ru/TiO<sub>2</sub> Katalysators mit geringer Sauerstoff Defektzahl und gleichen Ru Beladung, der durch konventionelle Imprägnierung hergestellt wurde. Zusätzlich wurden für dieselbe Reaktion Ru/ZrO<sub>2</sub> und MgO modifizierte Ru/ZrO<sub>2</sub> Katalysatoren verwendet, die durch Nassimprägnierung mit ca. 0.4 wt.% Ru hergestellt wurden. Der Katalysator mit einer größeren Menge an Sauerstoff Defekten (O-Defekten) mit 2.6 wt.% MgO zeigte wieder die höchste CH<sub>4</sub> Reaktionsgeschwindigkeit. Gemäß in-situ Spektroskopien ist der Anstieg der CH<sub>4</sub> Erzeugung auf die geförderte Destabilisierung der Zwischenprodukte (Formiat/Carbonyl) durch Elektronentransfer von O-Defekten zu aktiven Ru-Grenzflächenstellen zurückzuführen. Außerdem, obwohl mehrere Ru-CO Spezies identifiziert wurden, erwies sich nicht die gesamte Ru-CO Schicht als aktiv gegenüber CH<sub>4</sub>.

Für die Erzeugung von CO durch der umgekehrte Wasser-Gas-Shift Reaktion (RWGS) wurden Au/ZrO<sub>2</sub> und Au/TiO<sub>2</sub> Katalysatoren mit Au < 0.1 wt.% erforscht. Die Unterschiede zwischen den intrinsischen Aktivitäten wurden mit den verschiedenen elektronischen Wechselwirkungen an der Metall-Träger Grenze verbunden. Solche Interaktionen sind im Fall des höchstens defektives Au/TiO<sub>2</sub> Katalysators stärker ausgeprägt worden. In-situ Charakterisierung Techniken bewiesen, dass sowohl Hydroxycarbonyl (HOCO) als auch Formiat Spezies Zwischenprodukte für CO-Entwicklung sind. Dennoch wird einen Aufstieg der Reaktionsgeschwindigkeit beobachtet, im Gegenteil zu CO<sub>2</sub> Methanierung, wenn Formiat nicht als Primäres Zwischenprodukt gebildet wird.

Die Dissertation besteht aus 4 Kapiteln. Stand der Technik (Power to X Begriff), Grundlagen der Thermodynamik, Katalysator Eigenschaften, Reaktion Mechanismen und photo- und elektrochemisch Ansätze für CO<sub>2</sub> Aktivierung sind in **Kapitel 1** bemerkt. **Kapitel 2** befasst sich mit der Beschreibung von Synthese Methoden und verschiedene in-situ und ex-situ Charakterisierung Techniken für die Messung und Etablierung von Struktur-Reaktivität Beziehungen. Experimentelle Ergebnisse sind in **Kapitel 3** diskutiert. **Kapitel 4** erläutert sowohl die wichtigsten Schlussfolgerungen als auch die Perspektive der CO<sub>2</sub> Hydrierung.

## Abstract

The production of CH<sub>4</sub> and CO via CO<sub>2</sub> hydrogenation was studied on catalysts with low precious metal loading. Structure-reactivity relationships and reaction pathways were proposed according to in-situ and ex-situ characterization results.

The CO<sub>2</sub> methanation was investigated on Ru/TiO<sub>2</sub> and Ru/ZrO<sub>2</sub> catalysts. The conversion of CO<sub>2</sub> on a sol-gel prepared 0.9 wt.% Ru/TiO<sub>2</sub> catalyst (100 % CH<sub>4</sub> selectivity) overcome that of another less oxygen defective Ru/TiO<sub>2</sub> catalyst with the same Ru loading prepared via conventional impregnation. In addition, the same reaction was studied on Ru/ZrO<sub>2</sub> and MgO modified Ru/ZrO<sub>2</sub> catalysts prepared via wet impregnation with ca. 0.4 wt.% Ru. The catalyst with higher amount of oxygen vacancies (O-vacancies) with 2.6 wt.% MgO showed again the highest CH<sub>4</sub> rate. The increase of the CH<sub>4</sub> production is associated, according to in-situ spectroscopies, to the promoted destabilization of intermediates (format/carbonyl) by the electron transfer from O-vacancies to active interfacial Ru sites. Moreover, although several Ru-CO species were identified, not all the formed Ru-CO layer was found active to CH<sub>4</sub>.

The formation of CO via the reverse water gas shift reaction (RWGS) was studied on Au/ZrO<sub>2</sub> and Au/TiO<sub>2</sub> catalysts with < 0.1 wt.% Au. The differences in the intrinsic activities were associated to the distinct electronic interactions between the supported metal and the supporting matrix, being more pronounced in the case of the most active and defective Au/TiO<sub>2</sub> catalyst. In-situ characterization techniques indicated that hydroxycarbonyl (HOCO) and formate are intermediates in the reaction. However, in contrast to CO<sub>2</sub> methanation, an increase in the reaction rate can be observed when formate like species do not participate as the main intermediates.

The thesis is divided in 4 chapters. In **chapter 1** the state of the art (Power to X concept), fundamental thermodynamic aspects regarding equilibrium limitations, catalyst properties, reaction mechanisms, and photo- and electrochemical approaches for activation of CO<sub>2</sub> are mentioned. **Chapter 2** is dedicated to the description of the synthesis methods and different ex-situ and in-situ techniques used for the characterization and assessments of reactivity-structure relationships of the target catalysts. The results and discussion are presented in detail in **Chapter 3**. **Chapter 4** puts forward the main conclusions and future perspectives of CO<sub>2</sub> hydrogenation.

## Danksagung

Ich möchte zuerst mich bei **Prof. Dr. Angelika Brückner** bedanken, die mir die Möglichkeit in Ihrer Forschungsgruppe mitzuarbeiten gegeben hat. Besonderer Dank geht an **Dr. Jabor Rabeah**, der mir, in diesen 3 Jahren unterstützt hat. Er hat mit vergnügen seine Erfahrung mit mir geteilt, um die besten Ergebnisse meiner Forschung zu ermöglichen.

Außerdem möchte ich mich bei den Mitarbeitern, die verschiedene Messungen für die Charakterisierung der Katalysatoren durchgeführt haben. **Dr. Nils Rockstroh** and **Dr. Carsten Kreyenschulte** (Elektronenmikroskopie), **Frau Anja Simmula** (ICP-OES), **Dr. Stephan Bartling** (XPS), **Dr. Henrik Lund** (XRD), **Dr. Hanan Atia** (H<sub>2</sub>-TPR), **Herr Reinhard Eckelt** (N<sub>2</sub> Adsorption), **Dr. Dan Zhao** (RWGS-Reaktion). Abschließend, möchte ich mich auch für die Hilfe von **Herr Haider Abed**, **Frau Lorena Santa** und **Frau Laura Martinez** bedanken.

Eine besondere Auszeichnung gilt auch **Dr. Jawaher Mosrati**, die den Ru/TiO<sub>2</sub> sol-gel Katalysator vorbereitete. Ebenso bedanke ich mich bei **Dr. Abdallah Rabea**, der die Synthese der Au-basierte Katalysatoren durchgeführte und akzeptierte, dass ich Teil der entsprechenden Ergebnisse für diese Dissertation benutzte.

Natürlich, ich muss hier **Dr. Ali-Abdel Mageed** erwähnen, weil er den Kontakt zwischen Dr. Rabeah und Ich förderte.

Abschließend möchte ich meiner Familie für ihre Unterstützung trotz der Entfernung danken.

## Motivation and Objectives

Intensive anthropogenic activities cause continuous accumulation of CO<sub>2</sub> in the atmosphere. Natural sinks (plants, ocean, soil) cannot process these emissions at the same rate as they are produced by the human being. Consequently, the atmospheric CO<sub>2</sub> concentration has shown an increasing trend during decades (**Figure 1**) and by 2022 reached an historical record of 414.7 ppm.<sup>1</sup> The last report from the UN environment program ([Emissions Gap Report 2021 \(unep.org\)](#)) predicts an increase in the average global temperature of about 2.7 °C by the end of the 21st century. This is well above the goals of the Paris (2015) and Glasgow (COP26 2021) climate agreements and calls for more efficient policies and decisions come in practice.

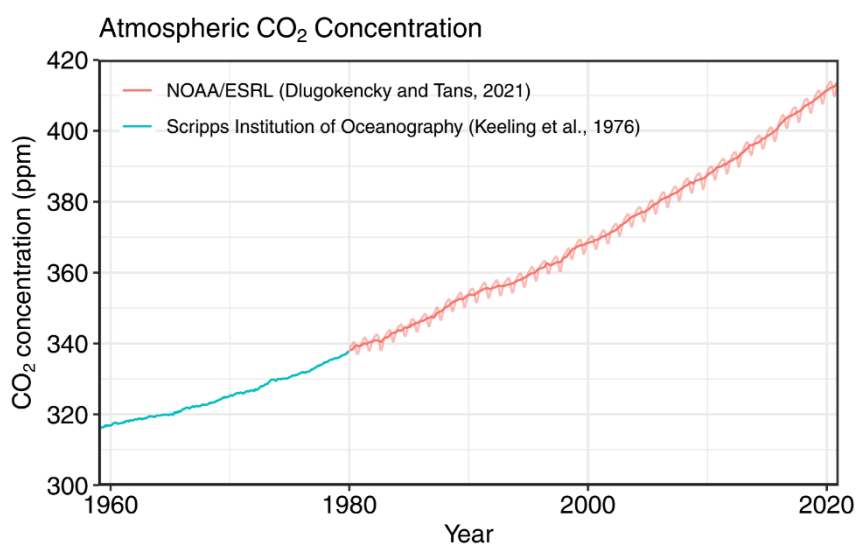


**Figure 1.** Surface average atmospheric CO<sub>2</sub> concentration (ppm).<sup>1</sup>

The burning of fossil fuels represents the highest contribution to CO<sub>2</sub> emissions.<sup>2</sup> Around 80 % of the primary energy is provided by these energy sources ([Energy Outlook | Energy economics | Home \(bp.com\)](#)). Among them, the major fraction of CO<sub>2</sub> arises from coal with ca. 46 % of the emissions followed by oil with 35 % and finally natural gas with about 14 %.<sup>1</sup> In addition, these fossil sources serve as raw materials for other production chains that generate further CO<sub>2</sub> emissions.<sup>3,4</sup> Accordingly, reducing CO<sub>2</sub> emissions via its conversion into valuable products, replacing fossil fuels, is one option to approach the problematic caused by this greenhouse gas. The reaction between CO<sub>2</sub> and H<sub>2</sub> can produce high energy density and feedstock molecules such as CH<sub>4</sub>, CO, CH<sub>3</sub>OH or C<sub>2+</sub> compounds (short olefines, alcohols). If the capture and transformation of CO<sub>2</sub> is focused on this type of strategical products, realistic advances in the mitigation of climate change could be foreseeable.<sup>5-9</sup>

The expansion of the use of renewable sources, e.g., wind and solar power, opens the door to such possibility. Electricity production by these seasonal means can surpass the demand in periods at which wind or solar irradiation are strong. Such excess energy can be stored in form of chemical energy carriers, e.g., H<sub>2</sub>, via water electrolysis. However, H<sub>2</sub> is a molecule with low volumetric energy density of ca. 0.0107 MJ l<sup>-1</sup> at normal conditions. Hence, its storage and transport demand for high pressure, and eventually, cryogenic conditions (~ -253 °C). For example, the energy density at 700 bar for gaseous H<sub>2</sub> reaches 5.6 MJ l<sup>-1</sup> and at the same pressure but T ~ -253 °C increases to ca. 10 MJ l<sup>-1</sup>. These values are still far below than those of CH<sub>4</sub> (9 MJ l<sup>-1</sup> at 250 bar) or liquid fuels (~ 33 – 34 MJ l<sup>-1</sup> at normal conditions).<sup>10</sup> That is, storing H<sub>2</sub> is energy intensive, requires very specific infrastructure, and is not competitive with traditional energy carriers. This encourages the use of molecules with superior volumetric energy density and available efficient infrastructure for its transport and storage as solution for chemical storage of electric energy. In this sense, CH<sub>4</sub> is highly attractive for this task as it possesses superior volumetric energy density than H<sub>2</sub> and is chemically compatible with the actual natural gas transport infrastructure.<sup>5, 11-15</sup>

Given the potential of CO<sub>2</sub> methanation in the context of CO<sub>2</sub> emissions mitigation, intensive research has been done to determine the requirements of reaction conditions and catalytic materials to optimize the process.<sup>16, 17</sup> In general, due to heat release and equilibrium limitations, it is desirable to drive the reaction below 300 °C.<sup>18, 19</sup> At such conditions, the reaction rates could be very limited on many catalytic materials. However, Ru based catalysts are known to cover this need as they show excellent activity and selectivity at mild conditions when compared with catalysts based on more abundant active metals, e.g., Ni, Fe, Co.<sup>20</sup> Yet, the high prices of this element and its precursors calls for minimizing the metal loading of Ru based catalysts to make them competitive for medium and large scale applications.<sup>19</sup> Although TiO<sub>2</sub> and ZrO<sub>2</sub> have been shown to be adequate supports for Ru,<sup>21, 22</sup> their use with Ru loading below 1 wt.% is barely found in the literature. This motivates to search for strategies to develop Ru/TiO<sub>2</sub> and Ru/ZrO<sub>2</sub> catalysts with such low Ru contents that can properly behave for CO<sub>2</sub> methanation at mild conditions.

Besides CO<sub>2</sub> methanation, the RWGS reaction represents another example of CO<sub>2</sub> valorization.<sup>23</sup> CO is an important chemical feedstock in a variety of well-established catalytic processes at industrial scales, e.g., Fischer–Tropsch (FT) synthesis.<sup>24</sup> Therefore, the search for stable, active, and selective heterogeneous catalysts to convert CO<sub>2</sub> into CO is a worthwhile task to produce carbon neutral compounds, e.g., liquid fuels for the transportation sector, especially in decentralized compact plants for which the chemical processes can be relatively



easy electrified by renewable electricity.<sup>25</sup> Au based catalysts are very suitable for the RWGS reaction since they can operate at mild conditions, i.e., < 400 °C, with excellent activity and selectivity. Nevertheless, to implement them in CO<sub>2</sub> hydrogenation at relevant scales requires also to minimize the Au loading while conserving high performance at low temperatures.<sup>26</sup> Au/TiO<sub>2</sub> catalysts have been extensively studied,<sup>27-30</sup> yet, information about these catalysts with Au well below 0.1 wt.% is so far not explored. Meanwhile, the establishment of structure-reactivity relationships of Au/ZrO<sub>2</sub> catalysts in this reaction is less widespread, even, for the case of typical Au loadings beyond 1 wt.%. Hence, Developing Au/TiO<sub>2</sub> and Au/ZrO<sub>2</sub> catalysts with Au loadings as low as 0.1 wt% is highly motivating to provide new insights into the reactivity-structure relationships of these materials for the RWGS reaction. Moreover, it is of high relevance to explore ways to promote CO selectivity under non-typical conditions for RWGS, e.g., at pressures greater than 1 bar and H<sub>2</sub>:CO<sub>2</sub> ratio > 1:1, at which RWGS competes with methane or even methanol production.<sup>31</sup>

It is the spirit of this thesis, instead of discouraging the implementation of precious elements in the catalytic transformation of CO<sub>2</sub>, to take advantage of associated electronic modifications induced by O-vacancies to design catalysts with minimized precious metal loadings but high activity and selectivity. Accordingly, this work is focused on the following aspects:

- i) Develop highly active and selective catalysts for CO<sub>2</sub> hydrogenation to CH<sub>4</sub> and CO at mild conditions by means of Ru and Au based catalysts with metal loading < 1 wt.%
- ii) Perform systematic investigations for the elucidation of the active sites, intermediates and reaction mechanisms involved in the transformation of CO<sub>2</sub> to the targeted products supported on multiple in-situ spectroscopies.
- iii) Highlight the role of oxygen defects in the respective structure-reactivity relationships.

## Contents

1. State of the Art.....	1
1.1. Power to X concept: CO <sub>2</sub> methanation and RWGS reaction in the practice	1
1.2. Thermodynamics of CO <sub>2</sub> hydrogenation .....	4
1.3. Catalysts for CO <sub>2</sub> methanation and RWGS reaction .....	7
1.4. Catalysts properties that affect the hydrogenation of CO <sub>2</sub> .....	10
1.5. CO <sub>2</sub> hydrogenation mechanisms .....	13
1.6. CO <sub>2</sub> hydrogenation by approaches different to thermal catalysis	18
2. Experiments and Methods .....	19
2.1. Materials preparation.....	20
2.2. Characterization techniques .....	24
3. Results and Discussion .....	44
3.1. CO <sub>2</sub> methanation on Ru/TiO <sub>2</sub> catalysts.....	44
3.2. CO <sub>2</sub> methanation on Ru/ZrO <sub>2</sub> and MgO modified Ru/ZrO <sub>2</sub> .....	63
3.3. Summary of results of CO <sub>2</sub> methanation on Ru catalysts.....	83
3.4. The RWGS reaction on ultra-low Au loaded Au/TiO <sub>2</sub> and Au/ZrO <sub>2</sub> catalysts	84
4. General Conclusions and Outlook.....	100
Appendix.....	101
A1. Gibbs free energy minimization method.....	101
A2. Additional information for chapter 3 .....	102
References .....	114
Lebenslauf .....	132

👤	Personal data .....	132
🎓	Education.....	132
✍️	List of publications .....	132
★	Oral presentations .....	133

### List of figures

<b>Figure 1.</b> Surface average atmospheric CO <sub>2</sub> concentration (ppm). <sup>1</sup> .....	iv
<b>Figure 2.</b> Schematic representation of CO <sub>2</sub> transformation to useful compounds by catalytic reaction with H <sub>2</sub> .....	1
<b>Figure 3.</b> Mean plant size (total, H <sub>2</sub> projects, CH <sub>4</sub> projects) and their floating means for the years 1993 – 2018. <sup>5</sup> .....	2
<b>Figure 4.</b> Simulation of process profitability for CO production. Conditions: 1:1 H <sub>2</sub> :CO <sub>2</sub> , 750 °C, 1.013 bar. Vertical lines indicate reported prices for grey, blue and green H <sub>2</sub> . <sup>39</sup> .....	3
<b>Figure 5.</b> CO <sub>2</sub> equilibrium conversion as function of temperature for distinct H <sub>2</sub> :CO <sub>2</sub> ratios at 1 and 3 bar (a-c). Equilibrium selectivity to CH <sub>4</sub> , CO, C and CH <sub>3</sub> OH as function of temperature for distinct H <sub>2</sub> :CO <sub>2</sub> ratios at 1 and 3 bar (d-f). The calculations were based on the Gibbs free energy minimization method using Aspen Plus V11. ....	6
<b>Figure 6.</b> a) Molecular orbital diagram of CO <sub>2</sub> and b) Molecular orbital diagram of CO <sub>2</sub> <sup>-</sup> .....	14
<b>Figure 7.</b> CO <sub>2</sub> hydrogenation mechanisms. Modified from references <sup>41, 52, 53, 137</sup> .....	14
<b>Figure 8.</b> a) Principle of photoexcited electron-hole pair formation. Taken from Álvarez et al. <sup>125</sup> and b) schematic example of photochemical cell to produce compounds from CO <sub>2</sub> photocatalysis. Taken from Chang et al. <sup>138</sup> .....	18

<b>Figure 9.</b> a) Scheme of laboratory electrochemical cell used for CO <sub>2</sub> hydrogenation and b) cathode materials and main products obtained during CO <sub>2</sub> electro-reduction. Taken from Kondratenko et al. <sup>139</sup> .....	19
<b>Figure 10.</b> Scheme of the harmonic and anharmonic potential. The arrows represent the allowed transitions. ....	25
<b>Figure 11.</b> Setup for DRIFTS assessments. Inset: praying mantis™ high temperature reaction chamber. ....	27
<b>Figure 12.</b> a) Light scattering from an oscillating molecule and b) schematic example of Raman active and Raman inactive transitions for CO <sub>2</sub> stretch changes upon interaction with a photon. ....	28
<b>Figure 13.</b> a) Alignment of the spin vector of a free electron ( $S = 1/2$ ) with the direction of the external magnetic field; b) energy levels of free electron in an external magnetic field with the expected EPR signal. ....	30
<b>Figure 14.</b> Energy splitting, transitions and expected EPR spectrum in the situation of a paramagnetic electron interacting with a nucleus with nuclear spin = 1. ....	31
<b>Figure 15.</b> a) Set-up for in-situ EPR assessments and b) quartz reactor. Photo in b) taken from Bonke et al. <sup>149</sup> .....	32
<b>Figure 16.</b> Excitation of a core electron (photoelectron) by the absorption of a photon with energy $E = h\nu$ . ....	34
<b>Figure 17.</b> Scheme showing the interaction between an electron beam with a sample and the type of generated signals during a typical electron microscopy experiment. ....	35
<b>Figure 18.</b> Principle of XRD (Bragg's condition). ....	36
<b>Figure 19.</b> N <sub>2</sub> adsorption isotherms of a) fresh bare TiO <sub>2</sub> -SG support; b) fresh Ru/TiO <sub>2</sub> -SG; c) fresh Ru/TiO <sub>2</sub> -Imp. Pore volume and specific pore area of d) fresh bare TiO <sub>2</sub> -SG support; e) fresh Ru/TiO <sub>2</sub> -SG; f) fresh Ru/TiO <sub>2</sub> -Imp. ....	46
<b>Figure 20.</b> a) XRD powder patterns of the fresh TiO <sub>2</sub> -SG support and fresh Ru catalysts; b) XRD powder patterns of Ru catalysts after 6h reaction in	

H<sub>2</sub>:CO<sub>2</sub>=4:1 flow up to 270 °C; c) Raman spectra of the fresh materials; d) H<sub>2</sub> TPR spectra of the bare TiO<sub>2</sub>-SG support, Ru/TiO<sub>2</sub>-SG and Ru/TiO<sub>2</sub>-Imp catalysts. .... 47

**Figure 21.** HAADF-STEM images and selected EDX spectra of fresh Ru/TiO<sub>2</sub>-SG a, b) and fresh Ru/TiO<sub>2</sub>-Imp c, d). .... 48

**Figure 22.** HAADF-STEM images of a, b) fresh Ru/TiO<sub>2</sub>-SG and c, d) Ru/TiO<sub>2</sub>-Imp. The red arrows indicate big particles/conglomerates formed on Ru/TiO<sub>2</sub>-Imp..... 49

**Figure 23.** HAADF-STEM images of a, b) spent Ru/TiO<sub>2</sub>-SG and c, d) Ru/TiO<sub>2</sub>-Imp. The red arrows indicate big particles/conglomerates formed on Ru/TiO<sub>2</sub>-Imp..... 50

**Figure 24.** a) CO<sub>2</sub> conversion and CH<sub>4</sub> selectivity on Ru/TiO<sub>2</sub>-Imp and Ru/TiO<sub>2</sub>-SG; b) CH<sub>4</sub> formation rates at different temperatures normalized on the Ru mass in Ru/TiO<sub>2</sub>-Imp and Ru/TiO<sub>2</sub>-SG; c) Apparent activation energy for CH<sub>4</sub> formation on Ru/TiO<sub>2</sub>-Imp and Ru/TiO<sub>2</sub>-SG; d) Ru mass normalized methane rate on Ru/TiO<sub>2</sub>-Imp and Ru/TiO<sub>2</sub>-SG assessed at 190 °C during 1000 min. Gas mixture: H<sub>2</sub>:CO<sub>2</sub> = 4:1 (24 ml min<sup>-1</sup> H<sub>2</sub>, 6 ml min<sup>-1</sup> CO<sub>2</sub>). .... 51

**Figure 25.** NAP-XP Spectra in the Ru 3d and C1s region of Ru/TiO<sub>2</sub>-SG and Ru/TiO<sub>2</sub>-Imp catalysts at different conditions: a, g) Fresh catalysts at RT in He; b, h) Pre-oxidation at 150 °C in 5 vol.% O<sub>2</sub>/He; c-k) Reaction in H<sub>2</sub> :CO<sub>2</sub> = 4:1 at different temperatures. Experimental (black line) and fitted (green line) NAP-XPS spectra at a total pressure of 2 mbar, including deconvoluted sub signals. .... 54

**Figure 26.** a, b) EPR spectra of Ru/TiO<sub>2</sub>-SG and Ru/TiO<sub>2</sub>-Imp catalysts up to 270 °C at different stages. The corresponding temperature at which the spectra were recorded is indicated in the figure; c) EPR spectra of the as received samples; d) EPR spectra of the samples after 6h reaction up to 270 °C. All spectra in c) and d) were recorded at -173 °C. .... 56

**Figure 27.** In-situ DRFT spectra recorded at 150 °C. Left side: Spectra of Ru/TiO<sub>2</sub>-SG a) C-H region, b) C-O region, c) O-C-O region. Right side: Spectra of Ru/TiO<sub>2</sub>-Imp d) C-H region, e) C-O region, f) O-C-O region. From bottom to top: 0-90 min. Flow conditions: H<sub>2</sub>:CO<sub>2</sub> = 4:1 (22.4 ml min<sup>-1</sup> H<sub>2</sub>, 5.6 ml min<sup>-1</sup> CO<sub>2</sub>, 2 ml min<sup>-1</sup> He)..... 59

**Figure 28.** In-situ DRIFT spectra during CO adsorption at 30 °C on the spent Ru/TiO<sub>2</sub>-SG and Ru/TiO<sub>2</sub>-Imp catalysts after 5 min reaction a) and on the spent catalysts after 6 h reaction b). Flow conditions: 30 ml min<sup>-1</sup> 5 vol.% CO/He. .... 61

**Figure 29.** Schematic representation of formation of O-vacancies and metallic Ru (A, B) and their role for activation of CO<sub>2</sub> (C) and H<sub>2</sub> (D)..... 63

**Figure 30.** XRD powder patterns of a) fresh ZrO<sub>2</sub> and Ru/ZrO<sub>2</sub>; b) fresh ZrO<sub>2</sub>-MgO and Ru/ZrO<sub>2</sub>-MgO..... 65

**Figure 31.** a) H<sub>2</sub>-TPR and b-e) CO<sub>2</sub>-TPD spectra of the fresh supports and supported Ru catalysts up to 350 °C. Blue, green, and purple peak represent the deconvoluted signals. The numbers indicate the peak temperature of each desorption signal..... 66

**Figure 32.** Representative HAADF-STEM images, EDX spectra recorded on selected regions and EDX map of fresh (a – c) and spent Ru/ZrO<sub>2</sub>-MgO (d – f) (Zr: green, Ru: red, Mg: yellow). The spent material was investigated after reaction at 270 °C. .... 67

**Figure 33.** a) Ru mass normalized CH<sub>4</sub> formation rate on Ru/ZrO<sub>2</sub> (black diamonds) and Ru/ZrO<sub>2</sub>-MgO (red stars) in the temperature range 220 – 300 °C; b) Arrhenius plot and activation energies for Ru/ZrO<sub>2</sub> (black diamonds) and Ru/ZrO<sub>2</sub>-MgO (red stars) in the temperature range 220 – 300 °C; c) CO<sub>2</sub> conversion and selectivity to CH<sub>4</sub> on Ru/ZrO<sub>2</sub> (black diamonds) and Ru/ZrO<sub>2</sub>-MgO (red stars) for 24 h reaction at 250 °C; d) CO<sub>2</sub> conversion and selectivity to CH<sub>4</sub> on Ru/ZrO<sub>2</sub>-MgO for ca. 100 h reaction at 300 °C (black squares) and 350

°C (red circles). Inlet gas flow conditions in all cases: 16 ml min<sup>-1</sup> H<sub>2</sub>, 4 ml min<sup>-1</sup> CO<sub>2</sub>, 10 ml min<sup>-1</sup> N<sub>2</sub>. ..... 69

**Figure 34.** XP spectra in the Ru 3p region of the fresh and spent Ru/ZrO<sub>2</sub> catalyst (a, b) and of fresh and spent Ru/ZrO<sub>2</sub>-MgO catalyst (c, d). The spectra corresponding to the spent catalysts were recorded after reaction at 270 °C. .... 71

**Figure 35.** EPR spectra recorded at -173 °C of a) ZrO<sub>2</sub> and Ru/ZrO<sub>2</sub>; b) ZrO<sub>2</sub>-MgO and Ru/ZrO<sub>2</sub>-MgO. The black lines represent the spectra of the bare supports while the red lines represent the spectra of the catalysts. All the spectra were recorded in He atmosphere after oxidative pre-treatment. .... 73

**Figure 36.** EPR spectra recorded at -173 °C of a) ZrO<sub>2</sub> and Ru/ZrO<sub>2</sub>; b) ZrO<sub>2</sub>-MgO and Ru/ZrO<sub>2</sub>-MgO. The black lines represent the spectra of the bare supports while the red lines represent the spectra of the catalysts. All the spectra were recorded after reaction and under H<sub>2</sub>:CO<sub>2</sub> = 4:1 atmosphere. .... 74

**Figure 37.** DRIFT spectra recorded at 250 °C on a) Ru/ZrO<sub>2</sub> and b) Ru/ZrO<sub>2</sub>-MgO. The total reaction time was set to 1 h (from bottom to top). Inlet gas flow conditions: 16 ml min<sup>-1</sup> H<sub>2</sub>, 4 ml min<sup>-1</sup> CO<sub>2</sub>, 10 ml min<sup>-1</sup> He. .... 75

**Figure 38.** DRIFT spectra recorded at 250 °C on the spent catalysts: a) Ru/ZrO<sub>2</sub> and b) Ru/ZrO<sub>2</sub>-MgO after He purge overnight at RT and 3 h purging also in He at 250 °C. The first spectrum from top to bottom correspond to the catalyst before H<sub>2</sub> admission. The total time was set to 30 min. Inlet gas flow conditions after switch (second spectrum from top to bottom): 16 ml min<sup>-1</sup> H<sub>2</sub>, 14 ml min<sup>-1</sup> He. .... 77

**Figure 39.** Normalized integral decay of the bands resolved in the spectra recorded at 250 °C during the dynamic experiment presented in **Figure 38**. a) Ru/ZrO<sub>2</sub> and b) Ru/ZrO<sub>2</sub>-MgO. The total time was set to 30 min. Inlet gas flow conditions after switch: 16 ml min<sup>-1</sup> H<sub>2</sub>, 14 ml min<sup>-1</sup> He. .... 78

**Figure 40.** DRIFT spectra recorded at 250 °C after switching from H<sub>2</sub>/He to CO<sub>2</sub>/He: a) Ru/ZrO<sub>2</sub> and b) Ru/ZrO<sub>2</sub>-MgO. The first spectrum from top to bottom corresponds to the catalyst before CO<sub>2</sub> admission. The total time was set

to 30 min. Inlet gas flow conditions after switch (second spectrum from top to bottom): 4 ml min<sup>-1</sup> CO<sub>2</sub>, 26 ml min<sup>-1</sup> He. .... 79

**Figure 41.** Normalized integral decay of the bands resolved in the spectra recorded at 250 °C during the dynamic experiment presented in **Figure 40**. a) Ru/ZrO<sub>2</sub> and b) Ru/ZrO<sub>2</sub>-MgO. The normalization was referred to the intensity of the maximum of respective band after the admission of CO<sub>2</sub> to the reaction cell. The red dotted line indicates the coincidence between the maximum intensity of the formate with the stepped increase of the CH<sub>4</sub> active Ru-CO band. The total time was set to 30 min. Inlet gas flow conditions after switch: 4 ml min<sup>-1</sup> CO<sub>2</sub>, 26 ml min<sup>-1</sup> He..... 80

**Figure 42.** Representation of b-HCOO adsorbed on Ru/ZrO<sub>2</sub> and Ru/ZrO<sub>2</sub>-MgO (Ru not shown) and the corresponding  $\nu_{\text{as}}(\text{O-C-O})$  as determined by DRIFTS during reaction at 250 °C..... 82

**Figure 43.** Proposed mechanism for CO<sub>2</sub> adsorption, b-HCOO<sup>\*-</sup> and Ru-CO formation on Ru/ZrO<sub>2</sub>-MgO. Further steps of Ru-CO hydrogenation to CH<sub>4</sub> are not shown. Dashed circle represents O-vacancy..... 83

**Figure 44.** N<sub>2</sub> adsorption isotherms of a) fresh bare TiO<sub>2</sub> and Au/TiO<sub>2</sub>; b) fresh bare ZrO<sub>2</sub> and Au/ZrO<sub>2</sub>; c) XRD powder patterns of the fresh TiO<sub>2</sub> support and fresh Au/TiO<sub>2</sub> catalyst; d) XRD powder patterns of the fresh ZrO<sub>2</sub> support and fresh Au/ZrO<sub>2</sub> catalyst..... 85

**Figure 45.** HAADF STEM images of the (a-c) Au/TiO<sub>2</sub> and (d-f) Au/ZrO<sub>2</sub> catalysts. .... 86

**Figure 46.** a) STEM-ADF image of the fresh Au/TiO<sub>2</sub> catalyst depicting the area used for spectral imaging; b) the corresponding EELS phase maps of Ti<sup>4+</sup> (red) and the unknown surface species (cyan); c) EELS obtained in the two positions marked in a) with the corresponding color..... 87

**Figure 47.** a) STEM-HAADF image of the spent Au/TiO<sub>2</sub> catalyst; b) EELS oxidation state and elemental maps with Ti<sup>4+</sup> in red, the potential Ti<sup>3+</sup> phase in cyan and carbon in yellow; c) corresponding STEM-ADF image of spectrum



imaging region with marks for the extracted spectra; d) EELS spectra obtained in the two positions marked in c) with corresponding colors. .... 88

**Figure 48.** a) CO<sub>2</sub> conversion; b) CO selectivity; c) rate of CO formation as a function of the testing temperature on the supported Au catalysts; d) Arrhenius plots of the rate of CO formation in the temperature range 250–350 °C, over Au/TiO<sub>2</sub> (black) and Au/ZrO<sub>2</sub> (red). Reaction conditions: P<sub>total</sub> = 3 bar, CO<sub>2</sub>: H<sub>2</sub>: N<sub>2</sub> = 1:3:2, 17.5 ml min<sup>-1</sup>. .... 89

**Figure 49.** a) CO<sub>2</sub> conversion and b) CO selectivity as a function of the testing temperature on the supported Au catalysts. Reaction conditions: P<sub>total</sub> = 20 bar, CO<sub>2</sub>: H<sub>2</sub>: N<sub>2</sub> = 1:3:2, 17.5 ml min<sup>-1</sup>. .... 90

**Figure 50.** Au 4f XP spectra of a) Au/TiO<sub>2</sub> and b) Au/ZrO<sub>2</sub>. .... 91

**Figure 51.** Single-pulse responses of CO<sub>2</sub> compared with the Ar response at 573 K over a) Au/TiO<sub>2</sub>; b) Au/ZrO<sub>2</sub>. Single-pulse responses of CO<sub>2</sub> compared with the Ar response at 573 K over c) Au/TiO<sub>2</sub>; d) Au/ZrO<sub>2</sub>. .... 92

**Figure 52.** In-situ DRIFT spectra of the RWGS reaction over a) Au/TiO<sub>2</sub> and b) Au/ZrO<sub>2</sub> catalysts. Reaction conditions: P = 3 bar, H<sub>2</sub>: CO<sub>2</sub>: N<sub>2</sub> = 3:1:2; total flow rate = 17.5 ml/min, T = 250 °C. .... 93

**Figure 53.** In-situ DRIFT spectra of the RWGS reaction over a) Au/TiO<sub>2</sub> and b) Au/ZrO<sub>2</sub> catalysts. Reaction conditions: P = 3 bar, H<sub>2</sub>: CO<sub>2</sub>: N<sub>2</sub> = 3:1:2; total flow rate = 17.5 ml/min. .... 95

**Figure 54.** In-situ EPR spectra obtained at -173 °C for the as-obtained fresh, reduced (at 280 °C in 50% H<sub>2</sub>/He for 2h), and spent samples of a) pure TiO<sub>2</sub> and b) Au/TiO<sub>2</sub>. Reaction conditions: P = 1 bar H<sub>2</sub>: CO<sub>2</sub> = 3:1; total flow rate = 17.5 ml min<sup>-1</sup>, T = 250 °C. .... 96

**Figure 55.** In-situ EPR spectra obtained at -173 °C for the as-obtained fresh, reduced (at 280 °C in 50% H<sub>2</sub>/He for 2h), and spent samples of a) pure ZrO<sub>2</sub> and b) Au/ZrO<sub>2</sub>; c) second derivative of the in situ EPR spectra obtained at -173 °C for the spent Au/ZrO<sub>2</sub> catalyst. Reaction conditions: P = 1 bar H<sub>2</sub>: CO<sub>2</sub> = 3:1; total flow rate = 17.5 ml min<sup>-1</sup>, T = 250 °C. .... 97

**Figure 56.** Proposed reaction mechanisms of the RWGS reaction over a) Au/ZrO<sub>2</sub> and b) Au/TiO<sub>2</sub> Catalysts. The dashed circle represents an O-vacancy.  
 ..... 99

**List of tables**

**Table 1.** Highly active reported Ru based catalysts for CO<sub>2</sub> methanation. 8

**Table 2.** Highly active reported Au based catalysts for CO<sub>2</sub> reduction to CO..... 10

**Table 3:** Pore and surface properties of the fresh TiO<sub>2</sub>-SG support and Ru/TiO<sub>2</sub>-SG and Ru/TiO<sub>2</sub>-Imp catalysts ..... 45

Table 4. Reported activity of CO<sub>2</sub> methanation on the Ru/TiO<sub>2</sub>-SG catalyst at distinct temperatures and H<sub>2</sub>:CO<sub>2</sub> ratio = 4:1..... 52

Table 5. Ru:Ti surface ratio estimated from NAP-XPS at different stages for Ru/TiO<sub>2</sub>-SG and Ru/TiO<sub>2</sub>-Imp catalysts. .... 55

**Table 6.** Infrared absorption bands and assignments for adsorbate species observed during CO<sub>2</sub> hydrogenation on Ru/TiO<sub>2</sub>-SG and Ru/TiO<sub>2</sub>-Imp catalysts.  
 ..... 60

**Table 7.** Structural properties, Mg and Ru loading of Ru/ZrO<sub>2</sub> and Ru/ZrO<sub>2</sub>-MgO catalysts..... 64

**Table 8.** Particle size, specific surface area and dispersion of Ru on Ru/ZrO<sub>2</sub> and Ru/ZrO<sub>2</sub>-MgO catalysts. .... 70

**Table 9.** Rates of reaction calculated at steady state in the range 220 – 300 °C on Ru/ZrO<sub>2</sub> and Ru/ZrO<sub>2</sub>-MgO catalysts. .... 70

**Table 10.** Surface atomic concentration of Ru quantified from Ru 3d XPS signals before and after reaction on Ru/ZrO<sub>2</sub> and Ru/ZrO<sub>2</sub>-MgO catalysts. .... 72

**Table 11.** Infrared absorption bands and assignments for adsorbate species observed during CO<sub>2</sub> hydrogenation on Ru/ZrO<sub>2</sub> and Ru/ZrO<sub>2</sub>-MgO catalysts. 76

**Table 12.** Structural properties of pure supports and gold catalysts ..... 84

**Table 13.** Infrared absorption bands and assignments for adsorbate species observed during RWGS reaction on Au/TiO<sub>2</sub> and Au/ZrO<sub>2</sub> catalysts..... 95

## 1. State of the Art

### 1.1. Power to X concept: CO<sub>2</sub> methanation and RWGS reaction in the practice

The importance of reacting CO<sub>2</sub> with renewable H<sub>2</sub> as a solution for the storage of surplus electric energy was highlighted in the motivation section. However, the context of coupling CO<sub>2</sub> and H<sub>2</sub> is wider. This has been coined as “Power to X” and consists in the production of value-added high energy density compounds by recycling the generated CO<sub>2</sub>, mainly from combustion activities, decreasing the exploitation of fossil resources and advancing towards carbon-neutrality.<sup>32</sup> A scheme of this approach is illustrated in **Figure 2**.

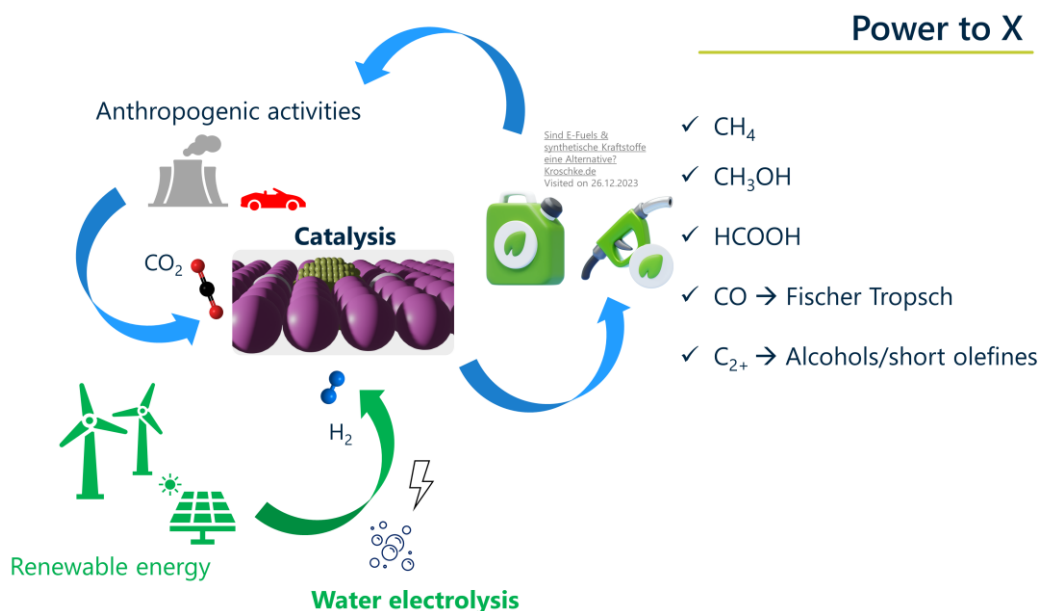
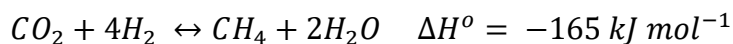


**Figure 2.** Schematic representation of CO<sub>2</sub> transformation to useful compounds by catalytic reaction with H<sub>2</sub>.

Among the products of interest, C<sub>1</sub> molecules (CH<sub>4</sub>, CO, CH<sub>3</sub>OH and formic acid) represent a first group with great potential in the short and medium terms. More complex molecules, with two or more carbon atoms, such as light olefins, which are very important in the chemical industry, represent a second group of interest that can be either produced via direct CO<sub>2</sub> hydrogenation or in secondary processes by means of CO and methanol as intermediates.<sup>4</sup>

33

As mentioned in the motivation section, CH<sub>4</sub> is a versatile molecule that can be used directly in energy storage, industry, house-hold heating, or transportation sector without the need of substantial changes in the available infrastructure. Investments for the impulse of CO<sub>2</sub> methanation technologies (based on reaction **R1**) advance worldwide.



**R1**

Thema et al.<sup>5</sup> reviewed a data base of 153 projects in 22 countries that involve the methanation of CO<sub>2</sub> with renewable H<sub>2</sub>. A total of 38 active projects were detected. These are executed in different countries and together amount a total installed capacity of 6 MW (based on low heating value of CH<sub>4</sub>) with 41 % electricity to gas efficiency. Moreover, the mean plant size and number of projects have increased since beginning of the 90's decade with an accelerated growth from 2012 (**Figure 3**).

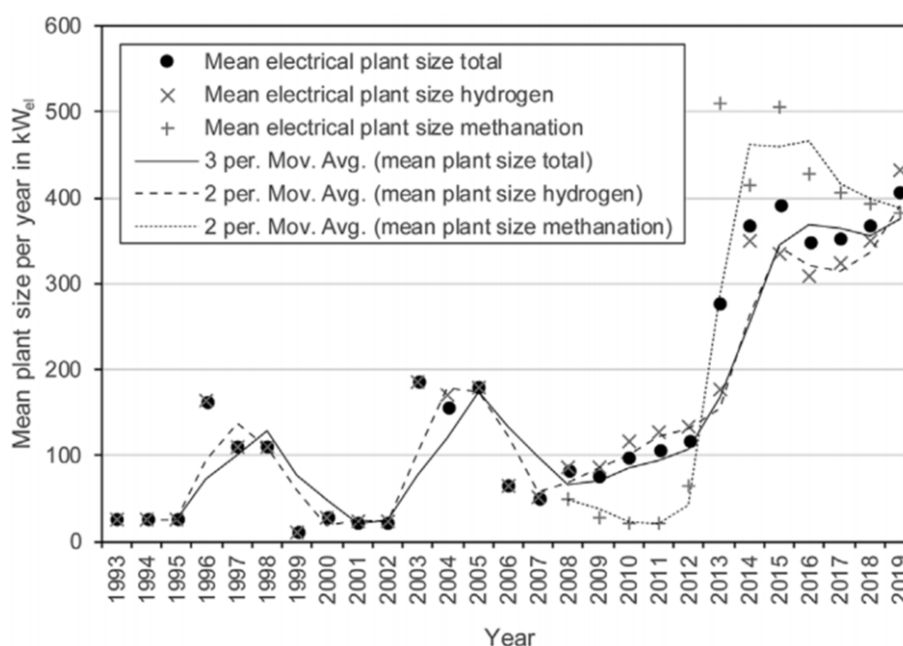
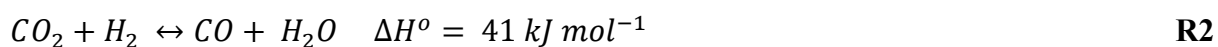


**Figure 3.** Mean plant size (total, H<sub>2</sub> projects, CH<sub>4</sub> projects) and their floating means for the years 1993 – 2018.<sup>5</sup>

Although most of the plants are still at pilot – scale, in the order of kW<sub>el</sub>, in countries such as Germany scaling up to 1 MW installed electric power has been successfully proved.<sup>34</sup> Ongoing projects for commercial scale up to 100 MW installed electric power are nowadays prospects in research institutions as well as in industry.<sup>35</sup> Predictions claim that through optimization and system engineering, synthetic CH<sub>4</sub> could compete with conventional natural gas in an scenario of 40 €/MWh, especially in countries where this energy carrier is currently imported, e.g., Germany and Spain.<sup>36</sup> Obviously these optimizations include the catalytic reactor which is the core of the process and this implicitly involves the development of efficient catalysts.<sup>19</sup>

On the other hand, CO is an important building block molecule in the chemical industry, e.g., in carbonylation and Fischer-Tropsch (FT) processes.<sup>3, 37</sup> Contrary to methanation, the RWGS reaction (reaction **R2**) is still far from commercialization.



CO is commonly produced via reaction of coal, biomass and CH<sub>4</sub> (natural gas) with steam. The resulting gas mixture is known as syngas and consists mainly in H<sub>2</sub> and CO.<sup>38</sup> The maturity of processes such as FT and the interest to decarbonize the chemical industry, however, make the RWGS very attractive as alternative route for CO production. Bown et al.<sup>39</sup> reported on different scenarios the profitability of RWGS by means of CO<sub>2</sub> capture and utilization. With the use of grey and blue H<sub>2</sub> (derived from fossil fuel without and with CO<sub>2</sub> capture, respectively) and a price < 3 \$ kg<sup>-1</sup> the process is economically feasible whereas by using green H<sub>2</sub> (derived from renewables) it is still not realizable (**Figure 4**). The evaluated scenarios consisted in:

- 1) CO<sub>2</sub> capture on site for an electrified process.
- 2) CO<sub>2</sub> capture on site for a gas heated process.
- 3) Zero cost of CO<sub>2</sub> capture on site for an electrified process.
- 4) Zero cost of CO<sub>2</sub> capture on site for a gas heated process.

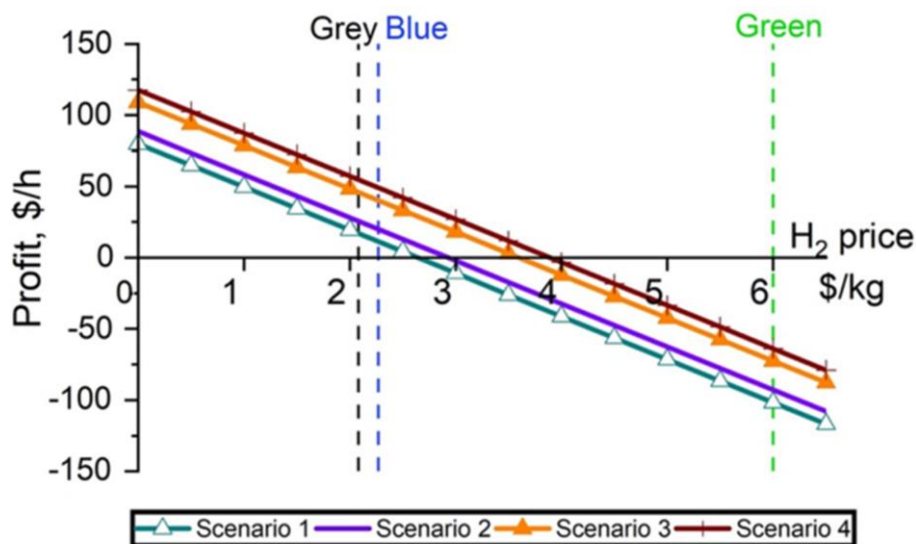


**Figure 4.** Simulation of process profitability for CO production. Conditions: 1:1 H<sub>2</sub>:CO<sub>2</sub>, 750 °C, 1.013 bar. Vertical lines indicate reported prices for grey, blue and green H<sub>2</sub>.<sup>39</sup>

Although the implementation of the RWGS into the context of Power to X is still at its infancy, beyond the need of an economical feasible source of H<sub>2</sub>, the technical viability of the RWGS reaction also relies in the use of highly efficient thermal energy sources due to the endothermic nature of this reaction. Furthermore, competitive production of CH<sub>4</sub> must be

minimized to avoid extra consumption of H<sub>2</sub>, otherwise CO<sub>2</sub> emissions will increase if H<sub>2</sub> sources are different to renewables. Hence, the implementation of highly active and selective catalysts for this process is mandatory and, not surprisingly, nowadays a very active research field.<sup>40</sup>

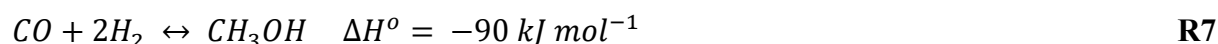
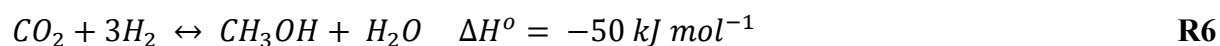
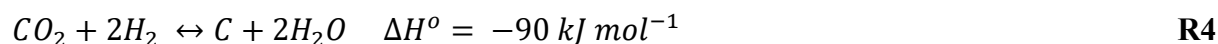
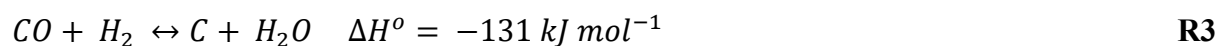
## 1.2. Thermodynamics of CO<sub>2</sub> hydrogenation

The hydrogenation of CO<sub>2</sub> is an equilibrium limited reaction, i.e., the conversion of reactants will reach a maximum dictated by the respective temperature, pressure, and feed composition.

The production of CH<sub>4</sub> from CO<sub>2</sub> (reaction **R1**) was performed at the beginning of the 20<sup>th</sup> century by the French scientist Paul Sabatier who used finely divided nickel as catalyst. Since then, the process is also known as the Sabatier's reaction.<sup>41</sup> The reaction is exothermic,  $\Delta H^\circ = -165 \text{ kJ mol}^{-1}$ , with a change from 5 moles of reactants to 3 moles of products. That is, the equilibrium will shift towards the products with raising pressure and decreasing temperature. Furthermore, this reaction involves transfer of 8 electrons (C changes from oxidation state 4<sup>+</sup> to 4<sup>-</sup>), which means that it is complex and exhibits significant kinetic limitations.<sup>42</sup>

On the other hand, the reduction of CO<sub>2</sub> to CO via reaction **R2**, contrary to reaction **R1**, is endothermic,  $\Delta H^\circ = 41 \text{ kJ mol}^{-1}$ , and involves the transfer of only 2 electrons (C changes from oxidation state 4<sup>+</sup> to 2<sup>+</sup>). The equilibrium would shift to the products at high reaction temperatures and the process pressure has no net effect as the net mole change is zero.

When CO<sub>2</sub> and CO coexist in the reaction system, they can compete for H<sub>2</sub>. The reactions **R3** – **R7** represent complementary possible linear independent reactions that might take place during CO<sub>2</sub> hydrogenation if **R1** and **R2** simultaneously occur.<sup>43, 44</sup> The production of higher hydrocarbons and alcohols (C<sub>2+</sub> products) is not considered as these types of compounds are normally not produced at the conditions of interest for the present study.



The catalyst selectivity is the property of highest importance when renewable H<sub>2</sub> is pretended to be used. Water electrolysis is highly demanding in technical and economic sense, especially when renewable electricity is the energy source.<sup>45</sup> Therefore, H<sub>2</sub> should be selectively

consumed for the evolution of the target product to avoid important energy and economic losses. A primary criterion for selectivity is the process temperature. As seen, low temperatures favor CH<sub>4</sub> while high ones lead to CO evolution. A precise definition of “low” and “high” temperature is provided by thermodynamic analysis. Therefore, a series of simulations has been conducted in this thesis using the Aspen Plus software, version 11. The calculations were based on the Gibbs free energy minimization method (see **Appendix A1** for details). This consists in finding the composition for which the Gibbs free energy of the system is at a minimum for the given reaction conditions. In the simulation a reactor fed with 40 ml min<sup>-1</sup> of CO<sub>2</sub> and H<sub>2</sub> mixture at different temperatures, compositions, and pressures was taken as model. The equilibrium CO<sub>2</sub> conversion and product selectivity were analyzed as function of H<sub>2</sub>:CO<sub>2</sub> ratio, temperature and pressure (**Figure 5**), according to equations **eq. 1** and **eq. 2**. F<sub>0\_CO2</sub> is the initial molar flow of CO<sub>2</sub> at the reactor inlet and F<sub>CO2</sub> the respective outlet flow.

$$X_{CO_2} = \frac{F_{CO_2,in} - F_{CO_2,out}}{F_{CO_2,in}} \quad \text{eq. 1}$$

$$S_i = \frac{(F_i)}{(F_{CH_4} + F_{CO} + F_{CH_3OH} + F_C)} \quad \text{eq. 2}$$

For stoichiometric feed ratio of H<sub>2</sub>:CO<sub>2</sub> = 1:1 the equilibrium CO<sub>2</sub> conversion is not superior to 50 % and slightly improves with the increase of pressure for temperature up to ca. 600 °C (**Figure 5a**).

For H<sub>2</sub>:CO<sub>2</sub> = 1:1 (**Figure 5d**) The formation of C is more favorable than that of CH<sub>4</sub> and CO for temperatures below 500 °C. This aspect is important as carbon deposition might lead to catalyst deactivation, depending on the type and location of the carbonaceous deposit. Graphitic carbon deposited on the supported metallic nanoparticles leads to deactivation and modifies the selectivity whereas filamentous carbon and carbonaceous deposits on the supporting material have no effect on the catalytic behavior.<sup>46,47</sup> At T > 500 °C CO<sub>2</sub> conversion increases again due to the pronounced enhancement of RWGS, particularly, at low pressure while C and CH<sub>4</sub> start to decrease (**Figure 5d**). For H<sub>2</sub>:CO<sub>2</sub> > 1 the CO<sub>2</sub> conversion is increased favoring CH<sub>4</sub> at temperatures below 400 °C and the increase in pressure further displaces the equilibrium towards CH<sub>4</sub>. CO production, in contrast, is predicted to appreciably contribute to the product mixture at T > 600 °C (**Figure 5b, c, e, f**). At those conditions carbon formation is suppressed with the increase in temperature whereas pressure changes exert only a slight effect (**Figure 5e, f**). In all cases no production of CH<sub>3</sub>OH is predicted (**Figure 5d-f**).



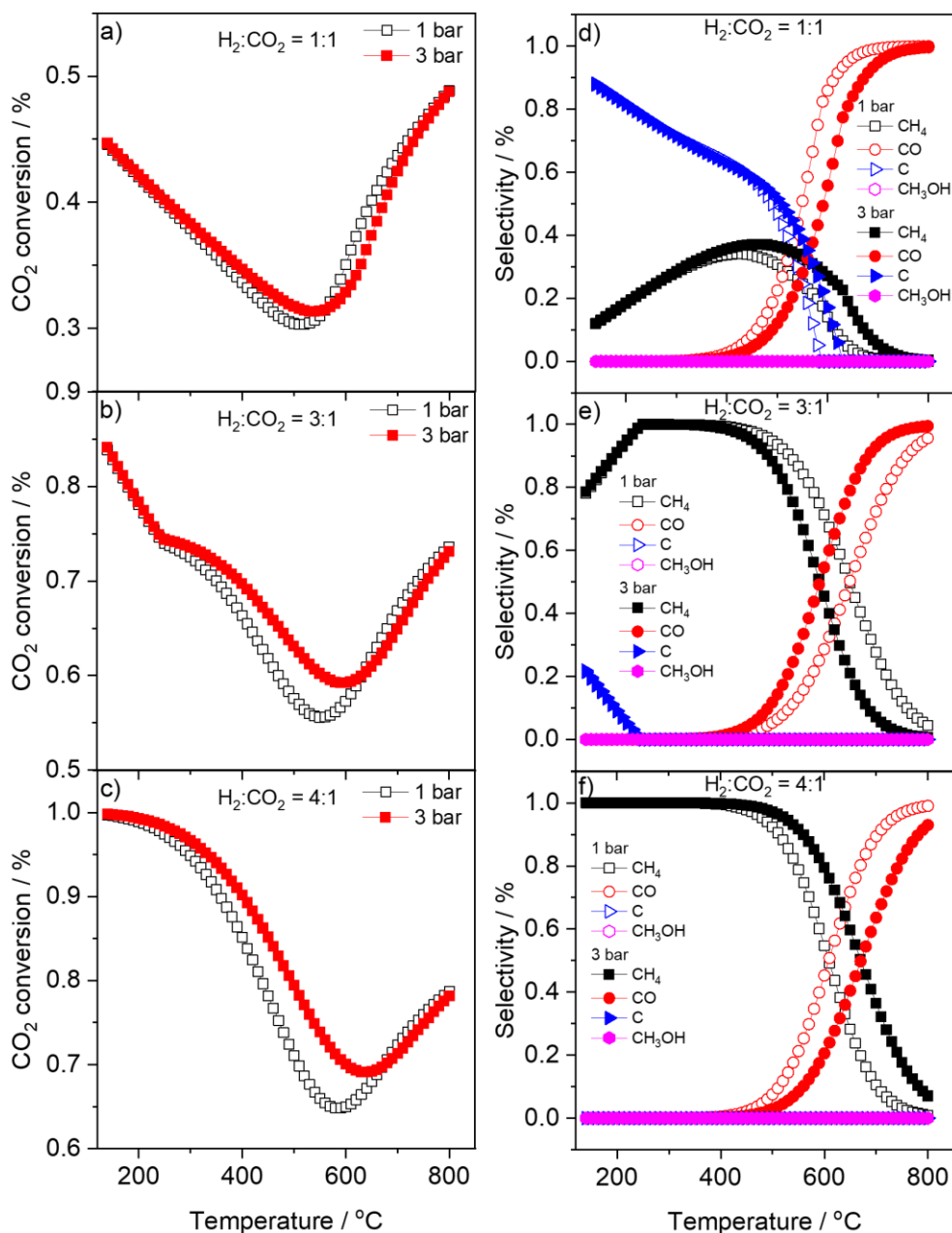


**Figure 5.** CO<sub>2</sub> equilibrium conversion as function of temperature for distinct H<sub>2</sub>:CO<sub>2</sub> ratios at 1 and 3 bar (a-c). Equilibrium selectivity to CH<sub>4</sub>, CO, C and CH<sub>3</sub>OH as function of temperature for distinct H<sub>2</sub>:CO<sub>2</sub> ratios at 1 and 3 bar (d-f). The calculations were based on the Gibbs free energy minimization method using Aspen Plus V11.

As mentioned, the methanation reaction would be preferable at H<sub>2</sub>:CO<sub>2</sub> ratio > 1, high pressure and low temperature. As the CH<sub>4</sub> selectivity can be in principle ca. 100 % at T < 400 °C with low dependence on the pressure, the main requirement for a methanation catalyst would be to operate below this limiting temperature and preferably at or near ambient pressure.

For the RWGS reaction, on the other hand, the requirements are more complex, especially because of the relative high temperature (T > 400 °C). With H<sub>2</sub>:CO<sub>2</sub> ratio of 1:1, low

pressures and  $T < 600\text{ }^{\circ}\text{C}$ , the formation of C cannot be disregarded. This situation imposes the requirement of resistance to deactivation by carbon deposition and sintering. Accordingly, modern RWGS catalysts should be sufficiently highly active and selective to allow operation at  $T < 400\text{ }^{\circ}\text{C}$  to decrease the complexity and costs of the process.<sup>18, 19</sup>

### 1.3. Catalysts for CO<sub>2</sub> methanation and RWGS reaction

**CO<sub>2</sub> methanation catalysts:** The explored routes for CH<sub>4</sub> production include biological, homogeneous, and heterogeneous processes. These last are preferred for large scale production due to facile handling, separation, reuse, and stability.<sup>48</sup> A variety of transition metals (Ru, Rh, Pd, Co, Fe, Pt, Mo) supported on diverse oxides (Al<sub>2</sub>O<sub>3</sub>, SiO<sub>2</sub>, TiO<sub>2</sub>, CeO<sub>2</sub>, ZrO<sub>2</sub>, Nb<sub>2</sub>O<sub>5</sub>) has been found active for this reaction.<sup>49-52</sup> However, the most attractive catalysts for technical applications are currently those based on Ni. Yet, Ru and Rh based catalysts are more active and stable than Ni catalysts.<sup>19, 20, 53-57</sup> The disadvantage is that Ru and Rh precursors are more expensive than Ni ones.

The use of reducible oxides has been found as the best option for supporting active metal nanoparticles. Several investigations point to the tailoring of O-vacancies in the support as an adequate strategy to adjust the electronic properties of catalysts that might result in the improvement of rate and selectivity during CO<sub>2</sub> hydrogenation as these defects can transfer electrons via interfacial active metal sites to empty  $\pi^*$  orbitals, affecting the activation of C-O bonds of key intermediates.<sup>21, 22, 58, 59</sup> This allows for the reduction of the operating temperature while conserving high CO<sub>2</sub> conversion rates.

Particularly, on Ru based catalysts, the effect of oxygen vacancies on the promotion of the activity has been investigated for samples prepared by the typical wetness impregnation method and, commonly, using a Ru loading of ca. 2 wt.%.<sup>21, 60</sup> **Table 1** contains a survey of the methanation activity of distinct Ru catalysts supported on reducible oxides, considered as highly active for low temperature reaction. It is observed that although some catalysts with Ru loading below 1 wt.% have been reported, most of them rely on Ru amounts larger than this. Therefore, more efforts to limit Ru loading well below 1 wt.% are needed to render those catalysts competitive for industrial applications.<sup>61</sup>

**Table 1.** Highly active reported Ru based catalysts for CO<sub>2</sub> methanation.

Catalyst	Synthesis method	Reaction temperature / °C	H <sub>2</sub> :CO <sub>2</sub>	Activity: TOF <sub>CO<sub>2</sub></sub> / mass normalized	Reference
2.2 wt.% Ru/TiO <sub>2</sub> (P-25)	Colloidal suspension deposition	200	4:1	1.16 x 10 <sup>-4</sup> molCH <sub>4</sub> g <sub>Ru</sub> <sup>-1</sup> s <sup>-1</sup> <sup>1 a</sup>	62
5 wt.% Ru/TiO <sub>2</sub> (rutile)	Wet impregnation	160	4:1	6.0 x 10 <sup>-3</sup> s <sup>-1</sup>	63
2.43 wt.% Ru (RuO <sub>2</sub> /TiO <sub>2</sub> -P25)	Colloidal suspension deposition (Annealed at 450 °C in static air before reaction)	200	4:1	1.06 x 10 <sup>-4</sup> molCH <sub>4</sub> g <sub>Ru</sub> <sup>-1</sup> s <sup>-1</sup> <sup>1 a</sup>	64
2.35-2.60 wt.% RuO <sub>2</sub> /TiO <sub>2</sub> (50% anatase – 50 % rutile)	Colloidal suspension deposition (Annealed at 450 °C in static air before reaction)	Up to 200	4:1	0.057 s <sup>-1</sup> <sup>a</sup>	65
2.1 wt.% Ru/TiO <sub>2</sub> (P-25)	Wetness impregnation	190	4:1	6.0 x 10 <sup>-5</sup> molCH <sub>4</sub> g <sub>Ru</sub> <sup>-1</sup> s <sup>-1</sup> <sup>1 a</sup>	21
2.2 wt.% Ru/TiO <sub>2</sub> (P-90)	Wetness impregnation	190	4:1	1.2 x 10 <sup>-4</sup> molCH <sub>4</sub> g <sub>Ru</sub> <sup>-1</sup> s <sup>-1</sup> <sup>1 a</sup>	21
0.8 wt.% Ru/TiO <sub>2</sub> (anatase)	Barrel sputtering	160	4:1	8.5 x 10 <sup>-3</sup> s <sup>-1</sup>	66
0.5 wt.% Ru/0.2 wt.% Na-TiO <sub>2</sub> (anatase + rutile)	Wet impregnation	250	4:1	0.16 s <sup>-1</sup>	67
2.39 wt.% Ru/TiO <sub>2</sub> (anatase 001)	Aqueous colloidal	300	4:1	7.24 x 10 <sup>-2</sup> s <sup>-1</sup>	68
1.5 wt.% Ru/TiO <sub>1.85</sub> N <sub>0.15</sub>	Impregnation-reduction	190 (under visible light irradiation)	4:1	3.3 x 10 <sup>-3</sup> s <sup>-1a</sup>	69
2.56 wt.% Ru/CeO <sub>2</sub>	Impregnation	190	4:1	7.41 x 10 <sup>-3</sup> s <sup>-1</sup>	70

<sup>a</sup> Estimated from the respective data.

**RWGS catalysts:** Similar to the Sabatier's reaction, a large list of active metals (Pd, Pt, Rh, Au, Fe, Ni, Co, Cu) and supports (TiO<sub>2</sub>, CeO<sub>2</sub>, SiO<sub>2</sub>, ZrO<sub>2</sub>, Nb<sub>2</sub>O<sub>5</sub>, MgO, Al<sub>2</sub>O<sub>3</sub>) has been investigated for the RWGS.<sup>52, 53, 71, 72</sup> Special attention has been given to Pt, Pt-Co alloys and Au as they have shown very attractive activity and selectivity at distinct reaction conditions.<sup>52, 73</sup> The major disadvantage of the best active metals for the RWGS, e.g., Pt and Au, is again their scarcity and high cost. Therefore, the use of non-noble transition metal-based catalysts is a common practice in research and applied technologies.<sup>71</sup> Their catalytic performance, however, is usually much below that of the noble metal-based catalysts. This issue becomes particularly important for low temperature reactions at which the reaction rates become slower. Although this limitation could be solved by increasing the metal loading,<sup>74</sup> the probability of clustering also increases together with the possibility of segregation of the metal phase into large particles that might result in activity loss.<sup>74-78</sup> The main reason is the loss in the activity for molecular H<sub>2</sub> splitting.<sup>79, 80</sup> While this process is markedly enhanced on nanoparticles and small clusters, bulk metals show inactive for H<sub>2</sub> dissociation.<sup>26, 28, 81-85</sup> Nevertheless, not only the supported metal properties must be considered. Several studies have shown that the rate of the RWGS reaction is highly dependent on the type of support since the activation of CO<sub>2</sub> mainly occurs at the oxide support or the interfacial sites between the metal and support.<sup>86</sup> Analogously to CO<sub>2</sub> methanation, the RWGS reaction tends to be favored when the corresponding active metal is supported on reducible carriers, as CO<sub>2</sub> can be more effectively stabilized/activated,<sup>87, 88</sup> e.g., by O-vacancies.<sup>56, 72</sup>

Au is excellent for the RWGS reaction and has therefore been extensively investigated while supported on several oxides, e.g., TiO<sub>2</sub>,<sup>26, 28, 89</sup> ZrO<sub>2</sub>, Fe<sub>2</sub>O<sub>3</sub>, CeO<sub>2</sub>,<sup>26, 83</sup> and Al<sub>2</sub>O<sub>3</sub>,<sup>28</sup> at mild reaction conditions. A direct correlation between CO<sub>2</sub> conversion and surface acidity has been determined, whereby TiO<sub>2</sub>, Fe<sub>2</sub>O<sub>3</sub> and ZrO<sub>2</sub> revealed the most promising results. This dependence of the activity on the acidic properties is associated to differences in the interaction between CO<sub>2</sub> and the support, i.e., the weaker the adsorption of CO<sub>2</sub> the higher is the hydrogenation activity.<sup>26</sup> In these studies, however, Au loadings of minimum 1 wt.% typically operating at T > 250 °C have been used (see **Table 2**). The growing demand for CO<sub>2</sub> hydrogenation requires Au catalysts with a much lower metal amount that can operate at milder conditions with high performance.<sup>26</sup>

**Table 2.** Highly active reported Au based catalysts for CO<sub>2</sub> reduction to CO.

Catalyst	Synthesis method	Reaction temperature / °C	Pressure / atm	H <sub>2</sub> : CO <sub>2</sub>	CO selectivity / %	CO <sub>2</sub> conversion / %	Activity: mass normalized	Reference
2.4 wt.% Au@UiO-67	Wet impregnation	400	20	3:1	100	30	-	90
3.93 wt.% Au-Mo <sub>0.1</sub> /SiO <sub>2</sub>	Controlled surface reaction	300	1	2:1	-	-	261.5 μmolCO <sub>2</sub> g <sub>Au</sub> <sup>-1</sup> min <sup>-1</sup>	91
3.93 wt.% Au-Mo <sub>0.1</sub> /SiO <sub>2</sub>	Controlled surface reaction	300	1	2:1	-	-	1238.5 μmolCO <sub>2</sub> g <sub>Au</sub> <sup>-1</sup> min <sup>-1</sup> (under visible light illumination)	91
1 wt.% Au/TiO <sub>2</sub>	Deposition-precipitation	400	1	9:1	> 99	50	-	89
1 wt.% Au/TiO <sub>2</sub>	Commercial catalyst	400	-	4:1	100	35	-	28
1 wt.% Au/TiO <sub>2</sub>	Deposition-precipitation	250	8	3:1	93.2	16.1	150 μmolCO <sub>2</sub> g <sub>cat</sub> <sup>-1</sup> min <sup>-1</sup>	92

#### 1.4. Catalysts properties that affect the hydrogenation of CO<sub>2</sub>

The common fundamental challenge in any catalytic process for CO<sub>2</sub> valorization is the activation of the highly stable C=O bond (energy of ca. 806 kJ mol<sup>-1</sup>).<sup>17</sup> This calls for very efficient catalysts. However, selecting very active elements, e.g., Ru and Au, is not enough for this task. Tailoring the metal-support interface results in the modification of structural and electronic properties which can lead to the promotion of the catalytic performance of the supported entities. Hence, a discussion about the effect of supported nanoparticles size, oxygen vacancies, alkali promoters, and second metal phase on the hydrogenation of CO<sub>2</sub> to C<sub>1</sub> compounds is provided.

**Supported particle size:** The size of the supported particles has been found to influence the catalytic behavior during CO<sub>2</sub> hydrogenation. In general, decreasing the particle size, i.e., increasing the dispersion, favors the RWGS reaction while the production of CH<sub>4</sub> tends to increase with the particle size.<sup>93, 94</sup> The catalytic changes have been associated to structural and

electronic effects. On highly dispersed small entities, e.g., isolated metallic atoms, the functionality for activation of H<sub>2</sub> is limited and hence the reduction of CO<sub>2</sub> to CO is favored.<sup>93</sup> <sup>95</sup> This relates to the relative contribution of coordinated and undercoordinated sites. Well dispersed small entities expose larger fractions of edges and corner sites (exhibiting undercoordinated atoms)<sup>96</sup> that are favorable for CO formation but less reactive for further hydrogenation than flat surfaces (exposing highly coordinated atoms) which are more effective for activating H<sub>2</sub>.<sup>51, 97</sup> This suggests that the size of the supported metallic nanoparticles tailors the relative coverage of adsorbed reactive CO\* and H\*. However, the particle size can also affect the electronic properties. On small particles, the adsorption energy of adsorbates, e.g., CO, decreases because electronic back-donation from the supported metal is less pronounced.<sup>98</sup> Accordingly, the less stabilized CO\* would preferably desorb as CO<sub>(g)</sub> instead of being activated, i.e., C-O cleavage would be less prone to occur. This insight has been corroborated in theory and practice over various supported catalysts.<sup>99, 100</sup>

Although a trend in the CO<sub>2</sub> hydrogenation behavior based on the particle size could be established, it is worth to annotate that the extend of interaction between the metal and the support is another factor that adds complexity to the understanding of structure-reactivity relationships. While a single site PtO<sub>x</sub> supported on TiO<sub>2</sub> presents low activity towards CO<sub>(g)</sub> production, single atom Pt<sup>0</sup> has been found very active for the same reaction.<sup>101</sup> Contrary effect has been reported for atomically dispersed RuO<sub>x</sub> supported on CeO<sub>2</sub> which was found highly selective to RWGS<sup>102</sup> whereas single atom Ru<sup>0</sup> can still selectively produce CH<sub>4</sub>.<sup>70</sup> Therefore, other properties distinct to the particle size might be considered for understanding the reactivity of CO<sub>2</sub> hydrogenation catalysts.

**Oxygen vacancies:** Defects determine mechanical, chemical, electrical, and optic properties of materials. Oxygen vacancies (O-vacancies) are a kind of point defects with high influence on the reactivity of the surface of metal oxides. They can be considered as finger print of the electronic structure of oxides.<sup>103</sup> Therefore, understanding their structure, distribution, and formation is indispensable for the development of efficient catalytic materials.<sup>104</sup> O-vacancies form in the following situations:<sup>105</sup>

- Dehydration of hydroxylated surfaces.
- Reduction of metal cations forming the oxide matrix.
- Substitution of oxide cations by lower valence foreign cations.
- Any combination of the previous cases.

As electrons can be released from the defect, the local charge density of the metal sites allocated at the perimeter interface can be increased. That is, O-vacancies influence the behavior of supported metal nanoparticles. In the case of d-block elements, charge back-donation from the filled orbitals to the empty  $\pi^*$  anti-bonding orbital of adsorbed molecules modifies the binding strength and hence the catalyst reactivity (activity/selectivity) can be altered.<sup>17, 22, 60</sup>

Another important effect, also a consequence of electron density release from the support to the supported metal species, is the control of the metal-oxide bonding. The binding energy of atoms/clusters of neighboring O-vacancies is stronger than on defect free surfaces.<sup>106, 107</sup> Although this effect could be element dependent, i.e., may not be generalized for all transition elements,<sup>108</sup> evidence has been found that nucleation processes are dominated by such kind of defects.<sup>109, 110</sup> A consequence of this strong interaction is the prevention of migration and sintering of isolated atoms/crystallites.<sup>105, 111</sup> That is, tuning the concentration of O-vacancies can be explored to regulate metal dispersion and particle size distribution.

A third effect of O-vacancies is that they facilitate the adsorption and activation of CO<sub>2</sub>. This has been corroborated by several investigations that correlated the methanation rate of CO<sub>2</sub> with the concentration/presence of O-vacancies.<sup>58, 59, 112</sup>

In summary, O-vacancies influence the local electronic charge density of supported metal entities, control nucleation and/or sintering processes, and serve as activation sites for CO<sub>2</sub>. Hence, the tailoring of these defects is a valuable strategy for developing efficient CO<sub>2</sub> hydrogenation catalysts. This task is, however, very challenging as properties such as reducibility, nature of mainly exposed oxide facets, and/or impurities affect the formation barriers of these defects. Nevertheless, this also justifies systematic investigations focusing on the interplay between O-vacancies and supported metal particles as it is one aim of this thesis.

**Alkali additives:** Elements of the group IA (Li, Na, K, Cs) have been investigated as additives for CO<sub>2</sub> hydrogenation. Petala and Panagiotopoulou<sup>113</sup> found that CH<sub>4</sub> activity and selectivity on 0.5 wt.% Ru/TiO<sub>2</sub> increased in the order unpromoted < Li ~ K < Cs < Na whereas 5 wt.% Ru/TiO<sub>2</sub> was insensitive to alkali addition. They associated the promotion to the electron donation from the alkali species to Ru sites which increased the local charge density on the small Ru particles enhancing C-O dissociation. Similar conclusion was reported by Gao et al.<sup>114</sup> who observed promoting effect of 0.92 wt.% Na on 0.95 wt.% Ru/ZrO<sub>2</sub>. They attributed the enhanced rate to lowering of C-O dissociation barrier at the metal-support interface active sites. In contrast, Heyl et al.<sup>115</sup> reported on the hampering of CH<sub>4</sub> formation and promotion of CO

evolution on K modified 0.34 – 0.5 wt.% Rh/Al<sub>2</sub>O<sub>3</sub> catalysts. They proposed that K favored the formation of a highly active formate that rapidly formed weakly adsorbed CO on Rh particles. Similarly, Li et al.<sup>116</sup> observed a switch from 100 % CH<sub>4</sub> selectivity to 99 % CO selectivity during CO<sub>2</sub> hydrogenation on 0.48 wt.% Ru/ZrO<sub>2</sub> modified with ca 1 wt.% Na. They attributed the selectivity change to the preferred formation of carboxy (COOH\*) intermediates and electron deficiency of Rh sites in presence of the alkali. Moreover, on 10 wt.% Ni/CeO<sub>2</sub>, Cs favored the RWGS reaction over CO<sub>2</sub> methanation.<sup>117</sup> This also contrasts with the results of Petala et al. for 0.5 wt.% Ru/TiO<sub>2</sub>. That is, the changes induced by alkali addition depend on the type of supported metal, particle size and support type.

In summary, alkali elements have been used for tailoring the selectivity of CO<sub>2</sub> hydrogenation. Although some trends have been identified regarding the modification of adsorptive properties of the supported metals and supporting oxides, the dependence on the nature of the supported particles (element, loading, size, metal-support interface), calls for more systematic research in this branch.

**Second supported metal:** Instead of using monometallic catalysts for CO<sub>2</sub> hydrogenation, the introduction of a second supported metal phase has also been explored. Metal alloying is a practice commonly reported for enhancing the productivity of poorly active catalysts based on metals such as Ni and Fe.<sup>118-120</sup> Several examples demonstrating the interplay between the rate of CO and CH<sub>4</sub> production on the presence of a second metal have been reported. Thus, Porosoff et al.<sup>88</sup> proposed that the decrease of the d-band center correlated with the enhancement RWGS reaction. In addition, the incorporation of Fe oxides into low loaded Ni catalysts a Ni-FeO<sub>x</sub> phase was formed, that weakly interacts with adsorbed CO, favoring release of CO<sub>(g)</sub>.<sup>118, 121</sup> Another example is the incorporation of MnO. Vrijburg et al.<sup>119</sup> showed for Ni-Mn catalysts that a fraction of segregated MnO likely covered Ni with the creation of new interfacial sites that facilitated the formation of adsorbed CO with lower C-O cleavage energy and resulted in increased CH<sub>4</sub> rate. The incorporation of noble metals, e.g., Pt or Pd, has been found to enhance the dispersion of metals such as Ni and Co, that tend to sinter at harsh reaction conditions, with the subsequent enhancement of H<sub>2</sub> activation and H spillover favoring CH<sub>4</sub> rate.<sup>122-124</sup>

## 1.5. CO<sub>2</sub> hydrogenation mechanisms

Understanding the mechanisms of a reaction processes is of primary importance for developing new/improved catalysts. The high stability of free CO<sub>2</sub> is provided by the linear structure of the molecule, bond angle 180°, and no net dipole moment. The electronic



configuration in the ground state is given by the sharing of 16 electrons distributed in molecular orbitals formed by the overlapping of the 2s and 2p orbitals of the C atom with 6 2p orbitals from the two O atoms. From these 16 electrons 12 contribute to bonding in the molecule while the remaining 4 do not participate in the bonding as they remain in the core level (**Figure 6a**). Such an electronic configuration in which the bonding orbitals as well as the non-bonding degenerate orbitals ( $1\pi^*_g$ ) are filled the free molecule remains almost inert. Yet, this unfavorable situation inertness can be reverted upon the interaction of  $\text{CO}_2$  with, e.g., a surface. The adsorption process implies a lowering in the energy level of the in-plane contribution of the  $2\pi^*_u$  orbital (Lowest Unoccupied Molecular Orbital LUMO), more localized on the C atom. The interaction induces a change in the dipole moment increasing the electrophilic character of the C atom making it susceptible of an attack from an electron rich species, e.g., a supported metal particle. The eventual electron transfer to the LUMO breaks the linear symmetry of the molecule and a bent  $\text{CO}_2^-$  radical forms with 17 electrons from which 13 are distributed in the hybrid molecular orbitals formed by the overlapping of the C and O atoms (**Figure 6b**). The electron population of the O atoms is further enhanced which promotes their interaction with electron deficient centers. This induces the bending of the molecule, making the C atom electrophilic.<sup>125</sup> This can happen, for example, when the C atom binds to a supported metal nanoparticle (electron rich center) while one of the O atoms can interact with an electron poor center, e.g., oxide cation or an O-vacancy.<sup>58, 87, 126</sup> Only at this state  $\text{CO}_2$  can be transformed into other molecules.

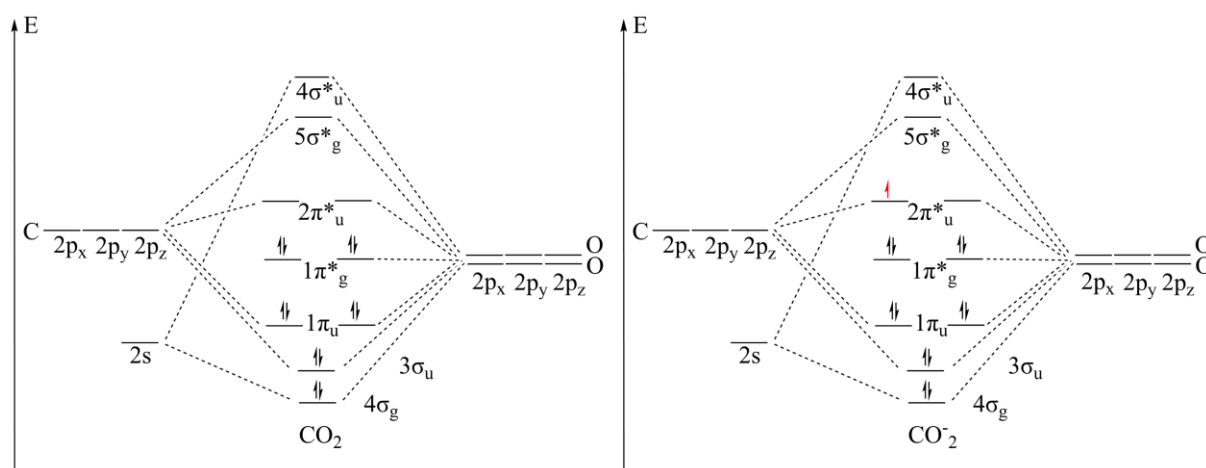


**Figure 6.** a) Molecular orbital diagram of  $\text{CO}_2$  and b) Molecular orbital diagram of  $\text{CO}_2^-$

The hydrogenation pathway can vary depending on the catalyst and reaction conditions.<sup>41, 52, 112, 127</sup> It is worth to anticipate, that no consensus has been reached in the determination of the reaction mechanism(s) for CO<sub>2</sub> hydrogenation.

Doubtless identification of key intermediates is frequently difficult as they might originate from different sources, i.e., formates (HCOO\*) carboxalate (COOH\*) and/or direct CO<sub>2</sub> dissociation.<sup>70, 97, 128-130</sup> Alternatively, this last could also dissociate into adsorbed CO\* and O\* without assistance of activated H\*. The first type of process is known as associative route while the second as dissociative route.<sup>131</sup> An overview of these reaction paths is illustrated in **Figure 7** and summarized below.

In the associative route that involves the formation of formate or carboxylate species, the following description can be given:

- i) In pathway I, HCOO\* is hydrogenated to H<sub>2</sub>COOH\* which decomposes into OH\* and H<sub>2</sub>CO\*. The subsequent hydrogenation could result either in H<sub>3</sub>CO\* or H<sub>2</sub>COH\*, i.e., path Ia and Ib, respectively. In both cases the addition of H can result in the formation of CH<sub>3</sub>OH. These hydrogenations compete with the rupture of the C-O bonding to produce either H<sub>2</sub>C\* or H<sub>3</sub>C\* that rapidly hydrogenate to CH<sub>4</sub>, steps Ib' and Ia', respectively.
- ii) Pathway II consists in the decomposition of HCOO\* to CO\* and OH\*. The intermediate CO\* can either desorb, producing CO<sub>(g)</sub> (RWGS reaction), or could be hydrogenated to HCO\* (IIb) or COH\* (IIb'). HCO\* can be hydrogenated to HCOH\* (IIc) or H<sub>2</sub>CO\* (IId). On the other hand, COH\* can further be reduced to HCOH\* (IIc') and subsequently to H<sub>2</sub>COH\* (IIe). Alternatively, COH\* might decompose into C\* and OH\* and finally result in CH<sub>4</sub> evolution (IIf). Analogously, HCOH\* can decompose into HC\* and OH\* and rise CH<sub>4</sub> evolution (IIg). There is also the possibility of decomposing HCOO\* into HCO\* + O\* / COH\* + O\* (pathways IIa' and IIa'', respectively). If HCO\* forms, it could subsequently follow the routes IIc/IId. Whereas, if COH\* forms, it will continue hydrogenation steps IIe/IIc'.

In turn, for the hydroxycarbonyl mechanism the following description can be provided:

- i) HOCO\* decomposes to CO\* and OH\*. The intermediate CO\* can either desorb producing CO<sub>(g)</sub> (RWGS reaction) or could be hydrogenated to either HCO\* (III) or COH\* (IV).

- ii) If the hydrogenation follows path III, the formation of  $\text{H}_2\text{CO}^*$  might result in the competitive evolution of  $\text{CH}_3\text{OH}$  or  $\text{CH}_4$  by the already mentioned pathways Ia', Ia'', Ib', Ib''.
- iii) In the case that  $\text{CO}^*$  is hydrogenated to  $\text{COH}^*$  (pathway II f)  $\text{CH}_4$  can be formed. Alternatively, further hydrogenation of  $\text{COH}^*$  to  $\text{HCOH}^*$  can proceed via II g leading to  $\text{CH}_4$  production. On the other hand, the possible hydrogenation to  $\text{H}_2\text{COH}^*$  might end again in the competitive routes to  $\text{CH}_4$  (Ib') and  $\text{CH}_3\text{OH}$  (Ib'').
- iv) A further possibility considers the hydrogenation of  $\text{HCO}^*$  to  $\text{HCOH}^*$  (IV a') which would lead to the competence between routes II g and IV b).

Finally, upon the direct dissociation of  $\text{CO}_2^*$  to  $\text{CO}^*$  and  $\text{O}^*$  (dissociative route) the formed  $\text{CO}^*$  can either desorb as  $\text{CO}_{(\text{g})}$  or be further hydrogenated to  $\text{COH}^*$  (Va) or  $\text{HCO}^*$  (Va') which after 5 consecutive hydrogenation steps result in  $\text{CH}_4$ . Note that in this dissociative sequence,  $\text{C}^*$  could also be formed without H assistance, i.e., by further decomposition of  $\text{CO}^*$  (Vb). Following this last reaction path, two routes involving 6 hydrogenation steps are required to obtain  $\text{CH}_4$  (Vb' or Vb'').

It is observed that all mechanisms involve the participation of  $\text{H}_x\text{C}_y\text{O}_z$  like intermediates which in several cases can be common initiators in the generation of distinct products. That is, competitive routes can occur starting from the same intermediate. The preferred reaction pathway would thus depend on the relative strength of interaction between the adsorbates and the catalyst surface.<sup>17</sup> Such interactions are susceptible to be tuned upon structural and electronic modifications of the metal-support perimeter, e.g., by manipulating the supported metal nanoparticle size, use of a second metal, doping with foreign additives and/or creation of oxygen defects in the support.<sup>17, 21, 22, 52, 67, 70, 93, 102, 119, 120, 132-135</sup> Furthermore, in all mechanisms the reaction route is initiated by adsorbed species ( $\text{CO}_2^*$  and  $\text{H}^*$ ), i.e., all cases can be described by the Langmuir-Hinshelwood model. Not surprisingly, rate equations based on this model accurately fit empirically collected kinetic and thermodynamic data.<sup>19, 97, 136</sup>



## 1.6. CO<sub>2</sub> hydrogenation by approaches different to thermal catalysis

As mentioned above, the activation of CO<sub>2</sub> implies the bending of the molecule, charge separation and electron/H transfer to the adsorbed CO<sub>2</sub><sup>\*</sup>. This can be done via thermal, photochemical or electrochemical processes.<sup>125</sup> So far, the discussion has involved only the first type of activation. Although the scaling-up of the alternative approaches to relevant scales of CO<sub>2</sub> capture and utilization (CCU) processes is less developed than in case of thermal catalysis, their investigation is highly intense in the scientific and academic communities. In the following, photochemical and electrochemical principles of CO<sub>2</sub> activation are shortly described.

**Photocatalysis:** In a photocatalytic reaction the process is typically mediated by a semiconductor material that absorbs light. If the energy of the absorbed photon ( $h\nu$ ) is equal or greater than the band gap of the semiconductor, an electron and a hole ( $h^+$ ) pair is produced. The electron is promoted to the conduction band (CB) while the hole stays in the valence band (VB). When CO<sub>2</sub> (dissolved in liquid) adsorbs on the surface of the semiconductor catalyst the electron can be transferred to produce the activated radical (reaction **R8**). To complete the process, a complementary oxidation reaction is required, which is commonly the oxidation of water (reaction **R9**).<sup>125, 138</sup> The principle and an example of the photocatalytic process are illustrated in **Figure 8**. The perspective research in this area is currently focused on the development of efficient stable photocatalysts and fundamental understanding of mechanisms.<sup>138</sup>

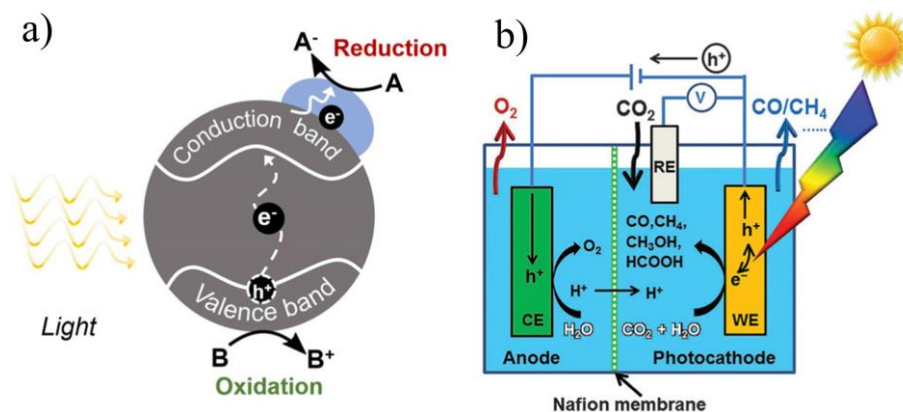


**Figure 8.** a) Principle of photoexcited electron-hole pair formation. Taken from Álvarez et al.<sup>125</sup> and b) schematic example of photochemical cell to produce compounds from CO<sub>2</sub> photocatalysis. Taken from Chang et al.<sup>138</sup>

**Electrocatalysis:** Analogously to photocatalysis, the activation of CO<sub>2</sub> is mediated by the electron transfer between a cathode and dissolved CO<sub>2</sub> in the liquid media. The difference is that in electrocatalytic processes the cathode is commonly a metallic (conductor) material. The process is completed also at another electrode (anode) where oxidation reaction(s) occur. A schematic representation of an electrochemical cell is shown in **Figure 9**.

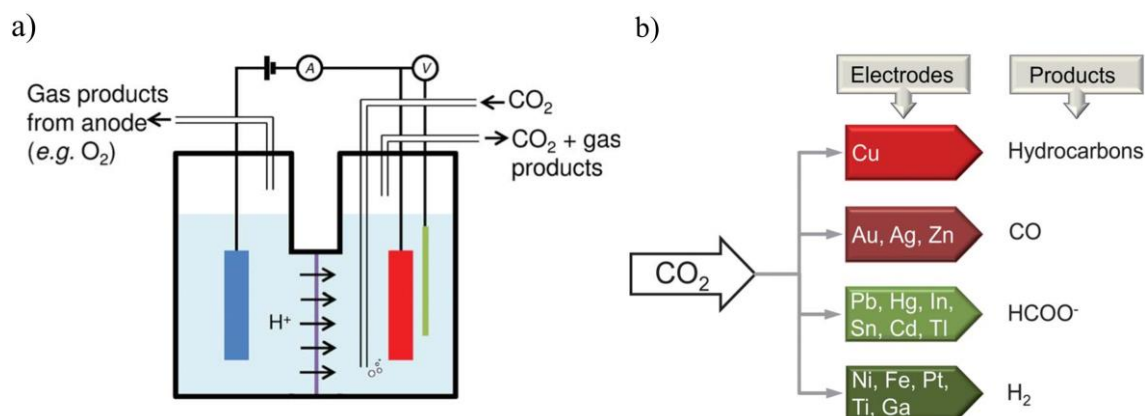


**Figure 9.** a) Scheme of laboratory electrochemical cell used for CO<sub>2</sub> hydrogenation and b) cathode materials and main products obtained during CO<sub>2</sub> electro-reduction. Taken from Kondratenko et al.<sup>139</sup>

A limitation of photo- and electrochemical processes is the difficult to control the selectivity. Besides the simultaneous formation of several CO<sub>2</sub> reduction products, the evolution of H<sub>2</sub> on the cathode contributes further to reducing the faradaic efficiency of the cell. Increasing efforts have been focused on increasing the efficiency of CO<sub>2</sub> dissolution and on improving cathode properties such as roughness, defects, porosity to have a better control of the selectivity, specially to hydrocarbons and alcohols, and to reduce the overpotential (difference between the thermodynamic and actual voltage to drive the reaction).<sup>139-141</sup>

## 2. Experiments and Methods

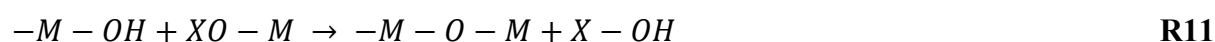
The previous chapter discussed the need to understand the physicochemical properties critical for the catalytic behavior that correlate with mechanistic observations, e.g., composition, particle size and/or presence of defects. However, other properties such as specific surface area, pore size, pore volume, support polymorphs among others are also of vital importance as they can influence these critical properties and determine the suitability of a catalyst for a certain reaction. This is highly dependent on the preparation procedure, i.e., the nature of the precursors (organic, inorganic), the mode of mixing (dropwise, stirring), heating/cooling rates, pH, solvent, calcination, reduction, etc. That is, the preparation method(s)

should be carefully selected to obtain adequate catalyst formulations. Hence, a detailed knowledge of the physical and chemical effects behind the synthesis procedure is helpful for the rational design of catalysts with defined characteristics. Therefore, the first part of this chapter is focused on the description of procedures and methodologies used for the preparation of supports and catalytic materials. The second part is dedicated to the description of the principles of the characterization techniques used in this investigation for extracting valuable information about the state of selected catalysts before, during and after the catalytic cycles of interest in this this thesis.

## 2.1. Materials preparation

The methods used for preparing the materials used in this work were sol-gel, wetness impregnation, precipitation, co-precipitation, and deposition-precipitation. Before describing the preparation procedures, a summary of the main characteristics of each method is provided.

**Sol-gel preparation:** This process involves first the formation of a sol phase followed by a gel. Typically, colloidal dispersions or inorganic precursors are used as starting materials.<sup>142</sup> A sol is a liquid suspension of solid particles ranging from 1 nm to 1  $\mu$ m obtained by the hydrolysis and partial condensation of an inorganic salt or metal alkoxide. Further condensation of the sol particles into a 3-D network produces the gel, i.e., the solid encapsulated by the liquid solvent. The latter can be removed by evaporative drying (xerogel) or supercritical extraction (aerogel). The sol-gel chemistry can be described by reactions **R10** – **R11**.<sup>143</sup> **R10** represents the hydrolysis step and **R11** the condensation. R can be an alkyl group and X could be either an alkyl or H.



The main advantages to highlight from this method are the high purity of the product and the ability to introduce several components in a single step.<sup>142, 143</sup> In the present thesis TiO<sub>2</sub> was prepared by supercritical extraction to support Ru on an area enriched with O-vacancies for the methanation of CO<sub>2</sub>.

### **Sol-gel prepared materials**

**Supports:** For the preparation of the TiO<sub>2</sub> support, Ti(IV) isopropoxide (3.75 mL) and ethyl acetoacetate (EAcAc) (1.62 mL) were mixed and magnetically stirred at 20 °C for 1 h. Afterwards HNO<sub>3</sub> (2.25 ml of 0.1 M) was dropwise added at 20 °C under continuous stirring to form a transparent gel by hydrolysis. The gel was subsequently extracted by supercritical ethanol (30 ml) in an autoclave (T = 245 °C, p = 60 bar) during 10 min to create an aerogel which was then calcined at 500 °C for 3 h in static air.

*Catalysts preparation:* For the synthesis of the Ru/TiO<sub>2</sub> sol-gel catalyst (Ru/TiO<sub>2</sub>-SG), RuCl<sub>3</sub>•H<sub>2</sub>O (0.16 g) dissolved in anhydrous ethanol (8.75 ml) was added to a mixture of Ti(IV) isopropoxide (3.75 mL) and ethyl acetoacetate (1.62 mL) at 20 °C. Subsequently, the followed procedure was identical to that described for synthesizing the bare TiO<sub>2</sub> support.

*Wetness impregnation preparation:* Impregnation consists in introducing a solution of a metal precursor into the pore space of a support. Ideally the precursor has no interaction with the solid surface. Two types of impregnation can be distinguished: capillary and diffusional. In the first the precursor pores are filled with air (after a drying pre-treatment). In the second the pore space is previously filled with the precursor solvent from the impregnation solution. In this thesis the former approach has been selected. It has the advantage that after contact between the previously dried solid (support) and the impregnation solution (active metal precursor) the pore volume barely changes, i.e., the pore structure and surface area remains almost unchanged.<sup>143</sup> This method was used to prepare Ru/TiO<sub>2</sub> for CO<sub>2</sub> methanation and its performance is further compared to their sol-gel counterpart.

*Wetness impregnation prepared material*

*Catalyst preparation:* Typically, RuCl<sub>3</sub>•H<sub>2</sub>O (0.018 g) dissolved in ultrapure water (13 ml) was homogeneously distributed on the surface of the sol-gel prepared TiO<sub>2</sub> support (0.5 g) using a syringe. The impregnated sample was left for 4 days at 20 °C and afterwards calcined in synthetic air at 500 °C during 3 h.

*Precipitation and co-precipitation preparation:* Precipitation is the most common method for preparing supports. The key step in precipitation preparation is the nucleation of the solid from a homogeneous solution. The formation of a particle is governed by the free energy of agglomerates of solution constituents, equation **eq. 3**,<sup>143</sup> in which  $\Delta G_{bulk}$  is the free energy difference between solution species and solid species,  $\Delta G_{interface}$  is the free energy change related to the formation of the interface, and  $\Delta G_{others}$  contains free energy changes due to contributions from other factors, e.g., impurities.

$$\Delta G = \Delta G_{bulk} + \Delta G_{interface} + \Delta G_{others} \quad (J \text{ mol}^{-1}) \quad \text{eq. 3}$$

If  $\Delta G < 0$ , the agglomeration will occur. Since  $\Delta G_{interface} > 0$  and if  $\Delta G_{others} \sim 0$ , the spontaneity of the process will depend on the contribution of  $\Delta G_{bulk}$  which is always negative. Assuming the formation of spherical particles, this term will increase proportional to  $r^3$  while



$\Delta G_{interface}$  will increase proportional to  $r^2$ . Equation **eq. 3** can be rewritten as equation **eq. 4**, in which  $\Delta\mu_{ls}$  represents the volumetric change in the chemical potential between the liquid and the solid ( $\text{J mol}^{-1} \text{m}^{-3}$ ) and  $\gamma_{ls}$  the surface free energy at the liquid-solid interface ( $\text{J mol}^{-1} \text{m}^{-2}$ ).

$$\Delta G = \frac{4}{3}\pi r^3 \Delta\mu_{ls} + 4\pi r^2 \gamma_{ls} \quad \text{eq. 4}$$

There is hence a critical size  $r_c$  at which the precipitation will begin which is inversely dependent on the precursor concentration, equation **eq. 5**.<sup>143</sup>

$$r_c = \frac{2\gamma_{ls}}{\Delta\mu_{sl}} \quad \text{eq. 5}$$

It is desirable to precipitate the target material in such a manner that the counterions of the precursor salts and the precipitation agent can easily be removed by a calcination step. Hence, the main advantage of this method is the high purity of the prepared materials while the main disadvantages are the requirement of relatively large volumes of salt containing solution and separation time.

Meanwhile, co-precipitation is usually applied in the preparation of materials based on more than one component. It consists in the simultaneous precipitation of a soluble components contained in the same solution.<sup>143</sup> This method is very suitable for the generation of homogeneous solids with a well-defined stoichiometry. After a pre-treatment step, e.g., calcination, the final product is normally composed by mixed crystallites of the components. In this work precipitation and co-precipitation were used for the synthesis of  $\text{ZrO}_2$  and  $\text{ZrO}_2\text{-MgO}$  supports, respectively. These matrixes were subsequently impregnated with  $\text{RuCl}_3$  solution to produce  $\text{CH}_4$  active catalysts ( $\text{Ru/ZrO}_2$  and  $\text{Ru/ZrO}_2\text{-MgO}$ ) which activities are compared based structural differences, especially O-defects contents, induced by the incorporation of MgO in the  $\text{ZrO}_2$  lattice after co-precipitation of the oxides.

### **Precipitation / co-precipitation prepared materials**

**Supports preparation:** The  $\text{ZrO}_2$  support was prepared by precipitation. For the synthesis, 50.7 g of  $\text{ZrOCl}_2 \cdot 8\text{H}_2\text{O}$  (Alfa-Aesar, 98% purity) were dissolved in ca. 2 l of distilled water. A solution of 1 M NaOH was subsequently dropwise added under stirring at 500 rpm at 20 °C until a pH of 12 was reached. The resulting slurry was aged during 1 h at 20 °C. Thereafter, the precipitate was separated by vacuum filtration and washed with distilled water until the pH of the filtrate reached 7. The solid was dried overnight at 100 °C and then calcined at 500 °C during 3 h under a flow of ca. 40 ml  $\text{min}^{-1}$  of synthetic air (2 °C  $\text{min}^{-1}$  heating ramp).

The MgO- $\text{ZrO}_2$  support was synthesized by co-precipitation. Typically, 48.9 g of  $\text{ZrOCl}_2 \cdot 8\text{H}_2\text{O}$  (Alfa-Aesar, 98% purity) plus 4.3 g of  $\text{MgN}_2\text{O}_6 \cdot 6\text{H}_2\text{O}$  (Sigma – Aldrich,

99% purity) were dissolved together in ca. 2 l of distilled water. The synthesis procedure followed the same steps as in the case of ZrO<sub>2</sub> preparation. The obtained solid was dried overnight at 100 °C and then calcined at 500 °C during 3 h under a flow of ca. 40 ml min<sup>-1</sup> of synthetic air (2 °C min<sup>-1</sup> heating ramp).

**Catalysts preparation:** For preparing Ru/ZrO<sub>2</sub> and Ru/MgO-ZrO<sub>2</sub> catalysts, typically 3 g of the corresponding calcined support were added to a solution of 67.3 mg of RuCl<sub>3</sub>.xH<sub>2</sub>O (Sigma – Aldrich) dissolved in 40 ml of distilled water under stirring at 450 rpm at 20 °C during 3 h. Afterwards, the solid was separated by vacuum filtration and washed with distilled water (ca. 2 l). Finally, each material was dried overnight at 100 °C and calcined at 500 °C during 3 h under a flow of ca. 40 ml min<sup>-1</sup> synthetic air (5 °C min<sup>-1</sup> heating ramp).

**Deposition-precipitation preparation:** It is normally difficult to systematically vary the size of active particles while maintaining a narrow particle size distribution by using a method such as wetness impregnation. However, by deposition-precipitation it is possible to disperse the active components uniformly over the surface of a support exerting a more stringent control on the phase particle size. This can be achieved by sufficiently strong interaction between the nuclei of an insoluble active precursor and the surface of a suspended support by changing the pH, the valence state of the active precursor or the concentration of a complexing agent.<sup>143</sup> The change in the free energy when considering the interaction of a hemispherical nucleus with the solid support is given by equation **eq. 6**. In which  $\gamma_{ls}$  represents the surface free energy at the liquid-solid interface and  $\gamma_{ss}$  at solid-solid interface (J mol<sup>-1</sup> m<sup>-2</sup>). Meanwhile  $\Delta\mu_{sl}$  represents the volumetric change in the chemical potential between the solid and the liquid solution (J mol<sup>-1</sup> m<sup>-3</sup>)<sup>143</sup>.

$$\Delta G = \frac{3}{2} \pi r^3 \Delta\mu_{sl} + 2\pi r^2 \gamma_{ls} + \pi r^2 \gamma_{ss} \quad \text{eq. 6}$$

Hence the critical size for precipitation in this case is given by equation **eq. 7**.

$$r_c = \frac{4(\gamma_{ls} + \gamma_{ss})}{9\Delta\mu_{sl}} \quad \text{eq. 7}$$

This equation indicates that the critical size of nuclei for initiating the precipitation rapidly decreases with the concentration of the precursor solution upon significant interaction with the surface of the support. This manner of precipitation within the pores will be more effective as the particles will tend to growth at smaller sizes than in the case of simple precipitation.<sup>143</sup> This is highly desirable in the preparation of stable (non-sintering) highly

dispersed precious based catalysts. In this work, this methodology is used to the fabrication of highly active ultra-low loaded Au/TiO<sub>2</sub> and Au/ZrO<sub>2</sub> catalysts for the RWGS reaction.

### **Precipitation / deposition-precipitation prepared materials**

**Supports preparation:** Aeroxide TiO<sub>2</sub> P25 was provided by Evonik Industries and used as received. Pure ZrO<sub>2</sub> was synthesized by precipitation in aqueous solution at 20 °C. 1 M NaOH (99.1 %, Fisher Chemical) was added dropwise to 200 mL of 0.1 M ZrOCl<sub>2</sub>.8H<sub>2</sub>O (98%, Alfa Aesar) under stirring at 450 rpm at 20 °C. The precipitate was left for 1 h in contact with the mother liquor and then filtered, washed with distilled water, and dried at 100 °C for 12 h. The dried material was ground and calcined at 500 °C (at 2 °C min<sup>-1</sup>) for 3h under synthetic air flow.

**Catalysts preparation:** Au/TiO<sub>2</sub> and Au/ZrO<sub>2</sub> catalysts with a nominal Au loading of 0.1 wt.% were prepared by a deposition–precipitation method. Typically, 1.0 g of the support powder were added to 20 mL of an aqueous solution of HAuCl<sub>4</sub> (99.995%, Sigma-Aldrich). The pH of the solutions was then adjusted to ~ 9 by adding 0.1 M NaOH dropwise. The suspensions were stirred at 450 rpm at 20 °C for 2 h, filtered and washed thoroughly with deionized water. Finally, the samples were dried at 80 °C for 12 h, and then used without any further heat treatment.

## **2.2. Characterization techniques**

**Infrared (IR) spectroscopy:** The IR radiation is characterized by electromagnetic waves with energy between 1.2 – 1240 meV or, equivalently, wavelengths in the range 1000 – 1 μm.<sup>144</sup> A molecule is said to be IR active when its electric dipole moment changes upon interaction with IR radiation.

At a certain distance between the atoms with mass  $m_1$  and  $m_2$  the potential energy is at a minimum (ground state). Upon radiation incidence deviations from this equilibrium state can occur. For small deviations, vibrational excitations can be explained upon the harmonic oscillator model, equation **eq. 8**.  $V(r)$  is the interatomic potential,  $r$  the distance between the vibrating atoms,  $r_{eq}$  the equilibrium distance between the atoms and  $k$  the force constant of the vibrating bond.

$$V(r) = \frac{1}{2}k(r - r_{eq})^2 \quad \text{eq. 8}$$

The harmonic oscillator potential energy in function of the distance separation between two atoms is illustrated in **Figure 10**. This model, however, is valid only for small deviations from the equilibrium and only transitions corresponding to  $\Delta n = 1$  are allowed. Atoms in a

molecule could be separated until their bond is broken and transitions with  $\Delta n > 1$  (overtones) are commonly observed. Hence, a more realistic model is provided by the anharmonic oscillator, equation **eq. 9**.  $D_{eq}$  is the dissociation energy of the vibrating bond and  $a$  is a parameter that controls the steepness of the potential well.

$$V(r) = D_{eq}(1 - e^{-a(r-r_{eq})})^2 \quad \text{eq. 9}$$

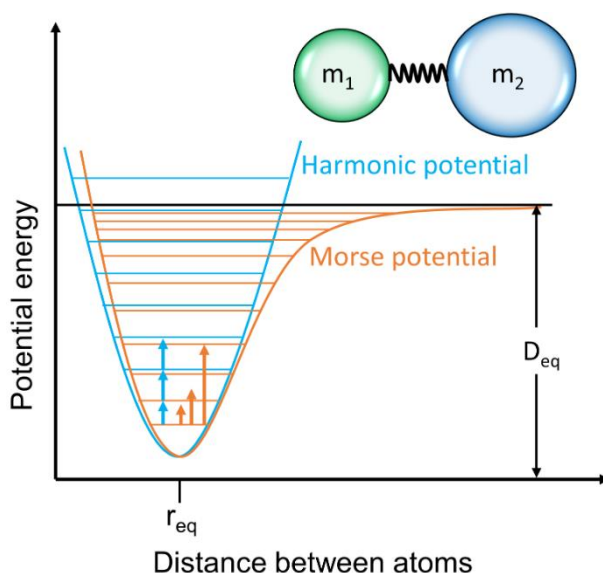


**Figure 10.** Scheme of the harmonic and anharmonic potential. The arrows represent the allowed transitions.

Molecules in the gas phase have rotational freedom and can be IR active if their electric dipole is affected by radiation. In that case the energy levels are represented by vibrational ( $n$ ) and rotational ( $j$ ) quantum numbers together with the moment of inertia  $I$ . Selection rules allow transitions corresponding to  $\Delta n = \pm 1, \pm 2, \pm 3 \dots$  and  $\Delta j = \pm 1$  for diatomic molecules and anharmonic motion. The energy of the discrete rotational energy levels as function of the rotational quantum number and moment of inertia are described by equations **eq. 10** and **eq. 11**.

$$E_n = \left(n + \frac{1}{2}\right) h\nu + \frac{h^2}{8\pi^2 I} j(j + 1) [J] \quad \text{eq. 10}$$

$$I = \mu r^2 \quad \text{eq. 11}$$

The IR absorption spectrum is described as a function of the intensity of the scattered radiation ( $R_\infty$ ) from a sample of infinite thickness in a range of frequencies. This is related to the ratio between the absorption coefficient ( $k$ ) and the scattering coefficient ( $S$ ) of the sample equation **eq. 12**, also known as Kubelka Munk function.

$$f(R_\infty) = \frac{(1-R_\infty)^2}{2R_\infty} = \frac{k}{S} \quad \text{eq. 12}$$

In the present study, IR spectroscopy was a very important technique that allowed for the identification of adsorbed intermediates and spectator species under reaction conditions. The gathered information served as initial insight for the proposal of reaction mechanisms in the studied system. Particularly, the form of IR spectroscopy known as diffuse reflectance infrared Fourier transform spectroscopy (DRIFTS) is the one used for the investigations in this work. Upon this technique the sample of interest can be measured as a loose powder.

**Description of performed IR experiments:** The equipment used for DRIFTS measurements during CO<sub>2</sub> methanation consisted in a Nicolet 6700 FTIR spectrometer using a high-temperature Praying Mantis reaction cell (Harrick) with CaF<sub>2</sub> windows equipped with a temperature control unit (Eurotherm) and connected to a gas dosing system with mass-flow controllers (Bronkhorst).

Each spectrum was recorded with a resolution of 4 cm<sup>-1</sup> and consisted of the average of 50 scans. Typically, 20 mg catalyst powder diluted with 60 mg α-Al<sub>2</sub>O<sub>3</sub> (pre-calcined at 900 °C in synthetic air for 8 h) were deposited over a layer of 80 mg pure α-Al<sub>2</sub>O<sub>3</sub> within the sample cup. This dilution was necessary to reduce light absorption of the pure dark catalyst. The cell was flushed with 30 ml min<sup>-1</sup> He after the oxidative pre-treatment while the temperature was increased to 300 °C at a rate of 15 °C min<sup>-1</sup>. Subsequently, the temperature was decreased at the same rate and background spectra were taken for each reaction temperature. The reaction was performed in a temperature range between 190 - 300 °C under 4:1 H<sub>2</sub>:CO<sub>2</sub> (22.4 ml min<sup>-1</sup> H<sub>2</sub>, 5.6 ml min<sup>-1</sup> CO<sub>2</sub>, 2 ml min<sup>-1</sup> He). The intensity of the signals is given in log(1/R) scale. The gas outlet was connected to a quadrupole mass spectrometer (Omnistar, Pfeiffer Vacuum GmbH) for online product analysis.

In addition to recording spectra at reaction conditions, with the aim to obtain more information about the adsorptive properties and the nature of the Ru surface species on the two catalysts, CO adsorption at 30 °C was performed. After reaction and subsequent flushing at 150 °C with He, the DRIFTS system was cooled down to 30 °C in He atmosphere. Once the target temperature was reached, a gas mixture consisting of 5 vol.% CO/He (30 ml min<sup>-1</sup>, atmospheric pressure) was fed into the reaction cell for 1 h (until saturation) and CO adsorption was followed by recording DRIFT spectra during this time with the same resolution as used for operando-DRIFTS assessments described before.

Meanwhile for the RWGS investigation the spectra were obtained in a Nicolet iS10 (Thermo Fischer Scientific) also with a high-temperature Praying Mantis reaction

cell (Harrick) with  $\text{CaF}_2$  windows equipped with a temperature control unit (Eurotherm) and connected to a gas dosing system with mass-flow controllers (Bronkhorst). The setup is shown in **Figure 11**.

Each spectrum consisted in an average of 64 scans recorded with a resolution of  $4\text{ cm}^{-1}$ . Typically, ca. 50 mg of catalyst powder were deposited over a layer of 80 mg pure calcined SiC. Before reaction, the catalyst surface was cleaned under synthetic air ( $30\text{ ml min}^{-1}$ ) at  $140\text{ }^\circ\text{C}$  to remove physisorbed atmospheric contaminants during 30 min. Thereafter, the cell was flushed with He ( $30\text{ ml min}^{-1}$ ) while the temperature was increased to  $270\text{ }^\circ\text{C}$  at a rate of  $10\text{ }^\circ\text{C min}^{-1}$ . Subsequently, the temperature was decreased at the same rate and background spectra were taken for each reaction temperature. The reaction was performed in a temperature range between  $140 - 270\text{ }^\circ\text{C}$  with a 4:1  $\text{H}_2:\text{CO}_2$  ratio ( $16\text{ ml min}^{-1}\text{ H}_2$ ,  $4\text{ ml min}^{-1}\text{ CO}_2$ ,  $10\text{ ml min}^{-1}\text{ He}$ ). The intensity of the signals is given in  $\log(1/R)$  scale.

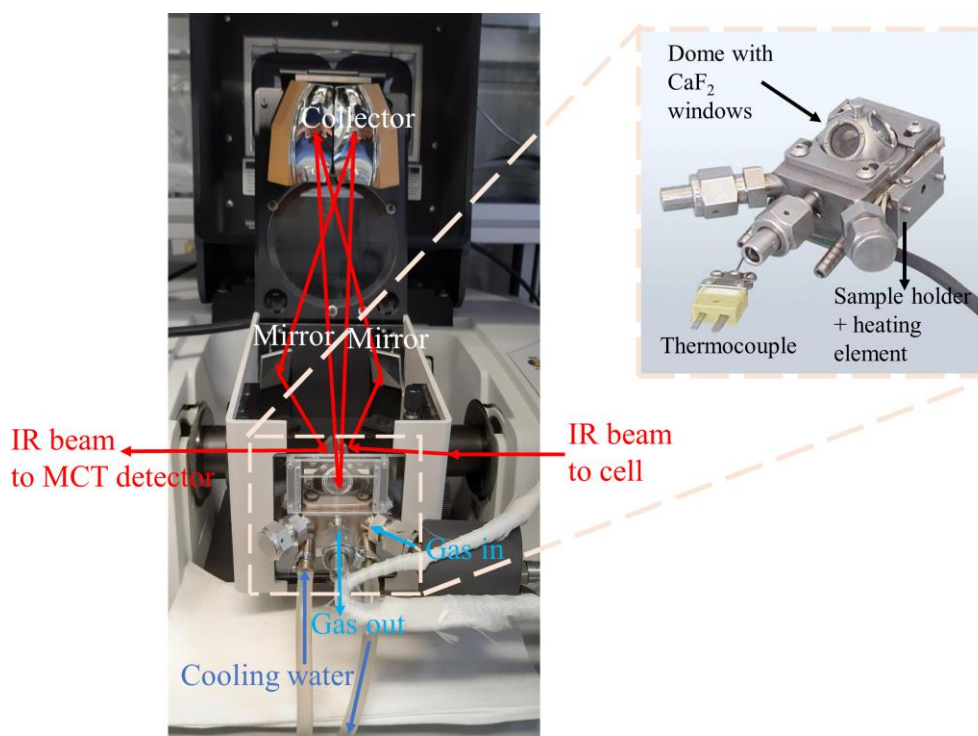


**Figure 11.** Setup for DRIFTS assessments. Inset: praying mantis<sup>TM</sup> high temperature reaction chamber.

**Raman spectroscopy:** In IR spectroscopy the energy transitions in vibrational and rotational energy states occur upon absorption of photons. It is also the case that a photon with energy  $h\nu_0$  instead of being absorbed, collide with a molecule with vibration energy ( $h\nu_{\text{vib}}$ ), and

result scattered either with the same ( $\nu_0$ ), lower ( $\nu_0 - \nu_{\text{vib}}$ ) or higher ( $\nu_0 + \nu_{\text{vib}}$ ) frequency than before the collision.<sup>145</sup> This is schematically shown in **Figure 12a**.

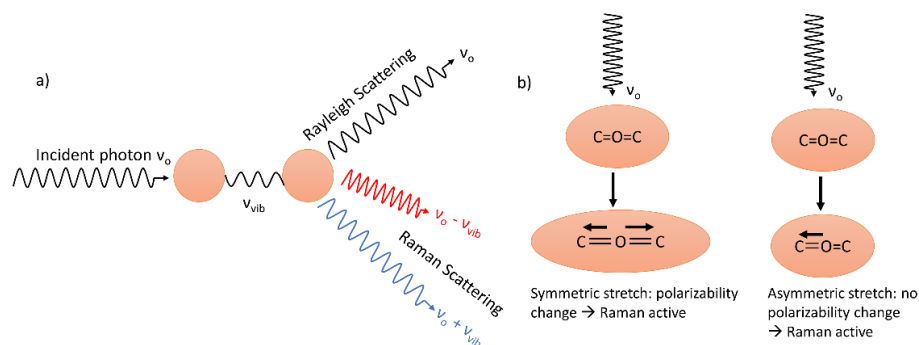


**Figure 12.** a) Light scattering from an oscillating molecule and b) schematic example of Raman active and Raman inactive transitions for CO<sub>2</sub> stretch changes upon interaction with a photon.

In the first case, the molecule that was excited to an energy level ( $h\nu_0$ ) returns to the original state, i.e., no net energy is exchanged in the collision. That is known as Rayleigh scattering. In the second case, the molecule after the excitation returns to an energy level above its original state since it gains energy from the photon. Hence, the scattered photon transferred energy to the molecule and its frequency shifts  $\nu_{\text{vib}}$  below the incidence frequency. Meanwhile in the third case, the excited molecule returns to a lower energy state as it transfers energy to the photon. Therefore, this last is scattered with a frequency shifted  $\nu_{\text{vib}}$  above the incidence frequency. The last 2 cases represent the Raman effect. In a Raman spectrum the signals recorded from the scattered photons correspond to vibration energy transitions. Like the case of IR spectroscopy, not all transitions can be observed. A molecule is said Raman active only in the case when its polarizability changes.<sup>146</sup> (**Figure 12b**). This technique is complementary to IR spectroscopy in the sense that changes in symmetrical molecules, e.g., H<sub>2</sub>, N<sub>2</sub>, O<sub>2</sub>, are observable. It results also useful in the case when vibrations tend to occur at frequencies of difficult access to IR spectrometers, as in the case of M-O bonds in some transition metal oxides.<sup>144</sup> In the present work, Raman spectroscopy has been ex-situ implemented to identify differences in the TiO<sub>2</sub> polymorphs in presence of RuO<sub>2</sub> added via sol-gel and wetness-impregnation procedure. The equipment consisted in a Horiba Jobin Yvon LabRam micro-spectrometer iHR 550 spectrometer using a 633 nm laser source.

**Description of performed Raman experiments:** Ex-situ Raman spectra were obtained at ambient temperature and pressure. Spectra were acquired from different areas of the sample to check for sample homogeneity, using a laser power of 0.1 mW to

10 mW with a power density of  $2.8 \times 10^5 \text{ W} \cdot \text{cm}^{-2}$ . Data analysis was performed by LabSpec 6, Jobin Yvon Horiba, built-in software.

**Electron paramagnetic resonance (EPR) spectroscopy:** Catalysts and/or reactive species can adopt paramagnetic states (one or various unpaired electrons). It results useful to follow the corresponding transitions of such electrons before, during and after reaction of such kind of systems. This can be done upon so called “quasi in-situ” or in-situ studies<sup>147</sup> The difference is that in the first case the spectra are recorded after treatment of the sample while in the second case the registration is performed simultaneously with the chemical process. Useful information that can be obtained by EPR in catalytic systems includes:<sup>147-151</sup>

- Oxidation states, e.g., of transition metal ions (d-block).
- Presence of defects, e.g., O-vacancies.
- Detection of radical species (organic and inorganic).
- Type of coordination geometry and associated changes of surface complexes.
- Aggregation state of supported species, e.g., isolation/clustering.
- Transference of electrons from defects to adsorbed species.

The fundamentals of this technique are explained below.

Paramagnetism is induced by the spin (angular momentum vector  $S$ ) of unpaired electrons in half-filled orbitals.<sup>147, 149</sup> When an external magnetic field ( $B_0$ ) is applied, a difference between the spin states of an unpaired electron (spin- up vs spin down) can be created (Zeeman interaction), **Figure 13a**.

Upon absorption of electromagnetic radiation, e.g., microwaves, a transition between these spin states can be induced while sweeping the external magnetic field until the microwave radiation matches the energy difference between the states (resonance), **Figure 13b**. The spin Hamiltonian in this simple case is given by equation **eq. 13**. Where  $g_e = 2.0023$  is the g factor of the free electron,  $\beta$  the Bohr magneton ( $9.27401 \cdot 10^{-28} \text{ J G}^{-1}$ ) and  $S_z$  represent the spin quantum numbers  $m_s = \pm 1/2$ .

$$H = g_e \beta S_z B_0 \tag{eq. 13}$$



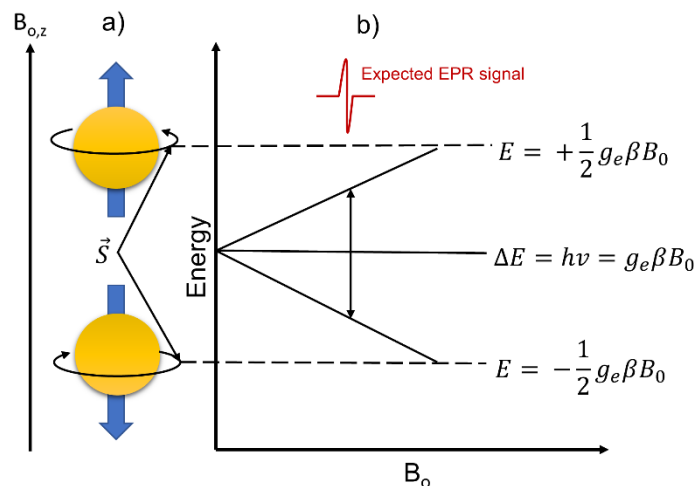


**Figure 13.** a) Alignment of the spin vector of a free electron ( $S = 1/2$ ) with the direction of the external magnetic field; b) energy levels of free electron in an external magnetic field with the expected EPR signal.

When the paramagnetic center is surrounded by other atoms the coordination sphere of the associated unpaired electron is not anymore isotropic and an anisotropic spin density distribution takes place. The transition energy, i.e., position and shape of the spectrum, will depend on the orientation of the paramagnetic complex with respect to the external magnetic field. In that case the Hamiltonian will then be represented by equation **eq. 14**, in which  $\vec{B}$  is a vector containing the components of the magnetic field.  $\mathbf{g}$  is a tensor (3x3 matrix) with non-zero diagonal components  $g_{xx}$ ,  $g_{yy}$  and  $g_{zz}$ .  $\hat{S}$  is the total electron spin matrix. In such a case the EPR spectrum would depict an asymmetrical shape and more than one sub-signal.

$$H = \beta \vec{B} \cdot \mathbf{g} \cdot \hat{S} \quad \text{eq. 14}$$

The energy of the paramagnetic electron(s) will also be affected by the nuclear magnetic moment of the nucleus of the associated atom as well as by the spin(s) of neighboring unpaired electrons (typical case of transition metal ions TMI). In the first case, the coupling of the electron with the nuclear magnetic moment of the atom it belongs to, gives place to additional energy levels (spectrum lines) known as hyperfine structure lines (hfs). In the second case, the interaction with more than one unpaired electron ( $S > 1/2$ ) gives place to other additional energy levels (spectrum lines) known as fine structure lines (fs). The spin Hamiltonian expression must consider these interactions, as shown by equation **eq. 15**. In which  $\mathbf{D}$  is the tensor accounting for the mutual interactions between electrons,  $\mathbf{A}$  the tensor accounting for the electron-nuclear spin interactions, and  $\hat{I}$  is the total nuclear spin matrix.<sup>147</sup>

$$H = \beta \vec{B} \cdot \mathbf{g} \cdot \hat{S} + \hat{S} \cdot \mathbf{D} \cdot \hat{S} + \hat{S} \cdot \mathbf{A} \cdot \hat{I} \quad \text{eq. 15}$$

In **Figure 14** a situation is shown in which one paramagnetic electron is contained in an atom with nuclear spin  $I = 1$ . Each energy of the electron spin splits in  $2I+1 = 3$  new energy

levels (quantum numbers -1, 0, 1). The transitions result in three lines separated by a distance “a” in magnetic field, also known as hyperfine coupling constant.

The spectra become more complicated with the complexity of the surrounding environment around the paramagnetic centers, in such cases.

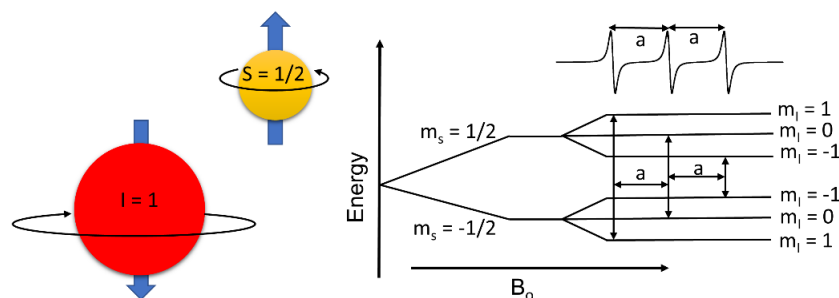


**Figure 14.** Energy splitting, transitions and expected EPR spectrum in the situation of a paramagnetic electron interacting with a nucleus with nuclear spin = 1.

In the present study this technique has been used for the in-situ detection of O-vacancies and electron transfer from these defects to surrounding metals in the support matrixes as well as to adjacent supported metal sites. The equipment employed for EPR measurements consisted in an ELEXSYS 500-10/12 X-band cw spectrometer (Bruker) using a modulation frequency of 100 kHz, microwave power of 6 - 10 mW and amplitude up to 5 G. The set-up and the quartz reactor are shown in **Figure 15**.

**Description of performed EPR experiments:** For CO<sub>2</sub> methanation, typically, 100 mg of sample were loaded in a quartz plug-flow reactor connected to a gas dosing unit equipped with mass flow-controllers (Bronkhorst) at the inlet while the outlet gases were conducted to a quadrupole mass spectrometer (Omnistar, Pfeiffer Vacuum GmbH) for online product analysis. In-situ EPR spectra were recorded in a temperature range between 190 – 270 °C, in a flow of 28.8 ml min<sup>-1</sup> H<sub>2</sub> + 7.2 ml min<sup>-1</sup> CO<sub>2</sub> + 4 ml min<sup>-1</sup> Ar after pre-oxidation in 40 ml min<sup>-1</sup> 5 vol.% O<sub>2</sub>/He followed by He flushing (40 ml min<sup>-1</sup>) at 150 °C. After the reaction, the temperature was cooled down to ca. -173 °C, and the corresponding spectra of the spent sample were recorded.

For RWGS Typically, 65 mg catalyst were placed inside a quartz plug-flow reactor. Spectra of fresh catalysts were first recorded at ca. -173 °C under a flow of 13 ml min<sup>-1</sup> He. Afterwards, the gas mixture was switched to 50 vol.% H<sub>2</sub>/He (13 ml min<sup>-1</sup>) while the temperature was increased to 280 °C. Under these conditions, the catalyst was reduced for 2 h. Subsequently, the temperature was decreased again to ca. -173 °C, and the corresponding spectra of the reduced sample were recorded. Next, the temperature

was increased to 250 °C in a flow of 13 ml min<sup>-1</sup> He. Once the desired temperature was reached, the gas was set to the reaction mixture (9.0 ml min<sup>-1</sup> H<sub>2</sub>, 3.0 ml min<sup>-1</sup> CO<sub>2</sub>, 6.0 ml min<sup>-1</sup> He, 2.0 ml min<sup>-1</sup> Ne). At these conditions, spectra were recorded for 2 h. After the reaction, the temperature was cooled down to ca. -173 °C, and the corresponding spectra of the spent sample were recorded.

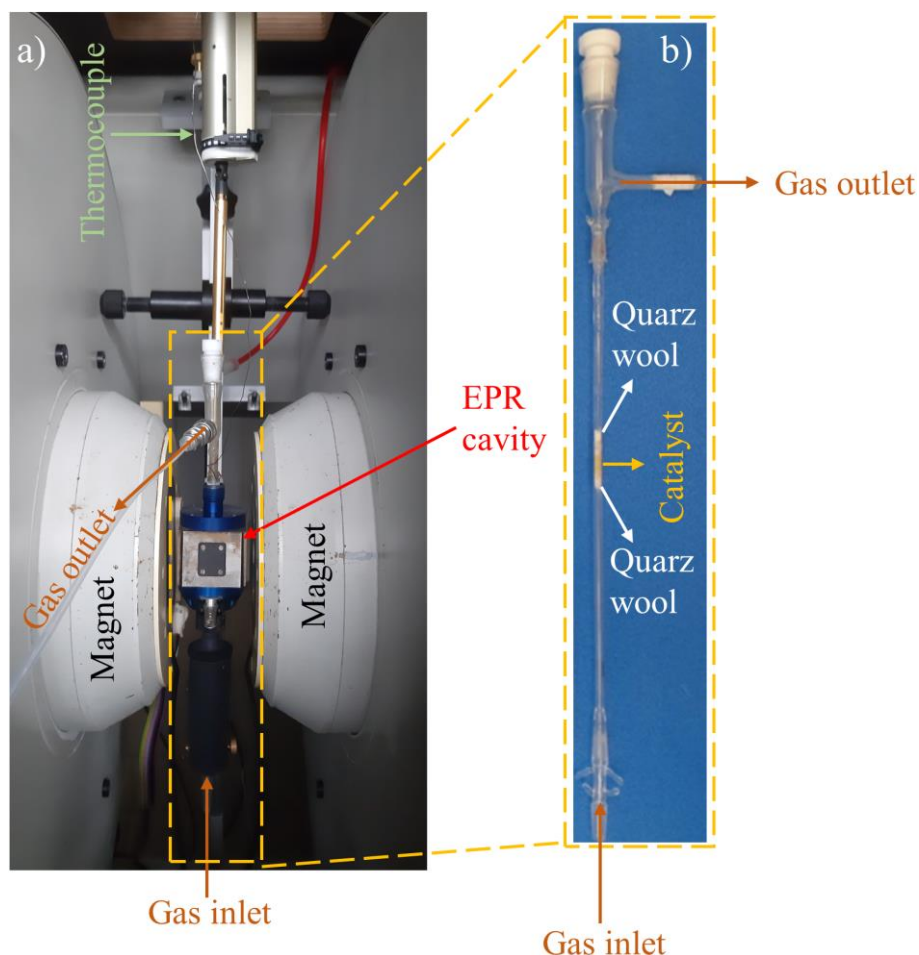


**Figure 15.** a) Set-up for in-situ EPR assessments and b) quartz reactor. Photo in b) taken from Bonke et al.<sup>149</sup>

**X-ray photoelectron spectroscopy (XPS):** Processes in heterogeneous catalysis occur on the materials surface. Therefore, surface sensitive techniques are of primary importance in this field. In this regard, techniques that utilize electrons, ions and atoms as exciting input provide the more detailed surface information as these particles are strongly absorbed or scattered and therefore their penetration depth is limited to the first few atomic layers.<sup>152</sup> In XPS most of the emitted electrons escape from depths up to 10 nm.<sup>153</sup> This technique is useful for determining material properties such as elemental composition and electronic properties of species on the surface.<sup>145</sup> In a XPS experiment the sample is exposed to a focused

monochromatic X-ray beam with an energy of about 1.5 keV (Al K $\alpha$  (1486.3 eV) / Mg K $\alpha$  (1253.6 eV)).<sup>145</sup> When a photon ( $E = h\nu$ ) with sufficient small wavelength (energy) is absorbed a core or valence electron with binding energy  $E_b$  can be excited to an empty state with an ejection kinetic energy  $E_k$ , as illustrated in **Figure 16**. This last variable can be measured using an energy selective electron detector. To determine the binding energy of the emitted photoelectron equation **eq. 16** is used, in which  $\phi$  represents the work function of the spectrometer. The binding energy is related to the atomic and molecular environment surrounding the absorbing atom. The binding energy is characteristic of each element, that is, all elements, except H<sub>2</sub> and He, can be detected by XPS.<sup>144</sup>

$$E_b = h\nu - (E_k + \phi) \quad \text{eq. 16}$$

Although this technique provides highly valuable surface information, scattering of electrons due to collisions with molecules in gas environments reduces their elastic mean path (< 1 mm) as they travel through condensed matter.<sup>152</sup> Hence, the measurements must commonly be performed in vacuum to avoid interferences related with the high absorption capacity of gas molecules, e.g., N<sub>2</sub> and O<sub>2</sub> from air.<sup>145</sup> Because of this drawback, information of the catalyst surface under relevant reacting environments is hardly obtained. Nevertheless a technique named near ambient X-ray photoelectron spectroscopy (NAP-XPS) has emerged to analyze systems at pressures up to about 2500 Pa.<sup>153</sup> The main difference with the conventional XPS is the addition of electrostatic lenses that refocus the electron trajectories into the apertures communicating the differential pumping stages. For more details the reader can consult reference.<sup>152</sup> NAP-XPS has been useful in this thesis to determine the distinct stability of formate-like species participating in the CO<sub>2</sub> methanation on Ru/TiO<sub>2</sub> catalysts.

In this thesis, XPS has been used to identify changes in the oxidation state of supported nanoparticles as well as for the identification of carbonaceous intermediates that participate in the reactions.

**Description of performed XPS experiments:** Ex-situ XPS assessments were performed on an ESCALAB 220iXL (Thermo Fisher Scientific) with monochromated Al K $\alpha$  radiation ( $E = 1486.6$  eV). The catalysts are prepared on a stainless-steel holder with conductive double-sided adhesive carbon tape. The electron binding energies were obtained with charge compensation using a flood electron source and referenced to the C 1s core level of carbon at 284.8 eV (C-C and C-H bonds). For quantitative analysis, the peaks were deconvoluted with Gaussian-Lorentzian curves using Unifit for windows version 2021. The peak areas were normalized by the transmission function of the spectrometer and the element-specific sensitivity factor of Scofield.<sup>154</sup>

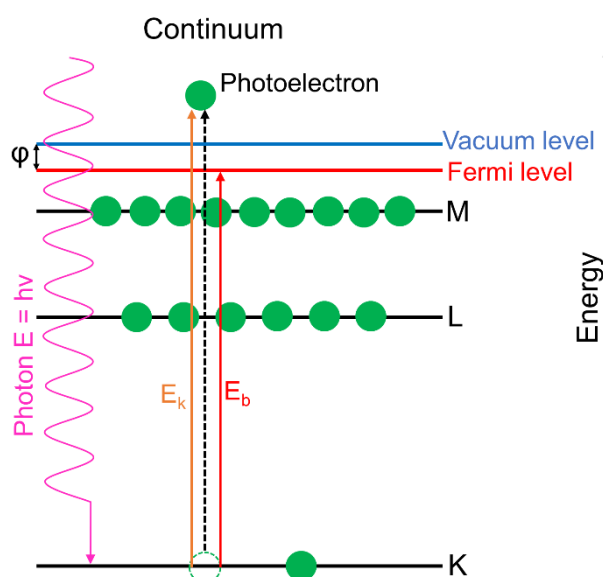


**Figure 16.** Excitation of a core electron (photoelectron) by the absorption of a photon with energy  $E = h\nu$ .

**Description of performed NAP-XPS experiments:** NAP-XPS were recorded on a laboratory NAP-XPS (SPECS Surface Nano Analysis GmbH, Germany). The setup is equipped with a differentially pumped Phoibos 150 electron energy analyser with a nozzle of 500  $\mu\text{m}$ , a monochromated Al  $K\alpha$  radiation source ( $E = 1486.6 \text{ eV}$ ) and a laser heating system for sample heating. The analysis chamber was connected to three mass flow controllers (Brooks, GF40) for dosing reaction mixtures up to a total pressure of 2 mbar. Reaction gases (4:1  $\text{H}_2:\text{CO}_2$ ) and formed products were monitored by a quadrupole mass spectrometer (QMS, MKS e-vision 2) attached to the lens system of the spectrometer. The powder samples were pressed on a stainless-steel sample plate using a laboratory press with 5 mm diameter and a load of about 0.5 t. Temperature was monitored by a thermocouple on the sample plate pressed to the sample surface. The electron binding energies were referenced to the C 1s core level of carbon at 284.8 eV (C-C and C-H bonds). For analysis, the peaks were deconvoluted into Gaussian Lorentzian curves using the software Unifit 2021. The peak areas were normalized by the transmission function of the spectrometer and the element-specific sensitivity factor of Scofield.<sup>154</sup>

**Scanning transmission electron microscopy (STEM):** Electron microscopies make use of an electron beam to yield information on the local chemistry and structure of a sample from macroscopic to atomic detail as the characteristic wavelength of electrons is below 1  $\text{\AA}$ . In

**Figure 17** it is schematically shown which kind of signals that can be obtained from electron microscopy. The main knowledge from these techniques includes:<sup>144</sup>

- Particle size, shape and distribution of supported nano particles and supporting phases.
- Chemical composition and internal structure of the solid (bulk, surface).
- Crystallographic information.

In this thesis only STEM and energy dispersive X-ray analysis (EDX) were used for analyzing the size, distribution, and chemical composition of the investigated catalysts before and after reaction.

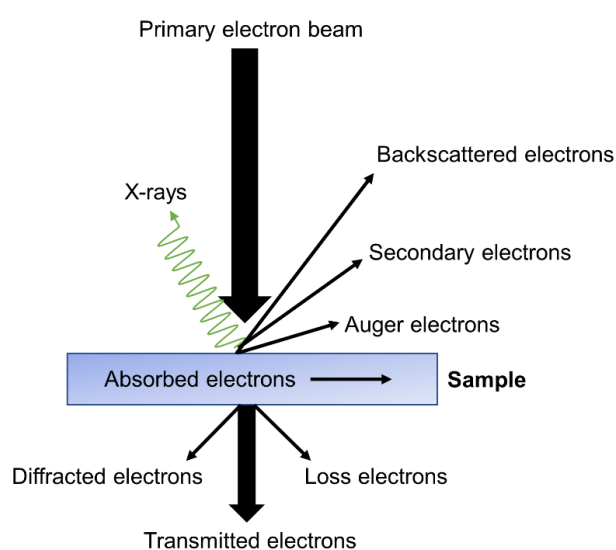


**Figure 17.** Scheme showing the interaction between an electron beam with a sample and the type of generated signals during a typical electron microscopy experiment.

In a TEM experiment a sample is exposed to an electron beam with energy in the range 100 – 400 keV. After passing through a system of condenser and electromagnetic lenses the electrons from the primary beam impinge the sample. The transmitted electrons are used to form a two-dimensional projection of the sample that is subsequently magnified to produce the bright field image, which requires the sample to be very thin. Meanwhile, the diffracted electrons are used to produce the dark field image. When these two modes of operation are combined with the use of scanning coils the technique is known as STEM.

Furthermore, the emitted X-rays from the interactions between absorbed electrons and the sample provide information about the chemical composition of the illuminated region and this is known as EDX. Other useful information, not in the scope of the present thesis, includes the use of secondary electrons (surface analysis); backscattered electrons that carry information

from subsurface regions; Auger and loss electrons used for composition analysis; diffraction patterns from crystals formed by diffracted electrons.<sup>144, 155</sup>

**Description of STEM performed experiments:** The micrographs were obtained with an aberration-corrected JEM-ARM200F (Jeol, Corrector: CEOS) at 200 kV. It is equipped with a Gatan Enfium ER electron energy loss spectrometer (EELS). A High-Angle Annular Dark Field (HAADF) and an Annular Bright Field (ABF) detector were used for STEM imaging, while during EELS acquisition, the Annular Dark Field (ADF) detector was used to acquire the positional reference image. The catalysts were deposited without further treatment onto a copper grid with holey carbon support (mesh 300), which was then transferred to the microscope.

**X-ray diffraction (XRD):** XRD probes the bulk (ordered) structure of materials. It is applied to identify crystal structures, estimate particle sizes and follow in-situ structure transitions at different stages/conditions of the catalyst.<sup>145</sup> It depends on the constructive interference of scattered radiation by relatively large parts of the sample, i.e., this technique is applicable for long range order.<sup>144</sup> Atoms in a periodic lattice elastically scatter X-rays. When the scattered X-rays are in phase constructive interference takes place and the path difference is equal for any integer number of the incoming X-ray wavelength wave (Bragg's condition), as given by equation **eq. 17**, where  $d$  is the space between planes,  $\theta$  the incidence angle,  $\lambda$  the wavelength of the incident X-ray. This is schematically illustrated in **Figure 18**.

$$n\lambda = 2d\sin(\theta)$$

**eq. 17**

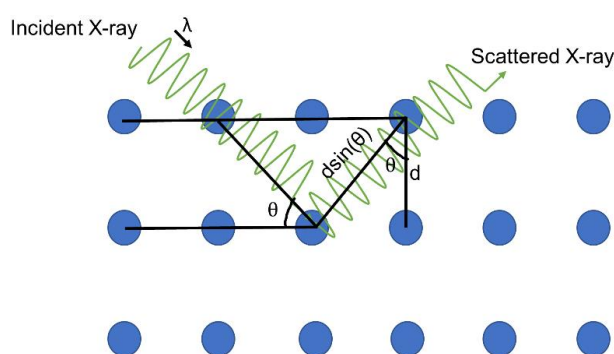


**Figure 18.** Principle of XRD (Bragg's condition).

In this thesis XRD has been used to identify the polymorphs constituting the supporting materials ( $\text{TiO}_2$ ,  $\text{ZrO}_2$ ) and the oxides of the supported nanoparticles, e.g.,  $\text{RuO}_2$ .

**Description of XRD performed experiments:** The XRD patterns were recorded using a PANalytical X'Pert PRO diffractometer equipped with a X'Celerator RTMS

detector using Ni-filtered Cu-K $\alpha$  radiation (1.544 Å) at 40 kV and 40 mA. Samples were mounted on silicon zero background holders, and the data were acquired stepwise (0.021° s<sup>-1</sup>) between 5-100° with a divergence slit of 2°. Peak positions and profiles were fitted with a Pseudo-Voigt function using the HighScore Plus software package (Panalytical). Phase identification was done using the PDF-2 database of the International Center of Diffraction Data (ICDD).

**H<sub>2</sub> Temperature programmed reduction (H<sub>2</sub>-TPR):** In a typical temperature programmed experiment a reaction is monitored while the temperature is linearly increased. Provided that the temperature interval is properly chosen, characteristic phase transformations can be detected. These will depend on the nature of the system under study and on factors affecting the kinetics of the transformation, e.g., flow rate of gaseous reactants, heat/mass transfer effectiveness between the catalyst and the surroundings, particle size, pore structure, chemical composition, among others.<sup>155</sup> The advantages of these techniques include straightforward qualitative interpretation and the rather simple and inexpensive instrumentation when compared to other spectroscopic methods.<sup>144</sup> The fundamentals of these the techniques are explained below.

Reduction is a mandatory step in the preparation of metallic catalysts. Knowing how to perform a reduction is of primary importance to obtain a catalyst at optimum state, e.g., avoiding sintering.<sup>144</sup> During H<sub>2</sub>-TPR the catalyst, normally in an oxidic state, is exposed to an H<sub>2</sub> containing stream while temperature is raised. The rate of reduction is continuously measured by monitoring the composition of the outlet gas. The reduction of the metal oxide MO<sub>n</sub> by H<sub>2</sub> is described by the reaction **R12**.



As water is produced in this process, its effective removal is crucial for during the experiment since it can re-oxidize the metal. The ratio between the partial pressure of H<sub>2</sub> and H<sub>2</sub>O determines the feasibility of the process. This is given by the equation **eq 18** for the free Gibbs energy change. As long as it is negative, i.e., the equilibrium ratio is larger than the actual ratio the reduction will proceed.<sup>144</sup> This is the case for most group VIII oxides, which constitute a vast amount of metallic catalytic phases.

$$\Delta G = nRT \ln \left( \frac{\left( \frac{p_{H_2O}}{p_{H_2}} \right)}{\left( \frac{p_{H_2O}}{p_{H_2}} \right)_{eq}} \right) \quad \text{eq. 18}$$



The effluent gas is monitored via a thermal conductivity detector (TCD). The principle consists in the transfer of heat from a hot wire, situated in a gas, at a rate proportional to the thermal conductivity of the gas. The main information given by plotting the TCD signal in function of temperature is related with the temperature(s) of reduction of the investigated material. Upon comparing different H<sub>2</sub>-TPR patterns for similar catalysts, it is possible to qualitatively determine the extent of metal-support interaction, distinct oxidic phases at the initial state or formation of bi-metallic alloys.<sup>144, 155</sup>

The usefulness of this characterization technique in the present thesis was to determine differences in the reducibility (peak temperature) of Ru when supported on oxidic carriers with different concentration of O-vacancies.

**Description of H<sub>2</sub>-TPR performed experiments:** For assessing the H<sub>2</sub> consumption on sol-gel prepared TiO<sub>2</sub> (TiO<sub>2</sub>-SG), 100 mg of bare support were loaded in U shaped quartz reactor. The H<sub>2</sub>-TPR run was carried out from RT to 800 °C in a 5% H<sub>2</sub>/Ar flow (30 ml min<sup>-1</sup>) with a heating rate of 10 K min<sup>-1</sup>. In the case of the Ru/TiO<sub>2</sub> catalysts, 50 mg were loaded and heated from RT to 700 °C with a heating rate of 20 °C min<sup>-1</sup>. The hydrogen consumption signals were recorded using a TCD detector.

In case of ZrO<sub>2</sub> and ZrO<sub>2</sub>-MgO materials for a typical H<sub>2</sub>-TPR run 150 mg of the corresponding as received sample were placed in a quartz U-shaped reactor. The temperature was increased from room temperature (RT) up to 700 °C with a heating rate of 10 K min<sup>-1</sup> in a 5 vol.% H<sub>2</sub>/Ar flow (30 ml min<sup>-1</sup>). A thermal conductivity detector (TCD) was used to monitor the consumption of H<sub>2</sub>.

**Low temperature N<sub>2</sub> physisorption:** In heterogeneous catalysis the knowledge of the catalyst surface area and pore properties (volume and size) is highly important as they influence the dispersion of the supported nanoparticles. Physical adsorption or physisorption of N<sub>2</sub> is the main technique used to determine the specific surface area of solid materials. The technique is based in the principle of the weak (non-dissociative) interaction between N<sub>2</sub> and the solid surface. The number of adsorbed molecules is measured and by knowing the area occupied by one molecule the surface area is determined.<sup>145</sup>

In a typical experiment, a known amount of sample is placed in a chamber that is evacuated to remove water and air and liberate the pores of the material. Afterwards a known amount of N<sub>2</sub> is admitted to the chamber and when the system reaches equilibrium pressure the amount of adsorbed gas can be estimated. The amount of gas adsorbed at equilibrium pressure is given as the difference between the amount of gas admitted and the amount of gas required

to fill the space around the adsorbent. By admission of successive charges of gas at a constant temperature as series of points can be constructed, this is known as the adsorption isotherm<sup>156</sup>.

The physisorption occurs in three different stages. The first is known as monolayer adsorption, all the adsorbed molecules are in contact with the surface layer of the solid. In the second stage, multilayer adsorption additional layers accommodate, but they are not in contact with the solid surface. The this stage is known as pore condensation and it occurs when the gas condensates in the pores at a pressure lower than the saturation pressure of the liquid phase of the adsorbent.<sup>156</sup> Only the information contained in the first stage is of interest for determining the surface area and pore properties.

The physisorption data are reported as the amount of adsorbed gas ( $\text{mol g}^{-1}$ ) as function of the pressure ratio  $p/p_0$ , with  $p_0$  the saturation pressure of the pure gas at the corresponding temperature. The most common method for determining the specific surface area is the BET (Brunauer, Emmett, and Teller). This model assumes that the first layer adsorbs with heat of adsorption  $\Delta H_{\text{ads}}$  while the subsequent layers adsorb with a heat of adsorption equal to the heat of condensation  $-\Delta H_{\text{cond}}$ . The BET equation is given by **eq. 19**.<sup>157</sup> In which  $n^a$  is the amount of adsorbed gas,  $n_m^a$  the monolayer capacity and C a constant related with the enthalpy of adsorption in the first layer. From the plot of  $\frac{p}{n^a(p_0-p)}$  in function of  $\frac{p}{p_0}$  the last parameters can be obtained.

$$\frac{p}{n^a(p_0-p)} = \frac{(C-1)}{n_m^a C} \frac{p}{p_0} + \frac{1}{n_m^a C} \quad \text{eq. 19}$$

By knowing  $n_m^a$  the specific surface area  $S$  ( $\text{m}^2 \text{g}^{-1}$ ) can be determined by equation **eq. 20**.  $N$  is the Avogadro number,  $\sigma$  the area occupied by a single  $\text{N}_2$  molecule ( $0.162 \text{ nm}^2 \text{ molecule}^{-1}$ ) and  $m$  the mass of sample used in the experiment.

$$S = \frac{n_m^a N \sigma}{m} \quad \text{eq. 20}$$

**Description of the  $\text{N}_2$  physisorption performed experiments:** In this work surface area measurements of the samples were performed on a Micromeritics ASAP 2010 device. For the assessments, 150 mg of sample were placed in the analysis tube and outgassed at  $200 \text{ }^\circ\text{C}$  for 4 h prior to the exposure to the adsorptive  $\text{N}_2$  atmosphere. BET surface area and pore volume were calculated from  $\text{N}_2$  adsorption isotherms measured at  $-196 \text{ }^\circ\text{C}$ . The average pore diameters were calculated from the desorption branch of the isotherm using the BJH method.

**Inductively coupled plasma optical emission spectroscopy (ICP-OES):** It is important to quantify the real amount of active metal as its composition could vary with respect to the nominal/expected quantity. Moreover, this allows for normalization of the reaction rates by

weight of active metal which is helpful to compare the catalytic behavior among distinct samples regardless the preparation methodology. The determination of metals in a variety of different sample matrices can be performed upon ICP-OES. The technique upon the spontaneous emission of photons from atoms and ions excited in a radio frequency (RF) discharge. Solid samples require the digestion in acid media to dissolve the analytes. Afterwards the sample solution is converted to an aerosol and directed to the central plane of the plasma which sustains a temperature ca. 1000 K. The elements liberated as free atoms in gaseous state transform into atoms in excited states which relax by emission of a photon with elemental specific wavelength. The number of photons is proportional to the concentration of the element from which they origin.<sup>158</sup>

**Description of the ICP-OES performed experiments:** For this investigation the bulk elemental composition of the materials was determined using a 715-ES ICP emissions spectrometer (Varian, Palo Alto, CA, USA). Prior to analysis, test samples were subjected to a microwave-assisted digestion process in a mixture of HF and aqua regia at 200 °C and 60 bar.

**Temporal analysis of products (TAP):** Processes in heterogeneous catalysis are complex and could occur at so short time scales that changes cannot be observed by steady state assessment techniques. To close this gap transient techniques have been developed. Transients are introduced into a system by perturbing one or more state variables (temperature, pressure, composition, flow rate) and then the relaxation/response of the system is analyzed. These techniques are highly useful to detect short-lived intermediates or estimating rate constants of elementary steps.<sup>159, 160</sup> TAP belongs to this type of techniques.

The most basic experiment consists in a single pulse ( $10^{13}$  -  $10^{15}$  molecules) introduced to the packed bed reaction chamber. At the experiment conditions ( $2 \cdot 10^{-6}$  –  $2 \cdot 10^{-4}$  bar) the intramolecular collisions are negligible, and the diffusion mechanism can be modelled by the Knudsen diffusion regime, equations **eq. 21** and **eq. 22**, in which  $\varepsilon$  is the fractional bed voidage,  $d_i$  internal diameter of channels between particles,  $\tau$  the bed tortuosity,  $r_p$  radius of particles,  $T$  the temperature in K,  $R$  the universal gas constant and  $M$  the molecular weight of the gas. The outlet gas is analyzed in a mass spectrometer.<sup>160</sup>

$$D = \frac{\varepsilon d_i}{\tau} \frac{1}{3} \sqrt{\frac{8RT}{\pi M}} \quad \text{eq. 21}$$

$$d_i = \frac{4\varepsilon}{3(1-\varepsilon)} r_p \quad \text{eq. 22}$$

**Description of the TAP performed experiments:** In this work TAP has been useful to determine the relative strength of adsorption of CO<sub>2</sub> and CO on Au/ZrO<sub>2</sub> and Au/TiO<sub>2</sub> during RWGS reaction. Transient tests were performed in a temporal analysis of products (TAP-2) reactor described in detail elsewhere.<sup>159-161</sup> Typically, 41 mg of a 310-750 μm sieve fraction of each catalytic material was packed between two layers of quartz particles (sieve fraction of 250–355 μm) in a quartz microreactor. Before the transient tests, catalytic materials were heated in an H<sub>2</sub> (3 ml min<sup>-1</sup>) and Ar (3 ml min<sup>-1</sup>) flow from room temperature to 300 °C and kept under these conditions for 30 minutes. Then, the reactor was evacuated to about 10<sup>-5</sup> Pa. Hereafter, mixtures of CO:Ar = 1:1 or CO<sub>2</sub>:Ar = 1:1 were pulsed at the same temperature. The feed mixtures were prepared using CO (Messer Griesheim, 4.7), CO<sub>2</sub> (Air Liquide, 4.5), and Ar (Air Liquide, 5.0) without additional purification. Transient responses related to the feed components and reaction products were monitored at the reactor outlet with a quadrupole mass spectrometer (HAL RD 301 Hiden Analytical) at m/z signals related to reactants, reaction products, and argon, with the latter being an inert standard: 44 (CO<sub>2</sub>), 32 (O<sub>2</sub>), 28 (CO<sub>2</sub>, CO) and 40 (Ar). For each m/z, pulses were repeated 10 times and averaged to improve the signal-to-noise ratio.

Using a model-free approach developed for this technique,<sup>161</sup> the experimental responses of CO<sub>2</sub>, CO and Ar were transformed into the dimensionless form according to **equations eq. 23 – 25**. Such transformation allows unambiguously determining the type of interaction of pulsed reactant with catalyst (diffusion, reversible or irreversible adsorption).

$$\text{Dimensionless flow} = \frac{\text{Flux}(\text{CO}_x) \cdot \text{reactor length}^2}{\text{pulse size} \cdot D_{\text{Knudsen}}^{\text{eff}}(\text{CO}_x)} \quad \text{eq. 23}$$

$$\text{Dimensionless time} = \frac{t \cdot D(\text{CO}_x)}{\text{reactor length}^2} \quad \text{eq. 24}$$

$$\text{Flux}(\text{CO}_x) = I(\text{CO}_x) \frac{N(\text{CO}_x)}{\int_0^t I(\text{CO}_x)} \quad \text{eq. 25}$$

$I(\text{CO}_x)$ ,  $N(\text{CO}_x)$ , and  $D_{\text{Knudsen}}^{\text{eff}}(\text{CO}_x)$  are the experimental mass spectroscopic signal intensity, the size of pulse, and the effective Knudsen diffusion coefficient of CO or CO<sub>2</sub>, respectively. To determine the diffusion coefficients of CO and CO<sub>2</sub>, the diffusion coefficient of Ar was initially derived by fitting the experimental response to the Knudsen diffusion model as described elsewhere.<sup>162, 163</sup> Equation **eq. 26** was used to obtain the required coefficients with  $M(\text{Ar})$  and  $M(\text{CO}_x)$  are the molecular weights of Ar and CO<sub>x</sub>, respectively.

$$D_{Knudsen}^{eff}(CO_x) = D_{Knudsen}^{eff}(Ar) \sqrt{\frac{M(Ar)}{M(CO_x)}} \quad \text{eq. 26}$$

**Catalytic evaluation:** The catalytic screening experiments were performed at differential reaction conditions, i.e., conversion of CO<sub>2</sub> (X<sub>CO<sub>2</sub></sub>) of maximum ca. 20 %. This parameter was calculated using **eq. 27**, where F<sub>CO<sub>2</sub>,in</sub> and F<sub>CO<sub>2</sub>,out</sub> corresponds to the initial and outlet molar flow rate of CO<sub>2</sub>.

$$X_{CO_2} = \frac{F_{CO_2,in} - F_{CO_2,out}}{F_{CO_2,in}} \quad \text{eq. 27}$$

The rate of formation of product i (*r<sub>i</sub>*) was calculated upon **eq. 28**, where F<sub>i,out</sub> corresponds to the molar flow of compound i in the effluent gas and m<sub>M</sub> to the absolute mass of active metal as determined by ICP-OES.

$$r_i = \frac{F_{i,out}}{m_M} \quad \text{eq. 28}$$

The selectivity to product i (*S<sub>i</sub>*) was calculated from **eq. 29**, where F<sub>i,out</sub> represents the molar flow of the corresponding compound in the effluent gas. Also, the selectivity can be calculated when comparing the rate of the interest product i with respect to the sum of rates of competing products j.

$$S_i = \frac{F_{i,out}}{F_{CO_2,in} - F_{CO_2,out}} = \frac{r_i}{\sum_j r_j} \quad \text{eq. 29}$$

The turnover frequencies (TOFs) were calculated by **eq. 30** using the molar mass of active metal (M<sub>M</sub>) and its dispersion (D<sub>M</sub>) obtained from either TEM or H<sub>2</sub> chemisorption. In case of the first option, **eq. 31 and 32** should be applied. In **eq. 31** d<sub>k</sub> is the estimated size of metal nanoparticles in nm estimated from a set of different micrographs. n<sub>k</sub> is the percentage of particles with a size d<sub>k</sub>. Analogously, v<sub>M</sub> is the volume of a metal atom in Å<sup>3</sup> and S<sub>M</sub> the its respective surface area in Å<sup>2</sup>.<sup>164</sup>

$$\text{TOF} = \frac{r_i M_M}{D_M} = \left( \frac{\text{moles}_i}{g_{cat} * s} \right) / \left( \frac{\text{moles}_{surface\ metal}}{g_{cat}} \right) \quad \text{eq. 30}$$

$$d_{va} = \left( \frac{\sum_k n_k d_k^3}{\sum_k n_k d_k^2} \right) \quad \text{eq. 31}$$

$$D_M = 10 \left( \frac{6v_M}{S_M} \right) \left( \frac{1}{d_{va}} \right) \quad \text{eq. 32}$$

If data from H<sub>2</sub> chemisorption are used, equations **eq. 33 – 35** must be applied, when assuming spherical shape of the nanoparticles.<sup>164</sup> In **eq. 33** ρ<sub>M</sub> the density of the metal (g cm<sup>-3</sup>), S<sub>M</sub> the specific surface area of metal (m<sup>2</sup> g<sup>-1</sup>). In **eq. 34** and **35** V<sub>ad</sub> the chemically adsorbed volume of H<sub>2</sub> (ml), SF the stoichiometric factor assuming that one atom of H is adsorbed per each atom of Ru (1), N<sub>A</sub> Avogadro's number, R<sub>A</sub> the atomic cross sectional area of metal (nm<sup>2</sup>),

$W_s$  the weight of the sample (g), wt% the percentage of supported metal in the sample (wt.%) and  $V_m$  the molar volume of  $H_2$  at standard conditions (22414 ml mol<sup>-1</sup>).

$$d_M = \frac{6 \cdot 10^3}{S_M \rho_M} \quad \text{eq. 33}$$

$$S_M = \frac{V_{ad} S F N_A R_A M_M}{M_M V_m} \quad \text{eq. 34}$$

$$D_M = \frac{V_{ad} M_M S F}{wt\% V_m} * 100 \quad \text{eq. 35}$$

**Description of activity measurements on Ru/TiO<sub>2</sub> catalysts:** The kinetic experiments were performed in a fixed-bed quartz tube micro-reactor (with 4 mm inner diameter) at atmospheric pressure under a total gas flow of 40 ml min<sup>-1</sup> with a 4:1 H<sub>2</sub>:CO<sub>2</sub> gas mixture (32 ml min<sup>-1</sup> H<sub>2</sub>, 8 ml min<sup>-1</sup> CO<sub>2</sub>). The catalyst was diluted in a ratio of 1:10 with inactive and thermally stable  $\alpha$ -Al<sub>2</sub>O<sub>3</sub> powder (calcined at 900 °C for 24 h) to ensure differential reaction conditions (conversion < 20%). In total, about 200 mg of the diluted catalyst was used during the measurements. After oxidative pre-treatment, the catalyst was in-situ reduced after switching to the reaction mixture. The influent and effluent gases were analyzed by online gas chromatography with a CO detection limit of ca. 5 ppm (DANI 86.10), using thermal conductivity detectors (H<sub>2</sub> used as carrier gas) and a standard test gas mixture for calibration.

**Description of activity measurements on Ru/ZrO<sub>2</sub> and Ru/ZrO<sub>2</sub>-MgO catalysts:** The performance of the catalysts was determined in a U-shaped fixed-bed quartz tube micro-reactor at atmospheric pressure. Typically, 50 mg of sample with particle size ca. 325  $\mu$ m were loaded in the center of the reactor and fixed by 225 mg of pure calcined SiC at both sides. Before reaction, the catalyst was pre-treated under synthetic air (30 ml min<sup>-1</sup>) at 140 °C during 30 min to remove contaminants from the surface. After this oxidative pre-treatment the reaction gas mixture was admitted into the reactor. The reaction flow (30 ml min<sup>-1</sup>) consisted in 16 ml min<sup>-1</sup> H<sub>2</sub>, 4 ml min<sup>-1</sup> CO<sub>2</sub> and 10 ml min<sup>-1</sup> N<sub>2</sub>. The flow rate was controlled with respective mass-flow controllers (Bronkhorst). Each gas had a purity  $\geq$  99.99%. The effluent gases were analyzed by on-line gas chromatography (Schimadzu 2014) equipped with thermal conductivity and FID detectors. Two columns were used to separate the gases. The first column (Molsieve 5 Å, Agilent) used to separate CO, O<sub>2</sub> and H<sub>2</sub> and the second column (PoraPLOT Q, Agilent) to separate CO and CO<sub>2</sub>. The Ru-mass-normalized reaction rates were

calculated for differential reaction conditions, i.e., conversion of CO<sub>2</sub> (X<sub>CO<sub>2</sub></sub>) of maximum ca. 20 %.

**Description of activity measurements on Au/TiO<sub>2</sub> and Au/ZrO<sub>2</sub> catalysts:**

Catalytic measurements were conducted in the temperature range of 250 – 350 °C at a total pressure of 3 and 20 bar. The catalysts were pressed, crushed, and sieved to 310 – 750 μm. Typically, the reactor (i.d. 4 mm) was filled with 200 mg of catalyst diluted with 800 mg SiC. Reduction of catalysts was performed at 300 °C in 50 vol.% H<sub>2</sub>/N<sub>2</sub> with a flow rate of 13 ml min<sup>-1</sup>. After cooling to reaction temperature, the reacting mixture CO<sub>2</sub>/H<sub>2</sub>/N<sub>2</sub> = 1/3/2 was fed at a flow rate of 17.5 ml min<sup>-1</sup>. The reaction products were detected with an on-line Agilent HP 7890 gas chromatograph equipped with both FID (FFAP and AL/M columns) and TCD (HP-Plot Q and Molsieve 5A columns).

### 3. Results and Discussion

#### 3.1. CO<sub>2</sub> methanation on Ru/TiO<sub>2</sub> catalysts

Ru was selected as the active metal for the methanation of CO<sub>2</sub>. As already discussed, CH<sub>4</sub> production on Ru catalysts represents a great potential for the development of CO<sub>2</sub> utilization technologies. Although their performance (activity and selectivity) can overcome that of typical Ni based catalysts, the use of Ru must be minimized for allowing economic feasibility and competitiveness in applications at relevant scales. Therefore, two samples with comparable Ru loading below 1 wt.%, i.e., ca. 0.9 wt.% were prepared by different methods. One preparation followed the sol-gel route (by now identified as Ru/TiO<sub>2</sub>-SG) while the other consisted on the typical wetness impregnation (by now identified as Ru/TiO<sub>2</sub>-imp). Meanwhile, in both cases the supporting matrix was the same TiO<sub>2</sub> prepared via sol-gel (by now identified as TiO<sub>2</sub>-SG).

**Support and catalysts characterization:** The Ru loading and textural properties from N<sub>2</sub> physisorption, i.e., mean pore diameters, pore volumes and BET specific surface area (BET SSA) of the distinct samples are shown in **Table 3**. For The bare TiO<sub>2</sub>-SG support a BET SSA of 141 m<sup>2</sup> g<sup>-1</sup>, a mean pore diameter of ca. 5 nm and a pore volume of 0.26 cm<sup>3</sup> g<sup>-1</sup> were determined. For the fresh Ru/TiO<sub>2</sub>-SG the lowest SSA (61 m<sup>2</sup> g<sup>-1</sup>) and pore volume (0.17 cm<sup>3</sup> g<sup>-1</sup>) with intermediate mean pore diameter (8-9 nm) were found. In contrast, for Ru/TiO<sub>2</sub>-Imp, BET SSA dropped only slightly (136 m<sup>2</sup> g<sup>-1</sup>) while the pore diameter (12 nm) and volume (0.43

cm<sup>3</sup> g<sup>-1</sup>) increased significantly with respect to the bare support. Although the Ru content was virtually the same, these structural differences suggest that incorporation of Ru via sol-gel methodology caused a partial disruption of the mesoscopic structure of TiO<sub>2</sub>-SG. However, the increase in the pore diameter and volume in Ru/TiO<sub>2</sub>-Imp provides a hint that Ru NPs grew comparatively more in this case. Considering that all samples, including the bare support, have experienced the same pretreatment after the synthesis (3h calcination at 500 °C in air) it can be assumed that the marked differences in BET SSA and pore volume between were not caused by this thermal pretreatment but might be due to special interactions of the Ru component with the support resulting from the preparation route.

**Table 3:** Pore and surface properties of the fresh TiO<sub>2</sub>-SG support and Ru/TiO<sub>2</sub>-SG and Ru/TiO<sub>2</sub>-Imp catalysts

Sample	Ru loading / wt.%	BET SSA / m <sup>2</sup> g <sup>-1</sup>	Pore diameter / nm	Pore volume / cm <sup>3</sup> g <sup>-1</sup>
TiO <sub>2</sub> -SG	-	141	5	0.26
Ru/TiO <sub>2</sub> -SG	0.90	61	8-9	0.17
Ru/TiO <sub>2</sub> -Imp	0.91	136	12	0.43

The SSA and pore volume/area as a function of the pore size are plotted in **Figure 19**. The N<sub>2</sub> isotherms of all samples showed the typical shape of isotherms of type IV with a hysteresis loop, characteristic of mesoporous materials (**Figure 19a-c**).<sup>156, 165</sup> The pore volume/area distribution is narrower for the bare support, wider for Ru/TiO<sub>2</sub>-Imp and intermediate for Ru/TiO<sub>2</sub>-SG (**Figure 19d-f**).

The XRD powder patterns of the bare support and catalysts are shown in **Figure 20a**. TiO<sub>2</sub>-SG showed only typical reflections of the anatase (101), (004) and (200) planes at 2θ = 25.3°, 37.9° and 48.0°, respectively (ICDD 01-075-2547). Meanwhile, the pattern of the Ru/TiO<sub>2</sub>-SG catalyst showed additional reflections of rutile TiO<sub>2</sub> at 2θ = 27.4°, 36.1° and 41.2° corresponding to rutile planes (110), (101) and (111) (ICDD 00-021-1276), respectively. This phase change has been ascribed to the similarity between the lattice constants of RuO<sub>2</sub> and rutile TiO<sub>2</sub>.<sup>166</sup> This was also reported by Kim et al. who detected the formation of rutile TiO<sub>2</sub> upon coverage of mesoporous TiO<sub>2</sub> (anatase) with RuO<sub>2</sub> nanoparticles after annealing at 250 °C.<sup>167</sup> In contrast, no rutile formation was observed in the Ru/TiO<sub>2</sub>-Imp catalyst. This suggests that intimate mixing of TiO<sub>2</sub> and Ru precursors, which is typical for the sol-gel method, promotes incorporation of Ru in Ti lattice positions of TiO<sub>2</sub> and induces crystal phase transitions.



The weight fraction of rutile TiO<sub>2</sub> in the fresh Ru/TiO<sub>2</sub>-SG (calculated by the method of Zhang and Banfield<sup>168</sup>) amounts to 18.6 wt.%, which is similar to commercial P-25 (80 wt.% anatase, 20 wt.% rutile).<sup>62</sup> Reflections of RuO<sub>2</sub> (110) and (101) planes (ICDD 01-088-0322) at  $2\theta = 28.1^\circ$  and  $35.1^\circ$  were present in both as-prepared Ru catalysts. The spent catalysts, on the other hand, did not show any RuO<sub>2</sub> reflections (**Figure 20b**), however, the reflections of TiO<sub>2</sub> rutile (19 wt.%) were still observed. Metallic Ru<sup>0</sup> crystallites were evidenced by a small peak at  $2\theta = 44.1^\circ$  which was most pronounced for the spent Ru/TiO<sub>2</sub>-SG sample.

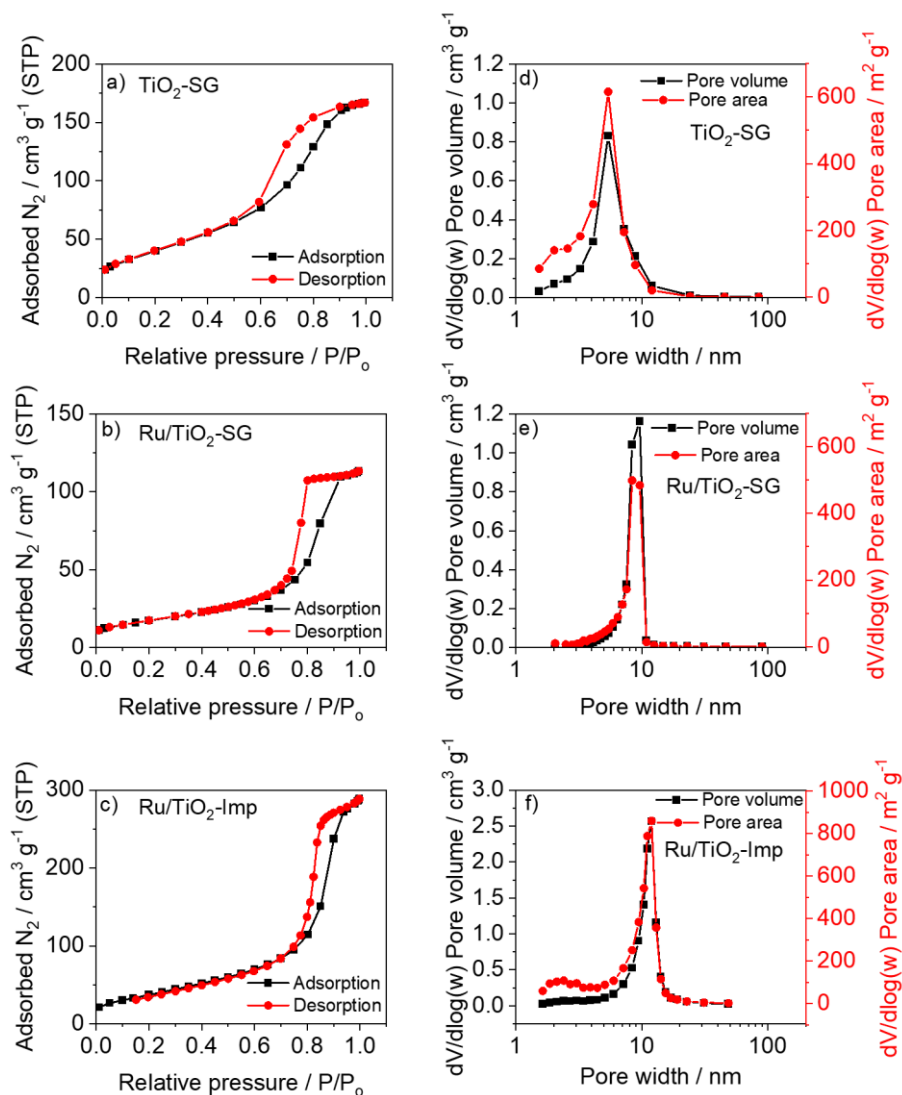


**Figure 19.** N<sub>2</sub> adsorption isotherms of a) fresh bare TiO<sub>2</sub>-SG support; b) fresh Ru/TiO<sub>2</sub>-SG; c) fresh Ru/TiO<sub>2</sub>-Imp. Pore volume and specific pore area of d) fresh bare TiO<sub>2</sub>-SG support; e) fresh Ru/TiO<sub>2</sub>-SG; f) fresh Ru/TiO<sub>2</sub>-Imp.

Ex-situ Raman spectra of the fresh TiO<sub>2</sub> and catalyst samples are shown in **Figure 20c**. Typical vibration modes of anatase at 144, 196, 397, 514 and 639 cm<sup>-1</sup> were detected in the spectrum of the bare support.<sup>169</sup> For Ru/TiO<sub>2</sub>-SG weak signals at 447 and 611 cm<sup>-1</sup> were also

resolved. These three spectral features were associated with the R- $E_g$  and R- $A_{1g}$  vibration modes of planar O-O and Ti-O stretching in rutile, respectively.<sup>170, 171</sup> On the other hand, these weak signals were not evident in the spectrum of the Ru/TiO<sub>2</sub>-Imp which, in agreement with XRD (Figure 20a), resembled that of bare anatase TiO<sub>2</sub>.

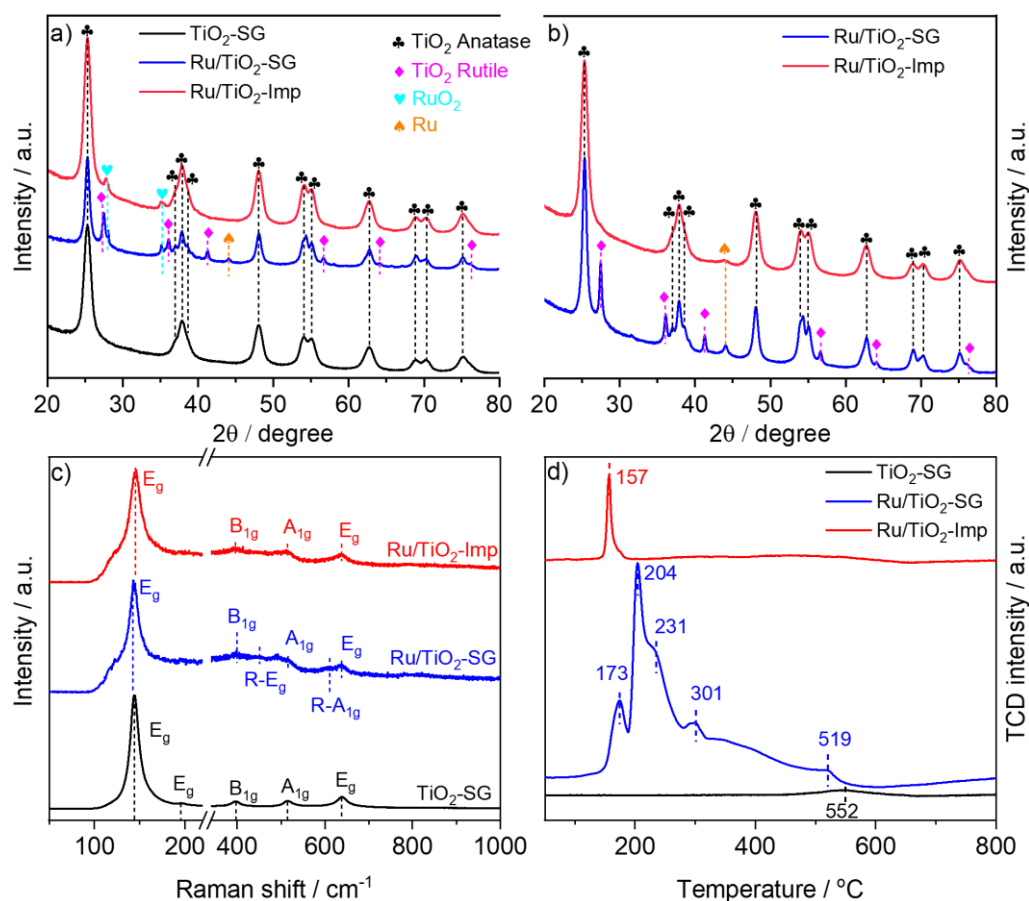


**Figure 20.** a) XRD powder patterns of the fresh TiO<sub>2</sub>-SG support and fresh Ru catalysts; b) XRD powder patterns of Ru catalysts after 6h reaction in H<sub>2</sub>:CO<sub>2</sub>=4:1 flow up to 270 °C; c) Raman spectra of the fresh materials; d) H<sub>2</sub> TPR spectra of the bare TiO<sub>2</sub>-SG support, Ru/TiO<sub>2</sub>-SG and Ru/TiO<sub>2</sub>-Imp catalysts.

The reducibility of TiO<sub>2</sub>-SG and Ru/TiO<sub>2</sub>-Imp samples has been evaluated by H<sub>2</sub>-TPR measurements (Figure 20d). While for the bare support only a weak single peak at ca. 552 °C was detected, Ru/TiO<sub>2</sub>-SG was characterized by several H<sub>2</sub> consumption peaks between 170 and 520 °C. The spectra suggested that Ru species differed in their oxidation states and/or the strength of their interaction with the carrier, being more pronounced in the case of Ru/TiO<sub>2</sub>-SG. For instance, the total consumed amount of H<sub>2</sub> for this catalyst was ca. 9 times higher than the stoichiometric amount that would be needed to reduce all Ru<sup>4+</sup> in the sample to Ru<sup>0</sup> (given that all reducible Ru was present as RuO<sub>2</sub>). This means that not only Ru<sup>n+</sup> species but also Ti<sup>4+</sup> ions from the support were reduced. This may indicate that, after reducing RuO<sub>x</sub> species, H<sub>2</sub> is

split into atoms on the surface of the formed Ru<sup>0</sup> particles from which spills H atoms over to the metal-support interface where they reacted with lattice oxygen to form water. This should lead to partial reduction of the support and would agree with previous observations on supported metal/TiO<sub>2</sub> catalysts in which the reduction of Ti<sup>4+</sup> was promoted by the vicinity of the metal. In contrast, for Ru/TiO<sub>2</sub>-Imp only a narrow reduction peak at 157 °C was detected and the amount of consumed H<sub>2</sub> was much lower, ca. 21 % of that observed for Ru/TiO<sub>2</sub>-SG. As mentioned above, the reason may be that in this case the interaction between Ru/RuO<sub>x</sub> and TiO<sub>2</sub> is weaker than in Ru/TiO<sub>2</sub>-SG.

HAADF-STEM and Ru EDX analysis of the as-prepared catalysts are presented in **Figure 21**. It was observed that the two catalysts contained relatively large and not uniformly distributed Ru particles. This was better visualized after selecting specific parts of the micrographs to record EDX spectra (**Figure 21b, d**). The zones marked as “1” in **Figures 21a, c** were found representative of regions with low or non-detectable signals from RuL $\alpha$ /RuL $\beta$  (2.40 – 2.70 keV in **Figure 21b, d**), while the zones labeled as “2” depicted strong signals of Ru. This means that, globally, no big differences in the distribution of Ru might be expected among the two synthesis procedures.

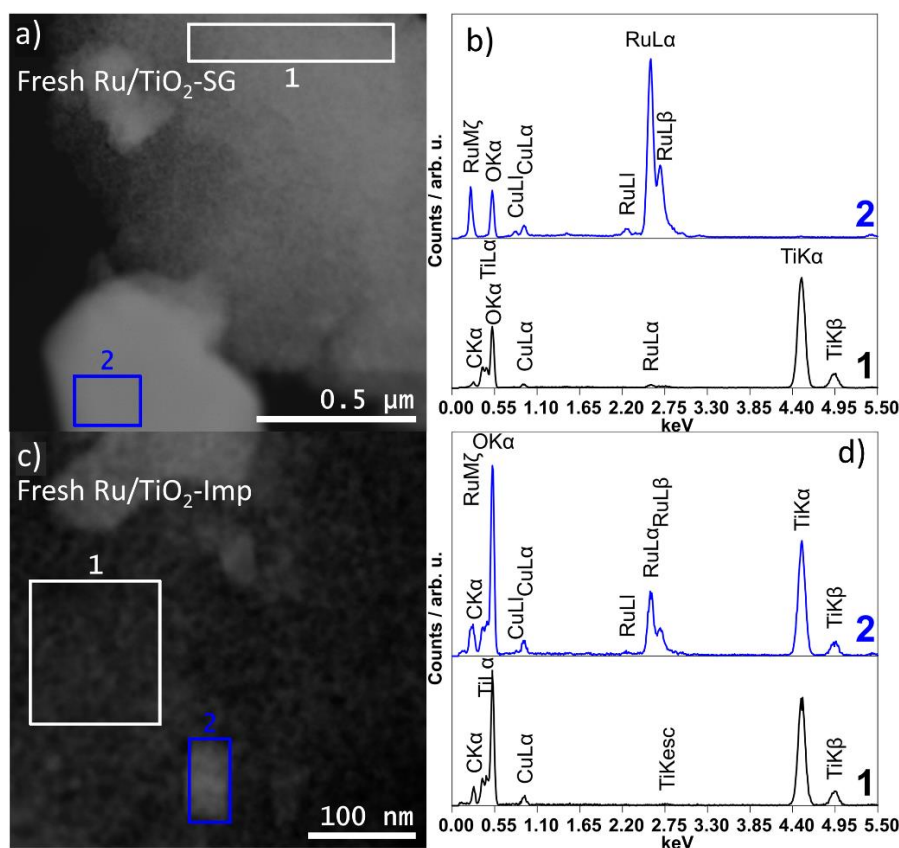


**Figure 21.** HAADF-STEM images and selected EDX spectra of fresh Ru/TiO<sub>2</sub>-SG a, b) and fresh Ru/TiO<sub>2</sub>-Imp c, d).

A better visualization of the distribution of Ru could be obtained by comparing representative STEM images at smaller scale. Apparently, Ru/TiO<sub>2</sub>-SG initially contained many small highly dispersed Ru species than Ru/TiO<sub>2</sub>-Imp for which large crystallites of RuO<sub>2</sub> were easily observed, compare **Figure 22a, b** (fresh Ru/TiO<sub>2</sub>-SG) and **Figure 22c, d** (fresh Ru/TiO<sub>2</sub>-Imp). This suggested that the support and the supported species presented differences in their interactions.

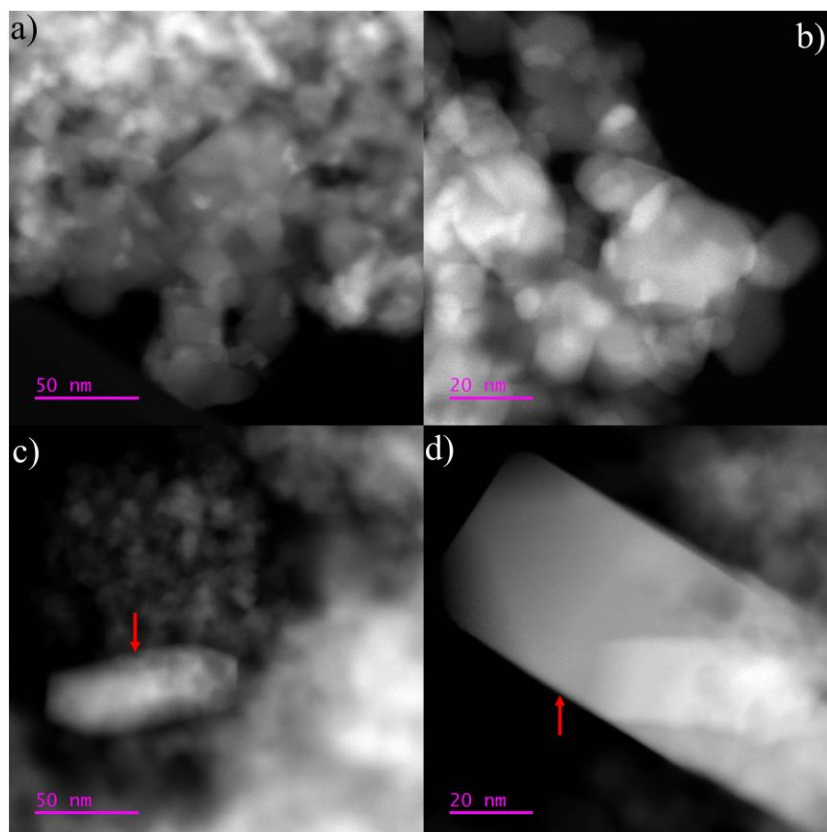


**Figure 22.** HAADF-STEM images of a, b) fresh Ru/TiO<sub>2</sub>-SG and c, d) Ru/TiO<sub>2</sub>-Imp. The red arrows indicate big particles/conglomerates formed on Ru/TiO<sub>2</sub>-Imp.

This was corroborated when observing micrographs recorded after reaction. The dispersion of Ru species was more effective than on Ru/TiO<sub>2</sub>-Imp, compare **Figure 23a, b** (spent Ru/TiO<sub>2</sub>-SG) and **Figure 23c, d** (spent Ru/TiO<sub>2</sub>-Imp). This enhanced dispersion is also suggested by NAP-XPS insights shown later. Hence, on Ru/TiO<sub>2</sub>-SG a more intimate electronic interaction at the metal-support interface can be anticipated. Such an effect could be related with the promotion in the concentration of O-vacancies (shown below by EPR spectra).

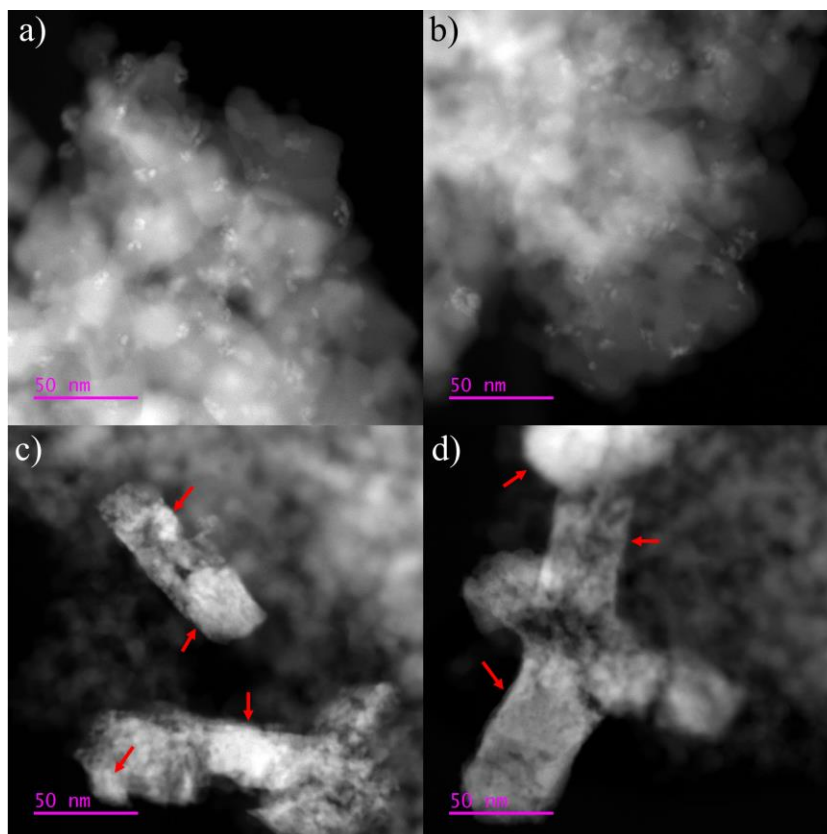


**Figure 23.** HAADF-STEM images of a, b) spent Ru/TiO<sub>2</sub>-SG and c, d) Ru/TiO<sub>2</sub>-Imp. The red arrows indicate big particles/conglomerates formed on Ru/TiO<sub>2</sub>-Imp.

**Activity assessments:** Temperature screening tests were performed in the temperature window 140 – 350 °C (**Figure 24a**). The selectivity to CH<sub>4</sub> was always 100% for both catalysts. At all conditions, the performance of Ru/TiO<sub>2</sub>-SG was found superior. Methane formation rates at differential conditions, i.e., CO<sub>2</sub> conversion < 20 % on both catalysts are plotted in **Figure 24b**. The rate on Ru/TiO<sub>2</sub>-SG was ca. 4-fold higher than on Ru/TiO<sub>2</sub>-Imp already at 190 °C. Similarly, when compared with other Ru/TiO<sub>2</sub> (P-90 or P-25) catalysts loaded with about 2 wt.% Ru,<sup>21, 62</sup> CH<sub>4</sub> rate on Ru/TiO<sub>2</sub>-SG was still found to be 2-7 times higher at relatively low temperatures, i.e., 190 – 200 °C. The apparent activation energies (**Figure 24c**) were in the order of magnitude reported for this reaction on distinct Ru based catalysts (~ 50 – 80 kJ mol<sup>-1</sup>).<sup>50, 70, 97, 172</sup> In the case of Ru/TiO<sub>2</sub>-SG (88.5 kJ mol<sup>-1</sup>), however, it was superior than on the less active Ru/TiO<sub>2</sub>-Imp (50.7 kJ mol<sup>-1</sup>).

Subsequently, the stability of the catalysts was also evaluated at 190 °C. The rates of CH<sub>4</sub> formation normalized on the Ru mass were determined on both catalysts during ca. 1000 min (17 h) on stream (**Figure 24c**). While Ru/TiO<sub>2</sub>-SG passed an activation period of about 200 min after which it reached roughly three times higher CH<sub>4</sub> formation rate the impregnated control catalyst Ru/TiO<sub>2</sub>-Imp did not show such activation though such an effect has been

observed previously also for other Ru/TiO<sub>2</sub> catalysts.<sup>60</sup> This behavior has been ascribed to the reduction of oxidized Ru and the creation of O-vacancies in the support. Moreover, this difference is in alignment with H<sub>2</sub>-TPR results (**Figure 20d**) where it was determined that reduction of RuO<sub>2</sub> on Ru/TiO<sub>2</sub>-SG required higher temperatures (peak maximum 204 °C) than on Ru/TiO<sub>2</sub>-Imp (157 °C). The net deactivation was around 6 % for Ru/TiO<sub>2</sub>-SG while it was ca. 19 % Ru/TiO<sub>2</sub>-Imp. The more pronounced decay in the activity of this last sample might, in part, be explained by the presence of bigger particles/ agglomerates, as shown by HAADF-STEM images (**Figure 23**), that resulted in a lower active surface area.

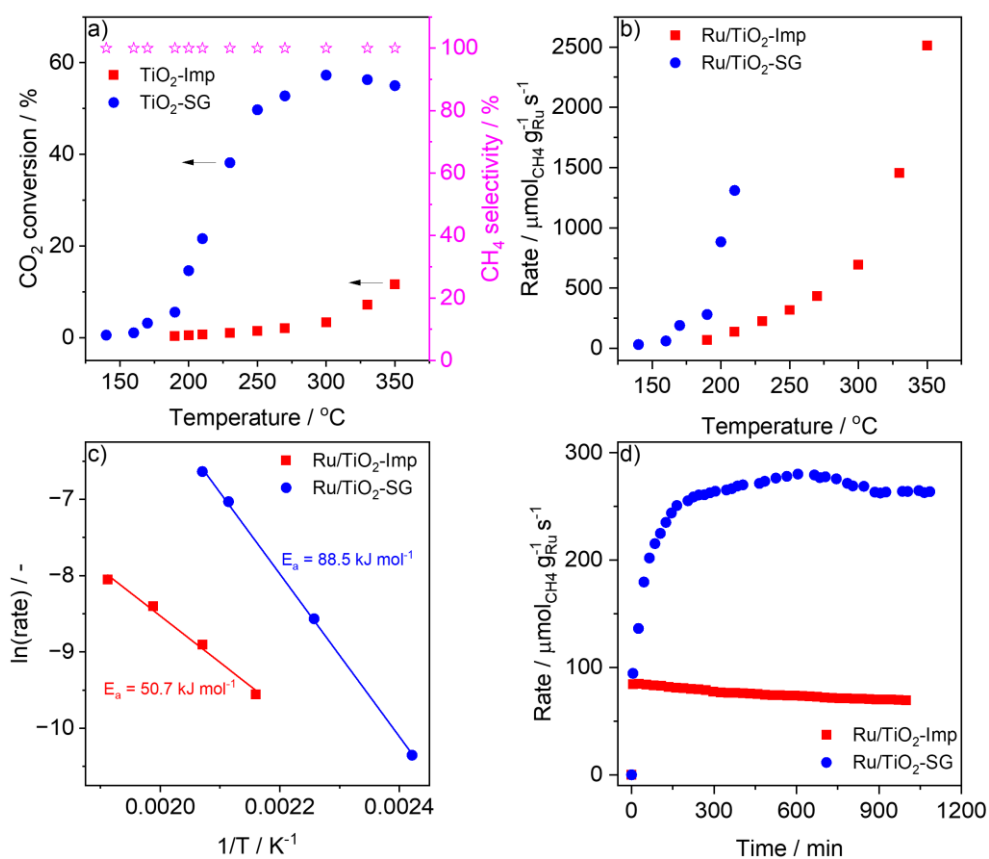


**Figure 24.** a) CO<sub>2</sub> conversion and CH<sub>4</sub> selectivity on Ru/TiO<sub>2</sub>-Imp and Ru/TiO<sub>2</sub>-SG; b) CH<sub>4</sub> formation rates at different temperatures normalized on the Ru mass in Ru/TiO<sub>2</sub>-Imp and Ru/TiO<sub>2</sub>-SG; c) Apparent activation energy for CH<sub>4</sub> formation on Ru/TiO<sub>2</sub>-Imp and Ru/TiO<sub>2</sub>-SG; d) Ru mass normalized methane rate on Ru/TiO<sub>2</sub>-Imp and Ru/TiO<sub>2</sub>-SG assessed at 190 °C during 1000 min. Gas mixture: H<sub>2</sub>:CO<sub>2</sub> = 4:1 (24 ml min<sup>-1</sup> H<sub>2</sub>, 6 ml min<sup>-1</sup> CO<sub>2</sub>).

To facilitate comparison of catalysts with different properties, e.g., metal loadings, a common basis is needed. Such a comparison can be referred to the turn-over frequency (TOF). This refers to the amount of turn-overs per catalytic site per time avoiding the rate normalization by mass of supported metal. In heterogeneous catalysis the number of atoms exposed on the

surface of the active metal nanoparticles must be estimated. This is not straightforward for polycrystalline materials and different values can be obtained depending on the selected plane(s) for the calculation.<sup>173</sup> A series of TEM images was selected (representative examples in **Figure A1a-c**). Around 300 particles were measured to obtain a particle size distribution as shown in **Figure A1d**. With the use of equations **eq. 31** and **eq. 32** a volume-area averaged diameter of 6.6 nm and a dispersion of 19.3 % was obtained that corresponded to a TOF of 0.029 s<sup>-1</sup>.<sup>174</sup> When using the methodology of Abe et al., which requires to assume the exclusive exposition of Ru(001) plane, the amount of surface atoms amounts to ca. 1.739 \* 10<sup>19</sup> atoms m<sup>-2</sup>.<sup>66</sup> The corresponding TOF was equivalent to 0.032 s<sup>-1</sup>. Further details about this calculation procedure can be found in the respective reference.<sup>66</sup> Both methods led to comparable TOF estimations. However, the first procedure is found more suitable for polycrystalline materials as it does not require the assumption of a preferentially exposed plane. The calculated TOFs up to 210 °C are shown in **Table 4**. Already at 160 °C, it was observed that the activity was by 3.4 times higher than that determined by Abe et al. for a 0.8 wt.% Ru/TiO<sub>2</sub> at the same reaction conditions.<sup>66</sup> These TOFs are among the highest reported for CO<sub>2</sub> methanation up to 210 °C (compare with **Table 2**). Hence, the adopted sol-gel method allows to maximize the methanation performance while decreasing the Ru loading. The sections below focus on determining the structural factors behind this attractive catalytic behaviour of Ru/TiO<sub>2</sub>-SG.

**Table 4.** Reported activity of CO<sub>2</sub> methanation on the Ru/TiO<sub>2</sub>-SG catalyst at distinct temperatures and H<sub>2</sub>:CO<sub>2</sub> ratio = 4:1.

Reaction temperature / °C	<sup>a</sup> TOF <sub>CO<sub>2</sub></sub> / s <sup>-1</sup>
140	0.017
160	0.032
170	0.099
190	0.14
200	0.46
210	0.69

<sup>a</sup>Calculated with equation **eq. 30**

**NAP-XPS measurements:** The XP spectra recorded at different conditions are shown in **Figure 25**. The C 1s signal at 284.8 eV from adventitious carbon was used as reference for all binding energies. The fresh catalysts without any pre-treatment (**Figure 25a, g**) showed that initially Ru consisted predominantly in metallic Ru<sup>0</sup> (3d5/2 peaks at 279.9 eV in Ru/TiO<sub>2</sub>-SG and 280.3 eV in Ru/TiO<sub>2</sub>-Imp).<sup>175, 176</sup> Small signals of Ru<sup>4+</sup> at ca. 281.3 eV (Ru/TiO<sub>2</sub>-SG) and 281.4 eV (Ru/TiO<sub>2</sub>-imp)<sup>177</sup> were resolved together with satellite peaks of Ru 3d5/2 at 281.7 eV (Ru/TiO<sub>2</sub>-SG) and 282.3 eV (Ru/TiO<sub>2</sub>-Imp).<sup>178, 179</sup> The signals at 288.5 eV (Ru/TiO<sub>2</sub>-SG) and

288.7 eV (Ru/TiO<sub>2</sub>-Imp) along with the shoulders at 286.5 eV (Ru/TiO<sub>2</sub>-SG) and 286.3 eV (Ru/TiO<sub>2</sub>-Imp) can be attributed to organic surface deposits with C-O and O=C-O moieties.<sup>180</sup> After ca. 30 min oxidative pre-treatment at 150 °C in a flow of 5 vol.% O<sub>2</sub>/He, the Ru<sup>0</sup> peak disappeared while a Ru<sup>4+</sup> signal at 280.8 eV grew on both catalysts (**Figure 25b, h**). This indicated oxidation of Ru<sup>0</sup> to RuO<sub>2</sub>. Still, a contribution from the Ru 3d5/2 satellite at 282.3 eV was observed. Upon switching to the reaction mixture (H<sub>2</sub>:CO<sub>2</sub>=4:1) at 190 °C, reduction of RuO<sub>2</sub> occurred again, as reflected by strong peaks at 280.8 eV for Ru/TiO<sub>2</sub>-SG (**Figure 25c**) and 279.8 eV for Ru/TiO<sub>2</sub>-Imp (**Figure 25i**). Moreover, two new C1s signals were distinguished. The one at 293.1 eV from gaseous CO<sub>2</sub>,<sup>132</sup> while the peaks at 287.5 eV (Ru/TiO<sub>2</sub>-SG) and 287.0 eV (Ru/TiO<sub>2</sub>-Imp) likely belonged to formate species.<sup>181</sup> The binding energies at ca. 288.7 – 288.8 eV, on the other hand, were associated to carbonates.<sup>181</sup> No further significant changes were detected upon stepwise raising the reaction temperature to 270 °C. It is worth to mention that no methoxy/methanol species were detected as it was the case in other reports.<sup>97, 132</sup> Hence, this type of intermediate/route is discarded for the present case. After stopping the CO<sub>2</sub>/H<sub>2</sub> supply and cooling to room temperature, the formate signals disappeared on Ru/TiO<sub>2</sub>-SG (**Figure 25f**). They were still visible on Ru/TiO<sub>2</sub>-Imp (**Figure 25l**). This suggested, in agreement with the DRIFTS results discussed below, less stability on the more active Ru/TiO<sub>2</sub>-SG. This keeps relation other studies that highlighted the role of these compounds as intermediates for the reduction of CO<sub>2</sub> at similar conditions.<sup>128, 129, 182</sup>



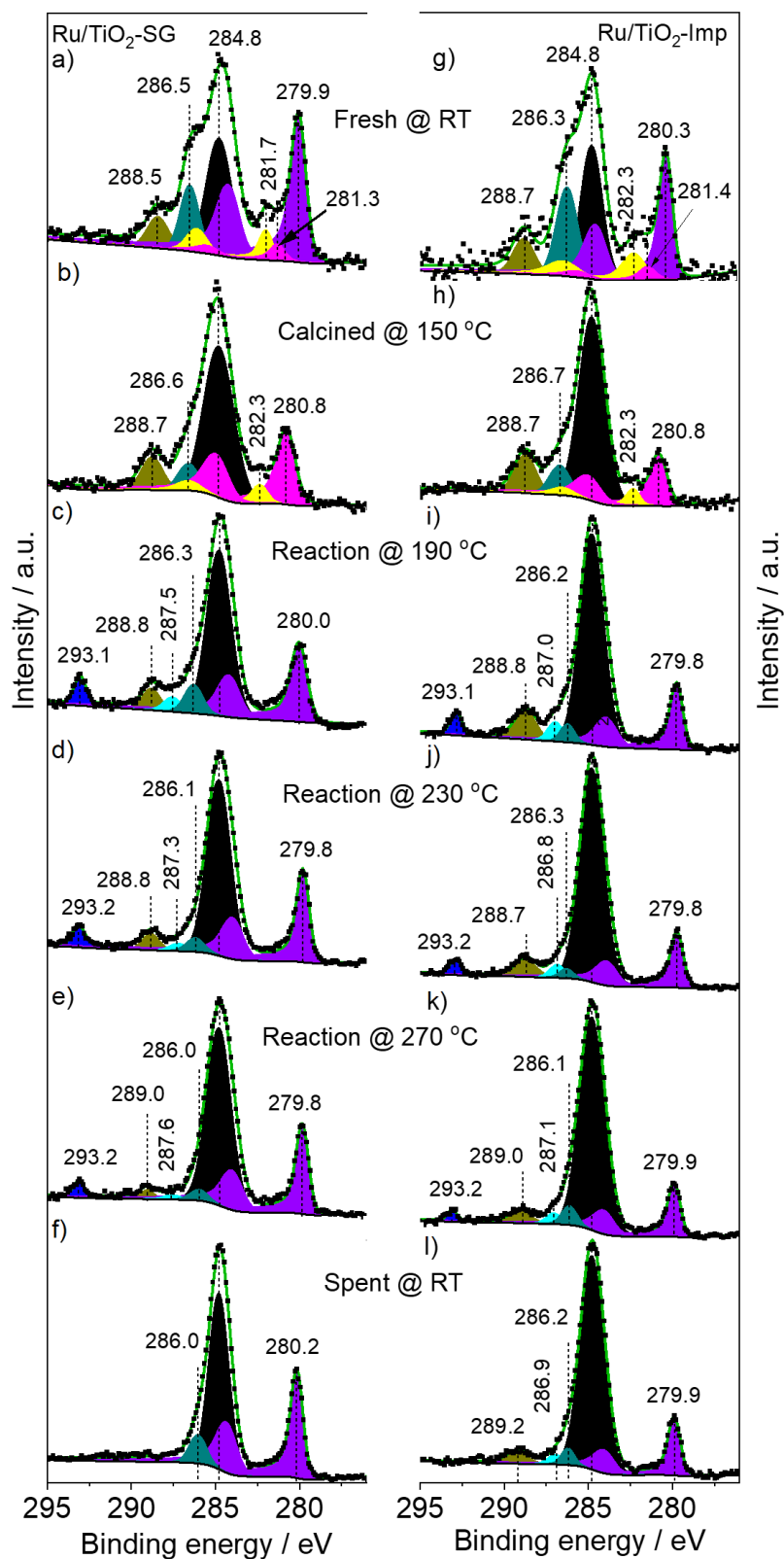


**Figure 25.** NAP-XPS Spectra in the Ru 3d and C1s region of Ru/TiO<sub>2</sub>-SG and Ru/TiO<sub>2</sub>-Imp catalysts at different conditions: a, g) Fresh catalysts at RT in He; b, h) Pre-oxidation at 150 °C in 5 vol.% O<sub>2</sub>/He; c-k) Reaction in H<sub>2</sub>:CO<sub>2</sub> = 4:1 at different temperatures. Experimental (black line) and fitted (green line) NAP-XPS spectra at a total pressure of 2 mbar, including deconvoluted sub signals.

The surface Ru/Ti ratios were calculated from the quantitative analysis of Ru3d and Ti 2p signals and shown in **Table 5**. For Ru/TiO<sub>2</sub>-SG the ratio was always higher. This pointed to a higher percentage of Ru surface species accessible to reactants which probably increased even more with rising reaction temperature and might be one reason for the higher activity when compared to Ru/TiO<sub>2</sub>-Imp (**Figure 24**).<sup>21, 60, 183, 184</sup> That is an important factor that proofs differences at the metal-support perimeter between the catalysts and that partially explains the distinct catalytic performances.

**Table 5.** Ru:Ti surface ratio estimated from NAP-XPS at different stages for Ru/TiO<sub>2</sub>-SG and Ru/TiO<sub>2</sub>-Imp catalysts.

Catalyst	Stage	Temperature / °C	Ru:Ti ratio / -
TiO <sub>2</sub> -SG	Fresh	RT	0.027
	Calcined	150	0.025
	Reaction	190	0.034
		230	0.041
		270	0.044
	Spent	RT	0.043
Ru/TiO <sub>2</sub> -Imp	Fresh	RT	0.013
	Calcined	150	0.014
	Reaction	190	0.025
		230	0.026
		270	0.023
	Spent	RT	0.023

***In-situ EPR assessments:*** In TiO<sub>2</sub> Ti<sup>3+</sup> (3d<sup>1</sup>) cations are formed by trapping electrons from oxygen vacancies, e.g., O<sup>2-</sup> + 2Ti<sup>4+</sup> → O<sub>v</sub> + 1/2O<sub>2</sub> + 2Ti<sup>3+</sup>. The presence of these defects has been shown to have a direct impact in the catalytic cycle during CO<sub>2</sub> methanation on Ru/TiO<sub>2</sub>.<sup>21</sup> Therefore, it is important to determine if the activity promotion of Ru/TiO<sub>2</sub>-SG could be correlated with these species. As EPR spectroscopy is a unique technique to detect species with paramagnetic properties that might be involved in the reaction path, in-situ assessments were performed to uncover any differences between the two catalysts under study.

The spectra of both catalysts at different stages are shown in **Figure 26**. First, before reaction at 150 °C a line at g<sub>iso</sub> = 2.000 associated to F-centers (an oxygen vacancy occupied by a single electron)<sup>185</sup> was resolved in both cases. With the increase of temperature and at reaction conditions its intensity decreased for the two samples. During the reaction, except of g<sub>iso</sub>, no more signals were observed (**Figure 26a**). The spectra of Ru/TiO<sub>2</sub>-Imp, on the other hand, still showed a pronounced axial signal of reduced Ti<sup>3+</sup> species with g<sup>1\*</sup><sub>⊥</sub> = 1.950 and g<sup>1\*</sup><sub>∥</sub> = 1.928 (**Figure 26b**). This points to differences of the dynamics of electrons between the catalysts at the metal-support interface. In Ru/TiO<sub>2</sub>-SG, electrons released from the anion vacancies after O removal were preferentially transferred to Ru<sup>n+</sup> species at the interface. Meanwhile in

Ru/TiO<sub>2</sub>-Imp Ti<sup>4+</sup> cations tend to trap these electrons to form Ti<sup>3+</sup> (Ti<sup>4+</sup> + e<sup>-</sup>(O-vacancy) → Ti<sup>3+</sup>). To improve the resolution, complementary spectra were recorded at low temperature (-173 °C) (**Figure 26c, d**). These spectra were recorded under an Ar atmosphere. As in this gas line traces of O<sub>2</sub> could exist, the formation of superoxide anion radicals (O<sub>2</sub><sup>-</sup>) might provide additional insights about the electronic properties of the samples. Indeed, the bare fresh TiO<sub>2</sub> support showed the typical axial signal with g<sub>||</sub><sup>1</sup>=2.012 associated to O<sub>2</sub><sup>-</sup> species. The respective g<sub>⊥</sub><sup>1</sup> component may be superimposed on the typical signal from F-centers (black line in **Figure 26c**). Additionally, an axial signal with g<sub>⊥</sub><sup>2</sup>=1.984 and g<sub>||</sub><sup>2</sup>=1.930 was also resolved and has been assigned to Ti<sup>3+</sup>.<sup>186-189</sup> Both signals also appeared in the case of the spent bare support, yet in this case they were slightly more intense, probably, due to the absence of other centers (Ru<sup>n+</sup>/Ru<sup>0</sup>) that could compete with Ti<sup>4+</sup> for electrons released from O-vacancies (black line **Figure 26d**).

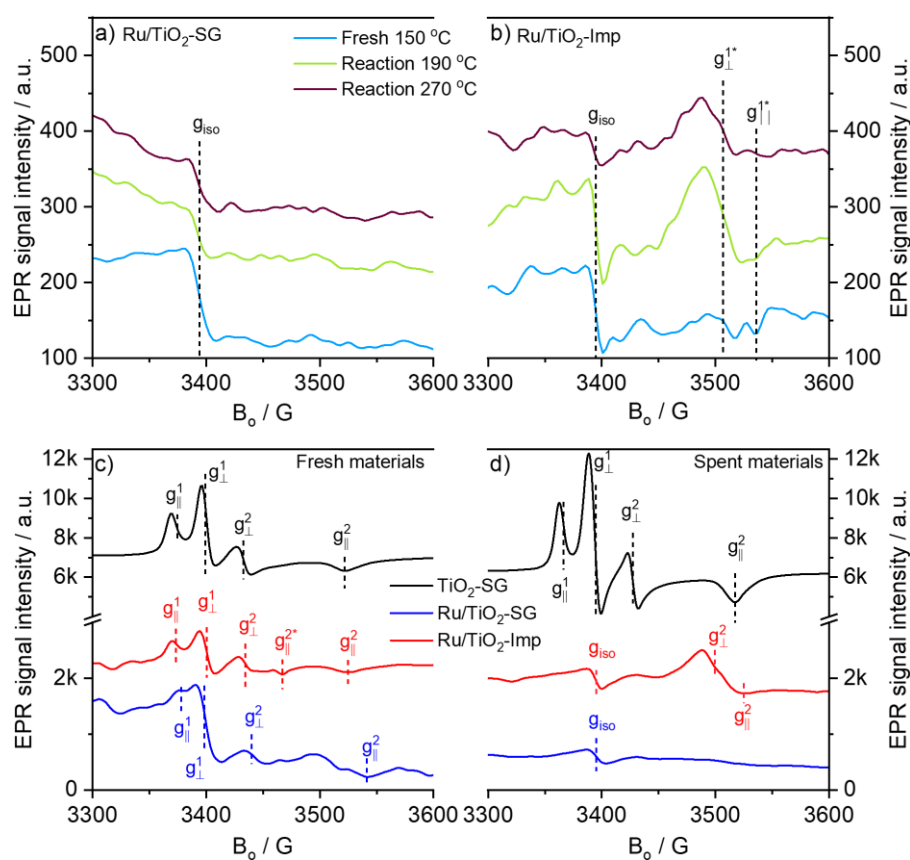


**Figure 26.** a, b) EPR spectra of Ru/TiO<sub>2</sub>-SG and Ru/TiO<sub>2</sub>-Imp catalysts up to 270 °C at different stages. The corresponding temperature at which the spectra were recorded is indicated in the figure; c) EPR spectra of the as received samples; d) EPR spectra of the samples after 6h reaction up to 270 °C. All spectra in c) and d) were recorded at -173 °C.

The EPR spectra of fresh Ru/TiO<sub>2</sub>-Imp (red line in **Figure 26c**) showed similar signals as the bare support but with lower intensity. This may be related to partial electron transfer from F-centers and surface Ti<sup>3+</sup> ions to Ru<sup>n+</sup> species, which were in turn reduced to EPR-silent Ru<sup>0</sup>. An additional weak axial feature was resolved with  $g_{\perp}^{*1} = 1.961$  while its perpendicular component might be superimposed at  $g_{\perp}^2 = 1.982$ . Such  $g$  values are characteristic for Ti<sup>3+</sup> ions located at regular lattice positions of anatase with moderate tetragonal distortion,<sup>186</sup> i.e., they are embedded in the support matrix. On the other hand, in Ru/TiO<sub>2</sub>-SG (blue line in **Figure 26c**), the signal of F-centers at  $g = 2.000$  was more intense while the O<sub>2</sub><sup>-</sup> feature at  $g_{\parallel}^1 = 2.010$  was weaker when compared with Ru/TiO<sub>2</sub>-Imp. Several poorly resolved features occurred between  $g_{\perp}^2 = 1.980$  and  $g_{\parallel}^2 = 1.924$ . As mentioned above, they may arise from  $g_{\parallel}^2$  signals of Ti<sup>3+</sup> ions with lower axial distortion embedded in lattice positions of TiO<sub>2</sub>. No signals from paramagnetic Ru<sup>3+</sup> and/or Ru<sup>+</sup> species<sup>190</sup> could be observed in the fresh catalysts, indicating that Ru in these materials might be present as EPR silent Ru<sup>4+</sup> and/or Ru<sup>0</sup>. For the spent catalysts (**Figure 26d**) no clear difference in the intensity of the signal related with oxygen vacancies was noted. In contrast, even at these cryogenic conditions, Ti<sup>3+</sup> could not be detected in Ru/TiO<sub>2</sub>-SG while the corresponding  $g$  components of axial Ti<sup>3+</sup> were resolved in Ru/TiO<sub>2</sub>-Imp. These spectral differences demonstrated that a fraction of the electrons released from defects in the less active Ru/TiO<sub>2</sub>-Imp were trapped by Ti<sup>4+</sup> which might limit their transfer to Ru<sup>n+</sup> and, thus, the formation of active Ru<sup>0</sup> species. By the contrary, this electron exchange at the perimeter interphase of Ru/TiO<sub>2</sub>-SG was more facile leading to a major population of active Ru<sup>0</sup> species. Evidence of these differences are corroborated by the distinct adsorptive properties determined upon DRIFTS assessments shown below.

***In-situ DRIFTS measurements:*** The formation of surface adsorbates and intermediates during the catalytic reaction was examined by in-situ DRIFT spectroscopy at 150 °C (**Figure 27**). The band intensity of gaseous CH<sub>4</sub>, located ca. 3016 cm<sup>-1</sup>,<sup>191</sup> was always much higher on Ru/TiO<sub>2</sub>-SG than on Ru/TiO<sub>2</sub>-Imp (**Figure 27a, d**), in line with the higher methane rate on the former catalyst. Signals at 2872 – 2887 cm<sup>-1</sup> resolved for catalyst Ru/TiO<sub>2</sub>-Imp could be associated with C-H stretching vibrations of formate species (**Figure 27d**).<sup>128</sup> The small signal ca. 2958 cm<sup>-1</sup> may correspond to the combination between C-H bending vibrations and symmetric  $\nu_{as}(\text{O-C-O})$  vibrations of formate species.<sup>128, 192</sup> In the spectra of Ru/TiO<sub>2</sub>-SG, such bands were obscured by the strong CH<sub>4</sub> bands (**Figure 27a**).

More interesting differences, however, were observed in the spectra of the respective carbonyl regions. For Ru/TiO<sub>2</sub>-SG a very broad feature was resolved between 2050 and 1870

$\text{cm}^{-1}$ . This is attributed to the superposition of CO adsorbed on different Ru sites (**Figure 27b**). In literature, bands around  $1960 \text{ cm}^{-1}$  have been related to terminal CO adsorbed on Ru sites at the metal support interface,<sup>51, 193</sup> while bands around  $1990 \text{ cm}^{-1}$  were attributed to monodentate CO species on Ru sites of different oxidation states, including reduced Ru sites.<sup>51, 194-196</sup> Also, the range  $1990 - 1960 \text{ cm}^{-1}$  could contain contributions from CO adsorbed on isolated metallic Ru sites surrounded by partially oxidized Ru.<sup>67, 197</sup> This is in agreement with  $\text{H}_2$ -TPR (**Figure 20d**) spectra, that showed the presence of partially oxidized Ru at these conditions. The most obvious difference between Ru/TiO<sub>2</sub>-SG and Ru/TiO<sub>2</sub>-Imp was the fact that the latter showed negligible band intensity in the C-O range around  $1998 \text{ cm}^{-1}$  (**Figure 27e**), indicating a much lower ability of the Ru sites to adsorb CO and/or a smaller number of such species accessible for reactants/intermediates on this catalyst. Although not as obvious, another key difference was the resolved weak band at  $2064 \text{ cm}^{-1}$  in case of Ru/TiO<sub>2</sub>-SG (**Figure 27b**) that was not present in the spectra of Ru/TiO<sub>2</sub>-Imp (**Figure 27e**). This could be due to CO linearly adsorbed on electronically modified Ru sites located at the periphery interphase.<sup>22, 198</sup>

Finally, spectral differences were also analyzed for the region between  $1200$  and  $1700 \text{ cm}^{-1}$  (**Figure 27c, f**). The band at  $1304\text{-}1305 \text{ cm}^{-1}$  belonged to CH<sub>4</sub> which was more intense in Ru/TiO<sub>2</sub>-SG. The band at  $1618 \text{ cm}^{-1}$  might be associated with bidentate bicarbonate species.<sup>199</sup> Bands at  $1363$  and  $1553 \text{ cm}^{-1}$  stem from symmetric  $\nu_s(\text{O-C-O})$  and asymmetric  $\nu_{as}(\text{O-C-O})$  vibrations of formate species.<sup>128, 192</sup> They appeared with higher intensity on sample Ru/TiO<sub>2</sub>-Imp, on which also a band at  $1380 \text{ cm}^{-1}$  from C-H bending vibrations of formates was evident.<sup>128, 192</sup> This band was missing on Ru/TiO<sub>2</sub>-SG. Apart from the above discussed bands, there were weak features in Ru/TiO<sub>2</sub>-SG at  $1437 \text{ cm}^{-1}$  from bicarbonate species.<sup>191, 200</sup> The bands at  $1552 \text{ cm}^{-1}$  and  $1339 \text{ cm}^{-1}$  likely stem from asymmetric  $\nu_{as}(\text{O-C-O})$  and symmetric  $\nu_s(\text{O-C-O})$  vibrations of bidentate carbonate species.<sup>118</sup> They may be located as spectators on the TiO<sub>2</sub>-SG support. On the other hand, they could also have formed after CO<sub>2</sub> adsorption on O-vacancies in the vicinity of active Ru species, from where they were finally hydrogenated. On sample Ru/TiO<sub>2</sub>-Imp, the band at  $1339 \text{ cm}^{-1}$  was less pronounced, possibly due to the lower concentration of O-vacancies.

From this information, a second insight about the distinct reactivity of the catalysts was obtained, i.e., formate-like species might be the source of the active carbonyl species that further hydrogenates to CH<sub>4</sub>.<sup>112</sup> However, formate signals could not be clearly distinguished on Ru/TiO<sub>2</sub>-SG as the intensity and signal to noise ratio of the respective spectra were rather low for this catalysts, even at such mild temperature ( $150 \text{ }^\circ\text{C}$ ). If it is the case that formates actively

participate in the reaction path, they quickly reacted on Ru/TiO<sub>2</sub>-SG while on Ru/TiO<sub>2</sub>-Imp were more stable. This keeps tight relation with NAP-XPS results (**Figure 25j, l**).

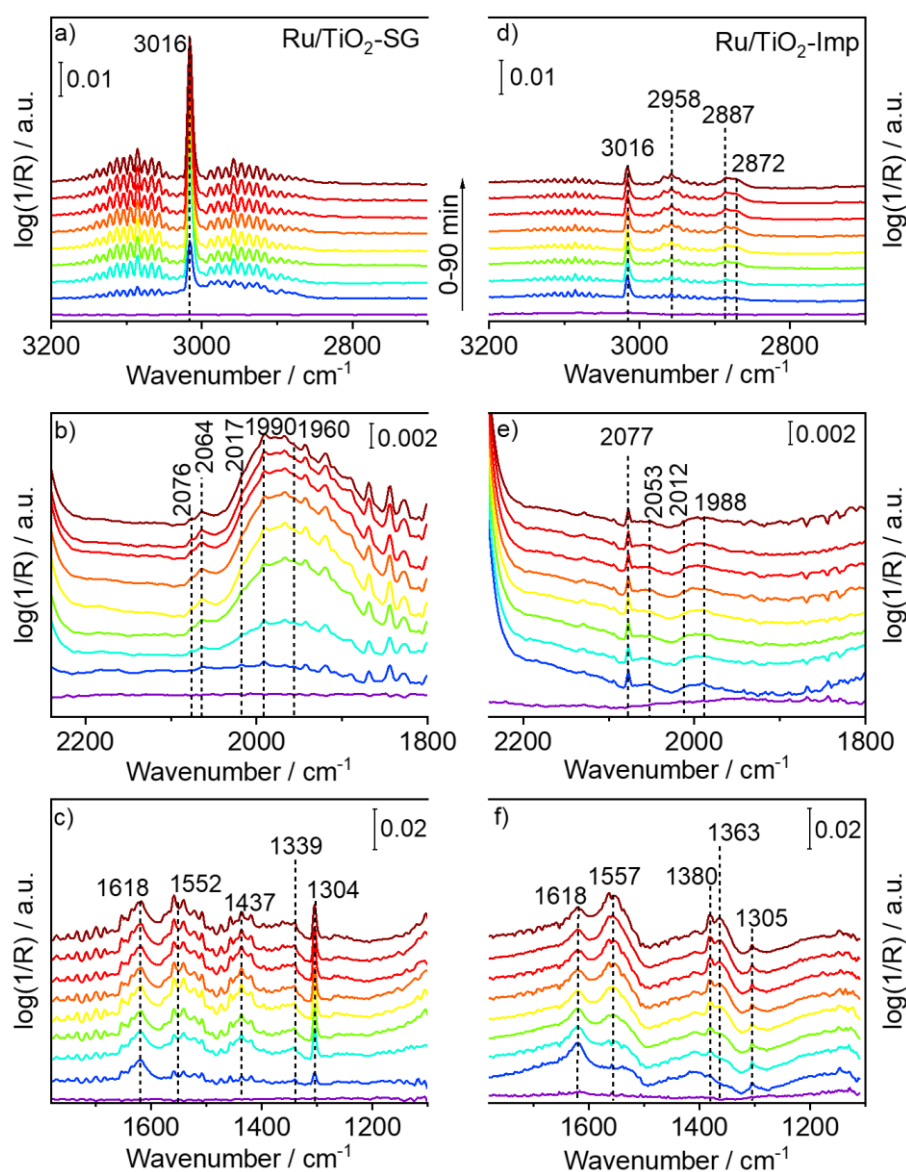


**Figure 27.** In-situ DRIFT spectra recorded at 150 °C. Left side: Spectra of Ru/TiO<sub>2</sub>-SG a) C-H region, b) C-O region, c) O-C-O region. Right side: Spectra of Ru/TiO<sub>2</sub>-Imp d) C-H region, e) C-O region, f) O-C-O region. From bottom to top: 0-90 min. Flow conditions: H<sub>2</sub>:CO<sub>2</sub> = 4:1 (22.4 ml min<sup>-1</sup> H<sub>2</sub>, 5.6 ml min<sup>-1</sup> CO<sub>2</sub>, 2 ml min<sup>-1</sup> He).

It was already determined that on Ru/TiO<sub>2</sub>-Imp clustering of Ru nanoparticles occurred while smaller entities were preserved on Ru/TiO<sub>2</sub>-SG. Moreover, these spectral differences indicated that the active CO species producing CH<sub>4</sub> might be different. That is, these DRIFT data reflect the observations from HAADF-STEM and EPR assessments. Ru/TiO<sub>2</sub>-SG presents

a larger Ru-support interface and the electronic (adsorptive) properties were more easily modified in this catalyst.

A summary of the observed bands and assignments from DRIFTS is given in **Table 6**.

**Table 6.** Infrared absorption bands and assignments for adsorbate species observed during CO<sub>2</sub> hydrogenation on Ru/TiO<sub>2</sub>-SG and Ru/TiO<sub>2</sub>-Imp catalysts.

Surface species	Wavenumber / cm <sup>-1</sup>	Assignment	Reference
Formate	2958	$\delta(\text{CH}) + \nu_{\text{as}}(\text{O-C-O})$	128
	2887 – 2872	$\nu(\text{CH})$	
Carbonyl	1960	Metal-support interface	51, 193
	1998 - 1990	Linear Ru-CO on top of Ru particles	51, 194-196
	2064	Ru-CO at electronically modified sites located at the periphery interphase	22, 198
Bidentate bicarbonate	1618	$\delta(\text{OH})$	199
Formate	1363	$\nu_{\text{s}}(\text{O-C-O})$	128, 192
	1557	$\nu_{\text{as}}(\text{O-C-O})$	
	1380	$\delta(\text{CH})$	
Bicarbonate	1552	$\nu_{\text{as}}(\text{O-C-O})$	191, 200
	1339	$\nu_{\text{s}}(\text{O-C-O})$	

Complementary information about the adsorptive properties of Ru on these catalysts was obtained upon CO adsorption at 30 °C recorded after reaction conditions at 150 °C for 5 min and 6 h, respectively. The spectrum of Ru/TiO<sub>2</sub>-SG after 5 min reaction (**Figure 28a**), showed a band at 2130 cm<sup>-1</sup> related to geminal CO adsorbed on low coordination Ru atoms.<sup>96</sup> The band at 2069 cm<sup>-1</sup> may stem from CO adsorbed on high coordination Ru<sup>0</sup> sites which is blue-shifted due to higher CO coverage with respect to the situation at reaction conditions.<sup>201</sup> Alternatively, the signal ca. 2069 cm<sup>-1</sup> might be assigned to CO linearly adsorbed on Ru sites located at the perimeter interface,<sup>198</sup> which might be electronically modified by close interaction with the support.<sup>22</sup> Finally, the band at 2001 cm<sup>-1</sup> is typical for carbonyl groups adsorbed on top of Ru<sup>0</sup> clusters.<sup>202</sup> In principle, the same bands were observed also for Ru/TiO<sub>2</sub>-Imp, yet they were all shifted to higher wavenumbers (**Figure 28**). This indicated that the C≡O bond on the latter catalyst was likely stronger than on Ru/TiO<sub>2</sub>-SG. The reason may be a more effective electron transfer from oxygen vacancies to Ru in the SG catalyst, as suggested by the in-situ EPR results (**Figure 26**). This might promote backdonation of electron density from occupied d orbitals of Ru to antibonding 2π\* orbitals of adsorbed CO, which weakened the C≡O bond in the SG catalyst. After 6h time on stream (**Figure 28b**) this shift to lower wavenumbers was even more pronounced in the most active Ru/TiO<sub>2</sub>-SG catalyst, confirming the above discussed electron transfer. Remarkably, almost no CO is adsorbed on the less active Ru/TiO<sub>2</sub>-Imp after

6h on stream. This may be due to a partial diffusion of exposed Ru species into subsurface layers where they were not accessible anymore for CO (also suggested by a lower Ru:Ti surface ratio, see NAP-XPS measurements below). Analogously, the partial increase of the Ru particle size that caused the decrease in the population of sites in the periphery interface constitutes another reasonable explanation for this limited adsorption of CO on Ru/TiO<sub>2</sub>-Imp.

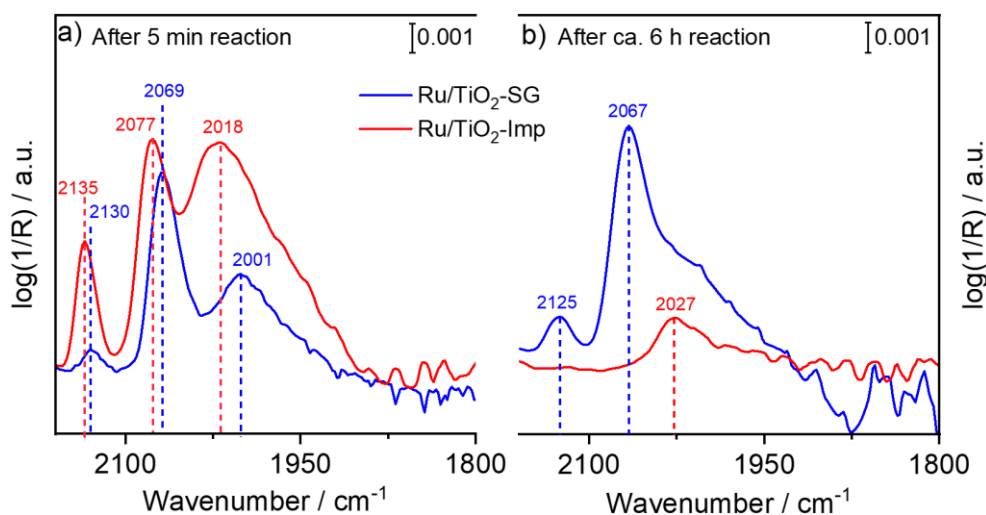


**Figure 28.** In-situ DRIFT spectra during CO adsorption at 30 °C on the spent Ru/TiO<sub>2</sub>-SG and Ru/TiO<sub>2</sub>-Imp catalysts after 5 min reaction a) and on the spent catalysts after 6 h reaction b). Flow conditions: 30 ml min<sup>-1</sup> 5 vol.% CO/He.

**Reactivity-structure relationships:** Upon applying multiple spectroscopic measurements it was identified that the superior CH<sub>4</sub> production on Ru/TiO<sub>2</sub>-SG was driven by O-vacancy-Ru sites with intimate electronic interactions. Such intimacy, was less pronounced on the less active Ru/TiO<sub>2</sub> prepared by impregnation, as proved by in-situ EPR assessments. Furthermore, the use of CO molecule as probe for adsorptive differences suggested a larger population of electronic modified sites at the interface of Ru/TiO<sub>2</sub>-SG than on Ru/TiO<sub>2</sub>-Imp, in accordance with in-situ EPR. The adsorption of CO on these sites was also stronger on Ru/TiO<sub>2</sub>-SG facilitating the rupture of the weakened C≡O bond by activated H. Moreover, DRIFTS and NAP-XPS spectra suggested that CH<sub>4</sub> evolution followed the formate pathway, yet the low stability of such species on the Ru/TiO<sub>2</sub>-SG complicated their unambiguous identification. In addition, micrography evidence indicated the enhancement in the dispersion of supported Ru entities before and after reaction on Ru/TiO<sub>2</sub>-SG which can be associated with the pinning effect of O-vacancies that suppresses agglomeration of particles after nucleation. All in all, the evidence indicated that the formation of moieties containing tiny Ru species neighboring O-



vacancies is responsible for the high activity to CH<sub>4</sub> of Ru/TiO<sub>2</sub>-SG catalyst. A dual role of O-vacancies is proposed for this reaction:

i). In the initial state of their formation, the electrons released by removal of oxygen atoms are quickly transferred to Ru<sup>n+</sup> species at the metal-support interface, forming Ru<sup>0</sup> sites for H<sub>2</sub> activation.

ii). The resulting empty O-vacancy acts as adsorption and activation site for CO<sub>2</sub>.<sup>58, 69, 203</sup> This stabilized CO<sub>2</sub> is quickly hydrogenated to oxygenated intermediates (likely formate species) that decompose to CO which is enough strongly attached at Ru-support interfacial sites to finally produce CH<sub>4</sub>.

Accordingly, the following catalytic cycle is proposed: after oxidative pre-treatment with 5 vol.% O<sub>2</sub> in He at 150 °C, the catalyst contains oxidic Ru particles of ca. 3-4 nm mean diameter (confirmed by NAP-XPS and HAADF-STEM) and a negligible number of O-vacancies in the support (**Figure 29a**). In the initial stage of the reaction, H<sub>2</sub> reduces RuO<sub>2</sub> to metallic Ru and removes lattice oxygen from the support to create O-vacancies (**Figure 29b**). Since no Ti<sup>3+</sup> ions were detected by in-situ EPR and NAP-XPS, the electrons released by the removed O<sup>2-</sup> species are most probably trapped by interfacial Ru<sup>n+</sup> sites instead of Ti<sup>4+</sup>, thus forming catalytically active Ru<sup>0</sup> atoms at the metal-support interface. Subsequently, CO<sub>2</sub> adsorbs with one of its O atoms in the oxygen vacancy (**Figure 29c**). This process weakens the C-O bond and makes it prone for facile hydrogenation by activated H species (**Figure 29d**).

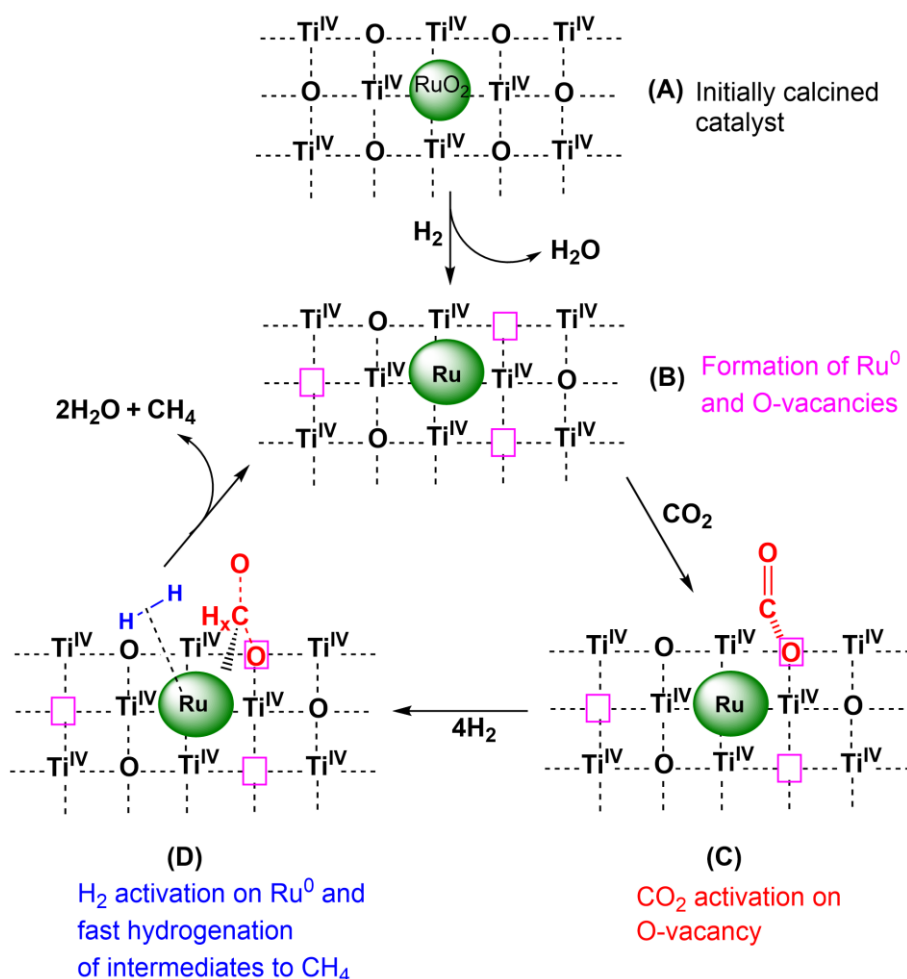


**Figure 29.** Schematic representation of formation of O-vacancies and metallic Ru (A, B) and their role for activation of CO<sub>2</sub> (C) and H<sub>2</sub> (D).

### 3.2. CO<sub>2</sub> methanation on Ru/ZrO<sub>2</sub> and MgO modified Ru/ZrO<sub>2</sub>

Despite the clear benefits of O-vacancies for the methanation of CO<sub>2</sub>, the nature of active sites/species that facilitate CH<sub>4</sub> evolution and their direct relation with O-defects lacks understanding. It was already shown that this becomes even more complicated on very active catalysts (with abundant O-vacancies) for which the signal to noise ratio, e.g., during in situ FTIR analysis, is small. In those cases, the reactivity of the H<sub>x</sub>C<sub>y</sub>O<sub>z</sub> and Ru-CO intermediates formed under reaction conditions is not easily correlated with CH<sub>4</sub> evolution. Hence, executing experiments to unambiguously determine key intermediates on Ru based catalysts is a difficult task that still needs deeper exploration to successfully accomplish the rational design of such materials.

The interactions between Ru and O-vacancies depend on the nature of the supporting oxide. While these interactions are very pronounced with TiO<sub>2</sub>, for the case of the less reducible ZrO<sub>2</sub> they are moderate as the energy cost for the removal of surface O is larger in this case.<sup>111</sup>

Consequently, less charge transfer from ZrO<sub>2</sub> to the supported Ru particles occurs (assuming similar surface area, Ru loading and Ru particle size) resulting in a lower catalyst activity.<sup>204</sup> The moderate Ru-ZrO<sub>2</sub> interaction is expected to be advantageous for the identification of key intermediates. Meanwhile, the formation of O-vacancies in ZrO<sub>2</sub> can be tailored by incorporation of foreign cations of lower valence than Zr. When ZrO<sub>2</sub> is mixed with MgO a fraction of this second oxide can dissolve to form defective solid solutions as Mg<sup>2+</sup> substitutes Zr<sup>4+</sup> in its lattice positions due to the similar ionic radii. In view of the relative wide solubility window of MgO in ZrO<sub>2</sub> (1 – 20 mol%),<sup>205-208</sup> a mixed ZrO<sub>2</sub>-MgO with a moderate amount of MgO of 2.6 wt.% (6.5 mol%) has been prepared. This way two supports with distinct concentration of O-vacancies while the same loading of Ru is impregnated on them have been prepared. Following this strategy, changes in the catalytic behavior can be strongly related to differences in the chemisorption properties at the metal-support interface.<sup>209</sup>

**Supports and catalysts characterization:** The results of N<sub>2</sub> physisorption on the fresh bare supports and supported catalysts as well as the respective contents of Mg and Ru are summarized in **Table 7**. The addition of MgO to ZrO<sub>2</sub> resulted in an increase in the specific surface area (SSA) by ca. 50 %. This increase in presence of MgO can be explained by the formation of smaller pores (**Figure A2a, c**). Meanwhile, Ru impregnation caused only a slight decrease in SSA without affecting the pore size distribution of the respective support (**Figure A2b, d**). The N<sub>2</sub> adsorption isotherms were found typical of mesopore materials<sup>156, 165</sup> and showed no remarkable changes with Ru addition (**Figure A3**).

**Table 7.** Structural properties, Mg and Ru loading of Ru/ZrO<sub>2</sub> and Ru/ZrO<sub>2</sub>-MgO catalysts.

Sample	Ru loading / wt.%	Mg loading / wt.%	BET SSA / m <sup>2</sup> g <sup>-1</sup>	Pore diameter / nm
ZrO <sub>2</sub>	-	-	81	6.3
Ru/ZrO <sub>2</sub>	0.43	-	75	6.4
ZrO <sub>2</sub> -MgO	-	1.54	123	3.3
Ru/ZrO <sub>2</sub> -MgO	0.39	1.54	120	3.5

XRD powder patterns of fresh ZrO<sub>2</sub> and Ru/ZrO<sub>2</sub> (**Figure 30a**) revealed a predominant monoclinic structure of ZrO<sub>2</sub> (ICDD 00-037-1484) with minor contribution of reflections from orthorhombic ZrO<sub>2</sub> at 2θ ca. 30.3° and 60.0° (ICDD 01-071-6425). Reflections of RuO<sub>2</sub> were not resolved in Ru/ZrO<sub>2</sub>, possibly due to superposition with sharper peaks of monoclinic ZrO<sub>2</sub> at 2θ 28.2° and 54.2°, respectively. In contrast, the patterns of ZrO<sub>2</sub>-MgO and Ru/ZrO<sub>2</sub>-MgO (**Figure 30b**) mainly showed reflections of a cubic ZrO<sub>2</sub>-MgO solid solution (ICDD 01-078-1809) together with two signals of tetragonal RuO<sub>2</sub> at 2θ close to 28.1° and 54.4° (ICDD 01-

074-6233). The presence of divalent impurities and O-vacancies which favor the stabilization of the cubic phase explains the change in the pattern after addition of MgO.<sup>210</sup>

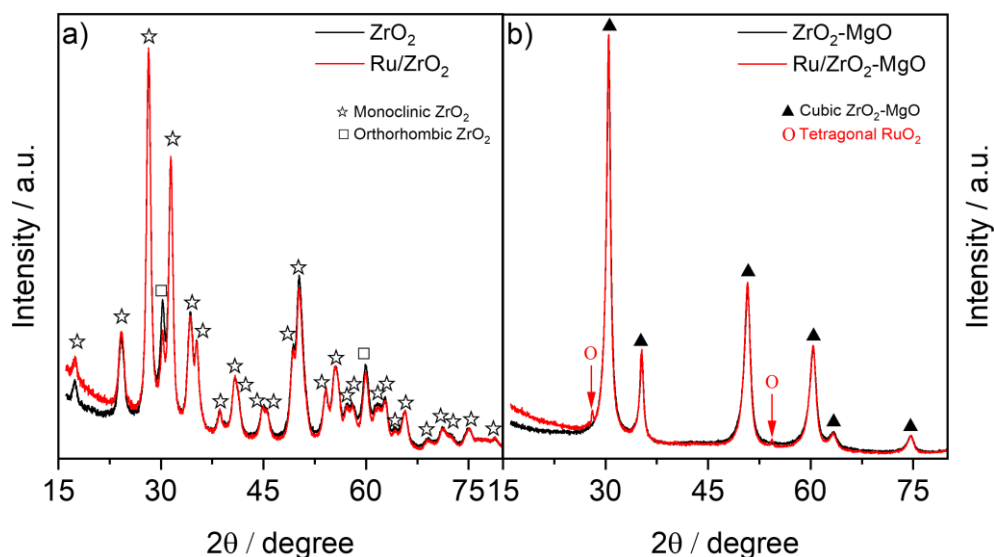


**Figure 30.** XRD powder patterns of a) fresh  $\text{ZrO}_2$  and  $\text{Ru/ZrO}_2$ ; b) fresh  $\text{ZrO}_2\text{-MgO}$  and  $\text{Ru/ZrO}_2\text{-MgO}$ .

$\text{H}_2$ -TPR (**Figure 31**) was recorded to determine the reducibility of the materials. The bare supports showed no reduction peaks below 600 °C (**Figure 31a**). In  $\text{Ru/ZrO}_2$  the sharp peak at 185 °C corresponds to the reduction of  $\text{RuO}_2$ <sup>211, 212</sup> while the peak at 430 °C and the poorly resolved shoulder around 516 °C may be attributed to the reduction of  $\text{ZrO}_2$  upon interaction with  $\text{H}^*$  activated and spilled over from Ru to the support.<sup>213</sup> In the case of  $\text{Ru/ZrO}_2\text{-MgO}$ , the corresponding reduction peaks appeared at higher temperatures. However, similarly, they can be attributed to the reduction of  $\text{RuO}_2$  (219 – 259 °C)<sup>211</sup> and the support (473 °C and 570 °C). In addition, the influence of the different support properties on the reducibility of the  $\text{RuO}_2$  particles<sup>59, 70, 214</sup> is also suggested by the detection of two reduction maxima (219 – 259 °C). This may be related with the location of  $\text{RuO}_x$  ( $x \leq 2$ ) on different zones of the support that differ in their  $\text{ZrO}_2/\text{MgO}$  distribution. Further evidence, from in-situ EPR assessments (shown below), indicates that the Ru oxidic species requiring high temperatures for reduction are closely related with  $\text{MgO/ZrO}_2\text{-MgO}$ .

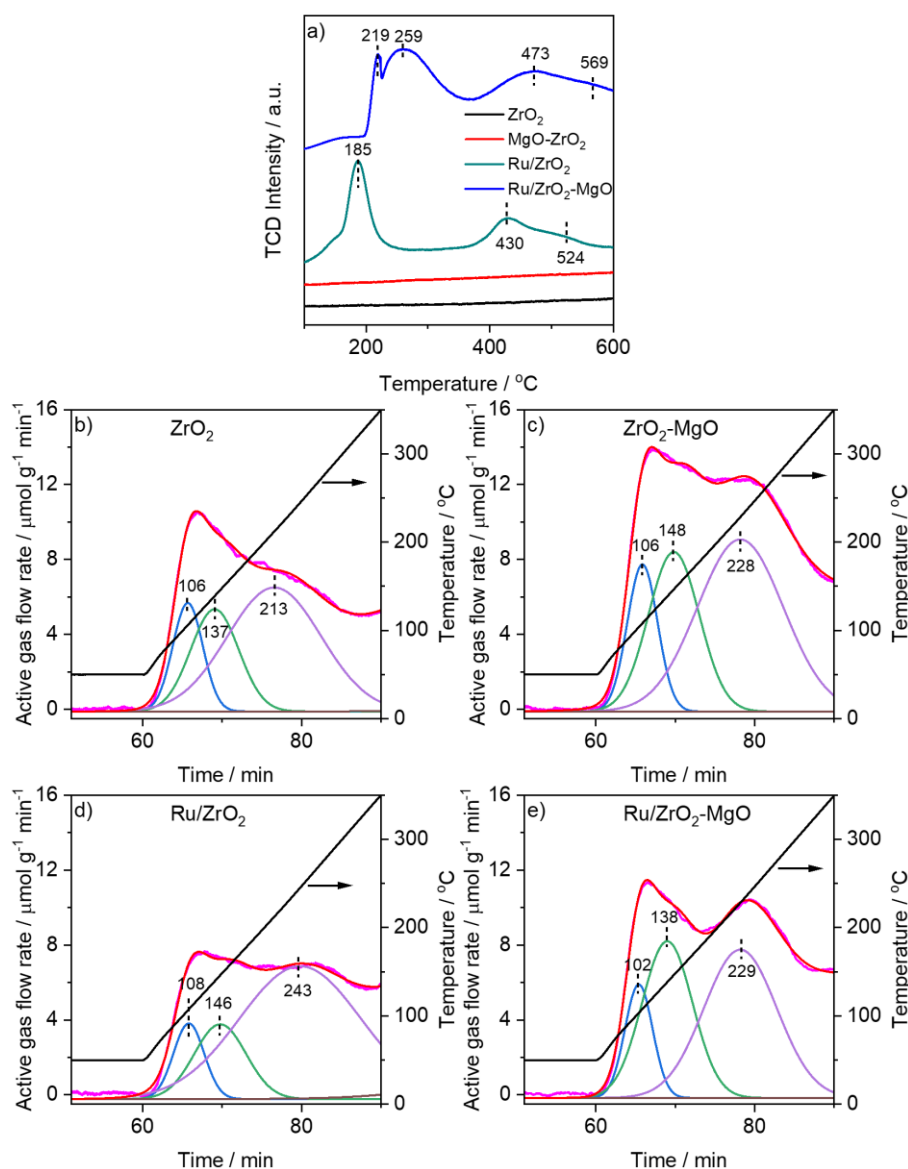


**Figure 31.** a)  $\text{H}_2$ -TPR and b-e)  $\text{CO}_2$ -TPD spectra of the fresh supports and supported Ru catalysts up to 350 °C. Blue, green, and purple peak represent the deconvoluted signals. The numbers indicate the peak temperature of each desorption signal.

$\text{CO}_2$ -TPD analysis and deconvolution of the desorption rate spectra has been performed to quantify the desorbed  $\text{CO}_2$  in the range up to 350 °C (**Figure 31b-e**). The complete spectra up to 750 °C with their respective deconvolution are shown in **Figure A4**. Peaks at 100 – 200 °C and 200 – 350 °C have been assigned to weak and medium-strong adsorption sites, respectively. The peak desorption temperatures of the deconvoluted sub-signals do not differ much, suggesting that the relative strength of the  $\text{CO}_2$  adsorbates is similar in all samples (numbers in **Figure A4b-e**). However, in the presence of MgO the amount of desorbed  $\text{CO}_2$  was higher (left y axis in **Figure A4b-e**).

Further examination of the catalysts was done by High-Angle Annular Dark Field-Scanning Transmission Electron Microscopy (HAADF-STEM) and EDX spectroscopy (**Figure 32**). For the as prepared Ru/ZrO<sub>2</sub>-MgO catalyst (**Figure 32a, c**), a non-homogeneous distribution of RuO<sub>2</sub>/Ru (red color) with large separate Ru containing particles was observed. This is well seen by EDX spectra recorded at different regions (**Figure 32b**). The zone marked as “1” is representative of a region relatively enriched with MgO in which the signals of Ru L<sub>α</sub> and Ru L<sub>β</sub> at about 2.56 and 2.68 keV were not clearly detected. In the case of zone “2”, ZrO<sub>2</sub> prevailed and strong signals of Ru were observed. In region “3”, it is seen that RuO<sub>2</sub>/Ru is also present but separated from the support as no signal of Zr and Mg can be observed in the EDX spectra. Here, the intense O K signal implies the presence of RuO<sub>2</sub>. In the case of spent Ru/ZrO<sub>2</sub>-MgO, i.e., after reaction at 270 °C, the inhomogeneous distribution of Ru prevailed (**Figure 32d-f**). The EDX spectrum of region “1” shows predominantly ZrO<sub>2</sub> with only little Mg and no Ru. However, extended zones, where Ru and Mg are present without Zr are detected (**Figure 32e, f**). The EDX spectrum of region “2” (**Figure 32e**) suggests a contact between Ru and Mg, which might be beneficial for the catalytic performance.

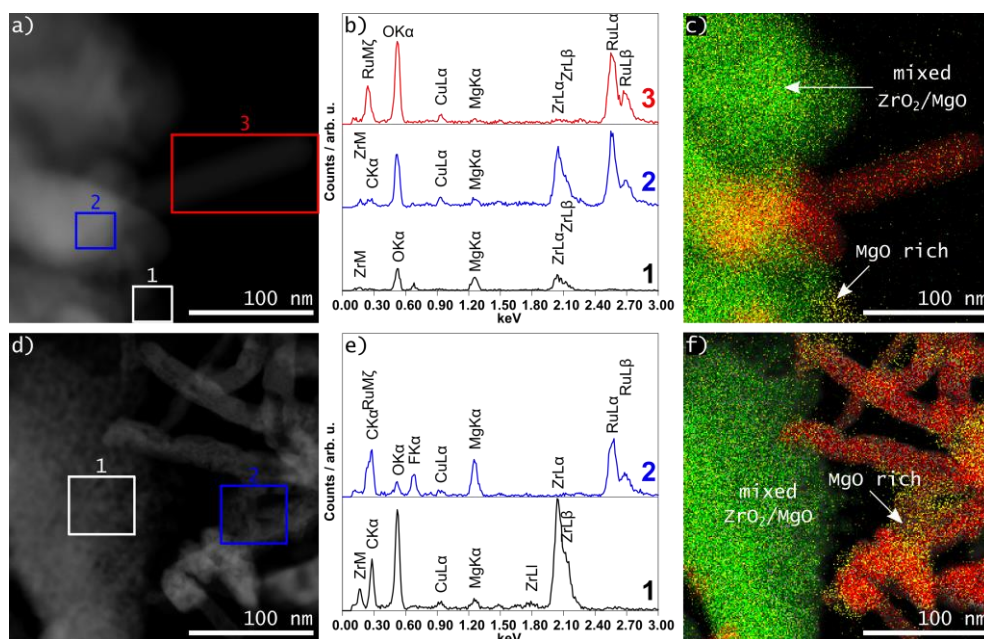


**Figure 32.** Representative HAADF-STEM images, EDX spectra recorded on selected regions and EDX map of fresh (a – c) and spent Ru/ZrO<sub>2</sub>-MgO (d – f) (Zr: green, Ru: red, Mg: yellow). The spent material was investigated after reaction at 270 °C.

These results would explain the resolved H<sub>2</sub>-TPR spectra of Ru/ZrO<sub>2</sub>-MgO (**Figure 31a**) where the detection of at least two peaks between 219 and 259 °C might point to the reduction of RuO<sub>2</sub> located in zones with distinct ZrO<sub>2</sub> and ZrO<sub>2</sub>-MgO contributions.

**Activity assessments:** The methanation behavior of the catalysts normalized by the Ru mass was evaluated in the temperature range 140 – 300 °C. The rates and the conversion were comparable up to 220 °C while the selectivity to CH<sub>4</sub> was 100 % in the whole explored temperature window for both catalysts (**Figure A5**). Once the temperature increased above 220 °C the rate of CH<sub>4</sub> formation was clearly larger on Ru/ZrO<sub>2</sub>-MgO (**Figure 33a**). It increased by ca. 1.9 times at 250 °C on Ru/ZrO<sub>2</sub>-MgO while at 300 °C the difference was slightly more pronounced, i.e., 2.8 times in favor of Ru/ZrO<sub>2</sub>-MgO. The respective CO<sub>2</sub> conversions at these conditions were of 21 % in the case of the MgO containing catalyst and of only 8 % on the unmodified catalyst (**Figure 33c**). As the conversion of CO<sub>2</sub> was below the thermodynamic limit at all temperatures (**Figure A6**), the reaction was under kinetic control in all cases.

The calculated apparent activation energies in the range 220 – 300 °C (**Figure 33b**) were in the expected order of magnitude as reported for this reaction on distinct Ru based catalysts (~ 50 – 80 kJ mol<sup>-1</sup>).<sup>50, 70, 97, 172</sup> However, in case of Ru/ZrO<sub>2</sub> ( $E_A = 58.1$  kJ mol<sup>-1</sup>) was lower than on Ru/ZrO<sub>2</sub>-MgO ( $E_A = 79.1$  kJ mol<sup>-1</sup>). This apparent contradiction can be solved by accounting for the pre-exponential factors. From the linear fitting of rates in **Figure 33b**, the logarithms of the pre-exponential factors corresponded to 5.6 and 11.0 for Ru/ZrO<sub>2</sub> and Ru/ZrO<sub>2</sub>-MgO, respectively. This can be interpreted as a relatively larger fraction of exposed active sites on Ru/ZrO<sub>2</sub>-MgO. This compensates the high activation energy for the reaction on this catalyst. Wang et al also noted a lower apparent activation energy for 0.5 wt.% Ru/Al<sub>2</sub>O<sub>3</sub> when compared to 5 wt.% Ru/Al<sub>2</sub>O<sub>3</sub>, being this last the most active catalyst. Despite the lower activation energy of the low Ru loaded catalyst, the higher fraction of inactive sites when compared with the high Ru loaded catalyst was the driver for the different activities.<sup>97</sup>

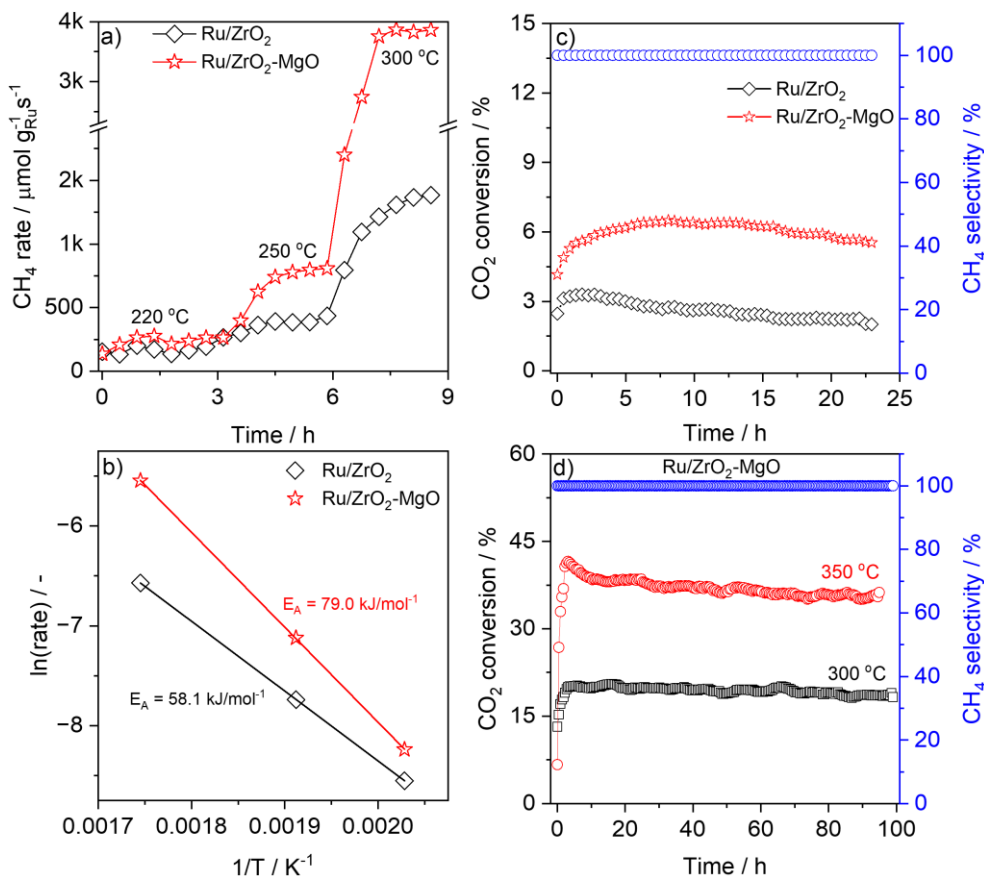


**Figure 33.** a) Ru mass normalized CH<sub>4</sub> formation rate on Ru/ZrO<sub>2</sub> (black diamonds) and Ru/ZrO<sub>2</sub>-MgO (red stars) in the temperature range 220 – 300 °C; b) Arrhenius plot and activation energies for Ru/ZrO<sub>2</sub> (black diamonds) and Ru/ZrO<sub>2</sub>-MgO (red stars) in the temperature range 220 – 300 °C; c) CO<sub>2</sub> conversion and selectivity to CH<sub>4</sub> on Ru/ZrO<sub>2</sub> (black diamonds) and Ru/ZrO<sub>2</sub>-MgO (red stars) for 24 h reaction at 250 °C; d) CO<sub>2</sub> conversion and selectivity to CH<sub>4</sub> on Ru/ZrO<sub>2</sub>-MgO for ca. 100 h reaction at 300 °C (black squares) and 350 °C (red circles). Inlet gas flow conditions in all cases: 16 ml min<sup>-1</sup> H<sub>2</sub>, 4 ml min<sup>-1</sup> CO<sub>2</sub>, 10 ml min<sup>-1</sup> N<sub>2</sub>.

The stability of the catalysts was also evaluated. First, at 250 °C during ca. 24 h (**Figure 33c**) it was observed an induction time before reaching the maximum conversion after which a slight decline occurred. For Ru/ZrO<sub>2</sub>, the induction time to reach maximum conversion was about 2 h while for Ru/ZrO<sub>2</sub>-MgO ca. 8 h were needed. This difference can be explained by the H<sub>2</sub>-TPR results (**Figure 31a**) where it was determined that reduction of RuO<sub>2</sub> on Ru/ZrO<sub>2</sub>-MgO required higher temperatures (peak maximum 260 °C) than on ZrO<sub>2</sub> (185 °C). The net deactivation during ca. 24 h under these conditions was around 1 %, independently on the presence or absence of MgO, i.e., the slight deactivation is not affected by the incorporation of MgO. Since RuO<sub>2</sub> reduction on Ru/ZrO<sub>2</sub>-MgO required higher temperatures, its catalytic performance and stability were also evaluated at 300 – 350 °C during a long-term experiment of ca. 100 h (**Figure 33d**). The catalyst showed a higher catalytic performance, high stability and shorter induction times to reach its maximum conversion in comparison with those obtained



at lower temperatures (**Figure 33d**). At 300 °C, the net deactivation at the end of the experiment was only 2%, while at 350 °C the CO<sub>2</sub> conversion decreased by 5 % (from ca. 41 % to 36 %) without any effect on the selectivity to CH<sub>4</sub>, which was 100 % during the whole experiment.

H<sub>2</sub> chemisorption was performed to estimate the particle size distribution and dispersion of Ru. The calculations were performed by equations eq. 33 – 35 and the results presented in **Table 8**.

**Table 8.** Particle size, specific surface area and dispersion of Ru on Ru/ZrO<sub>2</sub> and Ru/ZrO<sub>2</sub>-MgO catalysts.

Sample	Mean Ru particle size / nm	Ru specific surface area / m <sup>2</sup> g <sup>-1</sup>	Ru dispersion / %
Ru/ZrO <sub>2</sub> -spent	46.8	8.54	2.04
Ru/ZrO <sub>2</sub> -MgO-spent	4.93	81.1	19.4

With this information TOFs were calculated and are shown in **Table 9**. The activity per active surface site compensates the mass normalized rate in the case of the catalyst with bigger Ru particles. As CH<sub>4</sub> productivity is not in alignment with the TOF trends, this suggests that not all exposed Ru atoms on the surface are active. This fact has been previously demonstrated when observing that catalysts (Ru/TiO<sub>2</sub> and Ru/Al<sub>2</sub>O<sub>3</sub>) with similar Ru dispersion exhibited distinct CH<sub>4</sub> activity.<sup>21, 215, 216</sup> Furthermore, Guo et al. showed for a series of Ru/CeO<sub>2</sub> catalysts that with an optimum Ru particle size of around 1 nm better activity can be obtained than with single Ru atoms and Ru clusters of ca. 4 nm.<sup>70</sup> Therefore, effects distinct to Ru dispersion, contribute in major extent to the promotion of CH<sub>4</sub> activity on the Ru/ZrO<sub>2</sub>-MgO catalyst. This is in alignment with the formation of domains on which Ru preferably interacted with ZrO<sub>2</sub>-MgO in the spent catalyst (**Figure 32e, f**) that suggests that the metal-support interaction might be drastically affected by the presence of MgO, thus, leading to these catalytic differences.

**Table 9.** Rates of reaction calculated at steady state in the range 220 – 300 °C on Ru/ZrO<sub>2</sub> and Ru/ZrO<sub>2</sub>-MgO catalysts.

Temperature / °C	Catalyst	Rate / mol <sub>Ru</sub> CH <sub>4</sub> g <sup>-1</sup> s <sup>-1</sup>	<sup>a</sup> TOF / s <sup>-1</sup>
220	Ru/ZrO <sub>2</sub>	1.9*10 <sup>-4</sup>	0.95
250		4.3*10 <sup>-4</sup>	2.15
300		1.4*10 <sup>-3</sup>	6.90
220	Ru/ZrO <sub>2</sub> -MgO	2.6*10 <sup>-4</sup>	0.13
250		8.1*10 <sup>-4</sup>	0.42
300		3.9*10 <sup>-3</sup>	2.03

a: calculated with equation eq. 30

**X-ray photoelectron spectroscopy:** Ex-situ XPS spectra were recorded for the as prepared and spent catalysts. Since Ru 3d signals strongly overlap with those from C 1s species (**Figure A7a-d**), thus the oxidation state before and after reaction was determined using the Ru 3p spectra (**Figure 34a-d**). The fitted spectra of Ru 3p species clearly showed that Ru initially was present in its oxidized state, as the binding energy in the range 463.1 – 463.0 eV is typical for RuO<sub>2</sub>. In addition, a second signal corresponding to the satellite of RuO<sub>2</sub> was also resolved at 465.7 eV.<sup>177</sup> This agrees with XRD patterns (**Figure 30a, b**) and additional STEM images (**Figure A8a, c**) that allowed to observe rather big RuO<sub>2</sub> nanoparticles in the fresh materials. Meanwhile, after reaction dispersed Ru particles formed. This last in alignment with the downshift in the binding energy to values between 461.6 – 461.4 eV, i.e., typically reported for metallic Ru.<sup>177</sup>

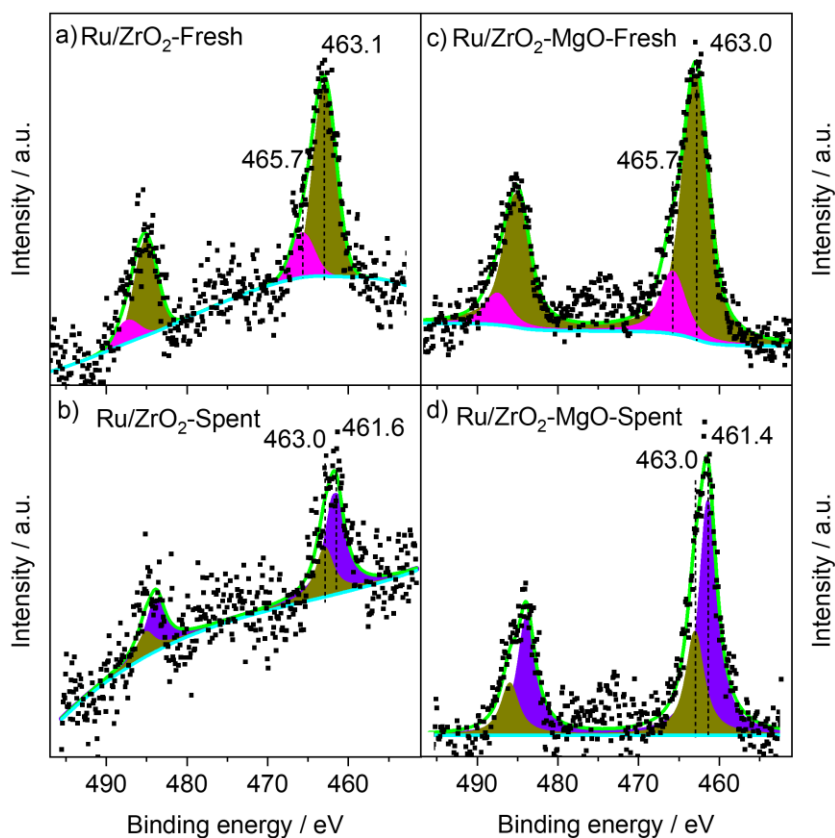


**Figure 34.** XP spectra in the Ru 3p region of the fresh and spent Ru/ZrO<sub>2</sub> catalyst (a, b) and of fresh and spent Ru/ZrO<sub>2</sub>-MgO catalyst (c, d). The spectra corresponding to the spent catalysts were recorded after reaction at 270 °C.

The quantification of the surface atomic Ru composition suggested a better dispersion of Ru on Ru/ZrO<sub>2</sub>-MgO. The surface concentration of Ru was higher on Ru/ZrO<sub>2</sub>-MgO before and after reaction (**Table 10**). This is further supported by STEM images (**Figure A8b, d**)

where nanoparticles of Ru appeared more dispersed on Ru/ZrO<sub>2</sub>-MgO. According to N<sub>2</sub> physisorption, the SSAs of the MgO modified support and catalyst were ca. 40 % larger thus, the possible enhancement in the dispersion of Ru might not be surprising. However, this promotion in the SSA/Ru dispersion by itself is probably not the main reason for the distinct reactivity behavior exhibited by the catalysts.

**Table 10.** Surface atomic concentration of Ru quantified from Ru 3d XPS signals before and after reaction on Ru/ZrO<sub>2</sub> and Ru/ZrO<sub>2</sub>-MgO catalysts.

Sample	Surface Ru / at. %
Ru/ZrO <sub>2</sub> -spent	0.34
Ru/ZrO <sub>2</sub> -MgO-spent	1.31

***In-situ electron paramagnetic resonance:*** It is worth to note that XRD patterns (**Figure 30**) revealed the formation of a solid ZrO<sub>2</sub>-MgO solution. Therefore, an enhancement in the concentration of oxygen vacancies might be expected. Nevertheless, surprisingly, Zr<sup>3+</sup> formation was not observed by XPS (**Figure A9**). The resolved signals showed maxima with binding energy about 182.2 eV typical of Zr<sup>4+</sup>.<sup>217</sup> As the measurements were performed ex-situ, it is possible that re-oxidation with atmospheric air would be the cause of this observation. Since EPR is more sensitive to paramagnetic species we performed assessments using this technique on the samples at in-situ conditions to uncover the involvement of O-vacancies/Zr<sup>3+</sup> in the present cases. First, spectra were recorded at -173 °C for the bare supports after oxidative pretreatment (black lines in **Figure 35a, b**). A typical signal of electrons trapped in O-vacancies<sup>218</sup> was resolved at  $g_{\text{iso}} = 2.003$  in both cases, although being ca. 1.8-fold more intense in the presence of MgO. A second axial signal ( $g^2_{\perp} = 1.974$  and  $g^2_{\parallel} = 1.963$ ), that was associated to Zr<sup>3+</sup>,<sup>218-220</sup> was only clearly resolved in case of the MgO modified ZrO<sub>2</sub>. This effect was already anticipated due to the expected formation of extra O-vacancies in the ZrO<sub>2</sub>-MgO solid solution, which could release electrons to Zr<sup>4+</sup> to form Zr<sup>3+</sup> ( $\text{Zr}^{4+} + e^-(\text{O-vacancy}) \rightarrow \text{Zr}^{3+}$ ). That is, the insertion of Mg<sup>2+</sup> in the structure of ZrO<sub>2</sub>, as suggested by the XRD patterns, is corroborated by EPR spectra. The corresponding spectra of the fresh catalysts (red lines in **Figure 35a, b**) revealed further differences. The impregnation of Ru on ZrO<sub>2</sub> resulted in the detection of a new axial signal ( $g^1_{\perp} = 2.067$  and  $g^1_{\parallel} = 1.890$ ) that is likely related with paramagnetic Ru species, presumably Ru<sup>3+</sup>.<sup>221, 222</sup> Moreover, after Ru addition, Zr<sup>3+</sup> could be detected, represented by the axial signal ( $g^2_{\perp} = 1.974$  and  $g^2_{\parallel} = 1.963$ ) (red lines in **Figure 35a**). For Ru/ZrO<sub>2</sub>-MgO a new axial signal ( $g^3_{\perp} = 2.097$  and  $g^3_{\parallel} = 1.907$ ) was resolved (red spectra

in **Figure 35b**). Probably this signal is representative of Ru species that interact with the support in regions containing a MgO/ZrO<sub>2</sub>-MgO solid solution (see **Figure 30**), as also evidenced by EDX mapping (**Figure 32**) and is a further indication of distinct electronic/structural properties induced by MgO. Signals representing Zr<sup>3+</sup> ( $g_{\perp}^2 = 1.974$  and  $g_{\parallel}^2 = 1.963$ ) were also clearly more pronounced when compared with the bare ZrO<sub>2</sub>-MgO support corroborating that the presence of Ru induced the formation of defects in the supports.

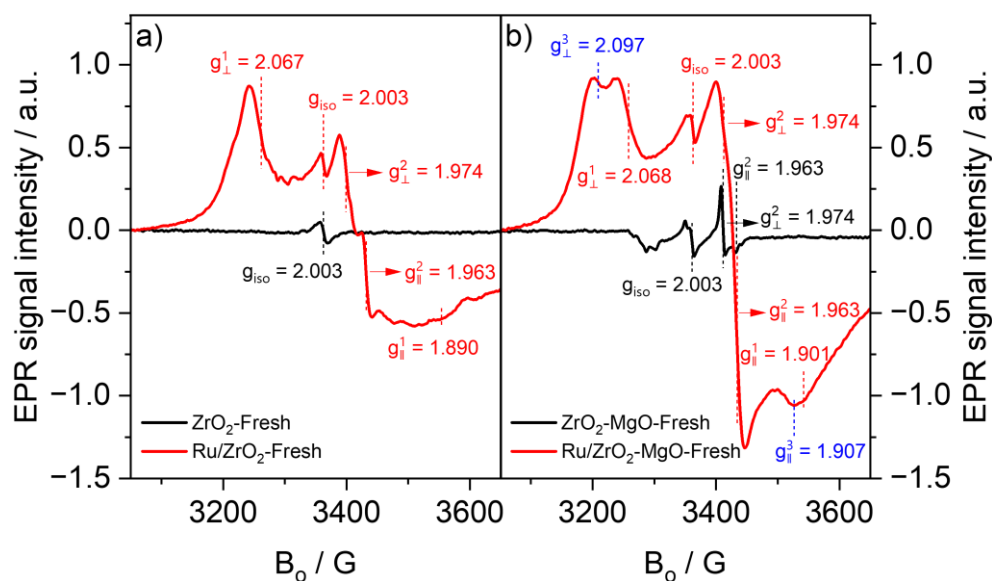


**Figure 35.** EPR spectra recorded at -173 °C of a) ZrO<sub>2</sub> and Ru/ZrO<sub>2</sub>; b) ZrO<sub>2</sub>-MgO and Ru/ZrO<sub>2</sub>-MgO. The black lines represent the spectra of the bare supports while the red lines represent the spectra of the catalysts. All the spectra were recorded in He atmosphere after oxidative pre-treatment.

The reaction was in-situ followed at 250 °C (**Figure A10**). Besides the changes in the first 2 min of reaction associated to reduction of Ru and increase in O-vacancies, no further differences could be resolved in the next hour at these conditions. To observe the changes after reaction with greater detail, spectra were also recorded at -173 °C (**Figure 36a, b**). The most remarkable difference was the appearance of a new signal with  $g = 2.008$  that overlapped with the oxygen vacancy signal at  $g_{\text{iso}} = 2.003$  in Ru/ZrO<sub>2</sub>-MgO. Previously, a similar effect was reported for Au/ZrO<sub>2</sub> catalysts and was attributed to the formation of carbonate/bicarbonate species<sup>219, 223</sup> upon the interaction of CO<sub>2</sub> with O-vacancies and surface hydroxyl groups.<sup>224</sup> The presence of such a signal only in the MgO modified catalyst suggests that interactions between the surface and molecules from the gas phase are more pronounced in this case. Another key difference between the spectra is that signals from Zr<sup>3+</sup> could not be resolved in case of Ru/ZrO<sub>2</sub>-MgO while in Ru/ZrO<sub>2</sub> still the perpendicular component ( $g_{\perp}^2 = 1.974$ ) could be observed. A third aspect to highlight is the presence of partially oxidized Ru still after

reaction in Ru/ZrO<sub>2</sub>-MgO ( $g_{\perp}^1 = 2.067$  and  $g_{\perp}^3 = 2.109$ ). This agrees with H<sub>2</sub>-TPR (**Figure 31a**) that showed the need of higher reduction temperatures to further reduce strongly interacting RuO<sub>x</sub> with the ZrO<sub>2</sub>-MgO support and was also reflected by STEM. In summary, regarding the activity-structure relationships, EPR results indicated that the promotion of O-vacancies by incorporation of MgO facilitated the interaction of CO<sub>2</sub> with the catalyst.

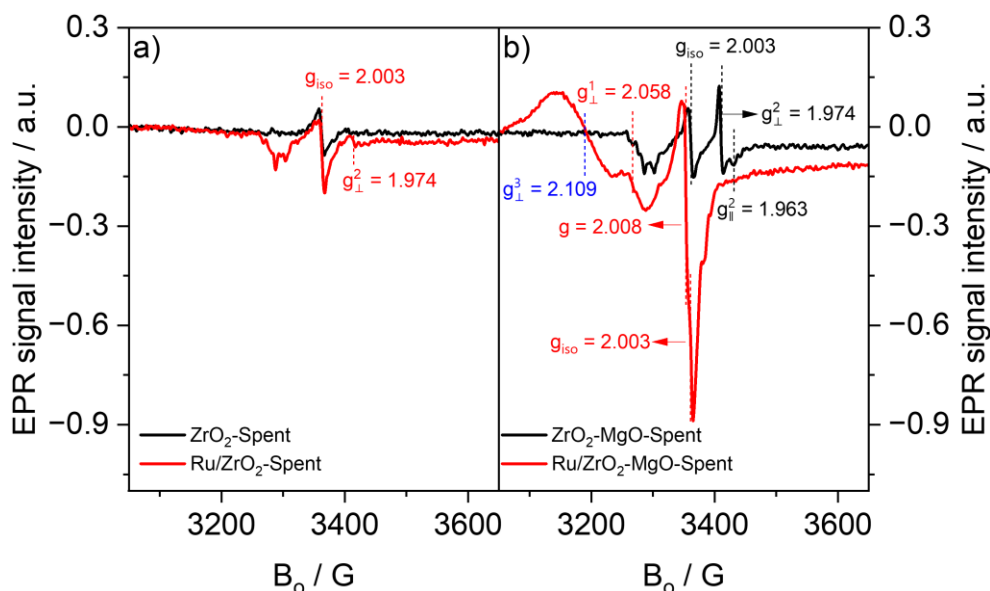


**Figure 36.** EPR spectra recorded at -173 °C of a) ZrO<sub>2</sub> and Ru/ZrO<sub>2</sub>; b) ZrO<sub>2</sub>-MgO and Ru/ZrO<sub>2</sub>-MgO. The black lines represent the spectra of the bare supports while the red lines represent the spectra of the catalysts. All the spectra were recorded after reaction and under H<sub>2</sub>:CO<sub>2</sub> = 4:1 atmosphere.

***In-situ DRIFTS measurements:*** The formation of surface adsorbates and intermediates was examined by in-situ DRIFT spectroscopy. Spectra recorded at 250 °C are shown in **Figure 37a, b**. In the case of Ru/ZrO<sub>2</sub> (**Figure 37a**) two main bands were identified in the carbonyl zone. The first, in the range 2059 – 2055 cm<sup>-1</sup>, has been commonly associated to CO linearly adsorbed on Ru clusters (Ru<sub>x</sub>-CO).<sup>198, 201</sup> The second signal appearing near 1981 cm<sup>-1</sup> could be assigned to bridge-like CO adsorbed on adjacent metallic Ru sites, e.g., Ru<sub>2</sub>-(CO).<sup>97, 197</sup> In contrast, for Ru/ZrO<sub>2</sub>-MgO (**Figure 37b**), the spectra in the carbonyl region were more complex. Two main bands centered at ca. 2033 and 1959 cm<sup>-1</sup> dominate the spectrum. They represent the asymmetric and symmetric stretching of two carbonyls attached to one Ru atom (Ru-(CO)<sub>2</sub>).<sup>195</sup> The band at 2064 cm<sup>-1</sup> might be attributed to CO linearly adsorbed on electronically modified Ru sites located at the periphery interphase.<sup>22, 198</sup> Meanwhile, the new extra signals in the range 1990 – 1960 cm<sup>-1</sup> could contain contributions from CO adsorbed on isolated metallic Ru sites surrounded by partially oxidized Ru.<sup>67, 197</sup> This is not surprising, as

H<sub>2</sub>-TPR (**Figure 31a**) and in-situ EPR (**Figure 36b**) assessments suggested that some fractions of partially oxidized Ru might remain on Ru/ZrO<sub>2</sub>-MgO at these conditions. The band with frequency at 2052 cm<sup>-1</sup> likely represents CO linearly adsorbed on Ru clusters (Ru<sub>x</sub>-CO), as in the case of Ru/ZrO<sub>2</sub>. The lower vibration is, however, an indication that the Ru sites could have a higher local electronic density in presence of MgO. Such electronic enrichment might occur by the facile interaction of these Ru sites with neighboring O-vacancies/Zr<sup>3+</sup> as determined by in-situ EPR measurements.

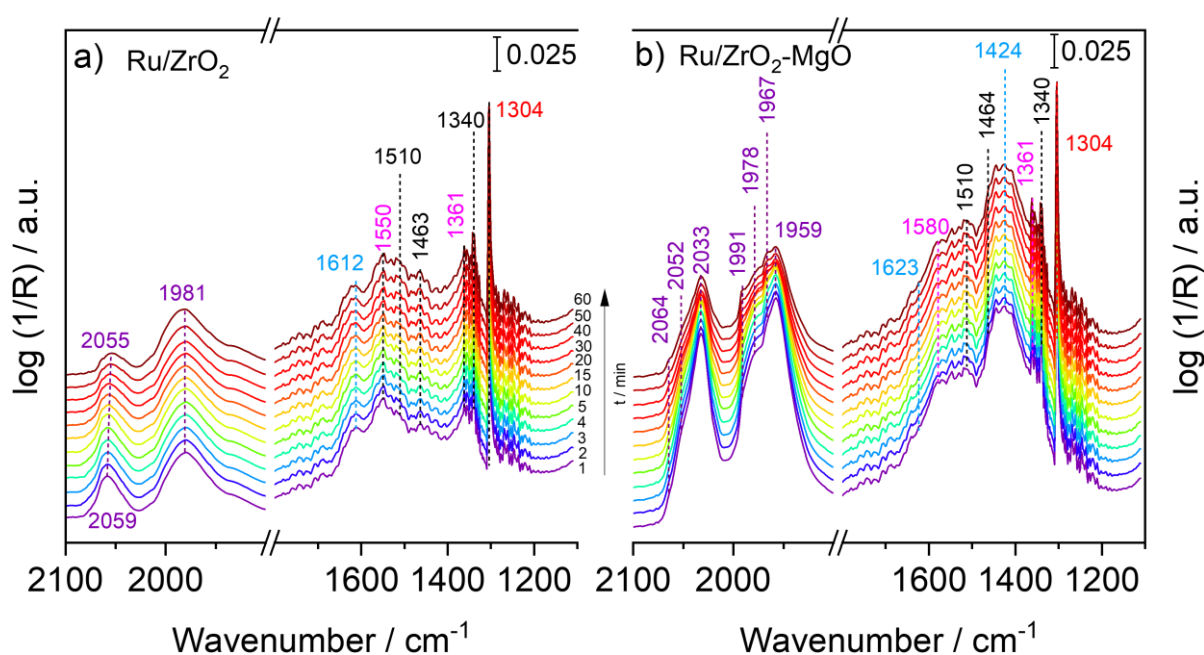


**Figure 37.** DRIFT spectra recorded at 250 °C on a) Ru/ZrO<sub>2</sub> and b) Ru/ZrO<sub>2</sub>-MgO. The total reaction time was set to 1 h (from bottom to top). Inlet gas flow conditions: 16 ml min<sup>-1</sup> H<sub>2</sub>, 4 ml min<sup>-1</sup> CO<sub>2</sub>, 10 ml min<sup>-1</sup> He.

When analyzing the region below 1800 cm<sup>-1</sup> a strong band was observed for Ru/ZrO<sub>2</sub> at ca. 1550 cm<sup>-1</sup> (**Figure 37a**). This signal could be associated with the asymmetric O-C-O stretching vibration,  $\nu_{\text{as}}(\text{O-C-O})$ , of formate species (HCOO<sup>\*</sup>). The sign “\*” denotes adsorbed species. The corresponding symmetric stretching signal for this species,  $\nu_{\text{s}}(\text{O-C-O})$ , might be represented by the band around 1361 cm<sup>-1</sup>.<sup>128, 225</sup> Moreover, the difference between  $\nu_{\text{as}}(\text{O-C-O})$  and  $\nu_{\text{s}}(\text{O-C-O})$  ( $\Delta\nu = 189 \text{ cm}^{-1}$ ) points to a bidentate like formate (b-HCOO<sup>\*</sup>).<sup>226</sup> In the case of Ru/ZrO<sub>2</sub>-MgO (**Figure 37b**) the corresponding signals associated to formate appeared at ca. 1580 and 1361 cm<sup>-1</sup> for  $\nu_{\text{as}}(\text{O-C-O})$  and  $\nu_{\text{s}}(\text{O-C-O})$ , respectively. The difference between  $\nu_{\text{as}}(\text{O-C-O})$  and  $\nu_{\text{s}}(\text{O-C-O})$  ( $\Delta\nu = 219 \text{ cm}^{-1}$ ) still suggests formation of a bidentate formate (b-HCOO<sup>\*</sup>).<sup>226, 227</sup> The location of the asymmetric vibration of b-HCOO<sup>\*</sup> at higher frequencies in Ru/ZrO<sub>2</sub>-MgO is another indication of the distinct reactivity of intermediates in the MgO

modified catalyst. Further corroboration that these signals are related to formates is given by spectra in the CH stretching region (**Figure A11**) in which signals at 2883 – 2887  $\text{cm}^{-1}$  together with bands at 2744, and 2970 – 2979  $\text{cm}^{-1}$  under reaction conditions can be associated to bidentate formates.<sup>225</sup> These bands become occluded at  $T \geq 220$  °C by the rotational modes of  $\text{CH}_4$  and absorption bands from water vapor. The corresponding CH bending bands,  $\delta_{\text{CH}}$ , are indicated by the vibration frequencies at 1384 – 1386  $\text{cm}^{-1}$  (**Figure A12**).

Spectra for the bare supports were recorded during reaction at 250 °C (**Figure A13a, b**). In these last cases no signals in the carbonyl region were resolved, as expected due to the absence of Ru. Only clear signals were detected in the O-C-O region. Moreover, no  $\text{CH}_4$  was detected, corroborating the kinetic assessments.

A summary of the bands observed during in-situ DRIFTS is seen in **Table 11**.

**Table 11.** Infrared absorption bands and assignments for adsorbate species observed during  $\text{CO}_2$  hydrogenation on Ru/ZrO<sub>2</sub> and Ru/ZrO<sub>2</sub>-MgO catalysts.

Surface species	Wavenumber / $\text{cm}^{-1}$	Assignment	Reference
Formate	2979 – 2970	$\delta(\text{CH}) + \nu_{\text{as}}(\text{O-C-O})$	128, 225
	2887 – 2883	$\nu(\text{CH})$	
	2744	$\delta(\text{CH}) + \nu_{\text{s}}(\text{O-C-O})$	
Carbonyl	2064	Ru-CO at electronically modified sites located at the periphery interphase	22, 198
	2059 – 2055	Ru-CO on top of Ru clusters	198, 201
	2033	asymmetric stretching of (Ru-(CO) <sub>2</sub> )	195
	1981	Ru <sub>2</sub> -(CO)	97, 197
	1990 – 1960	CO adsorbed on isolated metallic Ru sites surrounded by partially oxidized Ru	67, 197
	1959	symmetric stretching of (Ru-(CO) <sub>2</sub> )	195
Bidentate bicarbonate	1618	$\delta(\text{OH})$	199
Bidentate formate	1361	$\nu_{\text{s}}(\text{O-C-O})$	128, 192
	1580 – 1550	$\nu_{\text{as}}(\text{O-C-O})$	
Bicarbonate	1386 – 1384	$\delta(\text{CH})$	191, 200
	1552	$\nu_{\text{as}}(\text{O-C-O})$	
	1339	$\nu_{\text{s}}(\text{O-C-O})$	

Dynamic experiments were performed to determine which Ru-CO species could be the source of  $\text{CH}_4$ . First, after reaction, the spent catalysts were left under He overnight at 20 °C and then heated up to 250 °C. After 3 h in He atmosphere, the gas feed was changed to a mixture of 16  $\text{ml min}^{-1}$   $\text{H}_2$  and 14  $\text{ml min}^{-1}$  He. Spectra were recorded during 30 min for each sample (**Figure 38a, b**). Adsorbed CO on Ru was still present before starting the experiment (first

spectrum from top to bottom). Once H<sub>2</sub> was admitted to the reaction cell the typical signal of CH<sub>4</sub> at ca. 3014 cm<sup>-1</sup> appeared. At the same time of H<sub>2</sub> entrance, the corresponding Ru-CO signals (2064 – 2036 cm<sup>-1</sup>) began to decrease and shifted to lower wavenumber. In both catalysts the CH<sub>4</sub> signal disappeared together with the Ru-CO signal at highest frequency (2064 – 2050 cm<sup>-1</sup> on Ru/ZrO<sub>2</sub> and 2056 – 2036 cm<sup>-1</sup> on Ru/ZrO<sub>2</sub>-MgO).

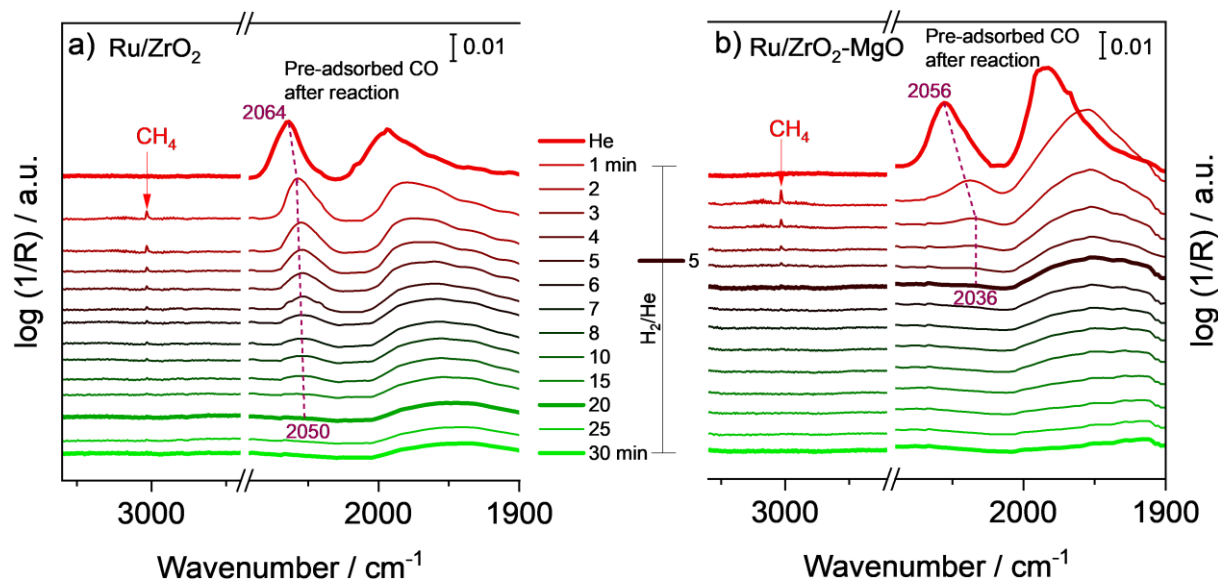


**Figure 38.** DRIFT spectra recorded at 250 °C on the spent catalysts: a) Ru/ZrO<sub>2</sub> and b) Ru/ZrO<sub>2</sub>-MgO after He purge overnight at RT and 3 h purging also in He at 250 °C. The first spectrum from top to bottom correspond to the catalyst before H<sub>2</sub> admission. The total time was set to 30 min. Inlet gas flow conditions after switch (second spectrum from top to bottom): 16 ml min<sup>-1</sup> H<sub>2</sub>, 14 ml min<sup>-1</sup> He.

These changes, however, occurred at different rates. While this carbonyl band vanished together with CH<sub>4</sub> after ca. 20 min on Ru/ZrO<sub>2</sub>, for Ru/ZrO<sub>2</sub>-MgO only 5 min were needed. Although low frequency Ru-CO species (< 2000 cm<sup>-1</sup>) were still detected after the decay of the high frequency one, no evolution of CH<sub>4</sub> could be detected despite the presence of H<sub>2</sub>. This situation is observed from the normalized temporal decay of these signals, shown in **Figure 39**. The normalization was referred to the intensity of the respective band before the admission of H<sub>2</sub> to the reaction cell. No correlation between the decay of CH<sub>4</sub> and Ru-CO (1992 – 1984 cm<sup>-1</sup>) signals was observed. On the other hand, the signal of Ru-CO (2064 – 2056 cm<sup>-1</sup>) followed almost the same decay of CH<sub>4</sub>.



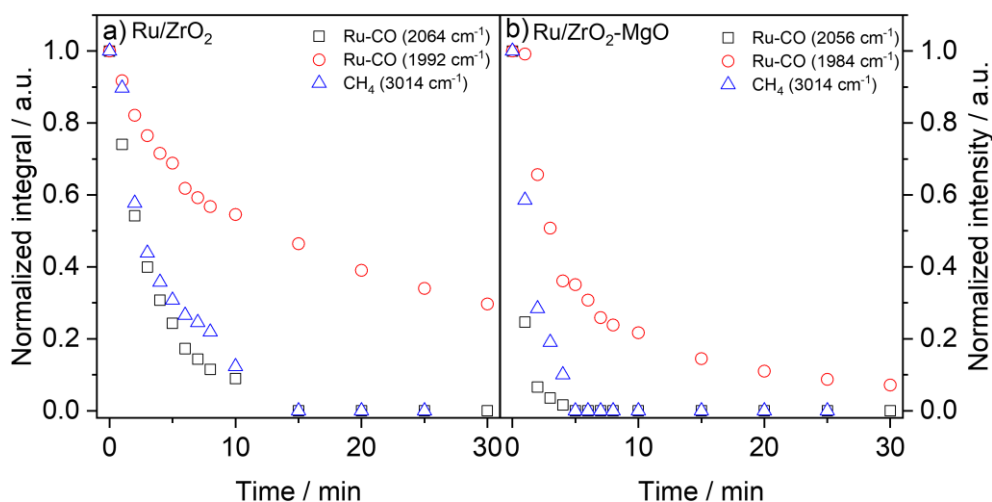


**Figure 39.** Normalized integral decay of the bands resolved in the spectra recorded at 250 °C during the dynamic experiment presented in **Figure 38**. a) Ru/ZrO<sub>2</sub> and b) Ru/ZrO<sub>2</sub>-MgO. The total time was set to 30 min.

Inlet gas flow conditions after switch: 16 ml min<sup>-1</sup> H<sub>2</sub>, 14 ml min<sup>-1</sup> He.

During a second dynamic experiment, using spent catalyst, the source of the reactive Ru-CO was determined. After a purge during 30 min in H<sub>2</sub>/He atmosphere, the gas mixture was exchanged to 4 ml min<sup>-1</sup> CO<sub>2</sub> in 26 ml min<sup>-1</sup> He. Spectra were again recorded during 30 min (**Figure 40a, b**). Contrary to the previous experiment, no pre-existing carbonyl species were present before the admission of CO<sub>2</sub> (first spectrum from top to bottom) because they were eliminated during the 30 min in H<sub>2</sub>/He purge. Once CO<sub>2</sub> was admitted to the chamber, CH<sub>4</sub> evolved. This occurred together with the formation of Ru-CO as well as of formate, bicarbonate and carbonate species. Methane disappeared after ca. 10 min on Ru/ZrO<sub>2</sub>, while it took only about 4 min for Ru/ZrO<sub>2</sub>-MgO.

The normalized integrated signals showed that the steepest increase in the intensity of the carbonyl with absorption frequency at ca. 2060 cm<sup>-1</sup> coincided with the maximum in the intensity of formate species and with the disappearance of the CH<sub>4</sub> signal (**Figure 41a, b**). In contrast, the temporal behavior of the bands assigned to bicarbonates and carbonates showed no correlation with CH<sub>4</sub> and Ru-CO (2060 cm<sup>-1</sup>) bands in any case. Hence, these last species seem to play a role of spectators.

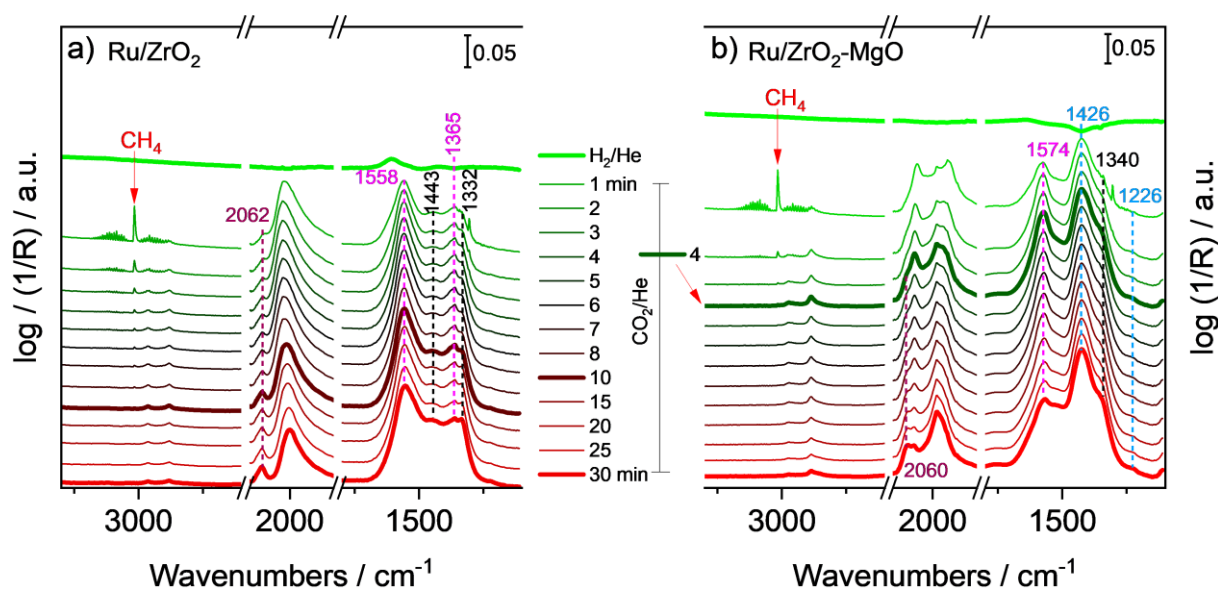


**Figure 40.** DRIFT spectra recorded at 250 °C after switching from H<sub>2</sub>/He to CO<sub>2</sub>/He: a) Ru/ZrO<sub>2</sub> and b) Ru/ZrO<sub>2</sub>-MgO. The first spectrum from top to bottom corresponds to the catalyst before CO<sub>2</sub> admission. The total time was set to 30 min. Inlet gas flow conditions after switch (second spectrum from top to bottom): 4 ml min<sup>-1</sup> CO<sub>2</sub>, 26 ml min<sup>-1</sup> He.

In summary, the in-situ IR measurements during reaction and during dynamic experiments allowed to distinguish the role of bi-dentate formate as intermediate of active Ru-CO species. Particularly, the behavior of the species with absorption ca. 2060 cm<sup>-1</sup> (associated with electronically modifies sites) correlated with CH<sub>4</sub> evolution. In contrast, the carbonyl species with vibrations below this value, e.g., Ru<sub>2</sub>-CO, and have been found inert for CH<sub>4</sub> evolution, according to other investigations.<sup>97, 195</sup> Moreover, the stability of the active Ru-CO was controlled by the presence of MgO. The reason that might explain this behavior is the facile electron transfer from the support to Ru sites. Back-donation of electrons from metal d-orbitals to the anti-bonding orbital of adsorbed CO ( $d(M) \rightarrow \pi^*(CO)$ ) might result in strengthened metal-carbon (M-CO) bonding while weakening the C≡O bonding,<sup>60, 100</sup> increasing its instability. Surprisingly, on Ru/TiO<sub>2</sub>-SG, also a Ru-CO signal ca. 2060 cm<sup>-1</sup> was detected and was the main difference with Ru/TiO<sub>2</sub>-imp catalyst (**Figures 27 and 28**). However, on the highly active Ru/TiO<sub>2</sub>-SG its intensity was too low to unambiguously relate it with CH<sub>4</sub> evolution.

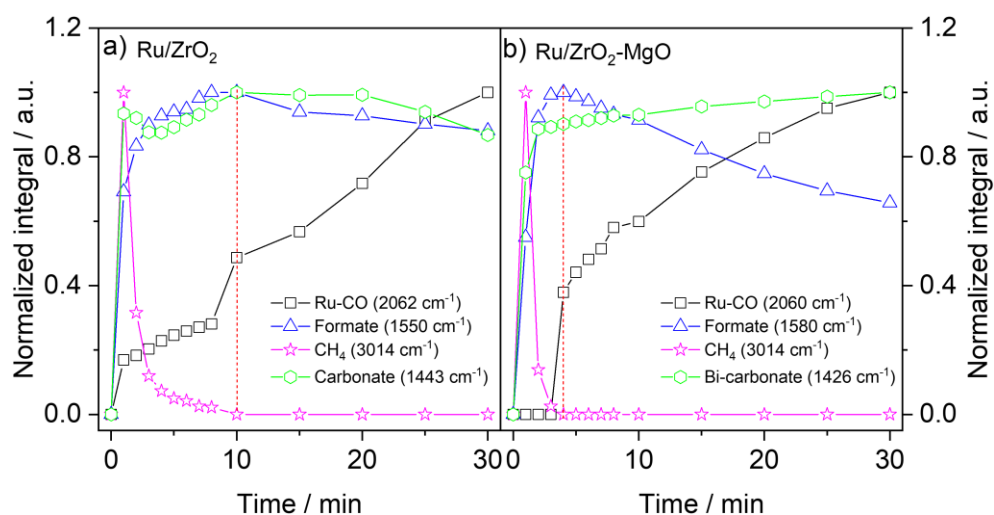


**Figure 41.** Normalized integral decay of the bands resolved in the spectra recorded at 250 °C during the dynamic experiment presented in **Figure 40**. a) Ru/ZrO<sub>2</sub> and b) Ru/ZrO<sub>2</sub>-MgO. The normalization was referred to the intensity of the maximum of respective band after the admission of CO<sub>2</sub> to the reaction cell. The red dotted line indicates the coincidence between the maximum intensity of the formate with the stepped increase of the CH<sub>4</sub> active Ru-CO band. The total time was set to 30 min. Inlet gas flow conditions after switch: 4 ml min<sup>-1</sup> CO<sub>2</sub>, 26 ml min<sup>-1</sup> He.

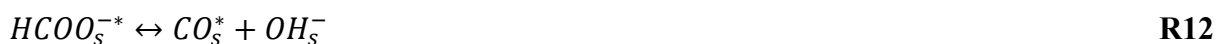
**Reactivity-structure relationships:** Complementary spectroscopy assessments provided extra information of the enhanced Ru-support interaction in presence of MgO. The following observations summarize the main findings in this study:

- i) EPR measurements evidenced that extra O-vacancies/Zr<sup>3+</sup> sites were present in the MgO containing support. These species might easily release electrons to the periphery, e.g., neighboring Ru sites. This was evidenced by the absence of a Zr<sup>3+</sup> signal in Ru/ZrO<sub>2</sub>-MgO after reaction, while it was still resolved in Ru/ZrO<sub>2</sub> catalyst at the same conditions. Furthermore, the presence of an additional signal in the spent Ru/ZrO<sub>2</sub>-MgO catalyst ( $g = 2.008$ ) was an indication of the facilitated interaction between electrons released from paramagnetic centers to surrounding species. Analogously, such a signal was not resolved in the case of Ru/ZrO<sub>2</sub>.
- ii) In-situ DRIFT spectra suggested the same source of CH<sub>4</sub> in both catalysts, i.e., Ru-CO species with a vibrational frequency in the range 2064 – 2055 cm<sup>-1</sup> that was produced from bidentate formate (b-HCOO<sup>-</sup>) species. However, the stability of the involved species was found different. First, b-HCOO<sup>-</sup> showed a higher O-C-O asymmetric stretching frequency  $\nu_{as}(\text{O-C-O})$  on the Ru/ZrO<sub>2</sub>-MgO catalyst, likely due to the interaction between one O atom with Mg<sup>2+</sup> replacing Zr<sup>4+</sup>. Second, the promoted release of electronic charge from MgO-ZrO<sub>2</sub> paramagnetic centers to Ru sites strengthened Ru-C while facilitating the breaking of the C≡O bonding of

carbonyl intermediate. The high reactivity of intermediates helps to keep a larger fraction of active sites available for reaction.

- iii) H<sub>2</sub>-TPR suggested the more pronounced interaction between RuO<sub>x</sub> and the MgO containing support as higher temperatures were required to reduce the oxidic Ru. HAADF-STEM micrographs and EDX spectroscopy as well as ex-situ XPS corroborated this effect by suggesting a major dispersion of Ru/RuO<sub>2</sub> after reaction.
- iv) N<sub>2</sub> physisorption measurements determined a larger surface area of the MgO modified materials, which correlated also with the enhanced dispersion of the supported metal after heating.
- v) XRD patterns suggested the formation of a solid solution between ZrO<sub>2</sub> and MgO, i.e., effective incorporation of Mg<sup>2+</sup> in the lattice of ZrO<sub>2</sub> that resulted in the enhanced presence of support defects.

Mechanisms for CO<sub>2</sub> methanation on distinct Ru based catalysts propose that HCOO<sup>-\*</sup> acts as carbonyl source,<sup>129, 182, 228</sup> e.g., following the equilibria in reaction **R12**.<sup>129</sup> In the present case, we also would expect that the reactive Ru-CO (~ 2060 cm<sup>-1</sup>) to come from formates that form at the support near Ru atoms at the metal support interphase (MSI) (reactions **R12** and **R13**). As already determined, the rate at which the resulting carbonyl is further hydrogenated to CH<sub>4</sub> is controlled by the local electronic charge released from O-vacancies/Zr<sup>3+</sup> centers neighboring the respective Ru atom.<sup>22</sup>



Moreover, similar to Ru-CO bonding, the higher band vibration frequency of O-C-O  $\nu_{as}$  (1574 cm<sup>-1</sup>) in case of Ru/ZrO<sub>2</sub>-MgO when compared to Ru/ZrO<sub>2</sub> (1558 cm<sup>-1</sup>) might also be associated with the distinct activity of the catalysts. This observation coincides with NAP-XPS results of Ru/TiO<sub>2</sub>, that showed that formate-like species became less stable at the same time as CH<sub>4</sub> rate increased on a highly active O-vacancy enriched Ru/TiO<sub>2</sub> catalyst. It can be thus expected that the promotion in the methane activity of Ru/ZrO<sub>2</sub>-MgO is given by the modification in the stability of bidentate formate due to interaction of one of the O atoms of CO<sub>2</sub> via a weaker bond with modified metal sites from the support, e.g., Mg<sup>2+</sup> instead of Zr<sup>4+</sup>. Meanwhile, the other O atom would occupy an O-vacancy. A representation of the bidentate formate in both situations is shown in **Figure 42**. The weaker the O-M bond the higher the vibration frequency of O-C-O.

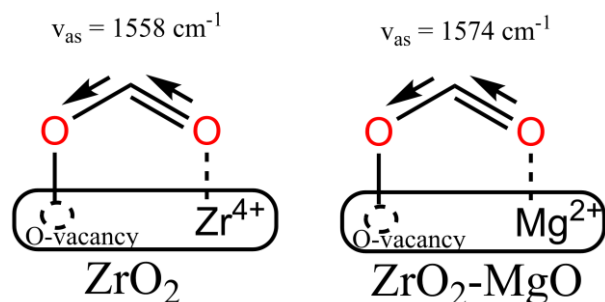


**Figure 42.** Representation of b-HCOO adsorbed on Ru/ZrO<sub>2</sub> and Ru/ZrO<sub>2</sub>-MgO (Ru not shown) and the corresponding  $\nu_{as}(\text{O-C-O})$  as determined by DRIFTS during reaction at 250 °C.

The faster rupture of the weaker O-C-O bonding on Ru/ZrO<sub>2</sub>-MgO catalyst might facilitate the formation of the highly reactive Ru-CO. Accordingly, a proposal of the structure-activity relationship is represented in **Figure 43**, which illustrates the steps from CO<sub>2</sub> adsorption until Ru-CO formation.

Another route that might lead to M-CO is the carbide pathway, initiated by the direct activation of CO<sub>2</sub> on the metal phase ( $\text{CO}_2 \rightarrow \text{CO}^* + \text{O}^*$ ).<sup>41, 118, 229</sup> However, this mechanism has normally not proposed for precious (Ru, Pd) based catalysts.<sup>97, 112, 129, 182</sup> Furthermore, our spectroscopic evidence supports the formate pathway. Yet, it is possible that alternative routes could also be operative although not detectable by the used techniques and must not be discarded.

The activation of the C-O bond is a structure-sensitive reaction, which means that, the rate is affected by the size of the Ru nanoparticles. The amount of active sites depends on this parameter and eventually, a maxima in the rate as a function of particle size might be observed.<sup>230</sup> Similar effect was reported for CO<sub>2</sub> methanation on distinct Ru/CeO<sub>2</sub> catalysts. For supported Ru particles of ca. 1 nm size optimal CH<sub>4</sub> activity was detected, while for larger particles of ca. 4 nm the activity decreased.<sup>70</sup> Our results are consistent with this trend, showing higher activity on the catalyst with better dispersion. That is, the enhanced methane rate upon MgO modification was the result of two effects: i) the bigger number of active sites formed on the extended metal-support perimeter and ii) changes in the adsorptive/electronic properties which depend on the concentration of O-vacancies. Since CO binding energy (chemisorption) is regarded as the key descriptor for this reaction,<sup>17, 118, 182</sup> this electronic effect is expected to predominate over geometric/structural effects for the enhancement of CH<sub>4</sub> formation.

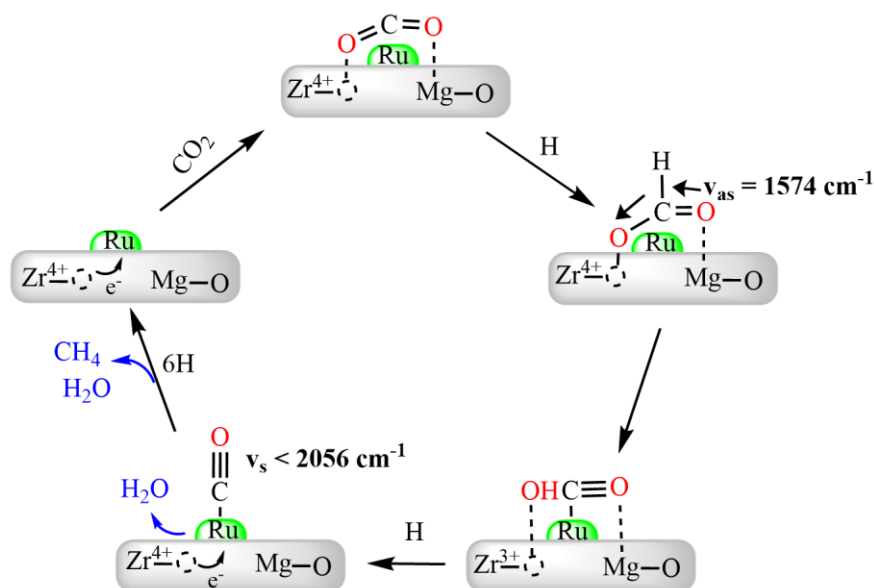


**Figure 43.** Proposed mechanism for CO<sub>2</sub> adsorption, b-HCOO\* and Ru-CO formation on Ru/ZrO<sub>2</sub>-MgO. Further steps of Ru-CO hydrogenation to CH<sub>4</sub> are not shown. Dashed circle represents O-vacancy.

### 3.3. Summary of results of CO<sub>2</sub> methanation on Ru catalysts

The methanation of CO<sub>2</sub> was performed on catalysts with relative low loading of Ru, i.e., below 1 wt.%. It was possible to highlight the importance of O-vacancies and to identify the nature of elusive intermediates during this reaction. Upon multiple spectroscopic techniques, it was shown how the electronic modification of the perimeter leads to changes in the chemisorption properties, boosting the methanation activity despite the minimized Ru concentration on the catalysts.

First, Ru/TiO<sub>2</sub> catalysts were investigated. Two catalysts with Ru around 0.9 wt.% were prepared by two different routes, i.e., sol-gel and wetness impregnation. Both catalysts showed 100 % selectivity for CH<sub>4</sub>, yet the rates were very different. The Ru-mass normalized reaction rate and TOF of Ru/TiO<sub>2</sub>-SG resulted superior and even surpassed the values reported for other Ru/TiO<sub>2</sub> catalysts. Already at a temperature as low as 200 °C, TOF was found to be at least 400 % higher than that of catalysts with higher more Ru contents under similar conditions. This superior methane activity was associated with the creation of strongly interacting O-vacancy-Ru<sup>0</sup> sites at the metal-support perimeter interface. Although the results demonstrated the suitability of the sol-gel preparation route for obtaining unique structural and electronic effects, required for maximizing the catalytic performance while minimizing the noble metal contents, the fast transformation of intermediates to CH<sub>4</sub> complicated the identification of the chemical identity of key intermediates.

Accordingly, a second study was performed by using catalysts with moderate activity. However, again the modification in the contribution of O-vacancies played a central role. Hence, two catalysts for the hydrogenation of CO<sub>2</sub> were prepared following a simple wet impregnation method, using ZrO<sub>2</sub> and MgO modified ZrO<sub>2</sub> as support. The Ru loading was similar in both cases (ca. 0.4 wt%). An enhancement in the CH<sub>4</sub> activity upon incorporation of MgO by ca. 3-fold in a Ru mass normalized basis was observed. This better activity was attributed to changes in the stability of CH<sub>4</sub> intermediates governed by electronic interactions at the metal-support interface, more pronounced upon increasing Ru dispersion on the most O-defective material. The fast process of bidentate formate decomposition to CO and its further fast hydrogenation to methane ( $\text{b-HCOO}^-_{\text{ads}} \rightarrow \text{CO}_{\text{ads}} \rightarrow \text{CH}_4$ ) helped to keep a larger fraction of available active sites than in the case of the unmodified Ru/ZrO<sub>2</sub>.

### 3.4. The RWGS reaction on ultra-low Au loaded Au/TiO<sub>2</sub> and Au/ZrO<sub>2</sub> catalysts

In **section 1.1** the potential relevance of the RWGS reaction in the context of Power to X was discussed together with the suitability of Au based catalysts for this reaction. Also, the need to minimize the Au loading to assure competitiveness of this type of catalyst was highlighted. Herein, the role of O-vacancies on two reducible supports, i.e., TiO<sub>2</sub> and ZrO<sub>2</sub> has been explored as an approach to produce highly active and selective RWGS catalysts with ultra-low supported Au amount.

**Supports and catalysts characterization:** The Au loading, the specific surface area, average pore size, and total pore volume of the samples (catalysts and supports) are listed in **Table 12**. It was observed that the after addition of Au, the specific surface areas were virtually equal. Same could be said regarding the average pore sizes of the supporting oxides.

**Table 12.** Structural properties of pure supports and gold catalysts

Sample	Au loading / wt. %	BET SSA / m <sup>2</sup> g <sup>-1</sup>	Pore diameter / nm	Pore volume / cm <sup>3</sup> g <sup>-1</sup>
TiO <sub>2</sub>	-	62	21	0.42
Au/TiO <sub>2</sub>	0.05	66	19	0.40
ZrO <sub>2</sub>	-	79	4.2	0.12
Au/ZrO <sub>2</sub>	0.08	81	4.3	0.12

An obvious difference between Au/TiO<sub>2</sub> and Au/ZrO<sub>2</sub> was observed in the size and volume of the pores. N<sub>2</sub> adsorption-desorption isotherms are shown in **Figure 44a, b**. TiO<sub>2</sub> and

Au/TiO<sub>2</sub> exhibited typical Type II isotherms macroporous materials<sup>156, 165</sup> (**Figure 44a**). Meanwhile type - IV isotherms for ZrO<sub>2</sub> and Au/ZrO<sub>2</sub> with hysteresis loops, indicating the mesoporous nature of these samples,<sup>156</sup> were observed in **Figure 44b**. Such hysteresis loops in all cases may be attributed to N<sub>2</sub> condensation in the corresponding pores. The possible incidence of this structural difference in the catalytic behavior is discussed in the next subsection.

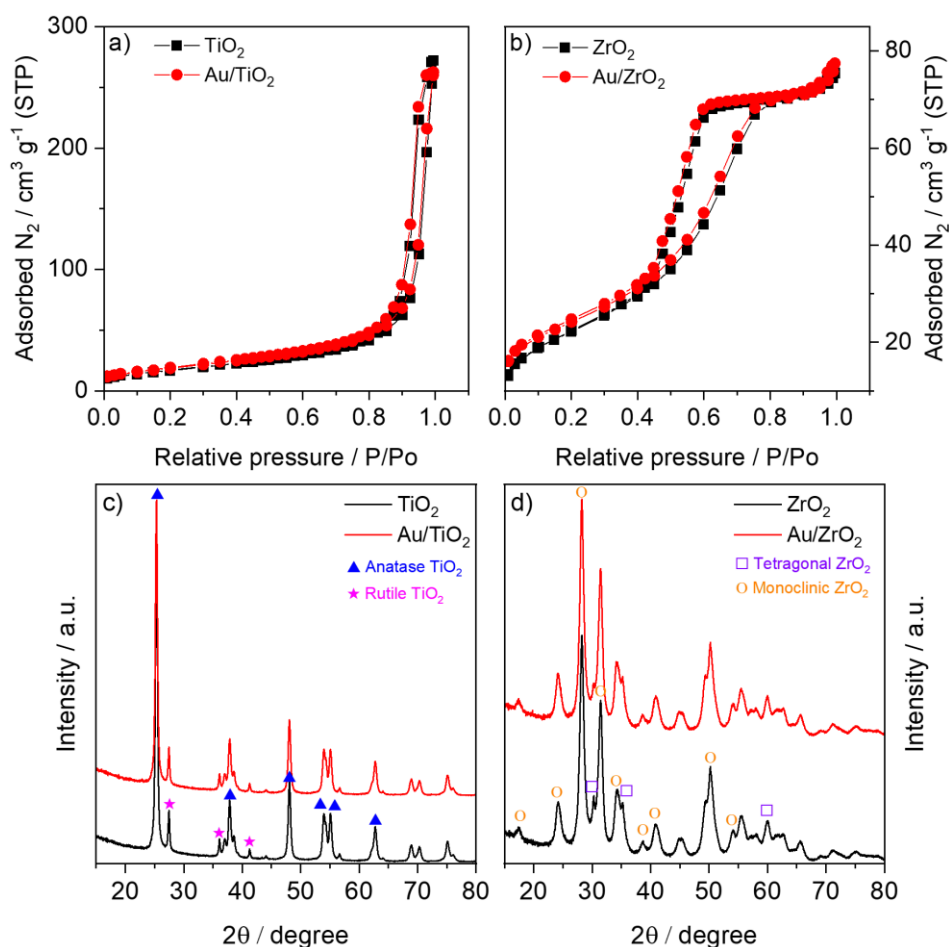


**Figure 44.** N<sub>2</sub> adsorption isotherms of a) fresh bare TiO<sub>2</sub> and Au/TiO<sub>2</sub>; b) fresh bare ZrO<sub>2</sub> and Au/ZrO<sub>2</sub>; c) XRD powder patterns of the fresh TiO<sub>2</sub> support and fresh Au/TiO<sub>2</sub> catalyst; d) XRD powder patterns of the fresh ZrO<sub>2</sub> support and fresh Au/ZrO<sub>2</sub> catalyst.

The XRD patterns of TiO<sub>2</sub>, ZrO<sub>2</sub>, and the corresponding Au-loaded catalysts are shown in **Figure 44c, d**. The crystal structure of TiO<sub>2</sub> was a mixture of anatase and rutile (**Figure 44c**). The reflections at 2 $\theta$  25.5, 37.5, 47.8, 53.8, 54.9 and 62.8° were assigned to the anatase structure. Meanwhile the reflections at 2 $\theta$  27.5 and 36.4° were associated to rutile structure.<sup>228</sup> Both bare TiO<sub>2</sub> and Au/TiO<sub>2</sub> samples exhibited the same diffraction pattern without obvious changes. Same situation was determined for the XRD patterns of ZrO<sub>2</sub> and Au/ZrO<sub>2</sub> (**Figure**



**44d**). These last were characterized by the presence of a mixed phase of tetragonal (30.2, 35.3, and 60.2°) and monoclinic (17.5, 24.2, 28.2, 31.5, 34.2, 38.5, 40.7, 50.1, and 54.1°) phases.<sup>231</sup> No reflections related to Au particles were resolved in the patterns of the catalysts, as expected for such low Au contents.

HAADF-STEM was used to probe the existence of gold entities with different sizes, i.e., nanoparticles (NPs), clusters, and single-sites. Representative STEM images of the Au/TiO<sub>2</sub> catalyst are shown in **Figure 45a-c**. Au species existed almost exclusively as small nanoparticles with an average particle size of 2-3 nm (for more images, see **Figure A15**). Due to the low particle density, it was not feasible to acquire sufficient data for statistical analysis. On the other hand, representative HAADF STEM images of the Au/ZrO<sub>2</sub> catalyst are shown in **Figure 45d-f**. According to the high-magnification image (**Figure 45e, f**), many well dispersed bright dots were detected on the surface of zirconia, indicating that most of the Au species were distributed as single sites. For clarity, some Au atoms are indicated by cyan arrows (**Figure 45e, f**). A minor fraction of Au species was also found as Au NPs and clusters (**Figure A16**).

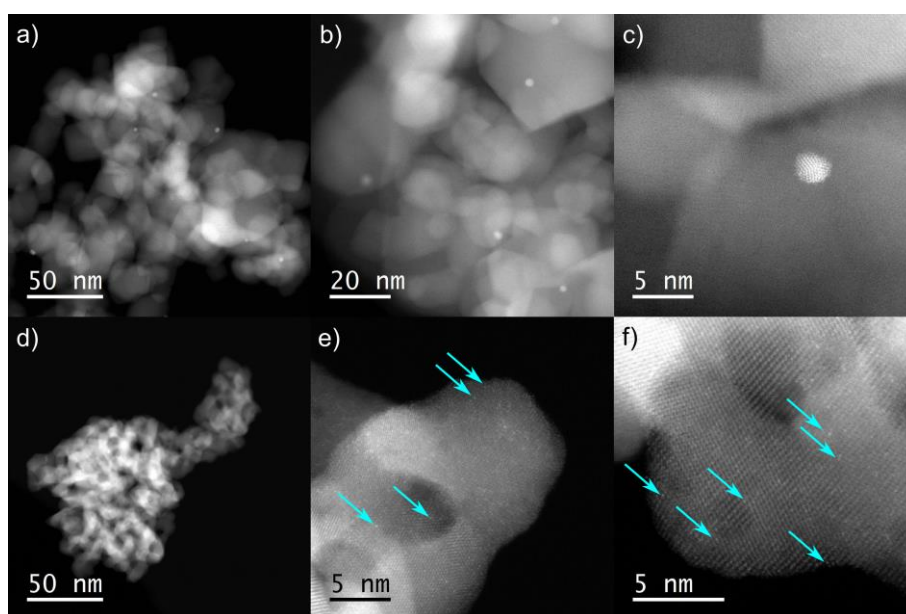


**Figure 45.** HAADF STEM images of the (a-c) Au/TiO<sub>2</sub> and (d-f) Au/ZrO<sub>2</sub> catalysts.

EELS measurements were only performed to investigate the electronic structure of the Au/TiO<sub>2</sub> catalyst (energy loss levels for Zr are not suitable for such an analysis.). EEL spectra of the catalyst before reaction were collected over the central and interface/surface region of the particles, as marked in **Figure 46**. EELS oxidation state maps have been calculated from the spectrum imaging dataset by multiple linear least square fits of model spectra from reference areas marked as “1” and “2” in **Figure 46a**. The oxidation state map of Ti (**Figure 46b**)

suggested that the interface and edge regions of the particles are dominated by  $\text{Ti}^{3+}$ . The contrast gradient indicated a shell-like distribution. The spectra showed a difference in the fine structure of the Ti  $L_{2,3}$ -edge (**Figure 46c**) which revealed the presence of two distinct Ti species. In the bulk region (red) the typical split of the  $L_{2,3}$  signal was similar to the Ti  $L_{2,3}$ -edge fingerprint of the rutile structure in which Ti species exists as  $\text{Ti}^{4+}$ .<sup>232, 233</sup> In contrast, at the interface region, the spectrum (cyan) contained two not split peaks, indicating the potential presence of  $\text{Ti}^{3+}$  species.<sup>232</sup>

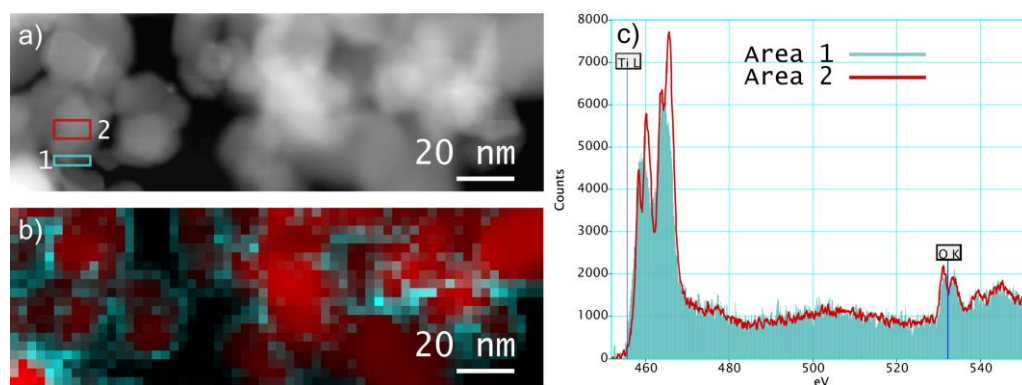


**Figure 46.** a) STEM-ADF image of the fresh Au/TiO<sub>2</sub> catalyst depicting the area used for spectral imaging; b) the corresponding EELS phase maps of  $\text{Ti}^{4+}$  (red) and the unknown surface species (cyan); c) EELS obtained in the two positions marked in a) with the corresponding color.

HAADF and EELS measurements were also performed for the spent Au/TiO<sub>2</sub> catalyst after 158 h (**Figure 47**). No notable changes in the Au particle size were visible. EELS-based elemental mapping revealed the presence of carbon at the interface/surface (yellow color), indicating the existence of strongly adsorbed carbon containing species (e.g., carbonate and formate species) and/or formation of a small amount of deposited carbon after reaction.

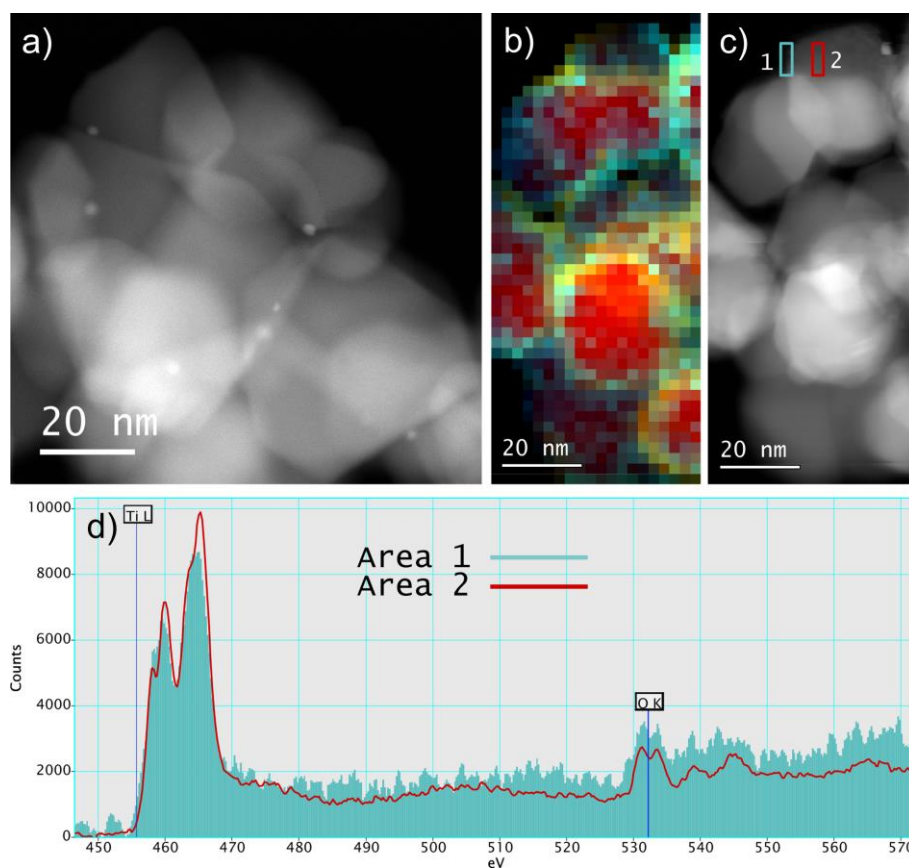


**Figure 47.** a) STEM-HAADF image of the spent Au/TiO<sub>2</sub> catalyst; b) EELS oxidation state and elemental maps with Ti<sup>4+</sup> in red, the potential Ti<sup>3+</sup> phase in cyan and carbon in yellow; c) corresponding STEM-ADF image of spectrum imaging region with marks for the extracted spectra; d) EELS spectra obtained in the two positions marked in c) with corresponding colors.

***Activity assessments:*** The catalytic performance for the RWGS reaction was evaluated in the temperature range of 250 to 350 °C (**Figure 48**). At 250 °C Au/TiO<sub>2</sub> showed a CO<sub>2</sub> conversion of 4.6%. In contrast, Au/ZrO<sub>2</sub> showed a poor CO<sub>2</sub> conversion of only 0.8 % at that temperature. For both catalysts, the conversion increased monotonically as the reaction temperature increased from 250 to 350 °C, being ca. 3-fold higher on Au/TiO<sub>2</sub> (**Figure 48a**). Furthermore, while on this last catalyst the selectivity to CO sustained at 100 %, on Au/ZrO<sub>2</sub> such high selectivity was reached only at 350 °C (**Figure 48b**). The rate of CO formation over the Au/TiO<sub>2</sub> catalyst at 250 °C was 69 mmol.g<sup>-1</sup><sub>Au</sub>.min<sup>-1</sup>, which is almost 10 times higher than that over Au/ZrO<sub>2</sub> catalyst (6.8 mmol.g<sup>-1</sup><sub>Au</sub>.min<sup>-1</sup>) (**Figure 48c**). The activity of Au/TiO<sub>2</sub> raised to ~ 216 mmol.g<sup>-1</sup><sub>Au</sub>.min<sup>-1</sup> when the temperature increased to 350 °C. As seen, the differences in activity are clear.

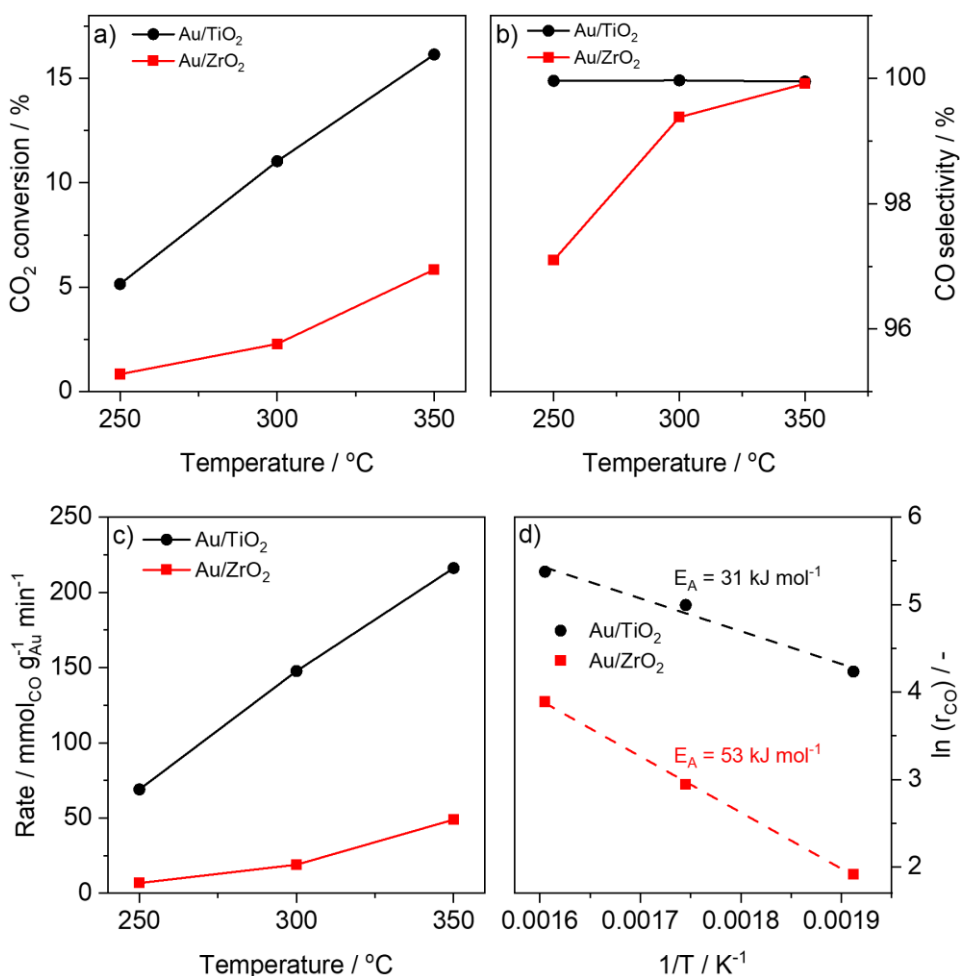


**Figure 48.** a) CO<sub>2</sub> conversion; b) CO selectivity; c) rate of CO formation as a function of the testing temperature on the supported Au catalysts; d) Arrhenius plots of the rate of CO formation in the temperature range 250–350 °C, over Au/TiO<sub>2</sub> (black) and Au/ZrO<sub>2</sub> (red). Reaction conditions: P<sub>total</sub> = 3 bar, CO<sub>2</sub>: H<sub>2</sub>: N<sub>2</sub> = 1:3:2, 17.5 ml min<sup>-1</sup>.

Considering the very low Au loading, the intrinsic activity of this Au/TiO<sub>2</sub> is much higher than that of other Au-based catalysts (**Table 2**) and is by ca. 2-fold that of Cs modified Ni/CeO<sub>2</sub> (10 wt.% Ni) at the same temperature.<sup>117</sup> That is, the current Au/TiO<sub>2</sub>, even surpasses the activity of RWGS catalysts with 200 times higher load of active metal.

The apparent activation energy over both catalysts was determined between 250 and 350 °C (**Figure 48d**). On Au/TiO<sub>2</sub> this was 31 kJ mol<sup>-1</sup>, which is the same value previously reported for a 1 wt% Au/TiO<sub>2</sub> catalyst.<sup>28</sup> In contrast, for Au/ZrO<sub>2</sub> the E<sub>A</sub> was estimated ca. 2-fold higher (53 kJ mol<sup>-1</sup>). Such distinct apparent activation energies may suggest a change in the reaction pathways and thereby different rate-determining steps. The CO<sub>2</sub> conversions at the conditions for E<sub>A</sub> calculations were well below 20 % for both catalysts (**Figure 48a**), thus the process occurred under kinetic control and diffusional limitations can be discarded.

As diffusion effects seem to be neglective the very different pore structures (see **Table 11**) might play a minority role. Analogously to CO<sub>2</sub> methanation the promotion in the activity can be associated with differences in the metal-support interactions. On the one hand, HAADF-STEM demonstrated big differences in the Au particle size (**Figure 45**). On the other hand, the almost half E<sub>A</sub> of Au/TiO<sub>2</sub>, which points to mechanistic differences in the route to CO evolution, is another indication of big contrast between the chemisorption properties (electronic properties) of these two materials. This is deeply analyzed below upon XPS, TAP, DRIFTS and EPR assessments.

The catalysts were also evaluated at conditions at which the CH<sub>4</sub> evolution could be thermodynamically favored. Therefore, catalytic tests were carried out at 20 bar with H<sub>2</sub>:CO<sub>2</sub> ratio of 3:1 (**Figure 49**). On Au/ZrO<sub>2</sub> the CO<sub>2</sub> conversion was almost twice that obtained at 3 bar for T ≥ 300 °C, while for Au/TiO<sub>2</sub> the conversion was not affected by the pressure increase. Meanwhile, no changes in CO selectivity were noticed in any case. Analogously to the test at 3 bar, this experiment was also carried out at differential reaction conditions (kinetic control). With this in mind, the enhanced activity of Au/ZrO<sub>2</sub> at 20 bar could be explained by the increased coverage of carbon-containing intermediates. The depreciable effect in CO selectivity with the increase in pressure over both catalysts can be explained by the weak adsorption of the formed CO on Au sites and supports, as proven later by the TAP experiments.

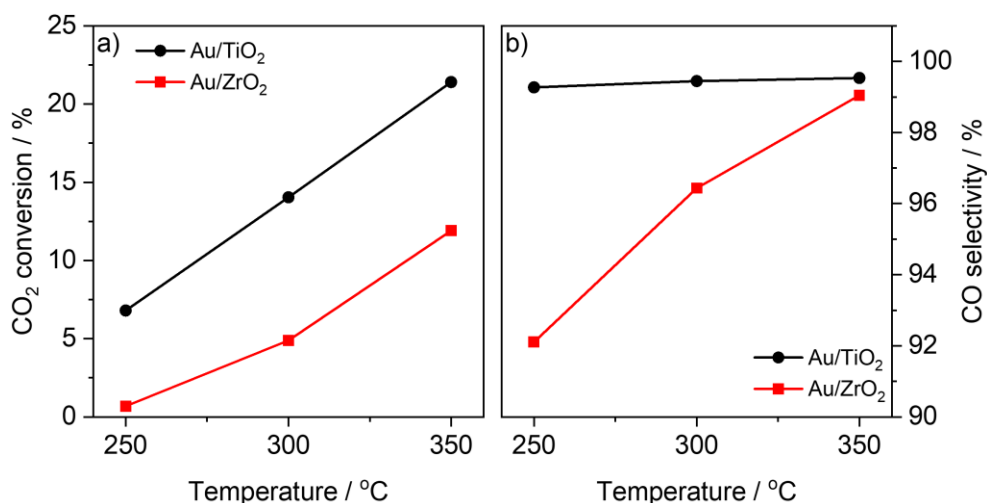


**Figure 49.** a) CO<sub>2</sub> conversion and b) CO selectivity as a function of the testing temperature on the supported Au catalysts. Reaction conditions: P<sub>total</sub> = 20 bar, CO<sub>2</sub>: H<sub>2</sub>: N<sub>2</sub> = 1:3:2, 17.5 ml min<sup>-1</sup>.

**XPS assessments:** The chemical nature of gold species was investigated via the Au 4f XP spectra of the catalysts (**Figure 50**). The binding energies of Au 4f<sub>7/2</sub> in the XP spectra of Au/TiO<sub>2</sub> and Au/ZrO<sub>2</sub> were found to be 83.4 and 83.9 eV, respectively. The binding energy

(BE) for Au<sup>0</sup> is ca. 84.0 eV.<sup>234</sup> That is, in case of Au/ZrO<sub>2</sub>, the oxidation state of Au particles was closer to the metallic character. The lower BE in case of Au/TiO<sub>2</sub>, by ca. 0.5 eV, might be correlated with the presence of partially negative supported Au species (Au<sup>δ-</sup>). Such a change can be induced by charge transfer from the oxygen vacancies surrounding Au on TiO<sub>2</sub>. Similar effect was already reported by Wang et al. for distinct Au/TiO<sub>2</sub> catalysts.<sup>235</sup> In that case it was observed that when Au was supported on a highly defective support, the Au particles adopted a partial negative charge. As the size of Au was dependent on the support (**Figure 45**), it might also be reasonable to assign the shift to final state effects, e.g., screening and delocalization of the hole formed during the photoionization of the core electrons.<sup>236</sup> Hence direct comparison of the shift in BE for different dispersions might in principle not be completely reasonable. However, in-situ EPR assessments (**Figures 55 and 56**) suggest that the transfer of electrons from O-defects to Au in Au/TiO<sub>2</sub> was maybe more feasible as in Au/ZrO<sub>2</sub>. That is, the electron delocalization in Au/TiO<sub>2</sub>, i.e., downshift in Au 4f BE might rather be due to the nature of the support rather than to the Au particle size.

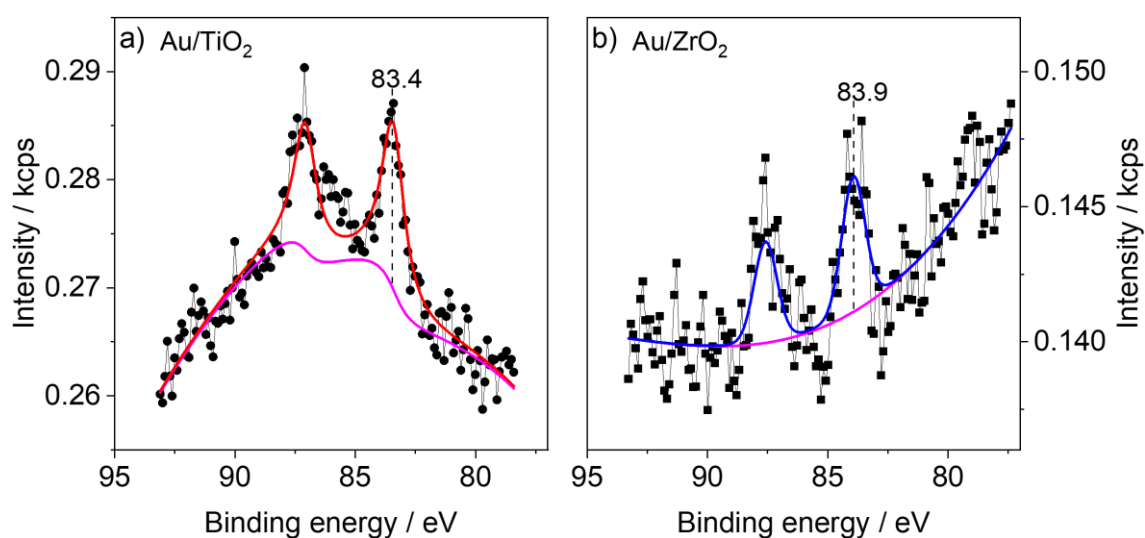


**Figure 50.** Au 4f XP spectra of a) Au/TiO<sub>2</sub> and b) Au/ZrO<sub>2</sub>.

**Single pulse TAP assessments:** The interaction of CO<sub>2</sub> with the reduced catalysts was investigated by injecting a single pulse of a CO<sub>2</sub>/Ar mixture (CO<sub>2</sub>: Ar = 1:1) at 300 °C. A distinct pulse of 100% Ar was used as reference. The dimensionless responses to the respective pulses are shown in **Figure 51**. In both cases no gas-phase CO could be observed. This unambiguously revealed that CO<sub>2</sub> cannot dissociate to CO under such conditions. Later, it is shown that this observation was also consistent with the in-situ DRIFT studies (**Figures 52 and 53**). The shape of the response to the CO<sub>2</sub> pulse on Au/TiO<sub>2</sub> was broader than the respective

response to the Ar pulse (**Figure 51a**). That could be attributed to the desorption and re-adsorption of CO<sub>2</sub>, i.e., moderate interaction of CO<sub>2</sub> with the catalyst.<sup>237</sup> In contrast, the very weak response to the CO<sub>2</sub> pulse on Au/ZrO<sub>2</sub> (**Figure 51b**) suggested a stronger adsorption strength of CO<sub>2</sub> compared to Au/TiO<sub>2</sub>. This difference in the CO<sub>2</sub>-catalyst interaction might correlate with the observed activity behavior of the catalysts. According to the Sabatier principle, the strong interaction of CO<sub>2</sub> with Au/ZrO<sub>2</sub> might decrease its reactivity while for the moderate interaction with Au/TiO<sub>2</sub> a higher activity might be observed. On the other hand, the dimensionless responses to pulses of CO (CO: Ar = 1:1) and Ar over the reduced catalysts revealed no noticeable differences between the catalysts (**Figure 51c, d**). This is a fingerprint for very weak adsorption of CO which might be the reason for the unprecedented CO selectivity observed over both catalysts even at pressure as high as 20 bar (**Figure 49b**).

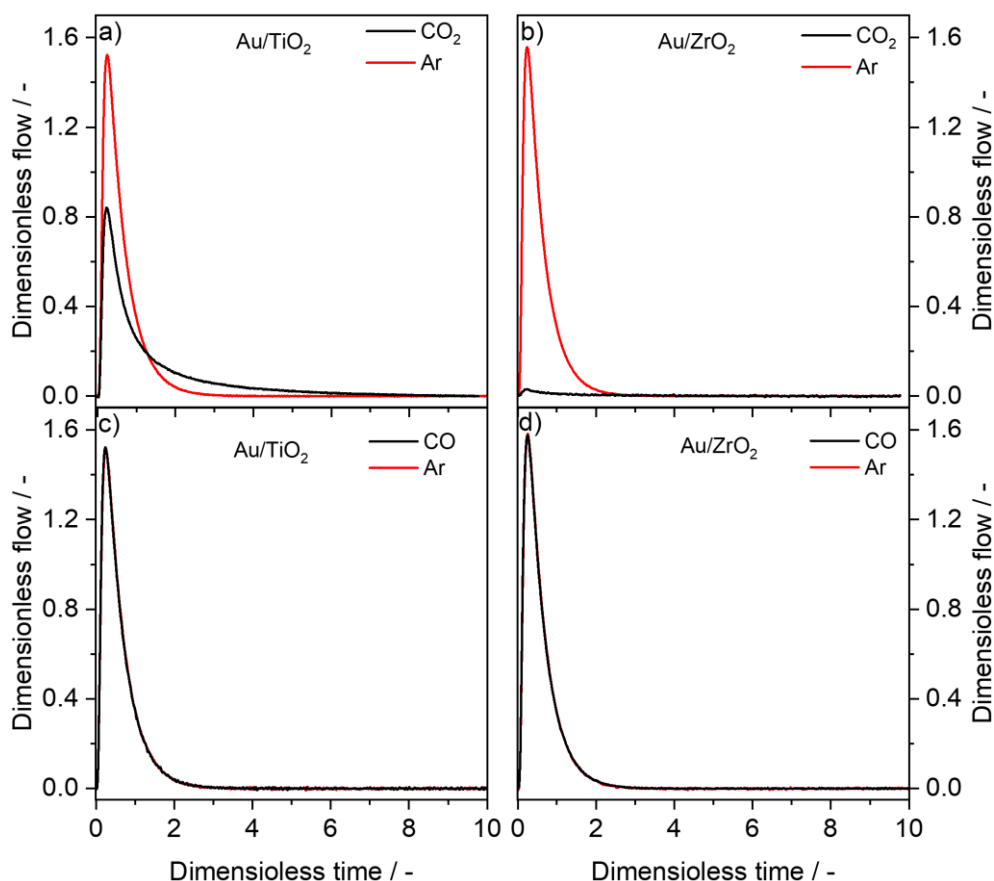


**Figure 51.** Single-pulse responses of CO<sub>2</sub> compared with the Ar response at 573 K over a) Au/TiO<sub>2</sub>; b) Au/ZrO<sub>2</sub>. Single-pulse responses of CO<sub>2</sub> compared with the Ar response at 573 K over c) Au/TiO<sub>2</sub>; d) Au/ZrO<sub>2</sub>.

**In-situ DRIFTS assessments:** In-situ DRIFTS experiments were performed to follow the evolution of adsorbed species during the reaction. The temporal evolution during the reaction at 250 °C and 3 bar is observed in **Figure 52**. For Au/TiO<sub>2</sub> (**Figure 52a**) the spectra

exhibit a doublet centered at  $2142\text{ cm}^{-1}$  typical of gaseous CO. In addition, several bands attributed to the formation of bidentate formate and carbonate species were also resolved. Bands at  $1560$  and  $1357\text{ cm}^{-1}$  were assigned to the asymmetric ( $\nu_{\text{as}}$ ) and symmetric ( $\nu_{\text{s}}$ ) OCO stretching vibrations of adsorbed bidentate formate ( $\text{HCOO}^*$ ) species, respectively.<sup>118, 238-241</sup> Meanwhile the band at  $1380\text{ cm}^{-1}$  was assigned to the CH bending ( $\delta(\text{CH})$ ) vibration of the same species.<sup>118, 238-241</sup> Bands at  $1522$  and  $1339\text{ cm}^{-1}$  can be assigned to the antisymmetric ( $\nu_{\text{as}}$ ) and symmetric ( $\nu_{\text{s}}$ ) OCO stretching vibrations of bidentate/unidentate carbonate ( $\text{CO}_3^{2-}$ ) species, respectively,<sup>238, 241</sup> whereas the band at  $1622\text{ cm}^{-1}$  could be attributed to the formation of bicarbonate or to a  $\delta(\text{OH})$ -vibration of adsorbed water.<sup>242, 243</sup> Carbonate and bicarbonate species are generally generated from the interaction of  $\text{CO}_2$  molecules with the coordinatively unsaturated  $\text{O}^{2-}$  of a metal oxide ( $\text{cus-O}^{2-}$ ) and the surface hydroxyl groups of support respectively.<sup>243, 244</sup>

For Au/ZrO<sub>2</sub> (**Figure 52b**), the bands at  $1580$ ,  $1383$ , and  $1359\text{ cm}^{-1}$  suggested the formation of formate species.<sup>239, 245</sup> Meanwhile, signals at  $1522$  and  $1470\text{ cm}^{-1}$  suggested the existence monodentate carbonates.<sup>118, 238, 243</sup> In addition, the spectra also depicted signals typical for bicarbonate like species ( $\text{HCO}_3^*$ )  $1622\text{ vas}(\text{OCO})$ ,  $1328\text{ vs}(\text{OCO})$ , and  $1223\text{ cm}^{-1}$   $\delta(\text{HOC})$ .<sup>199, 238, 243</sup> These can arise from the interaction of  $\text{CO}_2$  with the surface hydroxyl groups of the ZrO<sub>2</sub> support.<sup>243, 244</sup>

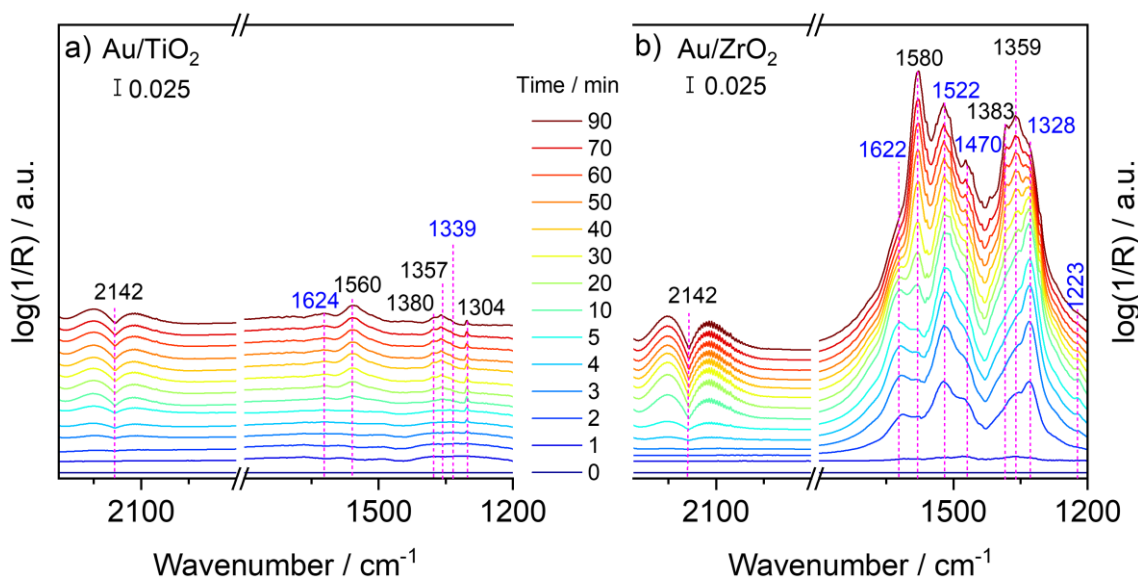


**Figure 52.** In-situ DRIFT spectra of the RWGS reaction over a) Au/TiO<sub>2</sub> and b) Au/ZrO<sub>2</sub> catalysts. Reaction conditions: P = 3 bar, H<sub>2</sub>: CO<sub>2</sub>: N<sub>2</sub> = 3:1:2; total flow rate = 17.5 ml/min, T = 250 °C.



At the beginning of the reaction, carbonate and bicarbonate formed rapidly already after 1 min. With prolonged reaction time, the bicarbonate-related bands (1622 and 1223  $\text{cm}^{-1}$ ) gradually began to decline, while the formate-related bands simultaneously grew. This suggests that the formate species might be formed from the reduction of bicarbonate species, in agreement with previous studies.<sup>28, 97, 246</sup> As the activation of  $\text{H}_2$  over  $\text{ZrO}_2$  is negligible,<sup>243</sup> the reduction of bicarbonate to formate species should occur by activated hydrogen spilled over from the gold species. In contrast, the carbonate and formates bands were barely visible until 10 min on  $\text{Au/TiO}_2$ .

DRIFT experiments were also performed for the bare supports ( $\text{TiO}_2$  and  $\text{ZrO}_2$ ) (**Figure A16**). Remarkably, the intensities were much lower when compared to  $\text{Au/ZrO}_2$ . The significant improvement of  $\text{CO}_2$  adsorption over  $\text{Au/ZrO}_2$  compared with  $\text{ZrO}_2$  might be related to the generation of oxygen vacancies as proved further by in-situ EPR. This observation highlighted the important role of oxygen vacancies for  $\text{CO}_2$  adsorption and activation.

DRIFTS results corroborated the observations of TAP assessments (**Figure 51**). The adsorption of  $\text{CO}_2$  was greatly enhanced on  $\text{Au/ZrO}_2$  in comparison with  $\text{Au/TiO}_2$ . Sakurai et al.<sup>26</sup> attributed this behavior to the difference in the acid-base properties of the supports. They showed that Au NPs supported on acidic oxides, e.g.,  $\text{TiO}_2$ , presented higher  $\text{CO}_2$  conversion than those supported on less acidic supports, e.g.,  $\text{ZrO}_2$ .<sup>26</sup> The relatively strong adsorption of  $\text{CO}_2$  on less acidic supports like  $\text{ZrO}_2$  resulted in a lower  $\text{CO}_2$  hydrogenation activity.<sup>26</sup>

Further experiments were also performed at 300 and 350  $^\circ\text{C}$  (**Figure 53**). The spectra were compared with those obtained at 250  $^\circ\text{C}$  at steady state. On both catalysts, with the increase in temperature from 250 to 350  $^\circ\text{C}$ , the signal intensity of bidentate formate species gradually decreased. In contrast, the signals related to bidentate/unidentate carbonates increased. These results indicated that the formate species could be intermediate species during the reaction whereas carbonates may act as spectators. Nevertheless, it is important to note that the intensities of the formate species on  $\text{Au/TiO}_2$  (**Figure 53a**) remained much lower than on  $\text{Au/ZrO}_2$  (**Figure 53b**). Hence, it seems obvious from DRIFTS that a formate mechanism might not be the main reaction pathway on  $\text{Au/TiO}_2$ . This is in agreement with spectrokinetic investigations on  $\text{Pt/CeO}_2$  catalysts, that concluded minor role of formates in the evolution of  $\text{CO}_{(\text{g})}$  during the RWGS reaction.<sup>247</sup>

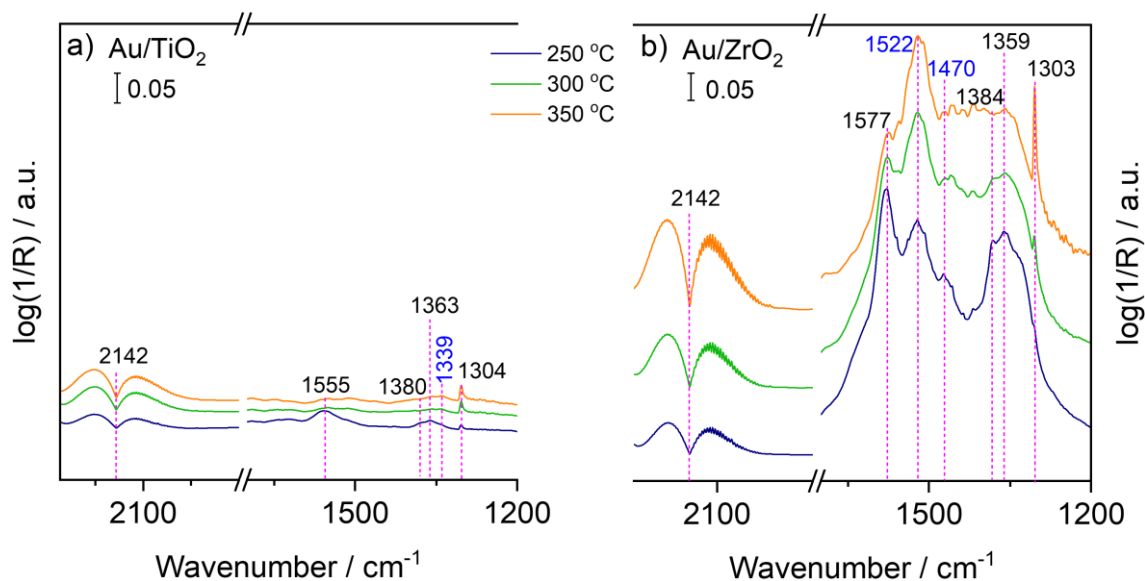


**Figure 53.** In-situ DRIFT spectra of the RWGS reaction over a) Au/TiO<sub>2</sub> and b) Au/ZrO<sub>2</sub> catalysts. Reaction conditions: P = 3 bar, H<sub>2</sub>: CO<sub>2</sub>: N<sub>2</sub> = 3:1:2; total flow rate = 17.5 ml/min.

A summary of the in-situ DRIFTS signals is seen in **Table 13**.

**Table 13.** Infrared absorption bands and assignments for adsorbate species observed during RWGS reaction on Au/TiO<sub>2</sub> and Au/ZrO<sub>2</sub> catalysts.

Surface species	Wavenumber / cm <sup>-1</sup>	Assignment	Reference
CO <sub>(g)</sub>	2142		
Bicarbonate	1622 – 1618	ν <sub>as</sub> (OCO)	242, 243
Bidentate formate	1359 – 1357	ν <sub>s</sub> (O-C-O)	118, 238-241
	1580 – 1560	ν <sub>as</sub> (O-C-O)	
	1383 – 1380	δ(CH)	
Carbonate/Bicarbonate	1522	ν <sub>as</sub> (O-C-O)	199, 238, 243
	1339 – 1328	ν <sub>s</sub> (O-C-O)	
	1322	δ(HOC)	

***In-situ EPR assessments:*** The spectrum of TiO<sub>2</sub> (**Figure 54a**) showed two EPR signals. One isotropic signal at  $g_{\text{iso}} = 2.003$  associated to the formation of O-vacancies with single trapped electrons<sup>185, 228</sup> and a second axial signal with  $g_{\perp} = 1.976$  and  $g_{\parallel} = 1.926$  attributed to the formation of Ti<sup>3+</sup> sites.<sup>188, 228, 248</sup> After reduction with H<sub>2</sub>, the signal intensity of O-vacancies and Ti<sup>3+</sup> slightly increased. With the feeding of the CO<sub>2</sub>/H<sub>2</sub> mixture (spent form), the vacancy signal strongly increased. In contrast, no appreciable change in the EPR signals of Ti<sup>3+</sup> was observed, suggesting that O-defects mostly trapped the unpaired electrons. This was more pronounced after reaction due to the exposure of the catalyst to hydrogen-rich atmosphere (75% H<sub>2</sub>) for further 2 h. In case of Au/TiO<sub>2</sub> (**Figure 54b**) it is important to note that the intensity of the oxygen vacancy signal was much lower as in the case of bare TiO<sub>2</sub> (**Figure 54a**) while the

axial signal of  $\text{Ti}^{3+}$  sites at  $g_{\perp} = 1.973$  became much stronger together with a broadening in the parallel component  $g_{\parallel} = 1.905$ . This indicated that Au nanoparticles significantly boosted the generation of different  $\text{Ti}^{3+}$  species by  $\text{H}_2$  activation and subsequent spillover to the  $\text{TiO}_2$  support. On the second hand, this information also suggests the possibility of electron transfer from oxygen vacancies to gold sites located at the perimeter interphase. This is consistent with XPS results which proved the formation of electron-enriched Au species ( $\text{Au}^{\delta-}$ ). After the reaction, the intensity of the  $\text{Ti}^{3+}$  signal slightly decreased, pointing to the partial transformation of  $\text{Ti}^{3+}$  to  $\text{Ti}^{4+}$  by re-filling the oxygen vacancies with  $\text{CO}_2$ .

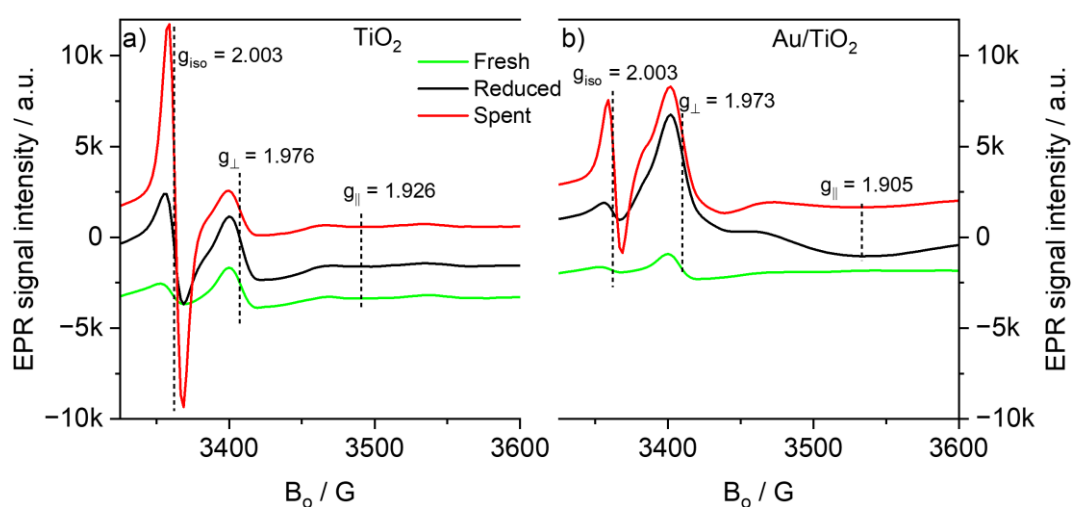


**Figure 54.** In-situ EPR spectra obtained at  $-173\text{ }^{\circ}\text{C}$  for the as-obtained fresh, reduced (at  $280\text{ }^{\circ}\text{C}$  in 50%  $\text{H}_2/\text{He}$  for 2h), and spent samples of a) pure  $\text{TiO}_2$  and b)  $\text{Au}/\text{TiO}_2$ . Reaction conditions:  $P = 1\text{ bar}$   $\text{H}_2$ ;  $\text{CO}_2 = 3:1$ ; total flow rate =  $17.5\text{ ml min}^{-1}$ ,  $T = 250\text{ }^{\circ}\text{C}$ .

For  $\text{ZrO}_2$  two main EPR signals were observed (**Figure 55a**). The lines at  $g_{\perp} = 1.974$  and  $g_{\parallel} = 1.961$  were assigned to paramagnetic  $\text{Zr}^{3+}$  species with axial symmetry,<sup>220,221</sup> whereas the one at  $g_{\text{iso}} = 2.002$  was attributed to a single electron trapped in an O-vacancy. Only a slight increase in the intensity of  $\text{Zr}^{3+}$  was observed when comparing the reduced and spent forms of the pure  $\text{ZrO}_2$ . The EPR spectrum of the fresh  $\text{Au}/\text{ZrO}_2$  catalyst (**Figure 55b**) showed the vacancy signal at  $g_{\text{iso}} = 2.003$  besides an axial signal with  $g_{\perp} = 1.974$  and  $g_{\parallel} = 1.954$  due to  $\text{Zr}^{3+}$  sites. After reduction, the  $\text{Zr}^{3+}$  signal did not change while the O-vacancy signal increased slightly. A further increase in the intensity of O-vacancy signal was detected for spent catalyst together with a line broadening and the appearance of a neighboring shoulder. This last observation indicated the superposition of two EPR signals.

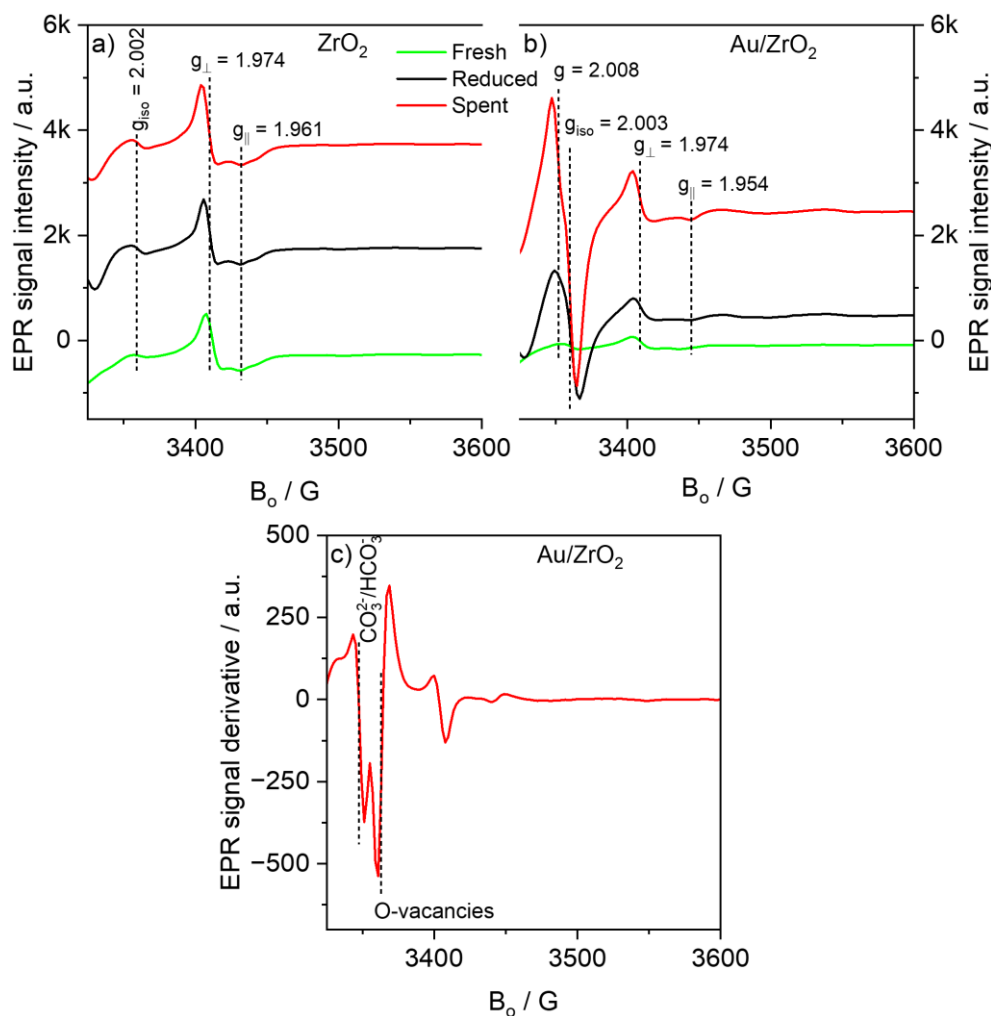


**Figure 55.** In-situ EPR spectra obtained at  $-173$  °C for the as-obtained fresh, reduced (at  $280$  °C in  $50\%$   $H_2/He$  for 2h), and spent samples of a) pure  $ZrO_2$  and b)  $Au/ZrO_2$ ; c) second derivative of the in situ EPR spectra obtained at  $-173$  °C for the spent  $Au/ZrO_2$  catalyst. Reaction conditions:  $P = 1$  bar  $H_2$ ;  $CO_2 = 3:1$ ; total flow rate  $= 17.5$  ml  $min^{-1}$ ,  $T = 250$  °C.

For a better resolution, the second derivative of the EPR spectrum was recorded and is presented in **Figure 55c**. The presence of an additional signal at a higher  $g$  value (2.008) was clearly observed. This could be attributed to the formation of adsorbed bicarbonate/carbonate radicals.<sup>223</sup> The bicarbonate radicals are most likely formed by the interaction of  $CO_2$  with the surface OH groups in the presence of O-vacancies.<sup>224</sup> These results suggested that both the surface hydroxyl groups and oxygen vacancies play a crucial role in the reaction mechanism of RWGS reaction over  $Au/ZrO_2$ . The strong increase of the intensity of the vacancy signal after exposing the reduced catalyst to the  $CO_2/H_2$  reaction mixture may be explained by the appearance of EPR-active defects that were EPR silent at previous stages. The transfer of the trapped electrons to  $CO_2$  molecules leading to bicarbonate/carbonate radicals would “dilute” the paramagnetic vacancies and thus reduce their mutual magnetic interactions.

A similar conclusion was also drawn by Gionco et al. who noticed that most of the formed O-vacancies on  $\text{ZrO}_2$  were EPR silent and transformed to EPR active ones upon interaction with  $\text{O}_2$  molecules. They attributed this spectral change to the electron transfer between the EPR-silent oxygen vacancies and the adsorbed  $\text{O}_2$  molecule.<sup>220</sup>

**Structure-reactivity relationship:** Considerable differences in the reaction mechanism between  $\text{Au/TiO}_2$  and  $\text{Au/ZrO}_2$  can be concluded. On  $\text{Au/ZrO}_2$  in-situ DRIFT spectra showed clear signals from bicarbonate and formate species that could act as intermediates for the RWGS reaction while carbonate species may be spectators although their participation in the reaction mechanism, cannot be excluded. Based on this information, the evolution of CO on  $\text{Au/ZrO}_2$  is proposed to via the formation of bicarbonate species due to the interaction of  $\text{CO}_2$  with hydroxyl groups adjacent to O-vacancies. These bicarbonates lead to formates upon hydrogenation from activated H on Au, restoring OH on the surface of the support. The formates further react to CO, e.g., following the route IIa shown in **Figure 7**. The corresponding catalytic cycle is shown in **Figure 56a**.

On  $\text{Au/TiO}_2$ , on the other hand, the observation of possible intermediates was not clear from DRFTS assessments which showed weak OCO signals at reaction conditions. Also, TAP results indicated that  $\text{CO}_2$  adsorption was weaker than on  $\text{Au/ZrO}_2$ . Moreover, HAADF-STEM images revealed the predominant formation of Au NPs ( $D_{\text{Au}} = 2\text{-}3$  nm) on  $\text{Au/TiO}_2$ , while the gold species were mainly distributed as single sites on  $\text{Au/ZrO}_2$  with very few contribution of Au NPs. It is known that  $\text{H}_2$  activation barriers tend to be higher on clusters and single sites than on metal nanoparticles.<sup>249-251</sup> Accordingly, it is expected that during reaction the population of activated H was much larger on  $\text{Au/TiO}_2$  than on  $\text{Au/ZrO}_2$  and, hence, the adsorbed  $\text{CO}_2$  rapidly hydrogenated to intermediates that decomposed very fast to be clearly detected at the conditions of the DRIFTS assessments. This facile decomposition of intermediates agrees with the lower  $E_A$  estimated from kinetic screening. Therefore, it is possible that the catalytic route for the RWGS reaction on  $\text{Au/TiO}_2$  was different to that on  $\text{Au/ZrO}_2$ . Rodriguez et al.<sup>252</sup> proposed the formation of hydroxycarbonyl (OCOH) as an active intermediate on  $\text{Au/TiO}_2$  interface which, however, had a very short lifetime on the gold surface and hence cannot be detected by DRIFTS assessments.<sup>28, 253</sup> Bobadilla et al.<sup>28</sup> also suggested the formation of this species as key intermediates for RWGS. They proposed that oxygen vacancies facilitated the formation of hydroxycarbonyl (OCOH) intermediates, which eventually decomposed to form CO and  $\text{H}_2\text{O}$ . The possibility of this pathway on the current  $\text{Au/TiO}_2$  can be explained by the activation of  $\text{CO}_2$  on the electron-enriched Au ( $\text{Au}^{\delta-}$ )<sup>82, 254-256</sup>

adjacent to  $O_v\text{-Ti}^{3+}$  sites. This activated  $\text{CO}_2$  formed  $\text{OCOH}$  that decomposed to weakly adsorbed  $\text{CO}$  on the Au surface leaving  $\text{OH}$  that further hydrogenated to  $\text{H}_2\text{O}$  regenerating the  $O$ -vacancies (**Figure 56b**).

Although the current experimental evidence is not conclusive about the formation of  $\text{CO}_2^\bullet$  radical and  $\text{CO}_2^-$  species, the involvement of the redox system ( $O_v\text{-Ti}^{3+} \leftrightarrow O\text{-Ti}^{4+}$ ) in the reaction mechanism during  $\text{CO}_2$  reduction cannot be ruled out. The  $\text{CO}_2^\bullet$  radical and  $\text{CO}_2^-$  species are expected to form by reducing  $\text{CO}_2$  molecules by transferring one and two electrons from support defects. Likewise, the participation of formate species also cannot be excluded, although their contribution to the overall catalytic reaction is expected to be small.

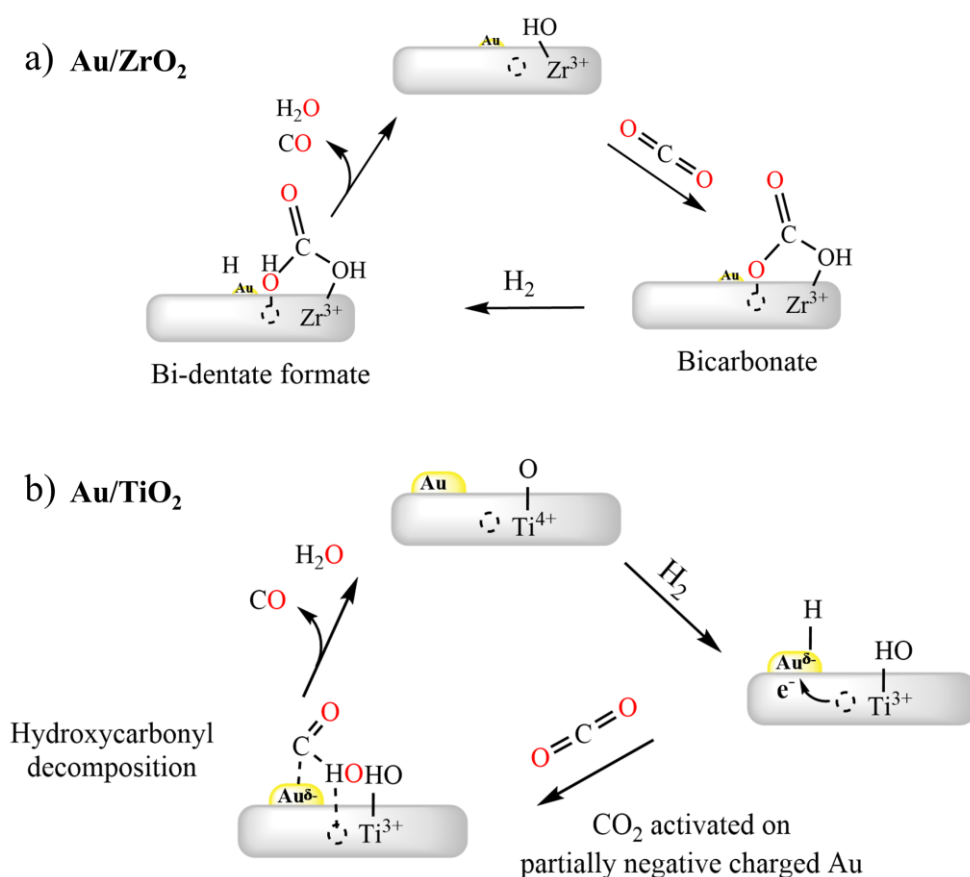


**Figure 56.** Proposed reaction mechanisms of the RWGS reaction over a) Au/ZrO<sub>2</sub> and b) Au/TiO<sub>2</sub> Catalysts. The dashed circle represents an O-vacancy.

## 4. General Conclusions and Outlook

The performance of low loaded precious metal heterogeneous catalysts for the hydrogenation of CO<sub>2</sub> has been discussed along this thesis. The focus has been centered in determining if the enhancement in O-vacancies can promote the rate of production of the desired compounds (CH<sub>4</sub>/CO) while minimizing the load of active metals (Ru/Au). Spectroscopic data gathered at relevant process conditions were determining for understanding the effect of these defects on the nature and stability of the key intermediates. Also, complementary techniques such as micrography and elemental mapping were helpful in observing structural features that can be attributed to the interaction between the supported particles and the O-vacancies. It was shown how the chemisorption properties of the catalysts were affected and subsequently modified the behavior of key intermediates: formates/CO (for CH<sub>4</sub> evolution) and hydroxycarbonyl (for CO evolution). The evidence suggested the creation/promotion of M<sub>1</sub><sup>δ-</sup>-O<sub>v</sub>-M<sub>2</sub><sup>n+</sup> sites, with M<sub>1</sub><sup>δ-</sup> (electron rich interfacial supported metal) and M<sub>2</sub><sup>n+</sup> (reduced support metal cation), in the promoted catalysts. This corroborated the importance of enhancing the defect concentration for favoring the rates of CO<sub>2</sub> conversion. Nevertheless, it was also observed that a highly defective support by itself is not enough to prepare highly active CO<sub>2</sub> hydrogenation catalysts. It is required to adequately prepare the catalysts in such a manner that the metal-O-vacancy interplay becomes effective. This was the case of the implementation of the sol-gel methodology to synthesize methanation catalysts. The so-called Ru/TiO<sub>2</sub>-SG catalyst was more effective than the Ru/TiO<sub>2</sub> catalyst prepared by impregnation of the Ru precursor on a highly defective sol-gel prepared TiO<sub>2</sub> support. That is, another important outcome of this thesis is the benefit of searching for alternative preparation routes that may potentially allow for the obtention of more efficient catalysts.

The application of catalytic processes in CO<sub>2</sub> capture and utilization has started to intensively investigate the production of more complex molecules such C<sub>2+</sub> alcohols and short olefines. These compounds are very desirable as energy vectors due to their high energy density and importance in extensive fossil fuel consuming and CO<sub>2</sub> producer transportation sector.<sup>257</sup> As such processes also require harsher conditions (temperature and pressure) than the production of C<sub>1</sub> compounds, the work is focused in the enhancement of catalysts to allow C-C coupling and suppressing C-O scission before hydrogenation.<sup>258</sup> These could also be modulated by O-vacancies (support reducibility),<sup>259</sup> hence increasing the knowledge about the influence of these defects is highly desirable in the race against global warming to create the carbon-neutral circular economy.

## Appendix

### A1. Gibbs free energy minimization method

In systems with multiple reactions each reaction has its reaction extent,  $\zeta$ .<sup>260</sup> The amount of each substance can be expressed as a function of the extent of the respective reactions it is participating in, equation **eq. A1**. In which  $n_{i\_in}$  represents the initial moles of compound  $i$ ,  $\vartheta_i$  the stoichiometric coefficient of compound  $i$  in the reaction  $j$  and  $\zeta_j$  the extend of reaction  $j$ . The composition at equilibrium will be determined when the Gibbs free energy of the system reaches a minimum at determined combination of the extent of distinct reactions, equation **eq. A2**.  $\Delta G_{f,i}^0$  represents the standard free Gibbs energy of formation of each compound in the system,  $\hat{f}_i$  is the fugacity of species  $i$  and  $f^0$  the fugacity at standard state. The method of free energy minimization is based in finding the minimum of this function while simultaneously satisfying the atom balance, equation **eq. A3**.

$$n_i = n_{i\_in} + \sum_i \vartheta_{ij} \zeta_j \quad \text{eq. A1}$$

$$G = \sum_i n_i (\Delta G_{f,i}^0 + RT \ln(\frac{\hat{f}_i}{f^0})) \quad \text{eq. A2}$$

$$\sum_i n_{i\_in} a_{ik\_in} - \sum_i n_{i\_out} a_{ik\_out} = 0 \quad \text{eq. A3}$$

Under the assumption of ideal gas, equation **eq. A2** can be written as equation **eq. A4**. In which  $P^0$  the standard pressure,  $y_i$  the mole fraction of each element at equilibrium,  $P$  the total system pressure.

$$G = \sum_i n_i (\Delta G_{f,i}^0 + RT \ln(\frac{y_i P}{P^0})) \quad \text{eq. A4}$$

$$y_i = \frac{n_i}{n_{total}} \quad \text{eq. A5}$$

$$n_{total} = \sum_i n_i \quad \text{eq. A6}$$



## A2. Additional information for chapter 3

### Supplementary data for CO<sub>2</sub> methanation on Ru/TiO<sub>2</sub> catalysts

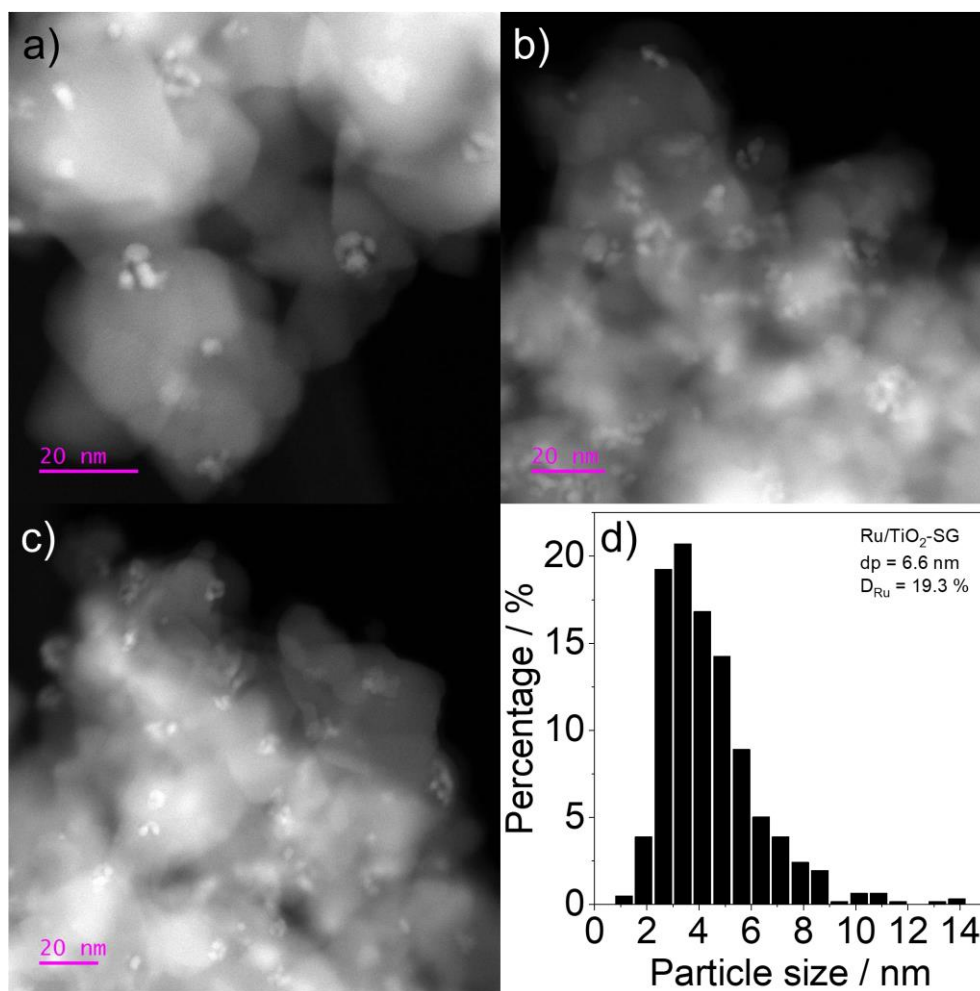


**Figure A1.** a-c) Representative Selected HAADF-STEM micrographs of the spent Ru/TiO<sub>2</sub>-SG; d) respective Ru particle size distribution and dispersion calculated after measuring ca. 300 particles. The micrographs were recorded after subjecting the fresh catalysts to the reaction conditions with up to 270 °C in H<sub>2</sub>:CO<sub>2</sub> = 4:1 (28.8 ml min<sup>-1</sup> H<sub>2</sub> + 7.2 ml min<sup>-1</sup> CO<sub>2</sub> + 4 ml min<sup>-1</sup> Ar).

## Supplementary data for CO<sub>2</sub> methanation on Ru/ZrO<sub>2</sub> and Ru/ZrO<sub>2</sub>-MgO

### catalysts

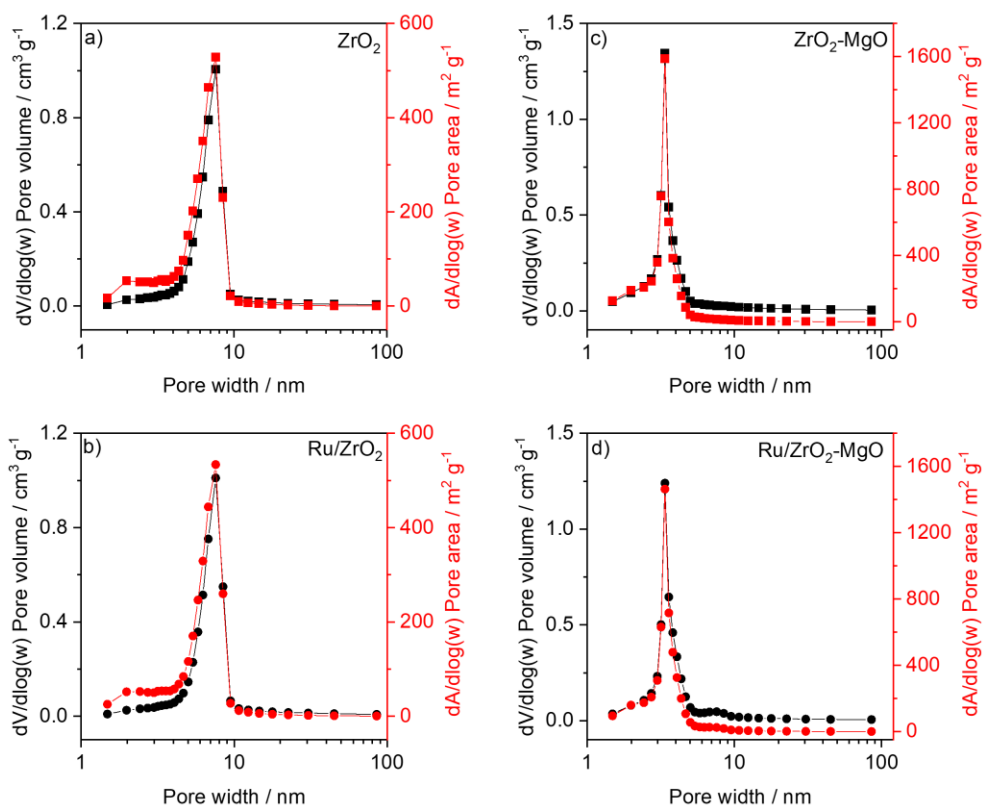


**Figure A2.** N<sub>2</sub> physisorption isotherms of a) ZrO<sub>2</sub> (black) and Ru/ZrO<sub>2</sub> (red); b) ZrO<sub>2</sub>-MgO and Ru/ZrO<sub>2</sub>-MgO.

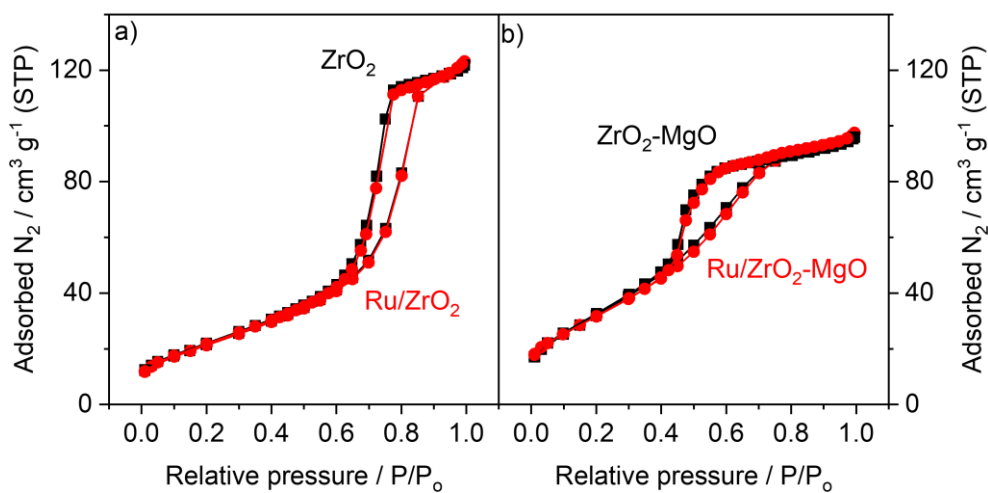


**Figure A3.** N<sub>2</sub> physisorption isotherms of a) ZrO<sub>2</sub> (black) and Ru/ZrO<sub>2</sub> (red); b) ZrO<sub>2</sub>-MgO and Ru/ZrO<sub>2</sub>-MgO.

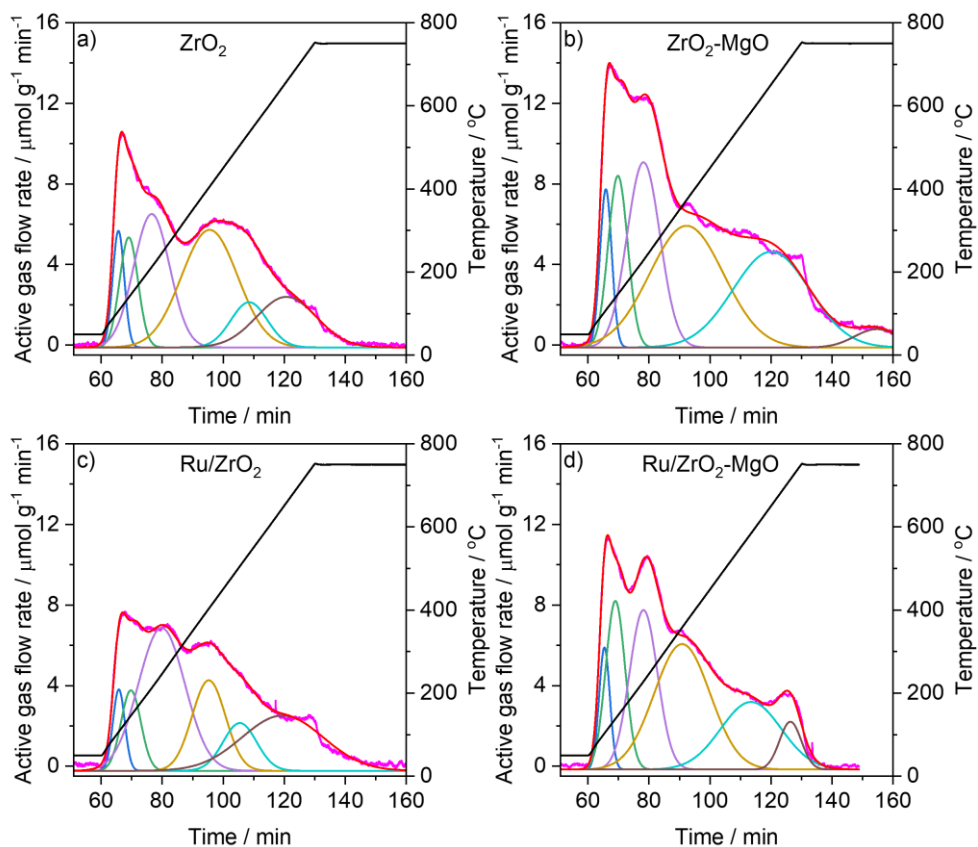


**Figure A4.** Deconvolution of the CO<sub>2</sub> desorption rates for a) ZrO<sub>2</sub>, b) Ru/ZrO<sub>2</sub>, c) ZrO<sub>2</sub>-MgO, d) Ru/ZrO<sub>2</sub>-MgO.

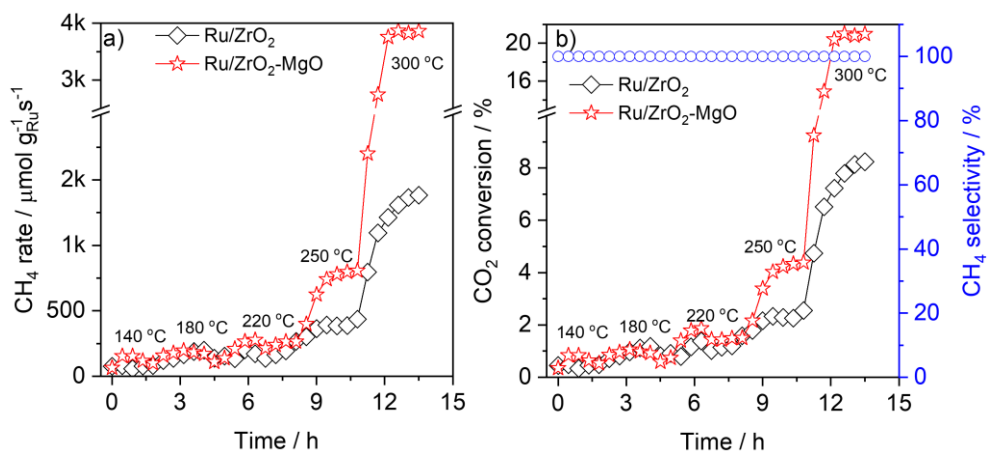


**Figure A5.** a) Ru mass normalized CH<sub>4</sub> formation rate on Ru/ZrO<sub>2</sub> (black diamonds) and Ru/ZrO<sub>2</sub>-MgO (red stars) in the temperature range 220 – 300 °C; b) CO<sub>2</sub> conversion on Ru/ZrO<sub>2</sub> (black diamonds), Ru/ZrO<sub>2</sub>-MgO (red stars), and selectivity to CH<sub>4</sub> (blue circles) in the temperature range 220 – 300 °C.

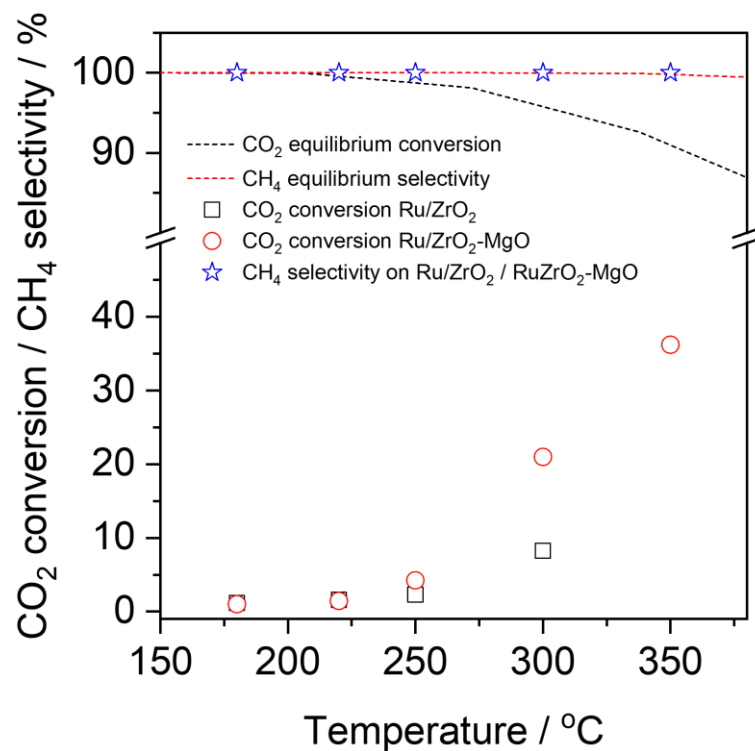


**Figure A6** Comparison between kinetic experimental data (squares, circles and stars) with the respective expected thermodynamic values (dotted lines). Inlet gas flow conditions: 16 ml min<sup>-1</sup> H<sub>2</sub>, 4 ml min<sup>-1</sup> CO<sub>2</sub>, 10 ml min<sup>-1</sup> N<sub>2</sub>.

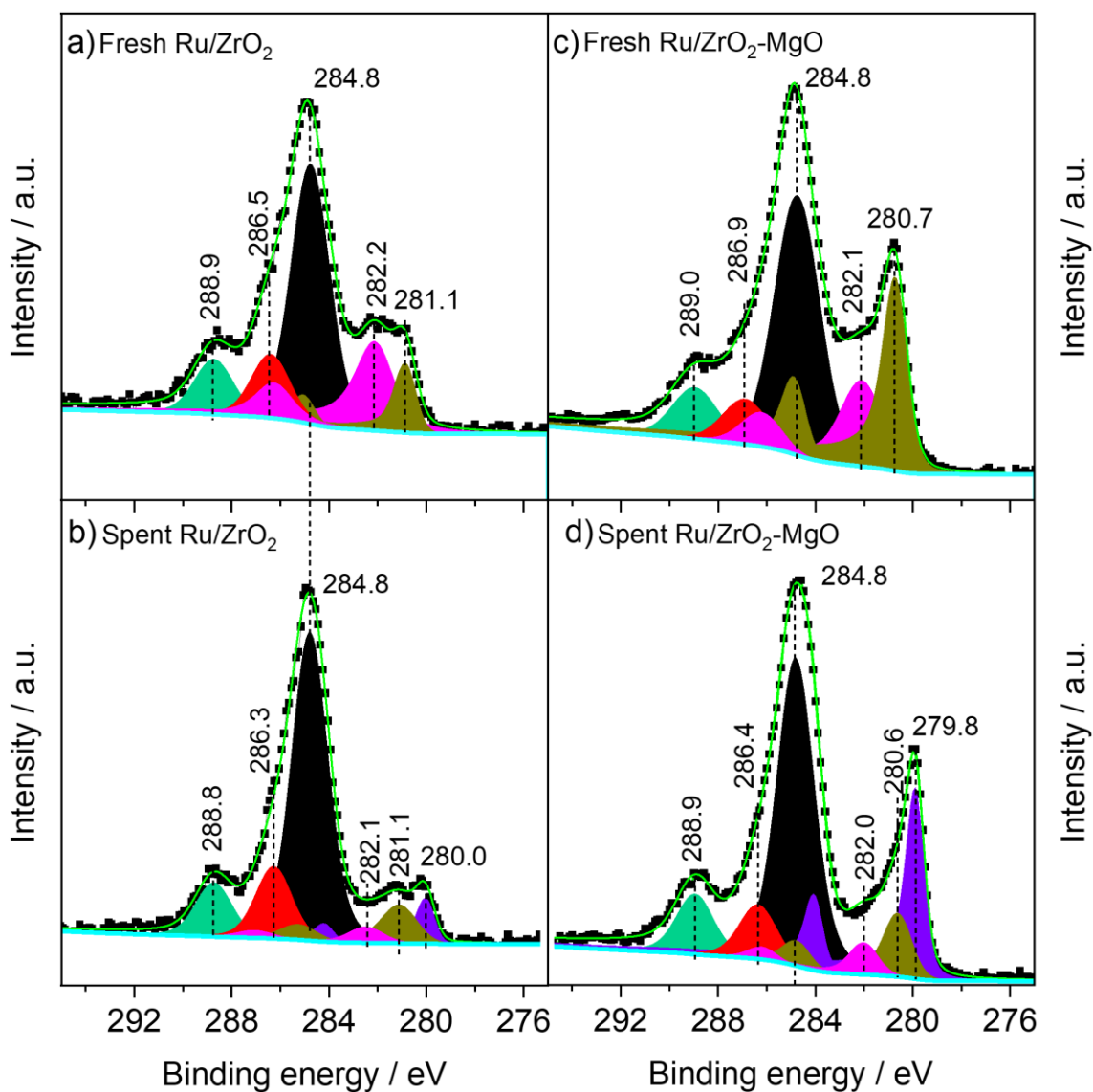


**Figure A7.** XP spectra of the C 1s region of the fresh and spent Ru/ZrO<sub>2</sub> catalyst (a, b) and of fresh and spent Ru/ZrO<sub>2</sub>-MgO catalyst (c, d). The green line represents the fitting curve. The spectra corresponding to the spent catalysts were recorded after reaction at 270 °C.

The spectra in the C1s and Ru3d were deconvoluted accounting for the contribution of C-C (284.8 eV), C-OH (286.5 – 286.9 eV) and O-C=O (288.8 – 289.0 eV) for C1s.<sup>261</sup> For Ru 3d, contributions from Ru<sup>4+</sup> (280.6 – 281.1 eV), Ru<sup>4+</sup> (satellite) (282.1 – 282.0 eV) and Ru<sup>0</sup> (279.8 – 280.0 eV) were considered.<sup>177</sup>

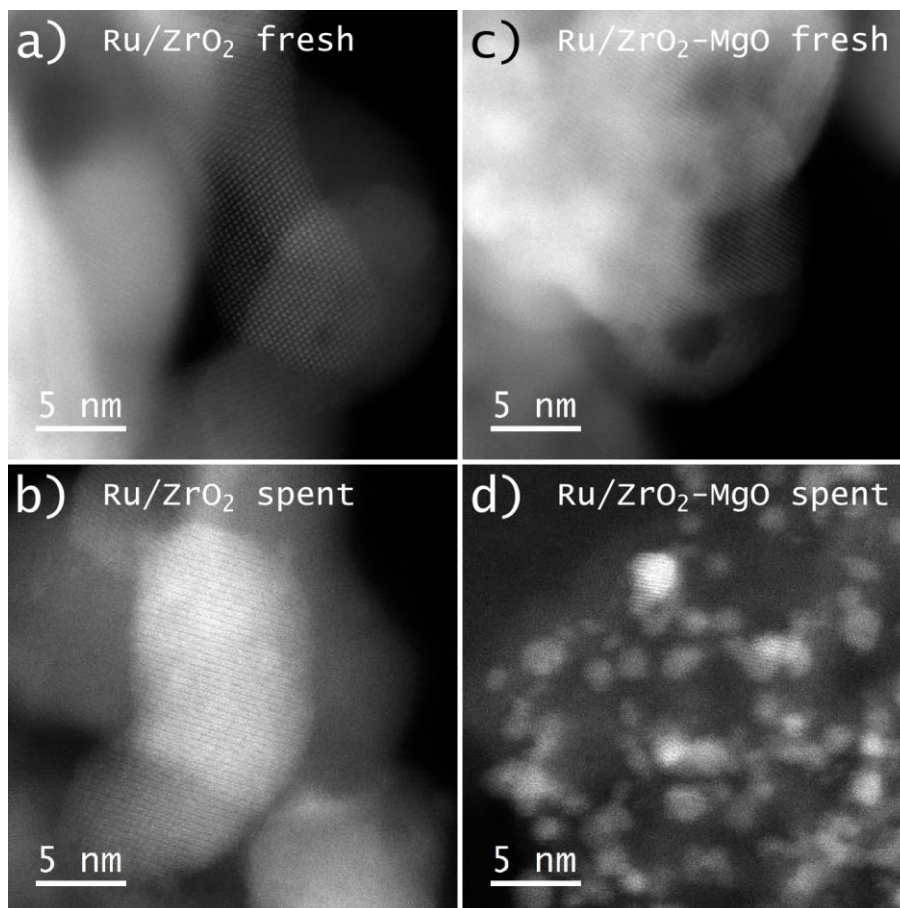


**Figure A8.** Selected HAADF-STEM micrographs of fresh and spent Ru/ZrO<sub>2</sub> (a, b) and fresh and spent Ru/ZrO<sub>2</sub>-MgO. In Ru/ZrO<sub>2</sub> spent some small Ru particles are observed (slightly brighter particles), while in Ru/ZrO<sub>2</sub>-MgO spent, much more of these particles are visible (the better contrast here is because of the presence of these Ru particles on MgO instead of ZrO<sub>2</sub>). The micrographs of the spent materials were recorded after reaction at 270 °C.

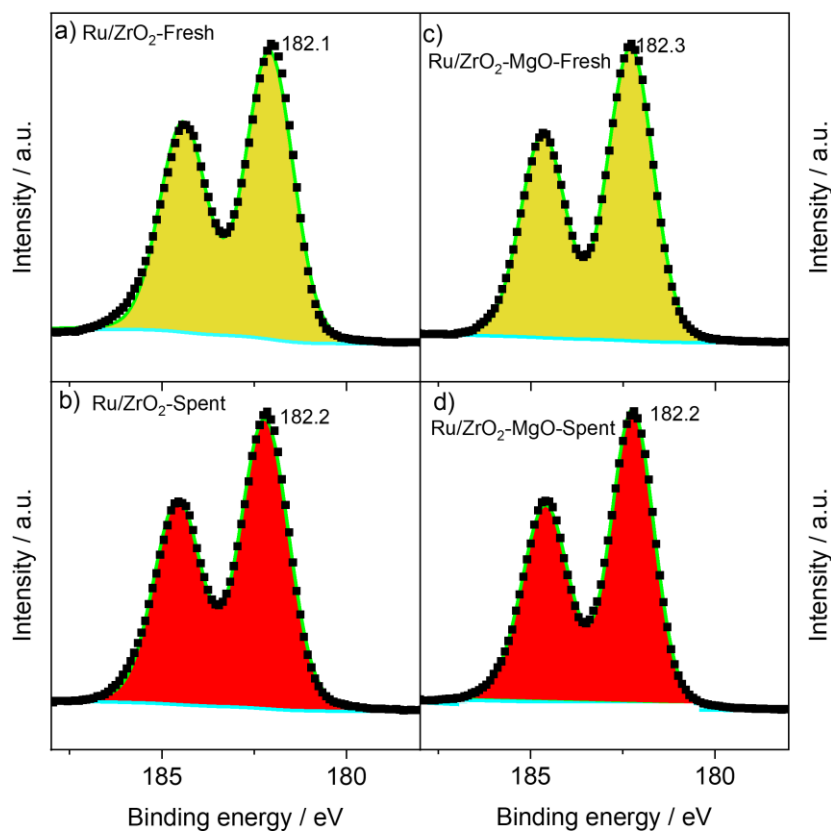


**Figure A9.** XP spectra of the Zr3d region of the fresh and spent Ru/ZrO<sub>2</sub> catalyst (a, b) and of fresh and spent Ru/ZrO<sub>2</sub>-MgO catalyst (c, d). The spectra corresponding to the spent catalysts were recorded after reaction at 270 °C.

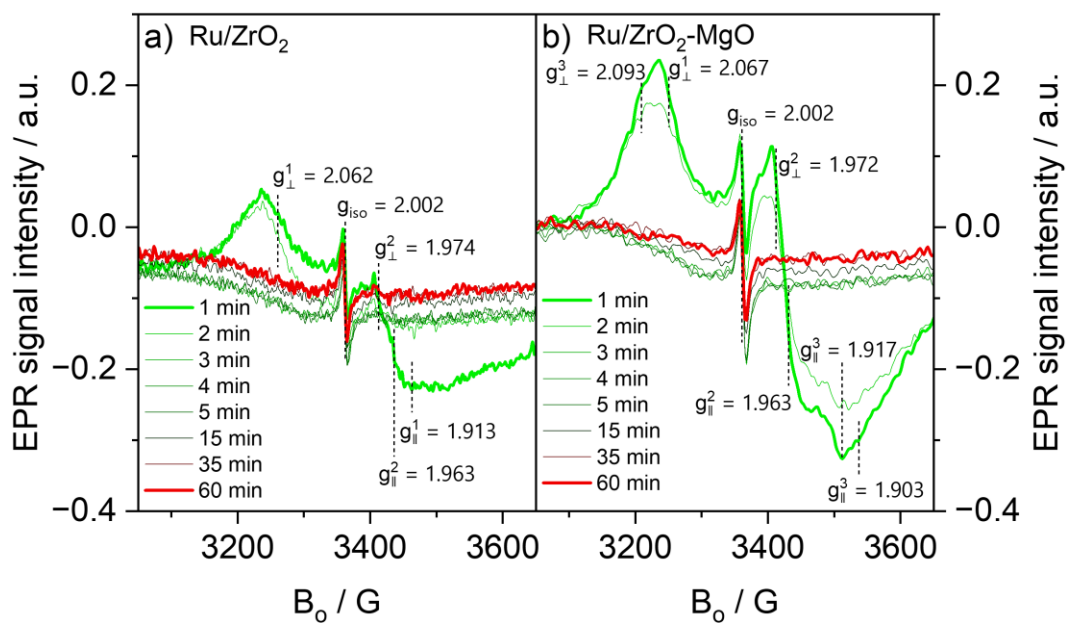


**Figure A10.** EPR spectra recorded at 250 °C of a) Ru/ZrO<sub>2</sub> and b) Ru/ZrO<sub>2</sub>-MgO during reaction (H<sub>2</sub>:CO<sub>2</sub> = 4:1)

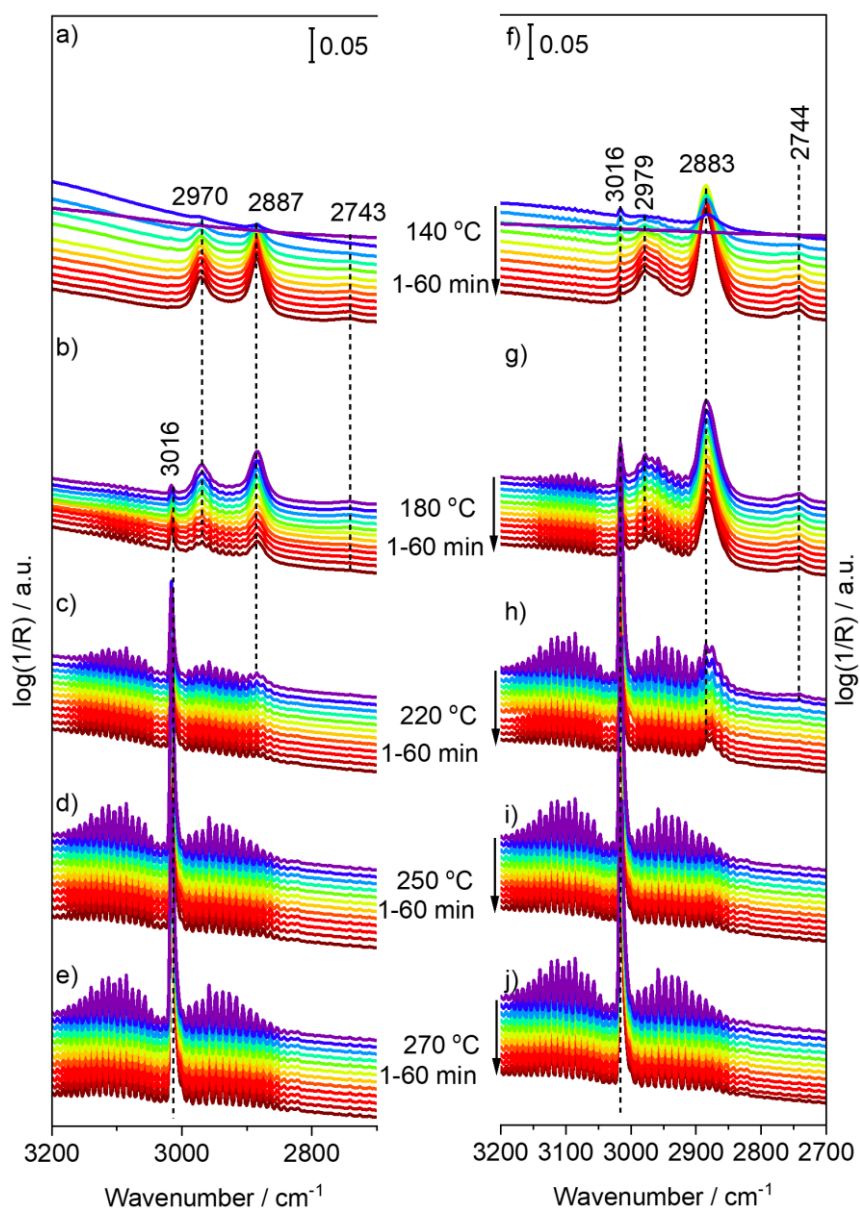


**Figure A11.** DRIFT spectra recorded between 140 – 270 °C in the CH region recorded for Ru/ZrO<sub>2</sub> a-e) Ru/ZrO<sub>2</sub>-MgO f-j). The total reaction time at each temperature was set to 1 h (top to bottom spectra as indicated by the arrows). Inlet gas flow conditions: 16 ml min<sup>-1</sup> H<sub>2</sub>, 4 ml min<sup>-1</sup> CO<sub>2</sub>, 10 ml min<sup>-1</sup> He.



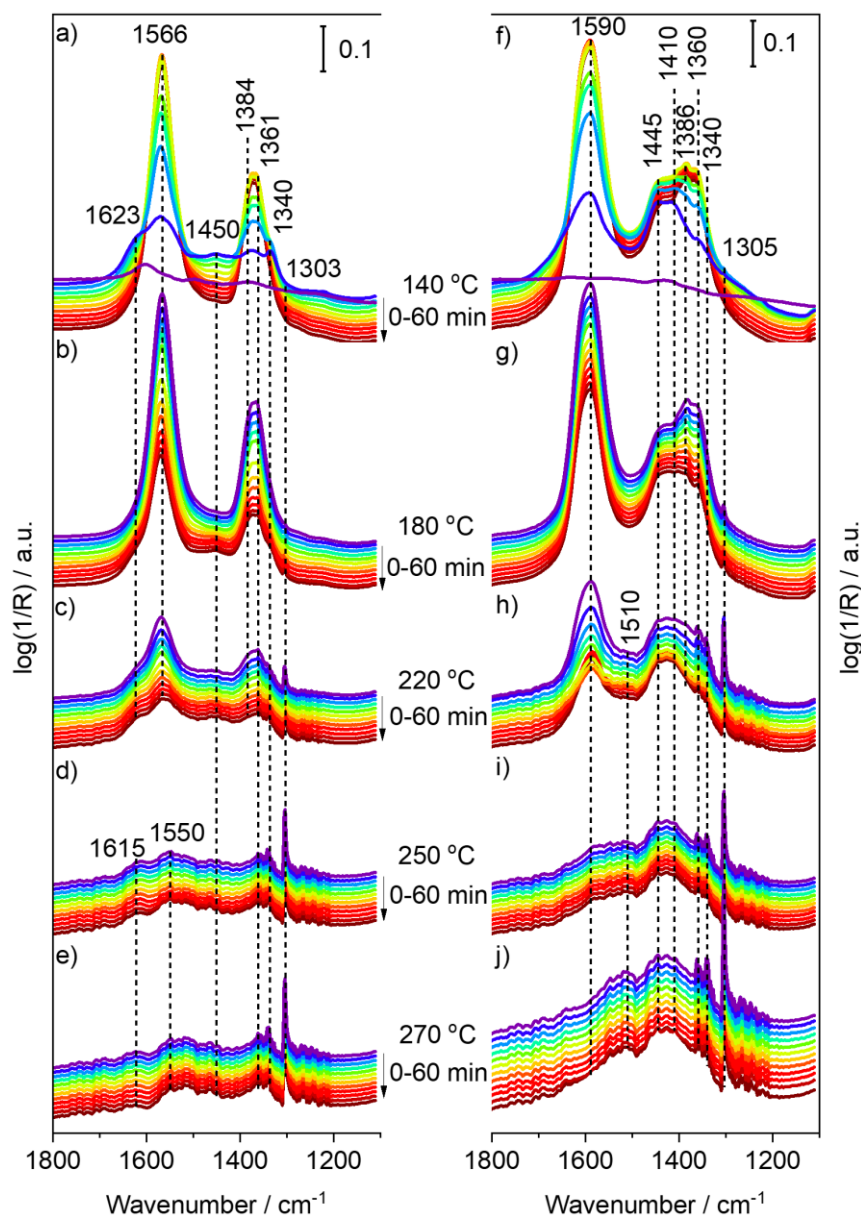


**Figure A12.** DRIFT spectra recorded between 140 – 270 °C in the O-C-O region recorded for Ru/ZrO<sub>2</sub> a-e) Ru/ZrO<sub>2</sub>-MgO f-j). The total reaction time at each temperature was set to 1 h (top to bottom spectra as indicated by the arrows). Inlet gas flow conditions: 16 ml min<sup>-1</sup> H<sub>2</sub>, 4 ml min<sup>-1</sup> CO<sub>2</sub>, 10 ml min<sup>-1</sup> He.

The analysis of the spectral IR characteristics in the O-C-O region at 250 °C is complemented here. First, on Ru/ZrO<sub>2</sub> (**Figure 37a**), the weak shoulder observed around 1612 cm<sup>-1</sup> could be attributed to adsorbed bidentate bicarbonate (b-HCO<sub>3</sub><sup>-\*</sup>).<sup>199</sup> The weak bands located around 1510 and 1463 cm<sup>-1</sup> might correspond to polydentate carbonate species (p-CO<sub>3</sub><sup>-\*</sup>).<sup>199, 200</sup> The weak shoulder about 1340 cm<sup>-1</sup> might be a contribution from bidentate carbonate species (b-CO<sub>3</sub><sup>-\*</sup>).<sup>118</sup> A signal ca. 1304 cm<sup>-1</sup> is associated to CH<sub>4</sub>. For Ru/ZrO<sub>2</sub>-MgO (**Figure 37b**) the corresponding asymmetric stretching of bidentate bicarbonate (b-HCO<sub>3</sub><sup>-\*</sup>) was barely resolved ca. 1620 cm<sup>-1</sup>.<sup>262</sup> The band ca. 1424 cm<sup>-1</sup> might be related to the symmetric stretching,

$\nu_s(\text{O-C-O})$ , of bicarbonate species.<sup>262, 263</sup> Finally, the bands ca.  $1340\text{ cm}^{-1}$  as well as ca.  $1304\text{ cm}^{-1}$  representative of  $\text{b-CO}_3^{*}$  and  $\text{CH}_4$ , respectively. It is worth to note that the signal at  $1424\text{ cm}^{-1}$  was selected at the center of a rather broad line that might also include other types of bicarbonate species identified in the literature.<sup>128, 199, 227, 262</sup>

The spectra of the bare supports evidenced the formation of the same species (formates and/or carbonates/bicarbonates).<sup>199, 227, 264</sup> The absence of the  $\text{CH}_4$  related signals ca.  $1304\text{ cm}^{-1}$  and  $3016\text{ cm}^{-1}$  corroborated the inactivity of the bare supports. From this information the unique certainty is the need of Ru to bind CO that subsequently hydrogenates to  $\text{CH}_4$ . However, no conclusion about the role of formates, bicarbonates and carbonates can still be obtained.

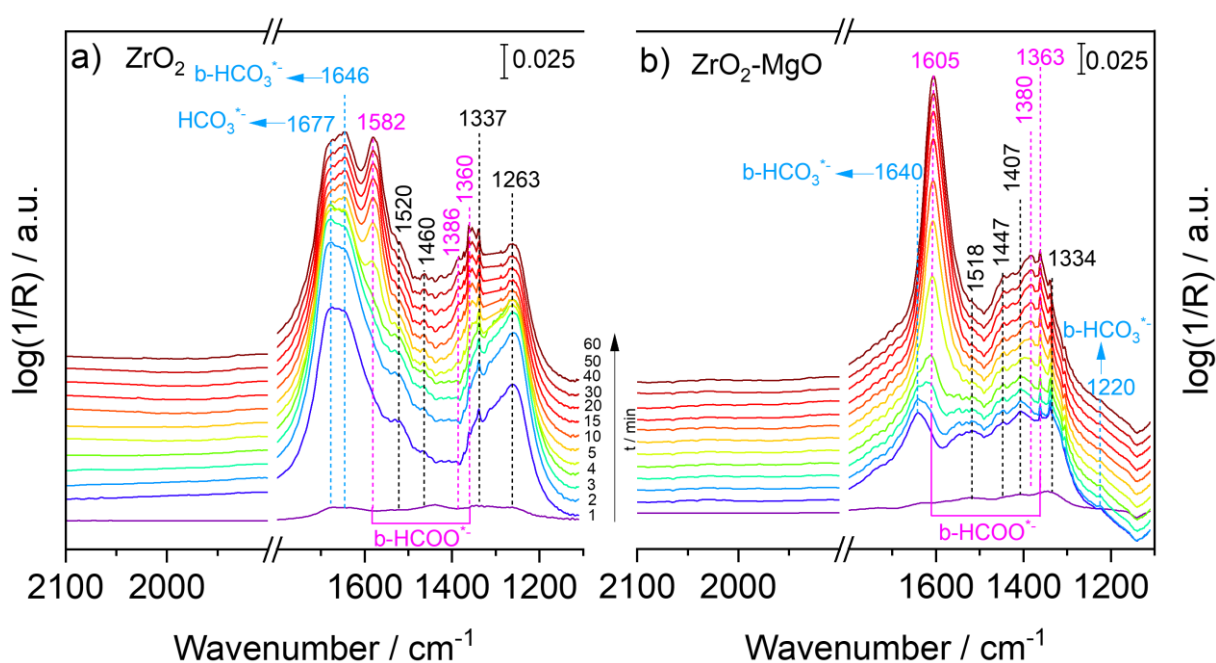


**Figure A13.** DRIFT spectra recorded at  $250\text{ }^{\circ}\text{C}$  on a)  $\text{ZrO}_2$  and b)  $\text{ZrO}_2\text{-MgO}$ . The total reaction time was set to 1 h (from bottom to top). Inlet gas flow conditions:  $16\text{ ml min}^{-1}\text{ H}_2$ ,  $4\text{ ml min}^{-1}\text{ CO}_2$ ,  $10\text{ ml min}^{-1}\text{ He}$ .

**Supplementary data for RWGS reaction on Au/TiO<sub>2</sub> and Au/ZrO<sub>2</sub> catalysts**

The signals at 1344 cm<sup>-1</sup> and 1449 cm<sup>-1</sup> were attributed to adsorbed carbonate species on TiO<sub>2</sub> (**Figure A16a**).<sup>265</sup> Bands centered around 1550, 1379, and 1359 cm<sup>-1</sup> likely correspond to formate species.

Analogously, the spectra over ZrO<sub>2</sub> (**Figure A16b**) showed the evolution of bicarbonate (1328 cm<sup>-1</sup>), carbonate (1470 cm<sup>-1</sup>), formate (1569 and 1375 cm<sup>-1</sup>), and bicarbonate (1622 cm<sup>-1</sup>) species.

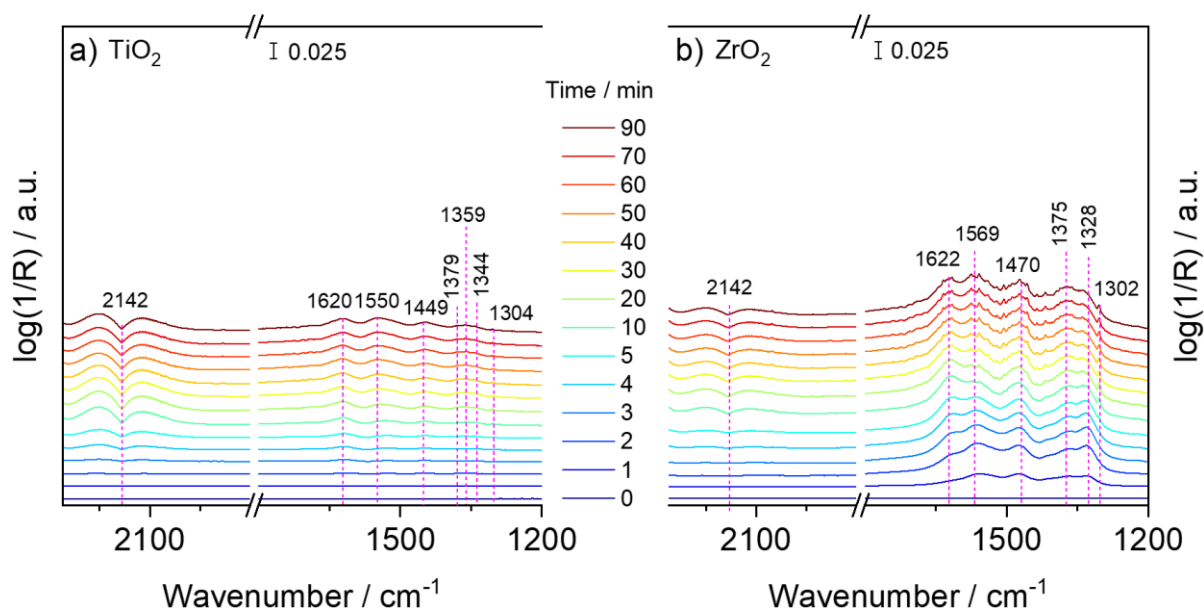


**Figure A14.** In-situ DRIFT spectra of the RWGS reaction over a) TiO<sub>2</sub> and b) ZrO<sub>2</sub> bare supports. Reaction conditions: P = 3 bar, H<sub>2</sub>: CO<sub>2</sub>: N<sub>2</sub> = 3:1:2; total flow rate = 17.5 ml/min, T = 250 °C.

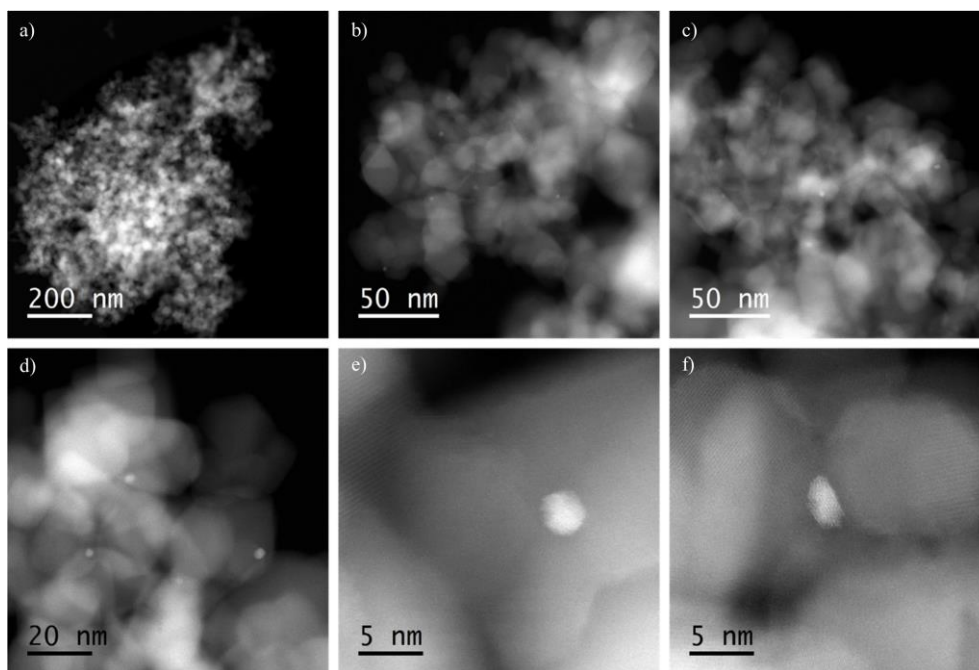


**Figure A15.** STEM-HAADF images of the reduced Au/TiO<sub>2</sub> catalysts.

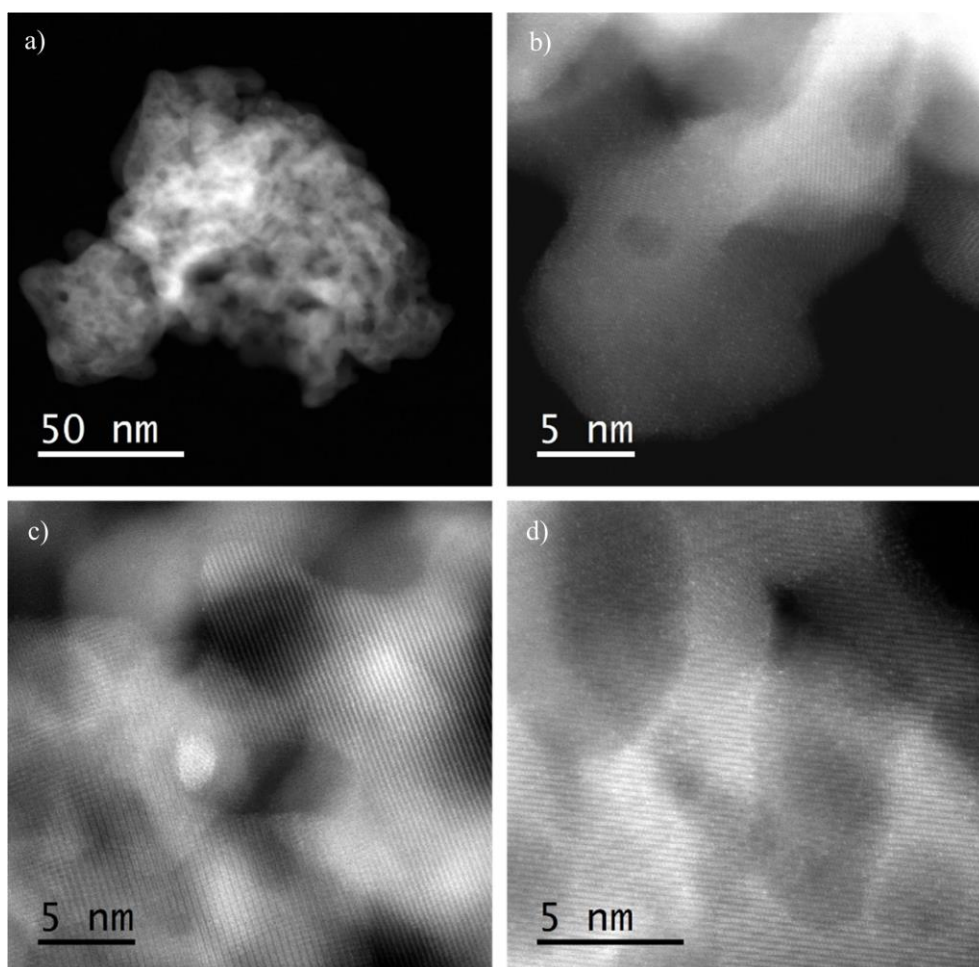


**Figure A16.** STEM-HAADF images of the reduced Au/ZrO<sub>2</sub> catalysts.

## References

- (1) Friedlingstein, P.; Jones, M. W.; O'Sullivan, M.; Andrew, R. M.; Bakker, D. C. E.; Hauck, J.; Le Quéré, C.; Peters, G. P.; Peters, W.; Pongratz, J.; et al. Global Carbon Budget 2021. *Earth Syst. Sci. Data* **2022**, *14* (4), 1917-2005. DOI: 10.5194/essd-14-1917-2022.
- (2) Marques Mota, F.; Kim, D. H. From CO<sub>2</sub> methanation to ambitious long-chain hydrocarbons: alternative fuels paving the path to sustainability. *Chem. Soc. Rev.* **2019**, *48* (1), 205-259. DOI: 10.1039/c8cs00527c.
- (3) Torres Galvis, H. M.; de Jong, K. P. Catalysts for Production of Lower Olefins from Synthesis Gas: A Review. *ACS Catal.* **2013**, *3* (9), 2130-2149. DOI: 10.1021/cs4003436.
- (4) Centi, G.; Quadrelli, E. A.; Perathoner, S. Catalysis for CO<sub>2</sub> conversion: a key technology for rapid introduction of renewable energy in the value chain of chemical industries. *Energy & Environmental Science* **2013**, *6* (6). DOI: 10.1039/c3ee00056g.
- (5) Thema, M.; Bauer, F.; Sterner, M. Power-to-Gas: Electrolysis and methanation status review. *Renew. Sustain. Energy Rev.* **2019**, *112*, 775-787. DOI: <https://doi.org/10.1016/j.rser.2019.06.030>.
- (6) Tackett, B. M.; Gomez, E.; Chen, J. G. Net reduction of CO<sub>2</sub> via its thermocatalytic and electrocatalytic transformation reactions in standard and hybrid processes. *Nat. Catal.* **2019**, *2* (5), 381-386. DOI: 10.1038/s41929-019-0266-y.
- (7) Ioannou, I.; Galán-Martín, Á.; Pérez-Ramírez, J.; Guillén-Gosálbez, G. Trade-offs between Sustainable Development Goals in carbon capture and utilisation. *Energy & Environmental Science* **2023**, *16* (1), 113-124, 10.1039/D2EE01153K. DOI: 10.1039/D2EE01153K.
- (8) Aresta, M.; Dibenedetto, A.; Angelini, A. Catalysis for the Valorization of Exhaust Carbon: from CO<sub>2</sub> to Chemicals, Materials, and Fuels. Technological Use of CO<sub>2</sub>. *Chem. Rev.* **2014**, *114* (3), 1709-1742. DOI: 10.1021/cr4002758.
- (9) Aresta, M.; Dibenedetto, A.; Quaranta, E. State of the art and perspectives in catalytic processes for CO<sub>2</sub> conversion into chemicals and fuels: The distinctive contribution of chemical catalysis and biotechnology. *J. Catal.* **2016**, *343*, 2-45. DOI: 10.1016/j.jcat.2016.04.003.
- (10) Mazloomi, K.; Gomes, C. Hydrogen as an energy carrier: Prospects and challenges. *Renew. Sustain. Energy Rev.* **2012**, *16* (5), 3024-3033. DOI: <https://doi.org/10.1016/j.rser.2012.02.028>.
- (11) Thema, M.; Sterner, M.; Lenck, T.; Götz, P. Necessity and Impact of Power-to-gas on Energy Transition in Germany. *Energy Procedia* **2016**, *99*, 392-400. DOI: <https://doi.org/10.1016/j.egypro.2016.10.129>.
- (12) Gahleitner, G. Hydrogen from renewable electricity: An international review of power-to-gas pilot plants for stationary applications. *Int. J. Hydrogen Energy* **2013**, *38* (5), 2039-2061. DOI: <https://doi.org/10.1016/j.ijhydene.2012.12.010>.
- (13) Walker, S. B.; Mukherjee, U.; Fowler, M.; Elkamel, A. Benchmarking and selection of Power-to-Gas utilizing electrolytic hydrogen as an energy storage alternative. *Int. J. Hydrogen Energy* **2016**, *41* (19), 7717-7731. DOI: <https://doi.org/10.1016/j.ijhydene.2015.09.008>.
- (14) Simonis, B.; Newborough, M. Sizing and operating power-to-gas systems to absorb excess renewable electricity. *Int. J. Hydrogen Energy* **2017**, *42* (34), 21635-21647. DOI: <https://doi.org/10.1016/j.ijhydene.2017.07.121>.
- (15) Schaaf, T.; Grünig, J.; Schuster, M. R.; Rothenfluh, T.; Orth, A. Methanation of CO<sub>2</sub> - storage of renewable energy in a gas distribution system. *Energy, Sustain. Soc.* **2014**, *4* (1). DOI: 10.1186/s13705-014-0029-1.

- (16) Ashok, J.; Pati, S.; Hongmanorom, P.; Tianxi, Z.; Junmei, C.; Kawi, S. A review of recent catalyst advances in CO<sub>2</sub> methanation processes. *Catal. Today* **2020**, *356*, 471-489. DOI: <https://doi.org/10.1016/j.cattod.2020.07.023>.
- (17) Wang, Y.; Winter, L. R.; Chen, J. G.; Yan, B. CO<sub>2</sub> hydrogenation over heterogeneous catalysts at atmospheric pressure: from electronic properties to product selectivity. *Green. Chem.* **2021**, *23* (1), 249-267, 10.1039/D0GC03506H. DOI: 10.1039/D0GC03506H.
- (18) Moiola, E.; Gallandat, N.; Züttel, A. Parametric sensitivity in the Sabatier reaction over Ru/Al<sub>2</sub>O<sub>3</sub> – theoretical determination of the minimal requirements for reactor activation. *React. Chem. Eng.* **2019**, *4* (1), 100-111. DOI: 10.1039/c8re00133b.
- (19) Moiola, E.; Züttel, A. A model-based comparison of Ru and Ni catalysts for the Sabatier reaction. *Sustain. Energy Fuels* **2020**, *4* (3), 1396-1408. DOI: 10.1039/c9se00787c.
- (20) Kuznecova, I.; Gusca, J. Property based ranking of CO and CO<sub>2</sub> methanation catalysts. *Energy Procedia* **2017**, *128*, 255-260. DOI: <https://doi.org/10.1016/j.egypro.2017.09.068>.
- (21) Abdel-Mageed, A. M.; Wiese, K.; Hauble, A.; Bansmann, J.; Rabeah, J.; Parlinska-Wojtan, M.; Brückner, A.; Behm, R. J. Steering the selectivity in CO<sub>2</sub> reduction on highly active Ru/TiO<sub>2</sub> catalysts: Support particle size effects. *J. Catal.* **2021**, *401*, 160-173. DOI: <https://doi.org/10.1016/j.jcat.2021.07.020>.
- (22) Chen, S.; Abdel-Mageed, A. M.; Li, M.; Cisneros, S.; Bansmann, J.; Rabeah, J.; Brückner, A.; Groß, A.; Behm, R. J. Electronic metal-support interactions and their promotional effect on CO<sub>2</sub> methanation on Ru/ZrO<sub>2</sub> catalysts. *J. Catal.* **2021**, *400*, 407-420. DOI: <https://doi.org/10.1016/j.jcat.2021.06.028>.
- (23) Wang, W.; Wang, S.; Ma, X.; Gong, J. Recent advances in catalytic hydrogenation of carbon dioxide. *Chem. Soc. Rev.* **2011**, *40* (7), 3703-3727, 10.1039/C1CS15008A. DOI: 10.1039/C1CS15008A.
- (24) Li, J.; He, Y.; Tan, L.; Zhang, P.; Peng, X.; Oruganti, A.; Yang, G.; Abe, H.; Wang, Y.; Tsubaki, N. Integrated tuneable synthesis of liquid fuels via Fischer–Tropsch technology. *Nat. Catal.* **2018**, *1* (10), 787-793. DOI: 10.1038/s41929-018-0144-z.
- (25) Kirsch, H.; Brübach, L.; Loewert, M.; Riedinger, M.; Gräfenhahn, A.; Böltken, T.; Klumpp, M.; Pfeifer, P.; Dittmeyer, R. CO<sub>2</sub>-neutrale Fischer-Tropsch-Kraftstoffe aus dezentralen modularen Anlagen: Status und Perspektiven. *Chem. Ing. Tech.* **2020**, *92* (1-2), 91-99. DOI: <https://doi.org/10.1002/cite.201900120>.
- (26) Sakurai, H.; Tsubota, S.; Haruta, M. *Appl. Catal., A* **1993**, *102*, 125.
- (27) Montini, T.; Melchionna, M.; Monai, M.; Fornasiero, P. Fundamentals and Catalytic Applications of CeO<sub>2</sub>-Based Materials. *Chem. Rev.* **2016**, *116* (10), 5987-6041. DOI: 10.1021/acs.chemrev.5b00603.
- (28) Bobadilla, L. F.; Santos, J. L.; Ivanova, S.; Odriozola, J. A.; Urakawa, A. Unravelling the Role of Oxygen Vacancies in the Mechanism of the Reverse Water–Gas Shift Reaction by Operando DRIFTS and Ultraviolet–Visible Spectroscopy. *ACS Catal.* **2018**, *8* (8), 7455-7467. DOI: 10.1021/acscatal.8b02121.
- (29) Wang, D.; Bi, Q.; Yin, G.; Zhao, W.; Huang, F.; Xie, X.; Jiang, M. Direct synthesis of ethanol via CO<sub>2</sub> hydrogenation using supported gold catalysts. *Chem. Commun.* **2016**, *52* (99), 14226-14229, 10.1039/C6CC08161D. DOI: 10.1039/C6CC08161D.
- (30) Ramesha, G. K.; Brennecke, J. F.; Kamat, P. V. Origin of Catalytic Effect in the Reduction of CO<sub>2</sub> at Nanostructured TiO<sub>2</sub> Films. *ACS Catal.* **2014**, *4* (9), 3249-3254. DOI: 10.1021/cs500730w.
- (31) Dostagir, N. H. M. D.; Rattanawan, R.; Gao, M.; Ota, J.; Hasegawa, J.-y.; Asakura, K.; Fukouka, A.; Shrotri, A. Co Single Atoms in ZrO<sub>2</sub> with Inherent Oxygen Vacancies for Selective Hydrogenation of CO<sub>2</sub> to CO. *ACS Catal.* **2021**, *11* (15), 9450-9461. DOI: 10.1021/acscatal.1c02041.

- (32) Bobadilla, L. F.; Azancot, L.; Luque-Álvarez, L. A.; Torres-Sempere, G.; González-Castaño, M.; Pastor-Pérez, L.; Yu, J.; Ramírez-Reina, T.; Ivanova, S.; Centeno, M. A.; et al. Development of Power-to-X Catalytic Processes for CO<sub>2</sub> Valorisation: From the Molecular Level to the Reactor Architecture. *Chemistry* **2022**, *4* (4), 1250-1280.
- (33) Ye, R.-P.; Ding, J.; Gong, W.; Argyle, M. D.; Zhong, Q.; Wang, Y.; Russell, C. K.; Xu, Z.; Russell, A. G.; Li, Q.; et al. CO<sub>2</sub> hydrogenation to high-value products via heterogeneous catalysis. *Nat. Commun.* **2019**, *10* (1), 5698. DOI: 10.1038/s41467-019-13638-9.
- (34) Held, M.; Schollenberger, D.; Sauerschell, S.; Bajohr, S.; Kolb, T. Power-to-Gas: CO<sub>2</sub> Methanation Concepts for SNG Production at the Engler-Bunte-Institut. *Chem. Ing. Tech.* **2020**, *92* (5), 595-602. DOI: <https://doi.org/10.1002/cite.201900181>.
- (35) Wiede, T.; Land, A. Sektorenkopplung: Amprion und Open Grid Europe Geben Power-to-Gas in Deutschland einen Schub. *Amprion GmbH, Open Grid Europe: Berlin, Germany* **2018**.
- (36) Guilera, J.; Ramon Morante, J.; Andreu, T. Economic viability of SNG production from power and CO<sub>2</sub>. *Energy Convers. Manage.* **2018**, *162*, 218-224. DOI: <https://doi.org/10.1016/j.enconman.2018.02.037>.
- (37) Brennführer, A.; Neumann, H.; Beller, M. Palladium-Catalyzed Carbonylation Reactions of Aryl Halides and Related Compounds. *Angew. Chem. Int. Ed.* **2009**, *48* (23), 4114-4133. DOI: <https://doi.org/10.1002/anie.200900013>.
- (38) Schwab, E.; Milanov, A.; Schunk, S. A.; Behrens, A.; Schödel, N. Dry Reforming and Reverse Water Gas Shift: Alternatives for Syngas Production? *Chem. Ing. Tech.* **2015**, *87* (4), 347-353. DOI: <https://doi.org/10.1002/cite.201400111>.
- (39) Bown, R. M.; Joyce, M.; Zhang, Q.; Reina, T. R.; Duyar, M. S. Identifying Commercial Opportunities for the Reverse Water Gas Shift Reaction. *Energy Technology* **2021**, *9* (11), 2100554. DOI: <https://doi.org/10.1002/ente.202100554>.
- (40) Bahmanpour, A. M.; Signorile, M.; Kröcher, O. Recent progress in syngas production via catalytic CO<sub>2</sub> hydrogenation reaction. *Appl. Catal. B: Environ.* **2021**, *295*, 120319. DOI: <https://doi.org/10.1016/j.apcatb.2021.120319>.
- (41) Vogt, C.; Monai, M.; Kramer, G. J.; Weckhuysen, B. M. The renaissance of the Sabatier reaction and its applications on Earth and in space. *Nat. Catal.* **2019**, *2* (3), 188-197. DOI: 10.1038/s41929-019-0244-4.
- (42) Park, J.-N.; McFarland, E. W. A highly dispersed Pd-Mg/SiO<sub>2</sub> catalyst active for methanation of CO<sub>2</sub>. *J. Catal.* **2009**, *266* (1), 92-97. DOI: <https://doi.org/10.1016/j.jcat.2009.05.018>.
- (43) Gao, J.; Wang, Y.; Ping, Y.; Hu, D.; Xu, G.; Gu, F.; Su, F. A thermodynamic analysis of methanation reactions of carbon oxides for the production of synthetic natural gas. *RSC Advances* **2012**, *2* (6). DOI: 10.1039/c2ra00632d.
- (44) Frei, M. S.; Mondelli, C.; Short, M. I. M.; Pérez-Ramírez, J. Methanol as a Hydrogen Carrier: Kinetic and Thermodynamic Drivers for its CO<sub>2</sub>-Based Synthesis and Reforming over Heterogeneous Catalysts. *ChemSusChem* **2020**, *13* (23), 6330-6337. DOI: <https://doi.org/10.1002/cssc.202001518>.
- (45) Schmidt, O.; Gambhir, A.; Staffell, I.; Hawkes, A.; Nelson, J.; Few, S. Future cost and performance of water electrolysis: An expert elicitation study. *Int. J. Hydrogen Energy* **2017**, *42* (52), 30470-30492. DOI: <https://doi.org/10.1016/j.ijhydene.2017.10.045>.
- (46) Bartholomew, C. H. Carbon Deposition in Steam Reforming and Methanation. *Catalysis Reviews* **1982**, *24* (1), 67-112. DOI: 10.1080/03602458208079650.
- (47) Mutz, B.; Sprenger, P.; Wang, W.; Wang, D.; Kleist, W.; Grunwaldt, J.-D. Operando Raman spectroscopy on CO<sub>2</sub> methanation over alumina-supported Ni, Ni<sub>3</sub>Fe and NiRh<sub>0.1</sub> catalysts: Role of carbon formation as possible deactivation pathway. *Appl. Catal. A: Gen.* **2018**, *556*, 160-171. DOI: 10.1016/j.apcata.2018.01.026.

- (48) Aziz, M. A. A.; Jalil, A. A.; Triwahyono, S.; Ahmad, A. CO<sub>2</sub> methanation over heterogeneous catalysts: recent progress and future prospects. *Green. Chem.* **2015**, *17* (5), 2647-2663, 10.1039/C5GC00119F. DOI: 10.1039/C5GC00119F.
- (49) Mills, G. A.; Steffgen, F. W. Catalytic Methanation. *Catalysis Reviews* **1974**, *8* (1), 159-210. DOI: 10.1080/01614947408071860.
- (50) Weatherbee, G. D.; Bartholomew, C. H. Hydrogenation of CO<sub>2</sub> on group VIII metals: IV. Specific activities and selectivities of silica-supported Co, Fe, and Ru. *J. Catal.* **1984**, *87* (2), 352-362. DOI: [https://doi.org/10.1016/0021-9517\(84\)90196-9](https://doi.org/10.1016/0021-9517(84)90196-9).
- (51) Panagiotopoulou, P. Hydrogenation of CO<sub>2</sub> over supported noble metal catalysts. *Appl. Catal. A: Gen.* **2017**, *542*, 63-70. DOI: 10.1016/j.apcata.2017.05.026.
- (52) Kattel, S.; Liu, P.; Chen, J. G. Tuning Selectivity of CO<sub>2</sub> Hydrogenation Reactions at the Metal/Oxide Interface. *J. Am. Chem. Soc.* **2017**, *139* (29), 9739-9754. DOI: 10.1021/jacs.7b05362.
- (53) Alam, M. I.; Cheula, R.; Moroni, G.; Nardi, L.; Maestri, M. Mechanistic and multiscale aspects of thermo-catalytic CO<sub>2</sub> conversion to C1 products. *Catal. Sci. Technol.* **2021**, *11* (20), 6601-6629, 10.1039/D1CY00922B. DOI: 10.1039/D1CY00922B.
- (54) Karn, F. S.; Shultz, J. F.; Anderson, R. B. Hydrogenation of Carbon Monoxide and Carbon Dioxide on Supported Ruthenium Catalysts at Moderate Pressures. *I&EC Product Research and Development* **1965**, *4* (4), 265-269. DOI: 10.1021/i360016a014.
- (55) Solymosi, F.; Erdöhelyi, A. Hydrogenation of CO<sub>2</sub> to CH<sub>4</sub> over alumina-supported noble metals. *J. Mol. Catal.* **1980**, *8* (4), 471-474. DOI: [https://doi.org/10.1016/0304-5102\(80\)80086-1](https://doi.org/10.1016/0304-5102(80)80086-1).
- (56) Leitenburg, C.; Trovarelli, A.; Kašpar, J. A Temperature-programmed and transient kinetic study of CO<sub>2</sub> activation and methanation over CeO<sub>2</sub> supported noble metals. *J. Catal.* **1997**, *166*, 98.
- (57) Karelavic, A.; Ruiz, P. Improving the Hydrogenation Function of Pd/ $\gamma$ -Al<sub>2</sub>O<sub>3</sub> Catalyst by Rh/ $\gamma$ -Al<sub>2</sub>O<sub>3</sub> Addition in CO<sub>2</sub> Methanation at Low Temperature. *ACS Catal.* **2013**, *3* (12), 2799-2812. DOI: 10.1021/cs400576w.
- (58) Sakpal, T.; Lefferts, L. Structure-dependent activity of CeO<sub>2</sub> supported Ru catalysts for CO<sub>2</sub> methanation. *J. Catal.* **2018**, *367*, 171-180. DOI: <https://doi.org/10.1016/j.jcat.2018.08.027>.
- (59) Wang, F.; Li, C.; Zhang, X.; Wei, M.; Evans, D. G.; Duan, X. Catalytic behavior of supported Ru nanoparticles on the {100}, {110}, and {111} facet of CeO<sub>2</sub>. *J. Catal.* **2015**, *329*, 177-186. DOI: <https://doi.org/10.1016/j.jcat.2015.05.014>.
- (60) Abdel-Mageed, A. M.; Wiese, K.; Parlinska-Wojtan, M.; Rabeah, J.; Brückner, A.; Behm, R. J. Encapsulation of Ru nanoparticles: Modifying the reactivity toward CO and CO<sub>2</sub> methanation on highly active Ru/TiO<sub>2</sub> catalysts. *Appl. Catal. B: Environ.* **2020**, *270*. DOI: 10.1016/j.apcatb.2020.118846.
- (61) Moiola, E.; Mutschler, R.; Züttel, A. Renewable energy storage via CO<sub>2</sub> and H<sub>2</sub> conversion to methane and methanol: Assessment for small scale applications. *Renew. Sustain. Energy Rev.* **2019**, *107*, 497-506. DOI: 10.1016/j.rser.2019.03.022.
- (62) Sassoie, C.; Muller, G.; Debecker, D. P.; Karelavic, A.; Cassaignon, S.; Pizarro, C.; Ruiz, P.; Sanchez, C. A sustainable aqueous route to highly stable suspensions of monodispersed nano ruthenia. *Green. Chem.* **2011**, *13* (11), 3230-3237, 10.1039/C1GC15769H. DOI: 10.1039/C1GC15769H.
- (63) Lin, Q.; Liu, X. Y.; Jiang, Y.; Wang, Y.; Huang, Y.; Zhang, T. Crystal phase effects on the structure and performance of ruthenium nanoparticles for CO<sub>2</sub> hydrogenation. *Catal. Sci. Technol.* **2014**, *4* (7), 2058-2063. DOI: 10.1039/c4cy00030g.
- (64) Kim, A.; Sanchez, C.; Patriarche, G.; Ersen, O.; Moldovan, S.; Wisnet, A.; Sassoie, C.; Debecker, D. P. Selective CO<sub>2</sub> methanation on Ru/TiO<sub>2</sub> catalysts: unravelling the decisive



role of the TiO<sub>2</sub> support crystal structure. *Catal. Sci. Technol.* **2016**, 6 (22), 8117-8128. DOI: 10.1039/c6cy01677d.

(65) Kim, A.; Debecker, D. P.; Devred, F.; Dubois, V.; Sanchez, C.; Sassoey, C. CO<sub>2</sub> methanation on Ru/TiO<sub>2</sub> catalysts: On the effect of mixing anatase and rutile TiO<sub>2</sub> supports. *Appl. Catal. B: Environ.* **2018**, 220, 615-625. DOI: 10.1016/j.apcatb.2017.08.058.

(66) Abe, T.; Tanizawa, M.; Watanabe, K.; Taguchi, A. CO<sub>2</sub> methanation property of Ru nanoparticle-loaded TiO<sub>2</sub> prepared by a polygonal barrel-sputtering method. *Energy & Environmental Science* **2009**, 2 (3). DOI: 10.1039/b817740f.

(67) Panagiotopoulou, P. Methanation of CO<sub>2</sub> over alkali-promoted Ru/TiO<sub>2</sub> catalysts: II. Effect of alkali additives on the reaction pathway. *Appl. Catal. B: Environ.* **2018**, 236, 162-170. DOI: <https://doi.org/10.1016/j.apcatb.2018.05.028>.

(68) Chai, S.; Men, Y.; Wang, J.; Liu, S.; Song, Q.; An, W.; Kolb, G. Boosting CO<sub>2</sub> methanation activity on Ru/TiO<sub>2</sub> catalysts by exposing (001) facets of anatase TiO<sub>2</sub>. *Journal of CO<sub>2</sub> Utilization* **2019**, 33, 242-252. DOI: 10.1016/j.jcou.2019.05.031.

(69) Lin, L.; Wang, K.; Yang, K.; Chen, X.; Fu, X.; Dai, W. The visible-light-assisted thermocatalytic methanation of CO<sub>2</sub> over Ru/TiO<sub>(2-x)</sub>N<sub>x</sub>. *Appl. Catal. B: Environ.* **2017**, 204, 440-455. DOI: <https://doi.org/10.1016/j.apcatb.2016.11.054>.

(70) Guo, Y.; Mei, S.; Yuan, K.; Wang, D.-J.; Liu, H.-C.; Yan, C.-H.; Zhang, Y.-W. Low-Temperature CO<sub>2</sub> Methanation over CeO<sub>2</sub>-Supported Ru Single Atoms, Nanoclusters, and Nanoparticles Competitively Tuned by Strong Metal-Support Interactions and H-Spillover Effect. *ACS Catal.* **2018**, 8 (7), 6203-6215. DOI: 10.1021/acscatal.7b04469.

(71) Daza, Y. A.; Kuhn, J. N. CO<sub>2</sub> conversion by reverse water gas shift catalysis: comparison of catalysts, mechanisms and their consequences for CO<sub>2</sub> conversion to liquid fuels. *RSC Advances* **2016**, 6 (55), 49675-49691. DOI: 10.1039/c6ra05414e.

(72) Kim, S. S.; Lee, H. H.; Hong, S. C. A study on the effect of support's reducibility on the reverse water-gas shift reaction over Pt catalysts. *Appl. Catal. A: Gen.* **2012**, 423-424, 100-107. DOI: <https://doi.org/10.1016/j.apcata.2012.02.021>.

(73) Zhu, M.; Ge, Q.; Zhu, X. Catalytic Reduction of CO<sub>2</sub> to CO via Reverse Water Gas Shift Reaction: Recent Advances in the Design of Active and Selective Supported Metal Catalysts. *Transactions of Tianjin University* **2020**, 26 (3), 172-187. DOI: 10.1007/s12209-020-00246-8.

(74) Ronda-Lloret, M.; Rico-Francés, S.; Sepúlveda-Escribano, A.; Ramos-Fernandez, E. V. CuO<sub>x</sub>/CeO<sub>2</sub> catalyst derived from metal organic framework for reverse water-gas shift reaction. *Appl. Catal. A: Gen.* **2018**, 562, 28-36. DOI: <https://doi.org/10.1016/j.apcata.2018.05.024>.

(75) Chen, C.-S.; Cheng, W.-H.; Lin, S.-S. Study of iron-promoted Cu/SiO<sub>2</sub> catalyst on high temperature reverse water gas shift reaction. *Appl. Catal. A: Gen.* **2004**, 257 (1), 97-106. DOI: [https://doi.org/10.1016/S0926-860X\(03\)00637-9](https://doi.org/10.1016/S0926-860X(03)00637-9).

(76) Jin, R.; Easa, J.; O'Brien, C. P. Highly Active CuO<sub>x</sub>/SiO<sub>2</sub> Dot Core/Rod Shell Catalysts with Enhanced Stability for the Reverse Water Gas Shift Reaction. *ACS Applied Materials & Interfaces* **2021**, 13 (32), 38213-38220. DOI: 10.1021/acsmi.1c06979.

(77) Su, X.; Yang, X.; Zhao, B.; Huang, Y. Designing of highly selective and high-temperature durable RWGS heterogeneous catalysts: recent advances and the future directions. *Journal of Energy Chemistry* **2017**, 26 (5), 854-867. DOI: <https://doi.org/10.1016/j.jechem.2017.07.006>.

(78) Zhang, X.; Zhu, X.; Lin, L.; Yao, S.; Zhang, M.; Liu, X.; Wang, X.; Li, Y.-W.; Shi, C.; Ma, D. Highly Dispersed Copper over β-Mo<sub>2</sub>C as an Efficient and Stable Catalyst for the Reverse Water Gas Shift (RWGS) Reaction. *ACS Catal.* **2017**, 7 (1), 912-918. DOI: 10.1021/acscatal.6b02991.

- (79) Hu, B.; Yin, Y.; Liu, G.; Chen, S.; Hong, X.; Tsang, S. C. E. Hydrogen spillover enabled active Cu sites for methanol synthesis from CO<sub>2</sub> hydrogenation over Pd doped CuZn catalysts. *J. Catal.* **2018**, *359*, 17-26. DOI: <https://doi.org/10.1016/j.jcat.2017.12.029>.
- (80) Xu, D.; Hong, X.; Liu, G. Highly dispersed metal doping to ZnZr oxide catalyst for CO<sub>2</sub> hydrogenation to methanol: Insight into hydrogen spillover. *J. Catal.* **2021**, *393*, 207-214. DOI: <https://doi.org/10.1016/j.jcat.2020.11.039>.
- (81) Ishito, N.; Hara, K.; Nakajima, K.; Fukuoka, A. Selective synthesis of carbon monoxide via formates in reverse water–gas shift reaction over alumina-supported gold catalyst. *Journal of Energy Chemistry* **2016**, *25* (2), 306-310. DOI: <https://doi.org/10.1016/j.jechem.2015.12.005>.
- (82) Wu, C.; Zhang, P.; Zhang, Z.; Zhang, L.; Yang, G.; Han, B. Efficient Hydrogenation of CO<sub>2</sub> to Methanol over Supported Subnanometer Gold Catalysts at Low Temperature. *ChemCatChem* **2017**, *9* (19), 3691-3696. DOI: <https://doi.org/10.1002/cctc.201700872>.
- (83) Zhu, X.; Qu, X.; Li, X.; Liu, J.; Liu, J.; Zhu, B.; Shi, C. Selective reduction of carbon dioxide to carbon monoxide over Au/CeO<sub>2</sub> catalyst and identification of reaction intermediate. *Chinese Journal of Catalysis* **2016**, *37* (12), 2053-2058. DOI: [https://doi.org/10.1016/S1872-2067\(16\)62538-X](https://doi.org/10.1016/S1872-2067(16)62538-X).
- (84) Liu, P.; Zhao, Y.; Qin, R.; Mo, S.; Chen, G.; Gu, L.; Chevrier, D. M.; Zhang, P.; Guo, Q.; Zang, D.; et al. Photochemical route for synthesizing atomically dispersed palladium catalysts. *Science* **2016**, *352* (6287), 797-800. DOI: doi:10.1126/science.aaf5251.
- (85) Vilé, G.; Albani, D.; Nachtegaal, M.; Chen, Z.; Dontsova, D.; Antonietti, M.; López, N.; Pérez-Ramírez, J. A Stable Single-Site Palladium Catalyst for Hydrogenations. *Angew. Chem. Int. Ed.* **2015**, *54* (38), 11265-11269. DOI: <https://doi.org/10.1002/anie.201505073>.
- (86) Pakhare, D.; Spivey, J. A review of dry (CO<sub>2</sub>) reforming of methane over noble metal catalysts. *Chem. Soc. Rev.* **2014**, *43* (22), 7813-7837, 10.1039/C3CS60395D. DOI: 10.1039/C3CS60395D.
- (87) Kattel, S.; Yan, B.; Chen, J. G.; Liu, P. CO<sub>2</sub> hydrogenation on Pt, Pt/SiO<sub>2</sub> and Pt/TiO<sub>2</sub>: Importance of synergy between Pt and oxide support. *J. Catal.* **2016**, *343*, 115-126. DOI: 10.1016/j.jcat.2015.12.019.
- (88) Porosoff, M. D.; Chen, J. G. Trends in the catalytic reduction of CO<sub>2</sub> by hydrogen over supported monometallic and bimetallic catalysts. *J. Catal.* **2013**, *301*, 30-37. DOI: 10.1016/j.jcat.2013.01.022.
- (89) Kyriakou, V.; Vourros, A.; Garagounis, I.; Carabineiro, S. A. C.; Maldonado-Hódar, F. J.; Marnellos, G. E.; Konsolakis, M. Highly active and stable TiO<sub>2</sub>-supported Au nanoparticles for CO<sub>2</sub> reduction. *Catal. Commun.* **2017**, *98*, 52-56. DOI: <https://doi.org/10.1016/j.catcom.2017.05.003>.
- (90) Xu, H.; Li, Y.; Luo, X.; Xu, Z.; Ge, J. Monodispersed gold nanoparticles supported on a zirconium-based porous metal–organic framework and their high catalytic ability for the reverse water–gas shift reaction. *Chem. Commun.* **2017**, *53* (56), 7953-7956, 10.1039/C7CC02130E. DOI: 10.1039/C7CC02130E.
- (91) Ro, I.; Carrasquillo-Flores, R.; Dumesic, J. A.; Huber, G. W. Intrinsic kinetics of plasmon-enhanced reverse water gas shift on Au and Au–Mo interfacial sites supported on silica. *Appl. Catal. A: Gen.* **2016**, *521*, 182-189. DOI: <https://doi.org/10.1016/j.apcata.2015.11.021>.
- (92) Sakurai, H.; Tsubota, S.; Haruta, M. Hydrogenation of CO<sub>2</sub> over gold supported on metal oxides. *Appl. Catal. A: Gen.* **1993**, *102* (2), 125-136. DOI: [https://doi.org/10.1016/0926-860X\(93\)80224-E](https://doi.org/10.1016/0926-860X(93)80224-E).
- (93) Kwak, J. H.; Kovarik, L.; Szanyi, J. CO<sub>2</sub> Reduction on Supported Ru/Al<sub>2</sub>O<sub>3</sub> Catalysts: Cluster Size Dependence of Product Selectivity. *ACS Catal.* **2013**, *3* (11), 2449-2455. DOI: 10.1021/cs400381f.

- (94) Wu, H. C.; Chang, Y. C.; Wu, J. H.; Lin, J. H.; Lin, I. K.; Chen, C. S. Methanation of CO<sub>2</sub> and reverse water gas shift reactions on Ni/SiO<sub>2</sub> catalysts: the influence of particle size on selectivity and reaction pathway. *Catal. Sci. Technol.* **2015**, *5* (8), 4154-4163. DOI: 10.1039/c5cy00667h.
- (95) Kwak, J. H.; Kovarik, L.; Szanyi, J. Heterogeneous Catalysis on Atomically Dispersed Supported Metals: CO<sub>2</sub> Reduction on Multifunctional Pd Catalysts. *ACS Catal.* **2013**, *3* (9), 2094-2100. DOI: 10.1021/cs4001392.
- (96) Loveless, B. T.; Buda, C.; Neurock, M.; Iglesia, E. CO Chemisorption and Dissociation at High Coverages during CO Hydrogenation on Ru Catalysts. *J. Am. Chem. Soc.* **2013**, *135* (16), 6107-6121. DOI: 10.1021/ja311848e.
- (97) Wang, X.; Hong, Y.; Shi, H.; Szanyi, J. Kinetic modeling and transient DRIFTS-MS studies of CO<sub>2</sub> methanation over Ru/Al<sub>2</sub>O<sub>3</sub> catalysts. *J. Catal.* **2016**, *343*, 185-195. DOI: 10.1016/j.jcat.2016.02.001.
- (98) Foppa, L.; Copéret, C.; Comas-Vives, A. Increased Back-Bonding Explains Step-Edge Reactivity and Particle Size Effect for CO Activation on Ru Nanoparticles. *J. Am. Chem. Soc.* **2016**, *138* (51), 16655-16668. DOI: 10.1021/jacs.6b08697.
- (99) Chen, X.; Su, X.; Su, H.-Y.; Liu, X.; Miao, S.; Zhao, Y.; Sun, K.; Huang, Y.; Zhang, T. Theoretical Insights and the Corresponding Construction of Supported Metal Catalysts for Highly Selective CO<sub>2</sub> to CO Conversion. *ACS Catal.* **2017**, *7* (7), 4613-4620. DOI: 10.1021/acscatal.7b00903.
- (100) Vogt, C.; Groeneveld, E.; Kamsma, G.; Nachtegaal, M.; Lu, L.; Kiely, C. J.; Berben, P. H.; Meirer, F.; Weckhuysen, B. M. Unravelling structure sensitivity in CO<sub>2</sub> hydrogenation over nickel. *Nat. Catal.* **2018**, *1* (2), 127-134. DOI: 10.1038/s41929-017-0016-y.
- (101) Chen, L.; Unocic, R. R.; Hoffman, A. S.; Hong, J.; Braga, A. H.; Bao, Z.; Bare, S. R.; Szanyi, J. Unlocking the Catalytic Potential of TiO<sub>2</sub>-Supported Pt Single Atoms for the Reverse Water-Gas Shift Reaction by Altering Their Chemical Environment. *JACS Au* **2021**, *1* (7), 977-986. DOI: 10.1021/jacsau.1c00111.
- (102) Aitbekova, A.; Wu, L.; Wrasman, C. J.; Boubnov, A.; Hoffman, A. S.; Goodman, E. D.; Bare, S. R.; Cargnello, M. Low-Temperature Restructuring of CeO<sub>2</sub>-Supported Ru Nanoparticles Determines Selectivity in CO<sub>2</sub> Catalytic Reduction. *J. Am. Chem. Soc.* **2018**, *140* (42), 13736-13745. DOI: 10.1021/jacs.8b07615.
- (103) Pacchioni, G. Oxygen Vacancy: The Invisible Agent on Oxide Surfaces. *ChemPhysChem* **2003**, *4* (10), 1041-1047. DOI: <https://doi.org/10.1002/cphc.200300835>.
- (104) Campbell, C. T.; Peden, C. H. F. Oxygen Vacancies and Catalysis on Ceria Surfaces. *Science* **2005**, *309* (5735), 713-714. DOI: doi:10.1126/science.1113955.
- (105) Sanchez, M. G.; Gazquez, J. L. Oxygen vacancy model in strong metal-support interaction. *J. Catal.* **1987**, *104* (1), 120-135. DOI: [https://doi.org/10.1016/0021-9517\(87\)90342-3](https://doi.org/10.1016/0021-9517(87)90342-3).
- (106) Campbell, C. T.; Starr, D. E. Metal Adsorption and Adhesion Energies on MgO(100). *J. Am. Chem. Soc.* **2002**, *124* (31), 9212-9218. DOI: 10.1021/ja020146t.
- (107) Farmer, J. A.; Campbell, C. T. Ceria Maintains Smaller Metal Catalyst Particles by Strong Metal-Support Bonding. *Science* **2010**, *329* (5994), 933-936. DOI: doi:10.1126/science.1191778.
- (108) Bogicevic, A.; Jennison, D. R. Effect of oxide vacancies on metal island nucleation. *Surf. Sci.* **2002**, *515* (2), L481-L486. DOI: [https://doi.org/10.1016/S0039-6028\(02\)02024-1](https://doi.org/10.1016/S0039-6028(02)02024-1).
- (109) Venables, J. A.; Harding, J. H. Nucleation and growth of supported metal clusters at defect sites on oxide and halide (001) surfaces. *J. Cryst. Growth* **2000**, *211* (1), 27-33. DOI: [https://doi.org/10.1016/S0022-0248\(99\)00837-4](https://doi.org/10.1016/S0022-0248(99)00837-4).
- (110) Wahlström, E.; Lopez, N.; Schaub, R.; Thostrup, P.; Rønnau, A.; Africh, C.; Lægsgaard, E.; Nørskov, J. K.; Besenbacher, F. Bonding of Gold Nanoclusters to Oxygen

- Vacancies on Rutile TiO<sub>2</sub> (110). *Phys. Rev. Lett.* **2003**, *90* (2), 026101. DOI: 10.1103/PhysRevLett.90.026101.
- (111) Chen, H.-Y. T.; Tosoni, S.; Pacchioni, G. Adsorption of Ruthenium Atoms and Clusters on Anatase TiO<sub>2</sub> and Tetragonal ZrO<sub>2</sub> (101) Surfaces: A Comparative DFT Study. *J. Phys. Chem. C* **2015**, *119* (20), 10856-10868. DOI: 10.1021/jp510468f.
- (112) Wang, F.; He, S.; Chen, H.; Wang, B.; Zheng, L.; Wei, M.; Evans, D. G.; Duan, X. Active Site Dependent Reaction Mechanism over Ru/CeO<sub>2</sub> Catalyst toward CO<sub>2</sub> Methanation. *J. Am. Chem. Soc.* **2016**, *138* (19), 6298-6305. DOI: 10.1021/jacs.6b02762.
- (113) Petala, A.; Panagiotopoulou, P. Methanation of CO<sub>2</sub> over alkali-promoted Ru/TiO<sub>2</sub> catalysts: I. Effect of alkali additives on catalytic activity and selectivity. *Appl. Catal. B: Environ.* **2018**, *224*, 919-927. DOI: 10.1016/j.apcatb.2017.11.048.
- (114) Gao, M.; Zhang, J.; Zhu, P.; Liu, X.; Zheng, Z. Unveiling the origin of alkali metal promotion in CO<sub>2</sub> methanation over Ru/ZrO<sub>2</sub>. *Appl. Catal. B: Environ.* **2022**, *314*, 121476. DOI: <https://doi.org/10.1016/j.apcatb.2022.121476>.
- (115) Heyl, D.; Rodemerck, U.; Bentrup, U. Mechanistic Study of Low-Temperature CO<sub>2</sub> Hydrogenation over Modified Rh/Al<sub>2</sub>O<sub>3</sub> Catalysts. *ACS Catal.* **2016**, *6* (9), 6275-6284. DOI: 10.1021/acscatal.6b01295.
- (116) Li, S.; Xu, Y.; Wang, H.; Teng, B.; Liu, Q.; Li, Q.; Xu, L.; Liu, X.; Lu, J. Tuning the CO<sub>2</sub> Hydrogenation Selectivity of Rhodium Single-Atom Catalysts on Zirconium Dioxide with Alkali Ions. *Angew. Chem.* **2023**, *135* (8), e202218167. DOI: <https://doi.org/10.1002/ange.202218167>.
- (117) Gandara-Loe, J.; Zhang, Q.; Villora-Picó, J. J.; Sepúlveda-Escribano, A.; Pastor-Pérez, L.; Ramirez Reina, T. Design of Full-Temperature-Range RWGS Catalysts: Impact of Alkali Promoters on Ni/CeO<sub>2</sub>. *Energy & Fuels* **2022**, *36* (12), 6362-6373. DOI: 10.1021/acs.energyfuels.2c00784.
- (118) Yan, B.; Zhao, B.; Kattel, S.; Wu, Q.; Yao, S.; Su, D.; Chen, J. G. Tuning CO<sub>2</sub> hydrogenation selectivity via metal-oxide interfacial sites. *J. Catal.* **2019**, *374*, 60-71. DOI: 10.1016/j.jcat.2019.04.036.
- (119) Vrijburg, W. L.; Moioli, E.; Chen, W.; Zhang, M.; Terlingen, B. J. P.; Zijlstra, B.; Filot, I. A. W.; Züttel, A.; Pidko, E. A.; Hensen, E. J. M. Efficient Base-Metal NiMn/TiO<sub>2</sub> Catalyst for CO<sub>2</sub> Methanation. *ACS Catal.* **2019**, *9* (9), 7823-7839. DOI: 10.1021/acscatal.9b01968.
- (120) Mutz, B.; Belimov, M.; Wang, W.; Sprenger, P.; Serrer, M.-A.; Wang, D.; Pfeifer, P.; Kleist, W.; Grunwaldt, J.-D. Potential of an Alumina-Supported Ni<sub>3</sub>Fe Catalyst in the Methanation of CO<sub>2</sub>: Impact of Alloy Formation on Activity and Stability. *ACS Catal.* **2017**, *7* (10), 6802-6814. DOI: 10.1021/acscatal.7b01896.
- (121) Winter, L. R.; Gomez, E.; Yan, B.; Yao, S.; Chen, J. G. Tuning Ni-catalyzed CO<sub>2</sub> hydrogenation selectivity via Ni-ceria support interactions and Ni-Fe bimetallic formation. *Appl. Catal. B: Environ.* **2018**, *224*, 442-450. DOI: 10.1016/j.apcatb.2017.10.036.
- (122) Mihet, M.; Lazar, M. D. Methanation of CO<sub>2</sub> on Ni/γ-Al<sub>2</sub>O<sub>3</sub>: Influence of Pt, Pd or Rh promotion. *Catal. Today* **2018**, *306*, 294-299. DOI: <https://doi.org/10.1016/j.cattod.2016.12.001>.
- (123) Beaumont, S. K.; Alayoglu, S.; Specht, C.; Michalak, W. D.; Pushkarev, V. V.; Guo, J.; Kruse, N.; Somorjai, G. A. Combining in Situ NEXAFS Spectroscopy and CO<sub>2</sub> Methanation Kinetics To Study Pt and Co Nanoparticle Catalysts Reveals Key Insights into the Role of Platinum in Promoted Cobalt Catalysis. *J. Am. Chem. Soc.* **2014**, *136* (28), 9898-9901. DOI: 10.1021/ja505286j.
- (124) Beaumont, S. K.; Alayoglu, S.; Specht, C.; Kruse, N.; Somorjai, G. A. A Nanoscale Demonstration of Hydrogen Atom Spillover and Surface Diffusion Across Silica Using the Kinetics of CO<sub>2</sub> Methanation Catalyzed on Spatially Separate Pt and Co Nanoparticles. *Nano Lett.* **2014**, *14* (8), 4792-4796. DOI: 10.1021/nl501969k.

- (125) Álvarez, A.; Borges, M.; Corral-Pérez, J. J.; Olcina, J. G.; Hu, L.; Cornu, D.; Huang, R.; Stoian, D.; Urakawa, A. CO<sub>2</sub> Activation over Catalytic Surfaces. *ChemPhysChem* **2017**, *18* (22), 3135-3141. DOI: <https://doi.org/10.1002/cphc.201700782>.
- (126) Huygh, S.; Bogaerts, A.; Neyts, E. C. How Oxygen Vacancies Activate CO<sub>2</sub> Dissociation on TiO<sub>2</sub> Anatase (001). *J. Phys. Chem. C* **2016**, *120* (38), 21659-21669. DOI: 10.1021/acs.jpcc.6b07459.
- (127) Sági, A.; Halasi, G.; Kiss, J.; Dobó, D. G.; Juhász, K. L.; Kolcsár, V. J.; Ferencz, Z.; Vári, G.; Matolin, V.; Erdőhelyi, A.; et al. In Situ DRIFTS and NAP-XPS Exploration of the Complexity of CO<sub>2</sub> Hydrogenation over Size-Controlled Pt Nanoparticles Supported on Mesoporous NiO. *J. Phys. Chem. C* **2018**, *122* (10), 5553-5565. DOI: 10.1021/acs.jpcc.8b00061.
- (128) Zhao, K.; Wang, L.; Calizzi, M.; Moioli, E.; Züttel, A. In Situ Control of the Adsorption Species in CO<sub>2</sub> Hydrogenation: Determination of Intermediates and Byproducts. *J. Phys. Chem. C* **2018**, *122* (36), 20888-20893. DOI: 10.1021/acs.jpcc.8b06508.
- (129) Falbo, L.; Visconti, C. G.; Lietti, L.; Szanyi, J. The effect of CO on CO<sub>2</sub> methanation over Ru/Al<sub>2</sub>O<sub>3</sub> catalysts: a combined steady-state reactivity and transient DRIFT spectroscopy study. *Appl. Catal. B: Environ.* **2019**, *256*. DOI: 10.1016/j.apcatb.2019.117791.
- (130) Xu, X.; Liu, L.; Tong, Y.; Fang, X.; Xu, J.; Jiang, D.-e.; Wang, X. Facile Cr<sup>3+</sup>-Doping Strategy Dramatically Promoting Ru/CeO<sub>2</sub> for Low-Temperature CO<sub>2</sub> Methanation: Unraveling the Roles of Surface Oxygen Vacancies and Hydroxyl Groups. *ACS Catal.* **2021**, *11* (9), 5762-5775. DOI: 10.1021/acscatal.0c05468.
- (131) Miao, B.; Ma, S. S. K.; Wang, X.; Su, H.; Chan, S. H. Catalysis mechanisms of CO<sub>2</sub> and CO methanation. *Catal. Sci. Technol.* **2016**, *6* (12), 4048-4058. DOI: 10.1039/c6cy00478d.
- (132) Kattel, S.; Yu, W.; Yang, X.; Yan, B.; Huang, Y.; Wan, W.; Liu, P.; Chen, J. G. CO<sub>2</sub> Hydrogenation over Oxide-Supported PtCo Catalysts: The Role of the Oxide Support in Determining the Product Selectivity. *Angew. Chem. Int. Ed. Engl.* **2016**, *55* (28), 7968-7973. DOI: 10.1002/anie.201601661.
- (133) Aitbekova, A.; Goodman, E. D.; Wu, L.; Boubnov, A.; Hoffman, A. S.; Genc, A.; Cheng, H.; Casalena, L.; Bare, S. R.; Cargnello, M. Engineering of Ruthenium-Iron Oxide Colloidal Heterostructures: Improved Yields in CO<sub>2</sub> Hydrogenation to Hydrocarbons. *Angew. Chem. Int. Ed. Engl.* **2019**, *58* (48), 17451-17457. DOI: 10.1002/anie.201910579.
- (134) Campbell, C. T. Electronic perturbations. *Nature Chemistry* **2012**, *4* (8), 597-598. DOI: 10.1038/nchem.1412.
- (135) Tauster, S. J.; Fung, S. C.; Baker, R. T. K.; Horsley, J. A. Strong Interactions in Supported-Metal Catalysts. *Science* **1981**, *211* (4487), 1121-1125. DOI: 10.1126/science.211.4487.1121.
- (136) Koschany, F.; Schlereth, D.; Hinrichsen, O. On the kinetics of the methanation of carbon dioxide on coprecipitated NiAl(O)<sub>x</sub>. *Appl. Catal. B: Environ.* **2016**, *181*, 504-516. DOI: <https://doi.org/10.1016/j.apcatb.2015.07.026>.
- (137) Avanesian, T.; Gusmão, G. S.; Christopher, P. Mechanism of CO<sub>2</sub> reduction by H<sub>2</sub> on Ru(0001) and general selectivity descriptors for late-transition metal catalysts. *J. Catal.* **2016**, *343*, 86-96. DOI: 10.1016/j.jcat.2016.03.016.
- (138) Chang, X.; Wang, T.; Gong, J. CO<sub>2</sub> photo-reduction: insights into CO<sub>2</sub> activation and reaction on surfaces of photocatalysts. *Energy & Environmental Science* **2016**, *9* (7), 2177-2196, 10.1039/C6EE00383D. DOI: 10.1039/C6EE00383D.
- (139) Kondratenko, E. V.; Mul, G.; Baltrusaitis, J.; Larrazábal, G. O.; Pérez-Ramírez, J. Status and perspectives of CO<sub>2</sub> conversion into fuels and chemicals by catalytic, photocatalytic and electrocatalytic processes. *Energy & Environmental Science* **2013**, *6* (11). DOI: 10.1039/c3ee41272e.

- (140) Gutiérrez-Sánchez, O.; Bohlen, B.; Daems, N.; Bulut, M.; Pant, D.; Breugelmans, T. A State-of-the-Art Update on Integrated CO<sub>2</sub> Capture and Electrochemical Conversion Systems. *ChemElectroChem* **2022**, *9* (5), e202101540. DOI: <https://doi.org/10.1002/celec.202101540>.
- (141) Bagger, A.; Ju, W.; Varela, A. S.; Strasser, P.; Rossmeisl, J. Electrochemical CO<sub>2</sub> Reduction: A Classification Problem. *ChemPhysChem* **2017**, *18* (22), 3266-3273. DOI: <https://doi.org/10.1002/cphc.201700736>.
- (142) Ward, D. A.; Ko, E. I. Preparing Catalytic Materials by the Sol-Gel Method. *Industrial & Engineering Chemistry Research* **1995**, *34* (2), 421-433. DOI: 10.1021/ie00041a001.
- (143) Ertl, G.; Knözinger, H.; Weitkamp, J. *Preparation of Solid Catalysts*; Wiley, 2008.
- (144) Niemantsverdriet, J. W. *Spectroscopy in Catalysis: An Introduction*; Wiley, 2007.
- (145) Hanefeld, U.; Lefferts, L. *Catalysis: An Integrated Textbook for Students*; Wiley, 2018.
- (146) Banwell, C. N.; McCash, E. M. *Fundamentals of Molecular Spectroscopy*; McGraw-Hill, 1994.
- (147) Brückner, A. In situ electron paramagnetic resonance: a unique tool for analyzing structure–reactivity relationships in heterogeneous catalysis. *Chem. Soc. Rev.* **2010**, *39* (12), 4673-4684, 10.1039/B919541F. DOI: 10.1039/B919541F.
- (148) Berger, P. A.; Roth, J. F. Copper oxide supported on alumina. II. Electron spin resonance studies of highly dispersed phases. *The Journal of Physical Chemistry* **1967**, *71* (13), 4307-4315.
- (149) Bonke, S. A.; Risse, T.; Schnegg, A.; Brückner, A. In situ electron paramagnetic resonance spectroscopy for catalysis. *Nature Reviews Methods Primers* **2021**, *1* (1), 33. DOI: 10.1038/s43586-021-00031-4.
- (150) Chiesa, M.; Giamello, E.; Che, M. EPR characterization and reactivity of surface-localized inorganic radicals and radical ions. *Chem. Rev.* **2010**, *110* (3), 1320-1347.
- (151) Weckhuysen, B. M.; Baetens, D.; Schoonheydt, R. A. Spectroscopy of the Formation of Microporous Transition Metal Ion Containing Aluminophosphates under Hydrothermal Conditions. *Angew. Chem. Int. Ed.* **2000**, *39* (19), 3419-3422. DOI: [https://doi.org/10.1002/1521-3773\(20001002\)39:19<3419::AID-ANIE3419>3.0.CO;2-R](https://doi.org/10.1002/1521-3773(20001002)39:19<3419::AID-ANIE3419>3.0.CO;2-R).
- (152) Salmeron, M.; Schlögl, R. Ambient pressure photoelectron spectroscopy: A new tool for surface science and nanotechnology. *Surf. Sci. Rep.* **2008**, *63* (4), 169-199. DOI: <https://doi.org/10.1016/j.surfrep.2008.01.001>.
- (153) Patel, D. I.; Roychowdhury, T.; Jain, V.; Shah, D.; Avval, T. G.; Chatterjee, S.; Bahr, S.; Dietrich, P.; Meyer, M.; Thißen, A.; et al. Introduction to near-ambient pressure x-ray photoelectron spectroscopy characterization of various materials. *Surf. Sci. Spectra* **2019**, *26* (1). DOI: 10.1116/1.5109118 (accessed 4/24/2023).
- (154) Scofield, J. H. Hartree-Slater subshell photoionization cross-sections at 1254 and 1487 eV. *J. Electron. Spectrosc. Relat. Phenom.* **1976**, *8* (2), 129-137. DOI: [https://doi.org/10.1016/0368-2048\(76\)80015-1](https://doi.org/10.1016/0368-2048(76)80015-1).
- (155) Delannay, F. *Characterization of Heterogeneous Catalysts*; M. Dekker, 1984.
- (156) Thommes, M.; Kaneko, K.; Neimark, A. V.; Olivier, J. P.; Rodriguez-Reinoso, F.; Rouquerol, J.; Sing, K. S. W. Physisorption of gases, with special reference to the evaluation of surface area and pore size distribution (IUPAC Technical Report). **2015**, *87* (9-10), 1051-1069. DOI: doi:10.1515/pac-2014-1117 (accessed 2022-10-20).
- (157) Sing, K. S. W. Reporting physisorption data for gas/solid systems with special reference to the determination of surface area and porosity (Recommendations 1984). *Pure Appl. Chem.* **1985**, *57* (4), 603-619. DOI: doi:10.1351/pac198557040603 (accessed 2023-04-28).
- (158) Hou, X. Inductively\_Coupled Plasma/Optical Emission Spectrometry. *Encyclopedia of Analytical Chemistry* **2000**, 9468-9485.

- (159) Pérez-Ramírez, J.; Kondratenko, E. V. Evolution, achievements, and perspectives of the TAP technique. *Catal. Today* **2007**, *121* (3), 160-169. DOI: <https://doi.org/10.1016/j.cattod.2007.01.001>.
- (160) Morgan, K.; Maguire, N.; Fushimi, R.; Gleaves, J. T.; Goguet, A.; Harold, M. P.; Kondratenko, E. V.; Menon, U.; Schuurman, Y.; Yablonsky, G. S. Forty years of temporal analysis of products. *Catal. Sci. Technol.* **2017**, *7* (12), 2416-2439, 10.1039/C7CY00678K. DOI: 10.1039/C7CY00678K.
- (161) Gleaves, J. T.; Yablonskii, G. S.; Phanawadee, P.; Schuurman, Y. TAP-2: An interrogative kinetics approach. *Appl. Catal. A: Gen.* **1997**, *160* (1), 55-88. DOI: [https://doi.org/10.1016/S0926-860X\(97\)00124-5](https://doi.org/10.1016/S0926-860X(97)00124-5).
- (162) Rothaemel, M.; Baerns, M. Modeling and Simulation of Transient Adsorption and Reaction in Vacuum Using the Temporal Analysis of Products Reactor. *Industrial & Engineering Chemistry Research* **1996**, *35* (5), 1556-1565. DOI: 10.1021/ie950379b.
- (163) Soick, M.; Wolf, D.; Baerns, M. Determination of kinetic parameters for complex heterogeneous catalytic reactions by numerical evaluation of TAP experiments. *Chem. Eng. Sci.* **2000**, *55* (15), 2875-2882. DOI: [https://doi.org/10.1016/S0009-2509\(99\)00553-9](https://doi.org/10.1016/S0009-2509(99)00553-9).
- (164) Bergeret, G.; Gallezot, P. Particle Size and Dispersion Measurements. In *Handbook of Heterogeneous Catalysis*, pp 738-765.
- (165) Sing, K. S. W. The use of gas adsorption for the characterization of porous solids. *Colloids and Surfaces* **1989**, *38* (1), 113-124. DOI: [https://doi.org/10.1016/0166-6622\(89\)80148-9](https://doi.org/10.1016/0166-6622(89)80148-9).
- (166) Wang, X.; Gordon, R. G. High-Quality Epitaxy of Ruthenium Dioxide, RuO<sub>2</sub>, on Rutile Titanium Dioxide, TiO<sub>2</sub>, by Pulsed Chemical Vapor Deposition. *Crystal Growth & Design* **2013**, *13* (3), 1316-1321. DOI: 10.1021/cg301801h.
- (167) Kim, A.; Sanchez, C.; Haye, B.; Boissière, C.; Sasse, C.; Debecker, D. P. Mesoporous TiO<sub>2</sub> Support Materials for Ru-Based CO<sub>2</sub> Methanation Catalysts. *ACS Applied Nano Materials* **2019**, *2* (5), 3220-3230. DOI: 10.1021/acsanm.9b00518.
- (168) Zhang, H.; Banfield, J. F. Understanding Polymorphic Phase Transformation Behavior during Growth of Nanocrystalline Aggregates: Insights from TiO<sub>2</sub>. *J. Phys. Chem. B.* **2000**, *104* (15), 3481-3487. DOI: 10.1021/jp000499j.
- (169) Zhang, W. F.; He, Y. L.; Zhang, M. S.; Yin, Z.; Chen, Q. Raman scattering study on anatase TiO<sub>2</sub> nanocrystals. *J. Phys. D: Appl. Phys.* **2000**, *33* (8), 912-916. DOI: 10.1088/0022-3727/33/8/305.
- (170) Ma, H. L.; Yang, J. Y.; Dai, Y.; Zhang, Y. B.; Lu, B.; Ma, G. H. Raman study of phase transformation of TiO<sub>2</sub> rutile single crystal irradiated by infrared femtosecond laser. *Appl. Surf. Sci.* **2007**, *253* (18), 7497-7500. DOI: <https://doi.org/10.1016/j.apsusc.2007.03.047>.
- (171) Zhang, M.-S.; Yin, Z.; Chen, Q.; Xijun, W.; Xiaoli, J. Raman scattering by nanophase titanium dioxide. *Ferroelectrics* **1995**, *168* (1), 131-137. DOI: 10.1080/00150199508007856.
- (172) Lunde, P. J.; Kester, F. L. Carbon Dioxide Methanation on a Ruthenium Catalyst. *Industrial & Engineering Chemistry Process Design and Development* **1974**, *13* (1), 27-33. DOI: 10.1021/i260049a005.
- (173) Shen, X.; Garces, L.-J.; Ding, Y.; Laubernds, K.; Zenger, R. P.; Aindow, M.; Neth, E. J.; Suib, S. L. Behavior of H<sub>2</sub> chemisorption on Ru/TiO<sub>2</sub> surface and its application in evaluation of Ru particle sizes compared with TEM and XRD analyses. *Appl. Catal. A: Gen.* **2008**, *335* (2), 187-195. DOI: <https://doi.org/10.1016/j.apcata.2007.11.017>.
- (174) Karim, A. M.; Prasad, V.; Mpourmpakis, G.; Lonergan, W. W.; Frenkel, A. I.; Chen, J. G.; Vlachos, D. G. Correlating Particle Size and Shape of Supported Ru/γ-Al<sub>2</sub>O<sub>3</sub> Catalysts with NH<sub>3</sub> Decomposition Activity. *J. Am. Chem. Soc.* **2009**, *131* (34), 12230-12239. DOI: 10.1021/ja902587k.

- (175) Bianchi, C. L.; Ragaini, V.; Cattania, M. G. An XPS study on ruthenium compounds and catalysts. *Mater. Chem. Phys.* **1991**, *29* (1), 297-306. DOI: [https://doi.org/10.1016/0254-0584\(91\)90025-P](https://doi.org/10.1016/0254-0584(91)90025-P).
- (176) Kim, K. S.; Winograd, N. X-Ray photoelectron spectroscopic studies of ruthenium-oxygen surfaces. *J. Catal.* **1974**, *35* (1), 66-72. DOI: [https://doi.org/10.1016/0021-9517\(74\)90184-5](https://doi.org/10.1016/0021-9517(74)90184-5).
- (177) Morgan, D. J. Resolving ruthenium: XPS studies of common ruthenium materials. *Surf. Interface Anal.* **2015**, *47* (11), 1072-1079, <https://doi.org/10.1002/sia.5852>. DOI: <https://doi.org/10.1002/sia.5852> (accessed 2021/04/26).
- (178) Gu, Q.; Gao, Z.; Yu, S.; Xue, C. Constructing Ru/TiO<sub>2</sub> Heteronanostructures Toward Enhanced Photocatalytic Water Splitting via a RuO<sub>2</sub>/TiO<sub>2</sub> Heterojunction and Ru/TiO<sub>2</sub> Schottky Junction. *Advanced Materials Interfaces* **2016**, *3* (4), 1500631, <https://doi.org/10.1002/admi.201500631>. DOI: <https://doi.org/10.1002/admi.201500631> (accessed 2021/04/27).
- (179) Kim, Y. J.; Gao, Y.; Chambers, S. A. Core-level X-ray photoelectron spectra and X-ray photoelectron diffraction of RuO<sub>2</sub> (110) grown by molecular beam epitaxy on TiO<sub>2</sub> (110). *Appl. Surf. Sci.* **1997**, *120* (3), 250-260. DOI: [https://doi.org/10.1016/S0169-4332\(97\)00233-X](https://doi.org/10.1016/S0169-4332(97)00233-X).
- (180) Greczynski, G.; Hultman, L. X-ray photoelectron spectroscopy: Towards reliable binding energy referencing. *Prog. Mater. Sci.* **2020**, *107*, 100591. DOI: <https://doi.org/10.1016/j.pmatsci.2019.100591>.
- (181) Deng, X.; Verdaguer, A.; Herranz, T.; Weis, C.; Bluhm, H.; Salmeron, M. Surface Chemistry of Cu in the Presence of CO<sub>2</sub> and H<sub>2</sub>O. *Langmuir* **2008**, *24* (17), 9474-9478. DOI: 10.1021/la8011052.
- (182) Wang, X.; Shi, H.; Szanyi, J. Controlling selectivities in CO<sub>2</sub> reduction through mechanistic understanding. *Nat Commun* **2017**, *8* (1), 513. DOI: 10.1038/s41467-017-00558-9.
- (183) Li, X.; Lin, J.; Li, L.; Huang, Y.; Pan, X.; Collins, S. E.; Ren, Y.; Su, Y.; Kang, L.; Liu, X.; et al. Controlling CO<sub>2</sub> Hydrogenation Selectivity by Metal-Supported Electron Transfer. *Angew. Chem. Int. Ed. Engl.* **2020**. DOI: 10.1002/anie.202003847.
- (184) Carencio, S.; Sassoie, C.; Faustini, M.; Eloy, P.; Debecker, D. P.; Bluhm, H.; Salmeron, M. The Active State of Supported Ruthenium Oxide Nanoparticles during Carbon Dioxide Methanation. *J. Phys. Chem. C.* **2016**, *120* (28), 15354-15361. DOI: 10.1021/acs.jpcc.6b06313.
- (185) Coronado, J. M.; Maira, A. J.; Conesa, J. C.; Yeung, K. L.; Augugliaro, V.; Soria, J. EPR Study of the Surface Characteristics of Nanostructured TiO<sub>2</sub> under UV Irradiation. *Langmuir* **2001**, *17* (17), 5368-5374. DOI: 10.1021/la010153f.
- (186) Mohajernia, S.; Andryskova, P.; Zoppellaro, G.; Hejazi, S.; Kment, S.; Zboril, R.; Schmidt, J.; Schmuki, P. Influence of Ti<sup>3+</sup> defect-type on heterogeneous photocatalytic H<sub>2</sub> evolution activity of TiO<sub>2</sub>. *Journal of Materials Chemistry A* **2020**, *8* (3), 1432-1442, 10.1039/C9TA10855F. DOI: 10.1039/C9TA10855F.
- (187) Howe, R. F.; Gratzel, M. EPR observation of trapped electrons in colloidal titanium dioxide. *The Journal of Physical Chemistry* **1985**, *89* (21), 4495-4499. DOI: 10.1021/j100267a018.
- (188) Livraghi, S.; Chiesa, M.; Paganini, M. C.; Giamello, E. On the Nature of Reduced States in Titanium Dioxide As Monitored by Electron Paramagnetic Resonance. I: The Anatase Case. *J. Phys. Chem. C.* **2011**, *115* (51), 25413-25421. DOI: 10.1021/jp209075m.
- (189) Chiesa, M.; Paganini, M. C.; Livraghi, S.; Giamello, E. Charge trapping in TiO<sub>2</sub> polymorphs as seen by Electron Paramagnetic Resonance spectroscopy. *Physical Chemistry*



- Chemical Physics* **2013**, *15* (24), 9435-9447, 10.1039/C3CP50658D. DOI: 10.1039/C3CP50658D.
- (190) Valigi, M.; Cordischi, D.; Gazzoli, D.; Keijzers, K. P.; Klaassen, A. A. K. Formation and stability of RuIII incorporated in TiO<sub>2</sub> (rutile). *Journal of the Chemical Society, Faraday Transactions 1: Physical Chemistry in Condensed Phases* **1985**, *81* (3), 813-820, 10.1039/F19858100813. DOI: 10.1039/F19858100813.
- (191) Gupta, N. M.; Kamble, V. S.; Kartha, V. B.; Iyer, R. M.; Ravindranathan Thampi, K.; Grätzel, M. FTIR spectroscopic study of the interaction of CO<sub>2</sub> and CO<sub>2</sub> + H<sub>2</sub> over partially oxidized Ru/TiO<sub>2</sub> catalyst. *J. Catal.* **1994**, *146*, 173.
- (192) Marwood, M.; Doepper, R.; Renken, A. In-situ surface and gas phase analysis for kinetic studies under transient conditions The catalytic hydrogenation of CO<sub>2</sub>. *Appl. Catal. A: Gen.* **1997**, *151* (1), 223-246. DOI: [https://doi.org/10.1016/S0926-860X\(96\)00267-0](https://doi.org/10.1016/S0926-860X(96)00267-0).
- (193) Panagiotopoulou, P.; Kondarides, D. I.; Verykios, X. E. Mechanistic aspects of the selective methanation of CO over Ru/TiO<sub>2</sub> catalyst. *Catal. Today* **2012**, *181* (1), 138-147. DOI: <https://doi.org/10.1016/j.cattod.2011.05.030>.
- (194) Kamble, V. S.; Londhe, V. P.; Gupta, N. M.; Thampi, K. R.; Grätzel, M. Studies on the Sulfur Poisoning of Ru–RuO<sub>x</sub>/TiO<sub>2</sub> Catalyst for the Adsorption and Methanation of Carbon Monoxide. *J. Catal.* **1996**, *158* (2), 427-438. DOI: <https://doi.org/10.1006/jcat.1996.0044>.
- (195) Kellner, C. S.; Bell, A. T. Infrared studies of carbon monoxide hydrogenation over alumina-supported ruthenium. *J. Catal.* **1981**, *71* (2), 296-307. DOI: [https://doi.org/10.1016/0021-9517\(81\)90232-3](https://doi.org/10.1016/0021-9517(81)90232-3).
- (196) Panagiotopoulou, P.; Verykios, X. E. Mechanistic Study of the Selective Methanation of CO over Ru/TiO<sub>2</sub> Catalysts: Effect of Metal Crystallite Size on the Nature of Active Surface Species and Reaction Pathways. *J. Phys. Chem. C.* **2017**, *121* (9), 5058-5068. DOI: 10.1021/acs.jpcc.6b12091.
- (197) Chin, S. Y.; Williams, C. T.; Amiridis, M. D. FTIR Studies of CO Adsorption on Al<sub>2</sub>O<sub>3</sub>- and SiO<sub>2</sub>-Supported Ru Catalysts. *J. Phys. Chem. B.* **2006**, *110* (2), 871-882. DOI: 10.1021/jp053908q.
- (198) Yan, Y.; Wang, Q.; Jiang, C.; Yao, Y.; Lu, D.; Zheng, J.; Dai, Y.; Wang, H.; Yang, Y. Ru/Al<sub>2</sub>O<sub>3</sub> catalyzed CO<sub>2</sub> hydrogenation: Oxygen-exchange on metal-support interfaces. *J. Catal.* **2018**, *367*, 194-205. DOI: 10.1016/j.jcat.2018.08.026.
- (199) Pokrovski, K.; Jung, K. T.; Bell, A. T. Investigation of CO and CO<sub>2</sub> Adsorption on Tetragonal and Monoclinic Zirconia. *Langmuir* **2001**, *17* (14), 4297-4303. DOI: 10.1021/la001723z.
- (200) Chen, S.; Cao, T.; Gao, Y.; Li, D.; Xiong, F.; Huang, W. Probing Surface Structures of CeO<sub>2</sub>, TiO<sub>2</sub>, and Cu<sub>2</sub>O Nanocrystals with CO and CO<sub>2</sub> Chemisorption. *J. Phys. Chem. C.* **2016**, *120* (38), 21472-21485. DOI: 10.1021/acs.jpcc.6b06158.
- (201) Robbins, J. L. Chemistry of supported Ru: CO-induced oxidation of Ru at 310 K. *J. Catal.* **1989**, *115* (1), 120-131. DOI: [https://doi.org/10.1016/0021-9517\(89\)90012-2](https://doi.org/10.1016/0021-9517(89)90012-2).
- (202) Solymosi, F.; Raskó, J. An infrared study of the influence of CO adsorption on the topology of supported ruthenium. *J. Catal.* **1989**, *115*, 107.
- (203) Nie, X.; Wang, H.; Li, W.; Chen, Y.; Guo, X.; Song, C. DFT insight into the support effect on the adsorption and activation of key species over Co catalysts for CO<sub>2</sub> methanation. *Journal of CO<sub>2</sub> Utilization* **2018**, *24*, 99-111. DOI: <https://doi.org/10.1016/j.jcou.2017.12.005>.
- (204) Chen, S.; Abdel-Mageed, A. M.; Gauckler, C.; Olesen, S. E.; Chorkendorff, I.; Behm, R. J. Selective CO methanation on isostructural Ru nanocatalysts: The role of support effects. *J. Catal.* **2019**, *373*, 103-115. DOI: <https://doi.org/10.1016/j.jcat.2019.03.015>.
- (205) SIM, S. M.; STUBICAN, V. S. Phase Relations and Ordering in the System ZrO<sub>2</sub>-MgO. *J. Am. Ceram. Soc.* **1987**, *70* (7), 521-526. DOI: <https://doi.org/10.1111/j.1151-2916.1987.tb05687.x>.

- (206) Buyakova, S. P.; Kalatur, E. S.; Buyakov, A. S.; Kulkov, S. S. Structure and properties of ZrO<sub>2</sub>-MgO powders. *IOP Conference Series: Materials Science and Engineering* **2016**, *123* (1), 012040. DOI: 10.1088/1757-899X/123/1/012040.
- (207) Kim, D.-J. Lattice Parameters, Ionic Conductivities, and Solubility Limits in Fluorite-Structure MO<sub>2</sub> Oxide [M = Hf<sup>4+</sup>, Zr<sup>4+</sup>, Ce<sup>4+</sup>, Th<sup>4+</sup>, U<sup>4+</sup>] Solid Solutions. *J. Am. Ceram. Soc.* **1989**, *72* (8), 1415-1421. DOI: <https://doi.org/10.1111/j.1151-2916.1989.tb07663.x>.
- (208) Yildirim, H.; Pachter, R. Extrinsic Dopant Effects on Oxygen Vacancy Formation Energies in ZrO<sub>2</sub> with Implication for Memristive Device Performance. *ACS Appl. Electron. Mater.* **2019**, *1* (4), 467-477. DOI: 10.1021/acsaelm.8b00090.
- (209) Chen, T.; Foo, C.; Edman Tsang, S. C. Interstitial and substitutional light elements in transition metals for heterogeneous catalysis. *Chem. Sci.* **2021**, *12* (2), 517-532, 10.1039/D0SC06496C. DOI: 10.1039/D0SC06496C.
- (210) Stefanovich, E. V.; Shluger, A. L.; Catlow, C. R. A. Theoretical study of the stabilization of cubic-phase ZrO<sub>2</sub> by impurities. *Physical Review B* **1994**, *49* (17), 11560-11571. DOI: 10.1103/PhysRevB.49.11560.
- (211) Mazzieri, V.; Coloma-Pascual, F.; Arcoya, A.; L'Argentière, P. C.; F1; x; goli, N. S. XPS, FTIR and TPR characterization of Ru/Al<sub>2</sub>O<sub>3</sub> catalysts. *Appl. Surf. Sci.* **2003**, *210* (3), 222-230. DOI: [https://doi.org/10.1016/S0169-4332\(03\)00146-6](https://doi.org/10.1016/S0169-4332(03)00146-6).
- (212) Yu, J.; Zhao, D.; Xu, X.; Wang, X.; Zhang, N. Study on RuO<sub>2</sub>/SnO<sub>2</sub>: Novel and Active Catalysts for CO and CH<sub>4</sub> Oxidation. *ChemCatChem* **2012**, *4* (8), 1122-1132. DOI: <https://doi.org/10.1002/cctc.201200038>.
- (213) Hoang, D. L.; Lieske, H. Effect of hydrogen treatments on ZrO<sub>2</sub> and Pt/ZrO<sub>2</sub> catalysts. *Catal. Lett.* **1994**, *27* (1), 33-42. DOI: 10.1007/BF00806975.
- (214) Li, D.; Ichikuni, N.; Shimazu, S.; Uematsu, T. Hydrogenation of CO<sub>2</sub> over sprayed Ru/TiO<sub>2</sub> fine particles and strong metal-support interaction. *Appl. Catal. A: Gen.* **1999**, *180* (1), 227-235. DOI: [https://doi.org/10.1016/S0926-860X\(98\)00335-4](https://doi.org/10.1016/S0926-860X(98)00335-4).
- (215) Cisneros, S.; Chen, S.; Fauth, C.; Abdel-Mageed, A. M.; Pollastri, S.; Bansmann, J.; Olivi, L.; Aquilanti, G.; Atia, H.; Rabeah, J.; et al. Controlling the selectivity of high-surface-area Ru/TiO<sub>2</sub> catalysts in CO<sub>2</sub> reduction - modifying the reaction properties by Si doping of the support. *Appl. Catal. B: Environ.* **2022**, *317*, 121748. DOI: <https://doi.org/10.1016/j.apcatb.2022.121748>.
- (216) Chen, S.; Abdel-Mageed, A. M.; Dyballa, M.; Parlinska-Wojtan, M.; Bansmann, J.; Pollastri, S.; Olivi, L.; Aquilanti, G.; Behm, R. J. Raising the CO<sub>x</sub> Methanation Activity of a Ru/γ-Al<sub>2</sub>O<sub>3</sub> Catalyst by Activated Modification of Metal-Support Interactions. *Angew. Chem. Int. Ed. Engl.* **2020**. DOI: 10.1002/anie.202007228.
- (217) Reddy, B. M.; Lakshmanan, P.; Khan, A. Investigation of Surface Structures of Dispersed V<sub>2</sub>O<sub>5</sub> on CeO<sub>2</sub>-SiO<sub>2</sub>, CeO<sub>2</sub>-TiO<sub>2</sub>, and CeO<sub>2</sub>-ZrO<sub>2</sub> Mixed Oxides by XRD, Raman, and XPS Techniques. *J. Phys. Chem. B.* **2004**, *108* (43), 16855-16863. DOI: 10.1021/jp047217q.
- (218) Occhuzzi, M.; Cordischi, D.; Dragone, R. Intrinsic and Extrinsic Paramagnetic Centers in Zirconia. *J. Phys. Chem. B.* **2002**, *106* (48), 12464-12469. DOI: 10.1021/jp0206830.
- (219) Rabeah, A. I. M.; Zhao, D.; Cisneros, S.; Kreyenschulte, C. R.; Kondratenko, V.; Bartling, S.; Kubis, C.; Kondratenko, E. V.; Brückner, A.; Rabeah, J. Role of interfacial oxygen vacancies in low-loaded Au-based catalysts for the low-temperature reverse water gas shift reaction. *Appl. Catal. B: Environ.* **2023**, *321*, 122083. DOI: <https://doi.org/10.1016/j.apcatb.2022.122083>.
- (220) Gionco, C.; Paganini, M. C.; Giamello, E.; Burgess, R.; Di Valentin, C.; Pacchioni, G. Paramagnetic Defects in Polycrystalline Zirconia: An EPR and DFT Study. *Chem. Mater.* **2013**, *25* (11), 2243-2253. DOI: 10.1021/cm400728j.

- (221) Cisneros, S.; Chen, S.; Diemant, T.; Bansmann, J.; Abdel-Mageed, A. M.; Goepel, M.; Olesen, S. E.; Welter, E. S.; Parlinska-Wojtan, M.; Gläser, R.; et al. Effects of SiO<sub>2</sub>-doping on high-surface-area Ru/TiO<sub>2</sub> catalysts for the selective CO methanation. *Appl. Catal. B: Environ.* **2021**, *282*. DOI: 10.1016/j.apcatb.2020.119483.
- (222) Kiwi, J.; Prins, R. EPR evidence for ruthenium variable valence states in active oxidative catalysts. *Chem. Phys. Lett.* **1986**, *126* (6), 579-582. DOI: [https://doi.org/10.1016/S0009-2614\(86\)80177-4](https://doi.org/10.1016/S0009-2614(86)80177-4).
- (223) Callens, F.; Vanhaelewyn, G.; Matthys, P.; Boesman, E. EPR of carbonate derived radicals: Applications in dosimetry, dating and detection of irradiated food. *Appl. Magn. Reson.* **1998**, *14* (2), 235-254. DOI: 10.1007/BF03161892.
- (224) Liu, B.; Li, C.; Zhang, G.; Yao, X.; Chuang, S. S. C.; Li, Z. Oxygen Vacancy Promoting Dimethyl Carbonate Synthesis from CO<sub>2</sub> and Methanol over Zr-Doped CeO<sub>2</sub> Nanorods. *ACS Catal.* **2018**, *8* (11), 10446-10456. DOI: 10.1021/acscatal.8b00415.
- (225) Kattel, S.; Yan, B.; Yang, Y.; Chen, J. G.; Liu, P. Optimizing Binding Energies of Key Intermediates for CO<sub>2</sub> Hydrogenation to Methanol over Oxide-Supported Copper. *J. Am. Chem. Soc.* **2016**, *138* (38), 12440-12450. DOI: 10.1021/jacs.6b05791.
- (226) Shido, T.; Asakura, K.; Iwasawa, Y. Reactant-promoted reaction mechanism for catalytic water-gas shift reaction on MgO. *J. Catal.* **1990**, *122* (1), 55-67. DOI: [https://doi.org/10.1016/0021-9517\(90\)90261-H](https://doi.org/10.1016/0021-9517(90)90261-H).
- (227) Zhao, K.; Wang, L.; Moiola, E.; Calizzi, M.; Züttel, A. Identifying Reaction Species by Evolutionary Fitting and Kinetic Analysis: An Example of CO<sub>2</sub> Hydrogenation in DRIFTS. *J. Phys. Chem. C* **2019**, *123* (14), 8785-8792. DOI: 10.1021/acs.jpcc.8b11105.
- (228) Cisneros, S.; Abdel-Mageed, A.; Mosrati, J.; Bartling, S.; Rockstroh, N.; Atia, H.; Abed, H.; Rabeah, J.; Brückner, A. Oxygen vacancies in Ru/TiO<sub>2</sub> - drivers of low-temperature CO<sub>2</sub> methanation assessed by multimodal operando spectroscopy. *iScience* **2022**, *25* (3), 103886. DOI: <https://doi.org/10.1016/j.isci.2022.103886>.
- (229) Franken, T.; Terreni, J.; Borgschulte, A.; Heel, A. Solid solutions in reductive environment – A case study on improved CO<sub>2</sub> hydrogenation to methane on cobalt based catalysts derived from ternary mixed metal oxides by modified reducibility. *J. Catal.* **2020**, *382*, 385-394. DOI: 10.1016/j.jcat.2019.12.045.
- (230) Van Santen, R. A. Complementary Structure Sensitive and Insensitive Catalytic Relationships. *Acc. Chem. Res.* **2009**, *42* (1), 57-66. DOI: 10.1021/ar800022m.
- (231) Rabea, A. I. M.; Le, S. D.; Higashimine, K.; Nishimura, S. Aerobic Oxidation of 5-Hydroxymethylfurfural into 2,5-Furandicarboxylic Acid over Gold Stabilized on Zirconia-Based Supports. *ACS Sustainable Chemistry & Engineering* **2020**, *8* (18), 7150-7161. DOI: 10.1021/acssuschemeng.0c01619.
- (232) Gloter, A.; Ewels, C.; Umek, P.; Arcon, D.; Colliex, C. Electronic structure of titania-based nanotubes investigated by EELS spectroscopy. *Physical Review B* **2009**, *80* (3), 035413. DOI: 10.1103/PhysRevB.80.035413.
- (233) Akita, T.; Kohyama, M. Visualization of the distribution of anatase and rutile TiO<sub>2</sub> crystals in Au/TiO<sub>2</sub> powder catalysts by STEM-EELS spectrum imaging. *Surf. Interface Anal.* **2014**, *46* (12-13), 1249-1252. DOI: <https://doi.org/10.1002/sia.5582>.
- (234) Radnik, J.; Mohr, C.; Claus, P. On the origin of binding energy shifts of core levels of supported gold nanoparticles and dependence of pretreatment and material synthesis. *Physical Chemistry Chemical Physics* **2003**, *5* (1), 172-177, 10.1039/B207290D. DOI: 10.1039/B207290D.
- (235) Wang, Y.; Widmann, D.; Behm, R. J. Influence of TiO<sub>2</sub> Bulk Defects on CO Adsorption and CO Oxidation on Au/TiO<sub>2</sub>: Electronic Metal-Support Interactions (EMSIs) in Supported Au Catalysts. *ACS Catal.* **2017**, *7* (4), 2339-2345. DOI: 10.1021/acscatal.7b00251.

- (236) Baron, M.; Bondarchuk, O.; Stacchiola, D.; Shaikhutdinov, S.; Freund, H. J. Interaction of Gold with Cerium Oxide Supports: CeO<sub>2</sub> (111) Thin Films vs CeO<sub>x</sub> Nanoparticles. *J. Phys. Chem. C*. **2009**, *113* (15), 6042-6049. DOI: 10.1021/jp9001753.
- (237) Kotobuki, M.; Leppelt, R.; Hansgen, D. A.; Widmann, D.; Behm, R. J. Reactive oxygen on a Au/TiO<sub>2</sub> supported catalyst. *J. Catal.* **2009**, *264* (1), 67-76. DOI: <https://doi.org/10.1016/j.jcat.2009.03.013>.
- (238) Bianchi, D.; Chafik, T.; Khalfallah, M.; Teichner, S. J. Intermediate species on zirconia supported methanol aerogel catalysts: II. Adsorption of carbon monoxide on pure zirconia and on zirconia containing zinc oxide. *Appl. Catal. A: Gen.* **1993**, *105* (2), 223-249. DOI: [https://doi.org/10.1016/0926-860X\(93\)80250-T](https://doi.org/10.1016/0926-860X(93)80250-T).
- (239) Araña, J.; Garriga i Cabo, C.; Doña-Rodríguez, J. M.; González-Díaz, O.; Herrera-Melián, J. A.; Pérez-Peña, J. FTIR study of formic acid interaction with TiO<sub>2</sub> and TiO<sub>2</sub> doped with Pd and Cu in photocatalytic processes. *Appl. Surf. Sci.* **2004**, *239* (1), 60-71. DOI: <https://doi.org/10.1016/j.apsusc.2004.04.039>.
- (240) Larmier, K.; Liao, W.-C.; Tada, S.; Lam, E.; Verel, R.; Bansode, A.; Urakawa, A.; Comas-Vives, A.; Copéret, C. CO<sub>2</sub>-to-Methanol Hydrogenation on Zirconia-Supported Copper Nanoparticles: Reaction Intermediates and the Role of the Metal–Support Interface. *Angew. Chem. Int. Ed.* **2017**, *56* (9), 2318-2323. DOI: <https://doi.org/10.1002/anie.201610166>.
- (241) Eckle, S.; Denkwitz, Y.; Behm, R. J. Activity, selectivity, and adsorbed reaction intermediates/reaction side products in the selective methanation of CO in reformat gases on supported Ru catalysts. *J. Catal.* **2010**, *269* (2), 255-268. DOI: <https://doi.org/10.1016/j.jcat.2009.10.025>.
- (242) Grunwaldt, J.-D.; Maciejewski, M.; Becker, O. S.; Fabrizioli, P.; Baiker, A. Comparative Study of Au/TiO<sub>2</sub> and Au/ZrO<sub>2</sub> Catalysts for Low-Temperature CO Oxidation. *J. Catal.* **1999**, *186* (2), 458-469. DOI: <https://doi.org/10.1006/jcat.1999.2564>.
- (243) Fisher, I. A.; Bell, A. T. In-Situ Infrared Study of Methanol Synthesis from H<sub>2</sub>/CO<sub>2</sub> over Cu/SiO<sub>2</sub> and Cu/ZrO<sub>2</sub>/SiO<sub>2</sub>. *J. Catal.* **1997**, *172* (1), 222-237. DOI: <https://doi.org/10.1006/jcat.1997.1870>.
- (244) Horiuchi, T.; Hidaka, H.; Fukui, T.; Kubo, Y.; Horio, M.; Suzuki, K.; Mori, T. Effect of added basic metal oxides on CO<sub>2</sub> adsorption on alumina at elevated temperatures. *Appl. Catal. A: Gen.* **1998**, *167* (2), 195-202. DOI: [https://doi.org/10.1016/S0926-860X\(97\)00318-9](https://doi.org/10.1016/S0926-860X(97)00318-9).
- (245) He, M.-Y.; White, J. M.; Ekerdt, J. G. CO and CO<sub>2</sub> hydrogenation over metal oxides: a comparison of ZnO, TiO<sub>2</sub> and ZrO<sub>2</sub>. *J. Mol. Catal.* **1985**, *30* (3), 415-430. DOI: [https://doi.org/10.1016/0304-5102\(85\)85051-3](https://doi.org/10.1016/0304-5102(85)85051-3).
- (246) Wang, X.; Shi, H.; Kwak, J. H.; Szanyi, J. Mechanism of CO<sub>2</sub> Hydrogenation on Pd/Al<sub>2</sub>O<sub>3</sub> Catalysts: Kinetics and Transient DRIFTS-MS Studies. *ACS Catal.* **2015**, *5* (11), 6337-6349. DOI: 10.1021/acscatal.5b01464.
- (247) Goguet, A.; Meunier, F. C.; Tibiletti, D.; Breen, J. P.; Burch, R. Spectrokinetic Investigation of Reverse Water-Gas-Shift Reaction Intermediates over a Pt/CeO<sub>2</sub> Catalyst. *J. Phys. Chem. B*. **2004**, *108* (52), 20240-20246. DOI: 10.1021/jp047242w.
- (248) Chiesa, M.; Paganini, M. C.; Livraghi, S.; Giamello, E. Charge trapping in TiO<sub>2</sub> polymorphs as seen by Electron Paramagnetic Resonance spectroscopy. *Phys. Chem. Chem. Phys.* **2013**, *15* (24), 9435-9447, 10.1039/C3CP50658D. DOI: 10.1039/c3cp50658d.
- (249) Gao, R.; Xu, J.; Wang, J.; Lim, J.; Peng, C.; Pan, L.; Zhang, X.; Yang, H.; Zou, J.-J. Pd/Fe<sub>2</sub>O<sub>3</sub> with Electronic Coupling Single-Site Pd–Fe Pair Sites for Low-Temperature Semihydrogenation of Alkynes. *J. Am. Chem. Soc.* **2022**, *144* (1), 573-581. DOI: 10.1021/jacs.1c11740.
- (250) Zhou, M.; Yang, M.; Yang, X.; Zhao, X.; Sun, L.; Deng, W.; Wang, A.; Li, J.; Zhang, T. On the mechanism of H<sub>2</sub> activation over single-atom catalyst: An understanding of

- Pt<sub>1</sub>/WO<sub>x</sub> in the hydrogenolysis reaction. *Chinese Journal of Catalysis* **2020**, *41* (3), 524-532. DOI: [https://doi.org/10.1016/S1872-2067\(19\)63517-5](https://doi.org/10.1016/S1872-2067(19)63517-5).
- (251) Chen, H.-Y. T.; Tosoni, S.; Pacchioni, G. Hydrogen Adsorption, Dissociation, and Spillover on Ru<sub>10</sub> Clusters Supported on Anatase TiO<sub>2</sub> and Tetragonal ZrO<sub>2</sub> (101) Surfaces. *ACS Catal.* **2015**, *5* (9), 5486-5495. DOI: 10.1021/acscatal.5b01093.
- (252) Rodríguez, J. A.; Evans, J.; Graciani, J.; Park, J.-B.; Liu, P.; Hrbek, J.; Sanz, J. F. High Water–Gas Shift Activity in TiO<sub>2</sub> (110) Supported Cu and Au Nanoparticles: Role of the Oxide and Metal Particle Size. *J. Phys. Chem. C* **2009**, *113* (17), 7364-7370. DOI: 10.1021/jp900483u.
- (253) Senanayake, S. D.; Stacchiola, D.; Liu, P.; Mullins, C. B.; Hrbek, J.; Rodriguez, J. A. Interaction of CO with OH on Au(111): HCOO, CO<sub>3</sub>, and HOCO as Key Intermediates in the Water-Gas Shift Reaction. *J. Phys. Chem. C* **2009**, *113* (45), 19536-19544. DOI: 10.1021/jp908169s.
- (254) Silaghi, M.-C.; Comas-Vives, A.; Copéret, C. CO<sub>2</sub> Activation on Ni/γ-Al<sub>2</sub>O<sub>3</sub> Catalysts by First-Principles Calculations: From Ideal Surfaces to Supported Nanoparticles. *ACS Catal.* **2016**, *6* (7), 4501-4505. DOI: 10.1021/acscatal.6b00822.
- (255) Li, J.; Zhao, X.; Ma, Z.; Pei, Y. Structure and Catalytic Activity of Gold Clusters Supported on Nitrogen-Doped Graphene. *J. Phys. Chem. C* **2021**, *125* (9), 5006-5019. DOI: 10.1021/acs.jpcc.0c08356.
- (256) Lin, L.-Y.; Kavadiya, S.; He, X.; Wang, W.-N.; Karakocak, B. B.; Lin, Y.-C.; Berezin, M. Y.; Biswas, P. Engineering stable Pt nanoparticles and oxygen vacancies on defective TiO<sub>2</sub> via introducing strong electronic metal-support interaction for efficient CO<sub>2</sub> photoreduction. *Chem. Eng. J.* **2020**, *389*, 123450. DOI: <https://doi.org/10.1016/j.cej.2019.123450>.
- (257) Prieto, G. Carbon Dioxide Hydrogenation into Higher Hydrocarbons and Oxygenates: Thermodynamic and Kinetic Bounds and Progress with Heterogeneous and Homogeneous Catalysis. *ChemSusChem* **2017**, *10* (6), 1056-1070. DOI: <https://doi.org/10.1002/cssc.201601591>.
- (258) Vieira, L. H.; Rasteiro, L. F.; Santana, C. S.; Catuzo, G. L.; da Silva, A. H. M.; Assaf, J. M.; Assaf, E. M. Noble Metals in Recent Developments of Heterogeneous Catalysts for CO<sub>2</sub> Conversion Processes. *ChemCatChem* **2023**, *15* (14), e202300493. DOI: <https://doi.org/10.1002/cctc.202300493>.
- (259) Have, I. C. t.; Kromwijk, J. J. G.; Monai, M.; Ferri, D.; Sterk, E. B.; Meirer, F.; Weckhuysen, B. M. Uncovering the reaction mechanism behind CoO as active phase for CO<sub>2</sub> hydrogenation. *Nat. Commun.* **2022**, *13* (1), 324. DOI: 10.1038/s41467-022-27981-x.
- (260) Elliott, J. R.; Lira, C. T. *Introductory Chemical Engineering Thermodynamics*; Prentice Hall, 2012.
- (261) Biesinger, M. C. Accessing the robustness of adventitious carbon for charge referencing (correction) purposes in XPS analysis: Insights from a multi-user facility data review. *Appl. Surf. Sci.* **2022**, *597*, 153681. DOI: <https://doi.org/10.1016/j.apsusc.2022.153681>.
- (262) Korhonen, S. T.; Calatayud, M.; Krause, A. O. I. Structure and Stability of Formates and Carbonates on Monoclinic Zirconia: A Combined Study by Density Functional Theory and Infrared Spectroscopy. *J. Phys. Chem. C* **2008**, *112* (41), 16096-16102. DOI: 10.1021/jp803353v.
- (263) Bachiller-Baeza, B.; Rodriguez-Ramos, I.; Guerrero-Ruiz, A. Interaction of Carbon Dioxide with the Surface of Zirconia Polymorphs. *Langmuir* **1998**, *14* (13), 3556-3564. DOI: 10.1021/la970856q.
- (264) Nagase, H.; Naito, R.; Tada, S.; Kikuchi, R.; Fujiwara, K.; Nishijima, M.; Honma, T. Ru nanoparticles supported on amorphous ZrO<sub>2</sub> for CO<sub>2</sub> methanation. *Catal. Sci. Technol.* **2020**, *10* (14), 4522-4531. DOI: 10.1039/d0cy00233j.

(265) Bando, K. K.; Sayama, K.; Kusama, H.; Okabe, K.; Arakawa, H. In-situ FT-IR study on CO<sub>2</sub> hydrogenation over Cu catalysts supported on SiO<sub>2</sub>, Al<sub>2</sub>O<sub>3</sub>, and TiO<sub>2</sub>. *Appl. Catal. A: Gen.* **1997**, *165* (1), 391-409. DOI: [https://doi.org/10.1016/S0926-860X\(97\)00221-4](https://doi.org/10.1016/S0926-860X(97)00221-4).

# Lebenslauf

## Personal data

Birth date / -place 11.02.1988 in Entrerrios, Colombia  
Nationality Colombian  
Family status Single

## Education

10.2020 - 07.2023 Promotion, Leibniz Institut für Katalyse, Rostock, Germany  
Topic: “*Structure-Reactivity Relationships in Heterogeneous Catalytic CO<sub>2</sub> Hydrogenation to CH<sub>4</sub> and CO on Low Loaded Precious Metal Catalysts*”  
supervised by Prof. Dr. Angelika Brückner

10.2016 - 12.2018 Master in Energy Science and Technology, Ulm university, Germany  
Topic: “*Selective CO Methanation on High Surface Ru/TiO<sub>2</sub> catalysts: Moderation of the Strong Metal-Support Interactions by SiO<sub>2</sub> doping*”  
supervised by Prof. Dr. Jürgen Behm

02.2012 - 08.2014 Master in Chemical Engineering, National university, Medellín, Colombia  
Topic: “*Cyclic Voltametry Evaluation of Different Anode Materials for the Electrooxidation of Coal in Molten KOH and Simulation of a Fuel Cell*”  
supervised by MSc. Carlos Ignacio Sánchez Sáenz

01.2005 - 11.2010 Bachelor in Chemical Engineering, National university, Medellín, Colombia  
Topic: “*Effect of the Fenton Process on Coal Desulfurization with Reduction of Iron Ions on a Graphite Electrode*” supervised by MSc. Carlos Ignacio Sánchez Sáenz

01.1999 - 10.2004 High School, Pontifical Bolivarian University School, Medellín, Colombia

## List of publications

2023 Rabeah, A. I. M.; Zhao, D.; Cisneros, S.; Kreyenschulte, C. R.; Kondratenko, V.; Bartling, S.; Kubis, C.; Kondratenko, E. V.; Brückner, A.; Rabeah, J. Role of interfacial oxygen vacancies in low-loaded Au-based catalysts for the low-temperature reverse water gas shift reaction. *Appl. Catal. B: Environ.* **2023**, 321, 122083. DOI: <https://doi.org/10.1016/j.apcatb.2022.122083>

2022 Cisneros, S.; Abdel-Mageed, A.; Mosrati, J.; Bartling, S.; Rockstroh, N.; Atia, H.; Abed, H.; Rabeah, J.; Brückner, A. Oxygen vacancies in Ru/TiO<sub>2</sub> - drivers of low-temperature CO<sub>2</sub> methanation assessed by multimodal operando spectroscopy. *iScience* **2022**, 25 (3), 103886. DOI: <https://doi.org/10.1016/j.isci.2022.103886>

Cisneros, S.; Chen, S.; Fauth, C.; Abdel-Mageed, A. M.; Pollastri, S.; Bansmann, J.; Olivi, L.; Aquilanti, G.; Atia, H.; Rabeah, J.; et al. Controlling

the selectivity of high-surface-area Ru/TiO<sub>2</sub> catalysts in CO<sub>2</sub> reduction - modifying the reaction properties by Si doping of the support. *Appl. Catal. B: Environ.* **2022**, 317, 121748. DOI: <https://doi.org/10.1016/j.apcatb.2022.121748>

Abed, H.; Mosrati, J.; Abdel-Mageed, A. M.; Cisneros, S.; Vuong, H.; Rockstroh, N.; Bartling, S.; Wohlrab, S.; Brückner, A.; Rabeah, J. Preferential CO Oxidation on a Highly Active Cu Single Atom Catalyst Supported by Ce-TiO<sub>x</sub>. *ChemCatChem.* **2022**, 14, e202200923. DOI: <https://doi.org/10.1002/cctc.202200923>

2021 Cisneros, S.; Chen, S.; Diemant, T.; Bansmann, J.; Abdel-Mageed, A.M.; Goepel, M.; Olesen, S. E.; Welter, E. S.; Parlinska-Wojtan, M.; Gläser, R.; et al. Effects of SiO<sub>2</sub>-doping on high-surface-area Ru/TiO<sub>2</sub> catalysts for the selective CO methanation. *Appl. Catal. B: Environ.* **2021**, 282. DOI: <https://10.1016/j.apcatb.2020.119483>

Chen, S.; Abdel-Mageed, A.M.; Li, M.; Cisneros, S.; Bansmann, J.; Rabeah, J.; Brückner, A.; Groß, A.; Behm, R. J. Electronic metal-support interactions and their promotional effect on CO<sub>2</sub> methanation on Ru/ZrO<sub>2</sub> catalysts. *J. Catal.* **2021**, 400, 407-420. DOI: <https://doi.org/10.1016/j.jcat.2021.06.028>

2019 Chen, S.; Abdel-Mageed, A.M.; Li, D.; Bansmann, J.; Cisneros, S.; Biskupek, J.; Huang, W.; Behm, J. Morphology Engineered Highly Active and Stable Ru/TiO<sub>2</sub> Catalysts for selective CO Methanation. *Angew. Chem. Int. Ed.* 58, 10732 – 10736. DOI: <https://doi.org/10.1002/anie.201903882>

★ Oral presentations

2021 “Modulating the chemical state of Ru supported on TiO<sub>2</sub> to control CO<sub>2</sub> hydrogenation selectivity” Cluster Meeting 2021, Prag

2022 “Methanation of CO<sub>2</sub> Promoted by Vacancies in Ru/TiO<sub>2</sub>-Sol-Gel Catalysts” ISGC 2022, La Rochelle

Rostock, 09.02.2024

Sebastian Cisneros